# Invited Speaker

**1185** Quantification of Potential Drops Across Semiconductor Heterointerfaces Using 4D-STEM: prospects and pitfalls
Prof. Dr. Kerstin Volz
**233** In situ TEM study of phase and electronic structure transformations in amorphous Ga2O3
Dr JIJUN ZHANG[1], Mr. Thilo Remmele[1], Miss. Wenshan Chen[2], Mr. Hans Tornatzky[2], Mr. Oliver Bierwagen[2], Dr. Dan Zhou[1], Mr. Martin Albrecht[1]
[1]Leibniz-Institut für Kristallzüchtung, Max-Born-Straße 2, 12489 Berlin, Germany, [2]Paul-Drude-Institut für Festkörperelektronik, Leibniz-Institut im Forschungsverbund Berlin e.V., Hausvogteiplatz 5-7, 10117, Berlin, Germany

# Oral Presentation

**149** Strain Sensitivity of STEM-GPA-based Strain Map
Bumsu Park[1], Minsik Kim[1], Jiwon Jeong[1], Sungho Lee[1]
[1]Samsung Electronics Advanced Analysis Science & Engineering Team, Hwaseong-si/Samnsungjeonja-ro, Republic of Korea
**198** Advanced EELS spectroscopy characterization of AlGaN/GaN materials
Mr Esteve Drouillas[1,2], Mrs. Bénédicte Warot-Fonrose[2], Mr. Jean-Gabriel Mattei[1]
[1]STMicroelectronics Crolles 2, Crolles, FRANCE, [2]CEMES-CNRS, Toulouse, FRANCE
**245** Investigating All-Inorganic Halide Perovskite Phase Transformations via in-situ 4D STEM Heating Experiments
Mr Tom Warwick[1], Mr. Paul Smeets[2,3], Mr. Roberto dos Reis[2,3]
[1]Gatan, Inc., Pleasanton, United States, [2]Department of Materials Science and Engineering, Northwestern University, Evanston, United States, [3]Northwestern University Atomic and Nanoscale Characterization Experimental (NUANCE) Center, Northwestern University, Evanston, United States
**257** Mapping electric fields in real nanodevices by operando electron holography
Dr Christophe Gatel[1], Dr Leigeng Zhang[2], Dr Kilian Gruel[2], Dr Frédéric Lorut[3], Dr Martin Hÿtch[2]
[1]CEMES-CNRS, University Toulouse III - Paul Sabatier, Toulouse, France, [2]CEMES-CNRS, Toulouse, France, [3]STMicroelectronics, Crolles, France
**353** Unveiling Strain Fields and Plastic Relaxation in Narrow-Core GaAs/In(Al,Ga)As Nanowires with High-Resolution Electron Microscopy
Mrs Polyxeni Chatzopoulou[1], Dr Isaak Vasileiadis[1], Mr Donovan Hillard[2,3], Dr Nikoletta Florini[1], Dr Vivek Devulapalli[4], Dr Christian Liebscher[4], Assoc. Prof. Liverios Lymperakis[5], Prof. Thomas Kehagias[1], Prof. Philomela Komninou[1], Dr. Emmanouil Dimakis[2], Professor George Dimitrakopulos[1]
[1]Physics Department, Aristotle University of Thessaloniki, Thessaloniki, Greece, [2]Helmholtz-Zentrum Dresden-Rossendorf, Dresden, Germany, [3]TUD Dresden University of Technology, Dresden, Germany, [4]Max-Planck Institut für Eisenforschung GmbH, Düsseldorf, Germany, [5]Physics Department, University of Crete, Heraklion, Greece
**578** Controlling heterostructures with atomic precision in III-V nanowires using microheaters in an in-situ TEM
Mr. Christopher Røhl Yskes Andersen[1,2], Mr. Marcus Tornberg[3,4,5], Mr. Sebastian Lehmann[4,5], Mr. Daniel Jacobsson[3,4], Prof. Jonas Johansson[4,5], Prof. Kimberly A. Dick[3,4,5], Prof. Kristian S. Mølhave[1]
[1]DTU Nanolab, Technical University of Denmark, Kgs. Lyngby, Denmark, [2]Quantum DTU, Technical University of Denmark, Kgs. Lyngby, Denmark, [3]nCHREM, Lund University, Lund, Sweden, [4]NanoLund, Lund University, Lund, Sweden, [5]Solid State Physics, Lund Uni., Lund, , Lund, Sweden
**83** Inversion of the Internal Electric Field in GaN/AlN Heterostructures Studied by Off-Axis Electron Holography
Lou Denaix[1], Dr Florian Castioni[1], Dr Matthew Bryan[1], Dr David Cooper[1], Dr Eva Monroy[2]

[1]Univ. Grenoble Alpes, CEA, Leti, Grenoble, France, [2]Univ. Grenoble Alpes, CEA, Grenoble INP, Irig, Pheliqs, Grenoble, France

**258** Detection limits of electric field characterization at a p-n junction by 4D-STEM

Bruno Cesar da Silva[1], Yiran Lu[1], Alexis Wartelle[1], Eva Monroy[2], Jean-Luc Rouviere[3], David Cooper[4], Dr Martien den Hertog[1]

[1]Univ. Grenoble Alpes, CNRS, Grenoble INP, Institut Néel, 38000 Grenoble, France, Grenoble, France, [2]Univ. Grenoble-Alpes, CEA, Grenoble INP, IRIG, PHELIQS, Grenoble, France, Grenoble, France, [3]Univ. Grenoble-Alpes, CEA-IRIG, MEM, Grenoble, France, Grenoble, France, [4]CEA, LETI, MINATEC, Grenoble, France, Grenoble, France

**399** Low-Dose 4D-STEM Investigations of the Octahedral Network Structure in Formamidinium Lead Bromide Nanocrystals

Nadine Schrenker[1,2], Mr. Tom Braeckevelt[3], Mrs. Annick De Backer[1,2], Mr. Nikolaos Livakas[4], Mr. Chu-Ping Yu[1,2], Mr. Thomas Friedrich[1,2], Mr. Daen Jannis[1,2], Mr. Armand Béché[1,2], Mr. Maarten Roeffaers[5], Mr. Johan Hofkens[6], Mr. Johan Verbeeck[1,2], Mr. Liberato Manna[4], Mrs. Veronique Van Speybroeck[3], Mrs. Sandra Van Aert[1,2], Mrs. Sara Bals[1,2]

[1]Electron Microscopy for Materials Science (EMAT), University of Antwerp, Antwerp, Belgium, [2]NANOlab Center of Excellence, University of Antwerp, Antwerp, Belgium, [3]Center for Molecular Modeling, Ghent University, , Belgium, [4]Department of Nanochemistry, Istituto Italiano di Tecnologia (IIT), Genova, Italy, [5]cMACS, Department of Microbial and Molecular Systems, KU Leuven, Leuven, Belgium, [6]Department of Chemistry, KU Leuven, Leuven, Belgium

**439** Picoseconds and nanometers; time and spatially resolved cathodoluminescence spectroscopy to characterise nonradiative defects in semiconductors.

Dr. Gunnar Kusch[1], Dr. Thomas Weatherley[2], Dr. Frank Mehnke[3], Dr. Eamon T. Hughes[4], Dr. Tim Wernicke[3], Dr. Justin Norman[4], Prof. John E. Bowers[4], Prof. Kunal Mukherjee[5], Prof. Michael Kneissl[3], Prof. Nicolas Grandjean[2], Prof. Rachel A. Oliver[1]

[1]University of Cambridge, Cambridge, United Kingdom, [2]Ecole Polytechnique Fédérale de Lausanne, Lausanne, Switzerland, [3]Technische Universität Berlin, Berlin, Germany, [4]University of California Santa Barbara, Santa Barbara, USA, [5]Stanford University, Stanford, USA

**471** In situ TEM thermal study of MBE and CVD GeSn layers: cross-section and plan-view geometries

Karí Martínez[1], Alexey Minenkov[1], Johannes Aberl[2], Moritz Brehm[2], Heiko Groiss[1]

[1]Christian Doppler Laboratory for Nanoscale Phase Transformations, Center for Surface and Nanoanalytics, Johannes Kepler University Linz, 4040 Linz, Austria, [2]Institute of Semiconductor and Solid-State Physics, Johannes Kepler University Linz, 4040 Linz, Austria

**503** Sn Alloying Impact on Structural and Electronic Properties of Core-Shell Ge-GeSn Nanowires: A TEM Study

Milenka Andelic[1], Dr. Alexandre Pofelski[1,4], Dr. Isobel Bicket[1,2,3], Dr. Simone Assali[5], Dr. Sebastian Koelling[5], Dr Lo Luo[5], Dr. Oussama Moutanabbir[5], Dr. Gianluigi Botton[1,6]

[1]McMaster University, Hamilton, Canada, [2]Atominstitut, TU Wien, Vienna, Austria, [3]University Service Centre for Transmission Electron Microscopy, TU Wien, Vienna, Austria, [4]Brookhaven National Laboratory, Upton, USA, [5]Ecole Polytechnique Montreal, Montreal, Canada, [6]Diamond Light Source, Oxfordshire, UK

**228** Study on local indium concentration in Ga(1-x)InxN quantum wells using quantitative scanning transmission electron microscopy

Daesung Park[1,3], Jannik Guckel[1,3], Philipp Horenburg[2], Heiko Bremers[2,3], Uwe Rossow[2], Andreas Hangleiter[2,3], Harald Bosse[1,3]

[1]Physikalisch-Technische Bundesanstalt (PTB), Braunschweig,, Germany, [2]Institute of Applied Physics (IAP), Technische Universität Braunschweig, Braunschweig,, Germany, [3]Laboratory for Emerging Nanometrology (LENA), Braunschweig,, Germany

**332** Growth of Au-seeded GaAs-GaSb nanowires explored in environmental TEM

Phd Candidate Mikelis Marnauza[1,2], Dr. Robin Sjökvist[1,2], Ms. Azemina Kraina[1,2], Dr. Daniel Jacobsson[1,2,3], Prof. Kimberly Dick-Thelander[1,2]

[1]Centre for Analysis and Synthesis, Lund University, Lund, Sweden, [2]NanoLund, Lund University, Lund, Sweden, [3]National Centre for High Resolution Electron Microscopy, Lund University, Lund, Sweden, [4]Solid State Physics, Lund University, Lund, Sweden

**514** Understanding phase and chemical transitions in Ge-rich GeSbTe based phase change memory: a (S)TEM tribute

Sijia RAN[1], Minh-Anh LUONG[1], Eloïse RAHIER[1], Elisa PETRONI[2], Daniel BENOIT[3], Alain CLAVERIE[1]
[1]CEMES-CNRS and University of Toulouse, Toulouse, France, [2]STMicroelectronics, Agrate Brianza, Italy, [3]STMicroelectronics, Crolles, France

**530** Momentum resolved band gap measurement by high energy resolution electron energy loss spectroscopy

Dr Dileep Krishnan[1], Dr. Ioannis Iatrakkis
[1]Thermofisher Scientific, Eindhoven, Netherlands

**640** Probing photonic resonant modes in InAs semiconductor nanostructures by STEM-EELS

Yajie Wang[1], Qingnan Cai[1], Zifan Huo[2], Yanhui Zhang[2], Pingping Chen[2], Kun Ding[1], Changlin Zheng[1]
[1]State Key Laboratory of Surface Physics and Department of Physics, Fudan University, Shanghai, China, [2]State Key Laboratory of Infrared Physics, Shanghai Institute of Technology Physics，Chinese Academy of Sciences, Shanghai, China

**656** Structural and optoelectronic properties of layered halide perovskites

Dr Giorgio Divitini[1], Dr Andrea Griesi[1], Mr Andrea Cicconardi[1], Dr Sirous Khabbazabkenar[1], Dr Yurii Ivanov[1], Dr Gunnar Kusch[2], Prof Rachel A Oliver[2]
[1]Istituto Italiano di Tecnologia, Genoa, Italy, [2]Department of Materials Science, University of Cambridge, Cambridge, UK

**705** In-Situ Charging and Charging Map for Characterization of Electronic Materials

Dr. Wen-Shan Zhang[1], Dr. Nikolai Hippchen[1], Prof. Dr. Rasmus R. Schröder[2], Prof. Dr. Uwe H. F. Bunz[1]
[1]Institute of Organic Chemistry, Ruprecht-Karls-University Heidelberg, Im Neuenheimer Feld 270, Heidelberg, Germany, [2]Bioquant, Ruprecht-Karls-University Heidelberg, Im Neuenheimer Feld 267, Heidelberg, Germany

**738** Band gap measurements of aluminum and indium doped Ga2O3 multilayers

Dr. Annett Thøgersen[1], Professor Lasse Vines[2], Dr. Georg Muntingh[1], Professor Øystein Prytz[2], Professor Holger von Wenckstern[3], Dr. Ingvild Julie Thue Jensen[1]
[1]SINTEF, Oslo, Norway, [2]UiO, Oslo, Norway, [3]University of Leipzig, Leipzig, Germany

# Poster Presentation

**82** Optimizing FIB-based sample preparation for quantitative in-situ biasing studies of semiconductors using 4D-STEM

Vitalii Lider[1], Franziska Hüppe[1], Saleh Firoozabadi[1], Shamail Ahmed[1], Jürgen Belz[1], Andreas Beyer[1], Kerstin Volz[1]
[1]Materials Science Centre and Department of Physics, Philipps University Marburg, Marburg, Germany

**109** Enhancing quantifiability of S/TEM-based composition mappings through correlative techniques

Kai-luis Jakob[1], Mr. Frederik Otto[1], Dr. Dirk Berger[2], Dr. Tore Niermann[1], Prof. Dr. Michael Lehmann[1]
[1]Technische Universität Berlin, Institute of Optics and Atomic Physics, Berlin, Germany, [2]Technische Universität Berlin, Zentraleinrichtung Elektronenmikroskopie (ZELMI), Berlin, Germany

**114** Electronic properties of W' twin domain walls in ferroelastic BiVO4

Yuwen Xu[1], Dr. Pankaj Sharma[2,3,4], Mr. Haotian Wen[1], Mr. Dawei Zhang[1,2], Dr. Charlie Kong[5], Dr. Zewu Yan[6], A/Prof. Shery L.Y. Chang[1,5], Prof. Jan Seidel[1,2]
[1]School of Materials Science and Engineering, UNSW Sydney, Sydney, Australia, [2]ARC Centre of Excellence in Future Low-Energy Electronics Technologies (FLEET), UNSW Sydney, Sydney, Australia, [3]College of Science and Engineering, Flinders University, Bedford Park, Australia, [4]Flinders Institute

for Nanoscale Science and Technology, Flinders University, Adelaide, Australia, [5]Electron Microscope Unit, Mark Wainwright Analytical Centre, UNSW Sydney, Sydney, Australia, [6]Laboratorium für Festkörperphysik, ETH Hönggerberg, Zürich, Switzerland

**141** Development and characterization of N2O-plasma oxide layers for high-temperature passivating contacts solar cells

Mrs Sofia Libraro[1], Mr Lars Bannenberg[2], Mr Theodosios Famprikis[2], Mr David Reyes[3], Mr Julien Hurni[1], Mr Christophe Ballif[1,4], Mr Franz-Josef Haug[1], Mrs Audrey Morisset[1], Aïcha Hessler-Wyser[1]
[1]Photovoltaics and thin-film electronics laboratory (PV-Lab), Institute of Electrical and Micro Engineering (IEM), École Polytechnique Fédérale de Lausanne (EPFL), 2000 Neuchâtel, Switzerland, [2]Department of Radiation Science and Technology, Faculty of Applied Sciences, DUT, Delft, the Netherlands, [3]Interdisciplinary Centre for Electron Microscopy, EPFL, 1015 Lausanne, Switzerland, [4]CSEM Sustainable Energy Center, 2000 Neuchâtel, Switzerland

**142** Characterization of aluminium diffusion in high-temperature passivating contacts by in situ scanning transmission electron microscopy

Mrs Sofia Libraro[1], Mr Janghyun Jo[2], Mr Maximilian Kruth[2], Mr Rafal Dunin-Borkowski[2], Mr Saul Estandia Rodrigez[3], Mr Pierpaolo Ranieri[3], Mr Christophe Ballif[1,4], Mrs Audrey Morisset[1], Mr Franz-Josef Haug[1], Aïcha Hessler-Wyser[1]
[1]Photovoltaics and thin-film electronics laboratory (PV-Lab), Institute of Electrical and Micro Engineering (IEM), École Polytechnique Fédérale de Lausanne (EPFL), Neuchâtel, Switzerland, [2]Ernst Ruska Center for Microscopy and Spectroscopy with Electrons, Jülich, Germany, [3]Institute of materials, École Polytechnique Fédérale de Lausanne (EPFL), Lausanne, Switzerland, [4]CSEM sustainable energy center, Neuchâtel, Switzerland

**271** Polar Discontinuity Governs Surface Segregation and Interface Termination: a case study of LaInO3/BaSnO3

Dr Martin Albrecht[1]
[1]Leibniz-Institut für Kristallzüchtung, Berlin, Germany, [2]Humboldt-Universität zu Berlin, Berlin, Germany, [3]ThermoFisher Scientific, Eindhoven, Netherlands, [4]Paul-Drude-Institut, Berlin, Germany

**279** Effect of Oxygen-Doping in Ferroelectric Wurtzite-type Al0.73Sc0.27N

Md Redwanul Islam[1], Dr. Niklas Wolff[1], Mr. Georg Schoenweger[2,4], Dr. Simon Fichtner[3,4], Dr. Lorenz Kienle[1]
[1]Synthesis and Real structure, Department of Material Science (Kiel University), Kiel, Germany, [2]Nanoelectronics, Institute of Electrical and Information Engineering (Kiel University), Kiel, Germany, Kiel, Germany, [3]Microsystem and technology transfer, Department of Material Science (Kiel University), Kiel, Germany, [4]Fraunhofer Institute for Silicon Technology, Itzehoe, Germany

**285** Fast and local determination of phases in (V1-xCrx)2O3 Mott materials

Mr Seyed-Mohammad Dolatabadi-Hamedi[1], Mr Eric Gautron[1], Mr Chris Leroux[1], Mohammed Haydoura[1], Mr Julien Tranchant[1], Mr Benoit Corraze[1], Mr Laurent Cario[1], Mr Etienne Janod[1], Seyed Mohammad Dolatabadi Hamedi[1]
[1]Nantes Université, CNRS, Institut des Matériaux de Nantes Jean Rouxel, NANTES, FRANCE

**302** Microstructure characterization of CIGS/GaP/Si tandem solar cells

Dr Eric Gautron[1], Mr. Eugène Bertin[2], Mr. Ludovic Arzel[1], Mr. Léo Choubrac[1], Mr. Antoine Létoublon[2], Mrs. Rozenn Gautheron[2], Mr. Charles Cornet[2], Mrs. Maud Jullien[2], Mrs. Sylvie Harel[1], Mr. Emmanuel Cadel[3], Mr. Olivier Durand[2], Mr. Nicolas Barreau[1]
[1]Nantes Université, CNRS, Institut des Matériaux de Nantes Jean Rouxel, IMN, Nantes, France, [2]INSA Rennes, CNRS, Institut Foton – UMR 6082, University of Rennes, Rennes, France, [3]Univ Rouen Normandie, INSA Rouen Normandie, CNRS, Normandie Univ, GPM UMR 6634, Rouen, France

**308** In-situ electrical characterization of MOSFET transistors using AFM-in-SEM solution

Ondrej Novotny[1], Libor Strakos[2], Marek Patocka[1], Vojtech Schanilec[1], Veronika Hegrova[1], Umberto Celano[3], Tomas Vystavel[2], Dr. Jan Neuman[1]
[1]NenoVision s. r. o., Brno, Czech Republic, [2]Thermo Fisher Scientific, Brno, Czech Republic, [3]Arizona State University, Tempe, USA

**320** Unraveling the composition of monolayer-thick InGaN/GaN quantum wells: A quantitative analysis via probe-corrected HRSTEM
Mr. Isaak G. Vasileiadis[1], Mr. Liverios Lymperakis[2], Mr. Adam Adikimenakis[3,4], Mr. Athanasios Gkotinakos[1], Mr. Vivek Devulapalli[2], Mr. Christian H. Liebscher[2], Mrs. Maria Androulidaki[3,4], Mr. Rene Hübner[5], Mr. Alexandros Georgakilas[3,4], Mr. Theodoros Karakostas[1], Professor Philomela Komninou[1], Mr. Emmanouil Dimakis[5], Mr. George P. Dimitrakopulos[1]
[1]School of Physics, Aristotle University of Thessaloniki, Thessaloniki, Greece, [2]Max-Planck Institut für Eisenforschung GmbH, Düsseldorf, Germany, [3]Microelectronics Research Group (MRG), IESL, FORTH, Heraklion, Greece, [4]Department of Physics, University of Crete, Heraklion, Greece, [5]Institute of Ion Beam Physics & Materials Research, Helmholtz-Zentrum Dresden-Rossendorf, Dresden, Germany
**345** Strain analysis comparison in complementary and nanosheet field-effect transistor devices: nanobeam vs Bessel electron diffraction
Paola Favia[1], Anabela Veloso[1], Geert Eneman[1], Ankit Nalin Mehta[1], Xiuju Zhou[1], Olivier Richard[1], Jef Geypen[1], Eva Grieten[1]
[1]Imec, Leuven, Belgium
**382** Atomic-scale Defects Critical to the Performance of Perovskite Solar Cells
Dr Weilun Li[1], Dr Mengmeng Hao[2,3], Dr Shanshan Ding[2,3], Mr Qimu Yuan[4], Prof. Michael Johnston[4], Prof. Lianzhou Wang[2,3], Prof. Joanne Etheridge[1,5,6]
[1]School of Physics and Astronomy, Monash University, Melbourne, Australia, [2]Nanomaterials Centre, Australian Institute for Bioengineering and Nanotechnology, The University of Queensland, St Lucia, Australia, [3]School of Chemical Engineering, The University of Queensland, St Lucia, Australia, [4]Department of Physics, University of Oxford, Clarendon Laboratory, United Kingdom, [5]Monash Centre for Electron Microscopy, Melbourne, Australia, [6]Department of Materials Science and Engineering, Monash University, Melbourne, Australia
**408** NBED investigations of coaxial (Al,In,Ga)As nanowires
Alina Friemel[1], Dr. Tore Niermann[1], Dr. Laura Niermann[1], Dr. Paul Schmiedeke[2], Dr. Gregor Koblmüller[2], Prof. Dr. Michael Lehmann[1]
[1]Technische Universität Berlin, Berlin, Germany, [2]Technische Universität München, Munic, Germany
**446** Electron microscopic investigation of photothermal laser printed ZnO nanoarchitectures
Kristian Kraft[1], Dr. Lukas Grünewald[1], Dr. Aina Quintilla[1], Dr. Erich Müller[1], Mr. Matthias Steurer[2,3,4,5], Dr. Paul Somers[3], Mr. Steven Kraus[2,3], Dr. Florian Feist[3], Dr. Bastian Weinert[3], Dr. Ben Breitung[3], Dr. Gabriel C. Marques[3], Prof. Dr. Stefanie Dehnen[3], Prof. Dr. Claus Feldmann[4], Prof. Dr. Christopher Barner Kowollik[3,5], Prof. Dr. Martin Wegener[2,3], Prof. Dr. Jasmin Aghassi[3], TT-Prof. Dr. Yolita Eggeler[1]
[1]Karlsruhe Institute of Technology (KIT), Laboratory for Electron Microscopy (LEM), Karlsruhe, Germany, [2]Karlsruhe Institute of Technology (KIT), Institute of Applied Physics (APH), Karlsruhe, Germany, [3]Karlsruhe Institute of Technology (KIT), Institute of Nanotechnology (INT), Karlsruhe, Germany, [4]Karlsruhe Institute of Technology (KIT), Institute of Inorganic Chemistry (AOC), Karlsruhe, Germany, [5]Queensland University of Technology (QUT), School of Chemistry and Physics, Brisbane, Australia
**495** Identification of the phases resulting from the thermal crystallization of Ge-rich GeSbTe alloys using EELS
Dr. Minh Anh Luong[1], Dr. Eloïse Rahier[1], Dr. Sijia Ran[1], Dr. Alain Claverie[1]
[1]CEMES-CNRS and University of Toulouse, 29 Rue Jeanne Marvig, 31055 Toulouse, France
**506** Strain mapping and simulation of transistor structures in a 22nm FDSOI technology
Dirk Utess[1], Dominik Martin Kleimaier[1], Etienne Billan[1], Tashfain Youssuf[1], Zhixing Zhao[1], Thorgund Nemec[1], Dr. Moritz Andreas Meyer[1], Dr. Jochen Rinderknecht[1]
[1]GlobalFoundries, Dresden, Germany
**558** STEM-EELS unveils atomic stacking in 2D MoSe2 ECM memristors.
Dr Khalil El Hajraoui[1,2], Dr Andrea Capasso[3], Mr Guilherme Araújo[3], Dr Demie Kepaptsoglou[1,2], Prof Quentin. M Ramasse[1,4]

[1]SuperSTEM Laboratory, SciTech Daresbury, Daresbury, United Kingdom, [2]School of Physics, Engineering and Technology, University of York, York, United Kingdom, [3]International Iberian Nanotechnology Laboratory, Braga, Portugal, [4]School of Chemical and Process Engineering & School of Physics and Astronomy, University of Leeds, Leeds, United Kingdom

**647** Effects of electron cascade and lamella preparation on InGaN quantum well recombination dynamics

Nika van Nielen[1], Delphine Lagard[2], Cleo Santini[3], Florian Castioni[4], Robin Cours[3], Andrea Balocchi[2], Teresa Hungria[5], Andrey Tsatsulnikov[6], Alexei Sakharov[6], Andrey Nikolaiev[6], Nikolay Cherkashin[3], Luiz Tizei[4], Albert Polman[1], Sophie Meuret[3]
[1]AMOLF, NWO, Amsterdam, Netherlands, [2]LPCNO, CNRS, Toulouse, France, [3]CEMES, CNRS, Toulouse, France, [4]Laboratoire de Physique des Solides, CNRS, Orsay, France, [5]Centre de Microcaracterisation Raimond Castaing, CNRS, Toulouse, France, [6]Ioffe Institute, , Russia

**679** The effects of solution processing methods on halide perovskite nanostructure

Dr Alexandra Sheader[1], Dr Ryley Ratnasingham[2], Dr Nakita Noel[1]
[1]University of Oxford, Oxford, UK, [2]Eindhoven University of Technology TU/e, Eindhoven, Netherlands

**730** Analysis of molecular packing and nanoscale atomic variation in polymer semiconductors

Sang Pham[1], Sean Collins[1,2]
[1]Bragg Centre for Materials Research & School of Chemical and Process Engineering, University of Leeds, Leeds, United Kingdom, [2]School of Chemistry, University of Leeds, Leeds, United Kingdom

**741** Characterization of 2DEG on WG semiconductors through sub-sampled 4DSTEM

Dr Giuseppe Nicotra[1], Dr Gianfranco Sfuncia[1], Dr Alex Robinson W[2], Dr Daniel Nicholls[3], Mr Jack Wells[2,3], Dr Antonio Mio M[1], Mr Corrado Bongiorno[1], Dr Cettina Bottari[5], Dr Salvatore Adamo[5], Dr Alfio Russo[5], Dr Santi Alessandrino[5], Prof. Nigel Browning D[4], Dr Corrado Spinella[1]
[1]CNR-IMM zona industriale strada VIII n.5, Catania, Italia, [2]SenseAI Innovations Ltd, Liverpool, UK, [3]Distributed Algorithms Centre for Doctoral Training, Liverpool, UK, [4]University of Liverpool, Liverpool, UK, [5]STMicroelectronics, Catania, Italy

**751** Structural and spectroscopic studies of Cu-doped NiO thin films

Mr Ahmad Althumali[1,2], Mr Ibrahim Aldawood[1], Mr Umit Dogan[3], Dr Adam Kerrigan[4], Dr Leonardo Lari[1,4], Dr Fahrettin Sarcan[3], Prof Ayse Erol[3], Prof Lidija Šiller[5], Prof Vlado K. Lazarov[1,4]
[1]School of Physics, Engineering and Technology, University of York, York , United Kingdom, [2]Department of Physics, Faculty of Science, Taif University, Taif , Saudi Arabia, [3]Department of Physics, Faculty of Science, Istanbul University, Istanbul, Turkey, [4]The York-JEOL Nanocentre, University of York, York, United Kingdom, [5]School of Engineering, Newcastle University, Newcastle upon Tyne , United Kingdom

**774** Observation of logic states of HfO2-based ferroelectric FETs using STEM-DPC

Thorgund Nemec[1,2], Dirk Utess[1], Stefan Duenkel[1], Martin Weisheit[1], Halid Mulaosmanovic[1], Sven Beyer[1], Moritz Andreas Meyer[1]
[1]GlobalFoundries Dresden Module One LLC & Co. KG, Dresden, Germany, [2]Institute of Materials Science, Faculty of Mechanical Science and Engineering, Dresden Technical University, Dresden, Germany

**890** Analytical TEM of materials for gas sensing

Catalina-Gabriela Mihalcea[1,2], Corneliu Ghica[1], Adelina Stanoiu[1], Cristian-Eugen Simion[1], Daniela Ghica[1], Mariana Stefan[1], Simona Somacescu[3], Ioana-Dorina Vlaicu[1], Alexandra-Corina Iacoban[1]
[1]National Institute of Materials Physics, Atomistilor 405A, 077125, Romania, [2]Faculty of Physics, University of Bucharest, Atomistilor 405, 077125 , Romania, [3]"Ilie Murgulescu" Institute of Physical Chemistry, Romanian Academy, Spl. Independentei 202, 060021, Romania

**898** TEM observations of threading dislocations in gallium nitride under external stimuli

Mrs. Eva Kolibalova[1,2], Daniel Citterberg[2], Richard Gazdik[3], Petr Babor[2,3], Tomas Sikola[2,3], Miroslav Kolibal[2,3]

[1]CEITEC Nano, Brno University of Technology, Brno, Czech Republic, [2]CEITEC, Brno University of Technology, Brno, Czech Republic, [3]Institute of Physical Engineering, Brno University of Technology, , Czech Republic

**926** TEM investigation of the defect structure in epitaxial corundum thin films

Claudio Bellani[1], Alberto Binetti[2], Wei-Fan Hsu[2], Simon Mellaerts[2], Koen Schouteden[2], Prof. Jean-Pierre Locquet[2], Prof. Jin Won Seo[1]
[1]Department of Materials Engineering, KU Leuven, Leuven, Belgium, [2]Department of Physics and Astronomy, KU Leuven, Leuven, Belgium

**932** In-situ TEM annealing of vanadium oxide thin films

Claudio Bellani[1], Simon Mellaerts[2], Koen Schouteden[2], Alberto Binetti[2], Wei-Fan Hsu[2], Prof. Jean-Pierre Locquet[2], Prof. Jin Won Seo[1]
[1]Department of Materials Engineering, KU Leuven, Leuven, Belgium, [2]Department of Physics and Astronomy, KU Leuven, Leuven, Belgium

**963** Robustness evaluation of electric field measurements via template matching in 4D-STEM

Alexis Wartelle[1], Matthew Bryan[2], Yiran Lu[1], David Cooper[2], Jean-Luc Rouvière[3], Martien den Hertog[1]
[1]Institut Néel, CNRS-UGA, Grenoble, France, [2]LETI, CEA, Grenoble, France, [3]MEM, IRIG, CEA, Grenoble, France

**999** Measurement of electrostatic fields in Ge-doped AlGaN structures by off-axis electron holography

Phd Student Alexis Palais[1], Director of Research David Cooper[1], Senior Researcher Eva Monroy[2], Director of Research Bérangère Hyot[1]
[1]CEA-LETI, Grenoble, France, [2]CEA, Grenoble INP, IRIG, PHELIQS, Grenoble, France

**1002** Structural and Electrical Characterization of $Hf_{0.5}Zr_{0.5}O_2$ Thin Films Crystallized by Rapid Thermal Annealing

Dr Jucheol Park[1], Miss Yeong Gyeong Park[1], Dr Min-Ho Kang[2], Mr Myung-Keun Lee[2], Mr Moon Seop Hyun[2]
[1]Gumi Electronics & Information Technology Research Institute (GERI), Gumi-si, Republic of Korea, [2]Department of Nano-process, National NanoFab Center (NNFC), Daejeon, Republic of Korea

**1033** Van der Waals heterostructures of nanopatterned 2D materials for novel device geometries

Michael Schlegel[1,2], Jonas Haas[1,2], Kevin Strobel[1,2], Teresa Tang[2], Prof. Dr. Jannik C. Meyer[1,2]
[1]Institute for Applied Physics at University of Tübingen, Tübingen, Germany, [2]Natural and Medical Sciences Institute at the University of Tübingen, Reutlingen, Germany

**1055** Structural characterization of partially relaxed hybrid radial (Pb,Sn)Te/WZ-GaAs nanowires as candidates for topological insulator nano-devices

Dr Maciej Wójcik[1], M.sc Sania Dad[1], M.sc Wiktoria Zajkowska-Pietrzak[1], M.sc Piotr Dziawa[1], Prof. Slawomir Kret[1], Prof. Wojciech Pacuski[2], Prof. Janusz Sadowski[3]
[1]Institute of Physics, Polish Academy of Sciences, Warsaw, Poland, [2]Faculty of Physics, University of Warsaw, Warsaw, Poland, [3]Ensemble3 Centre of Excellence, Warsaw, Poland

**1096** Nanowire field emitters fabricated using focused electron, gallium and helium ion beam methods

Ewelina Gacka[1], Krzysztof Kwoka[1], Tomasz Piasecki[1], Gregor Hlawacek[2], Bartosz Pruchnik[1], Ivo W. Rangelow[3], Andrzej Sierakowski[4], Paweł Janus[4], René Hübner[2], Teodor Gotszalk[1]
[1]Department of Nanometrology, Wrocław University of Science and Technology, 50-372, Wrocław, Poland, [2]Institute of Ion Beam Physics and Materials Research, Helmholtz-Zentrum Dresden-Rossendorf, 01328, Dresden, Germany, [3]Technische Universität Ilmenau, 98693, Ilmenau, Germany, [4]The Łukasiewicz Research Network - Institute of Microelectronics and Photonics, , Poland

**1121** Investigation of composition and origin of the intermediate layers at the Ga2O3/AlN and Ga2O3/Al2O3 interfaces

Dr. Marco Schowalter[1], S. Raghuvansy[1], Dr. A. Karg[1], Dr. P. Vogt[1,2], Dr. D. Schlom[3], Dr. D. Jena[3], Dr M. Eickhoff[1,2], Dr. A. Rosenauer[1,2]

[1]Institut für Festkörperphysik, Universität Bremen, Bremen, Germany, [2]MAPEX center for material science and processes, Universität Bremen, Bremen, Germany, [3]Department of Material Science and Engineering, Cornell University, Ithaca, USA

**1159** Real-Time Studies of Resistive Switching Mechanisms

Dr. Janghyun Jo[1], Xue Bai[1], Stephan Aussen[2], Sebastian Walford[3], Susanne Hoffmann-Eifert[2], Martin Salinga[3], Rafal E. Dunin-Borkowski[1]

[1]Ernst Ruska-Centre for Microscopy and Spectroscopy with Electrons, Forschungszentrum Jülich, Jülich, Germany, [2]Peter Grünberg Institut (PGI-7), Forschungszentrum Jülich, Jülich, Germany, [3]Institute of Materials Physics, University of Münster, Münster, Germany

## Late Poster Presentation

**1217** Multi-scale characterisation of laser-induced defects in the production of heterojunction photovoltaic cells

Dr Anacleto Proietti[1], Dr Luca Buccini[1], Dr Pierfrancesco Atanasio[1], Dr. Giancarlo La Penna[1], Dr. Chiara Mancini[1], Dr. Corrado Di Conzo[1,3], Dr. Francesco Mura[1,2], Dr Marco Galiazzo[4], Dr Nicola Frasson[4], Prof. Daniele Passeri[1,2], Prof. Marco Rossi[1,2]

[1]Department of Basic and Applied Sciences for Engineering, Sapienza University of Rome, Rome, Italy, [2]Research Center for Nanotechnology applied to Engineering of Sapienza University of Rome (CNIS), Rome, Italy, [3]Department of Applied Science and Technology (DISAT), Polytechnic of Turin, Turin, Italy, [4]Applied Materials Italia, , Italy

**1251** Phase Transformation of GeO2 Glass to Nanocrystals via High-Temperature Annealing

Dr JIJUN ZHANG[1], Wenshan Chen[2], Thilo Remmele[1], Dr. Hans Tornatzky[2], Dr. Oliver Bierwagen[2], Dr. Dan Zhou[1], Dr. Martin Albrecht[1]

[1]Leibniz - Institut für Kristallzüch, Max-Born-Straße 2, 12489 Berlin, Germany, [2]Paul-Drude-Institut für Festkörperelektronik, Leibniz-Institut im Forschungsverbund Berlin e.V., Hausvogteiplatz 5-7, 10117, Berlin, Germany

**1331** Screening of surface Fermi level pinning governs contrast of modulation-doped n-type GaN by electron holography

Dr. Keyan Ji[1], Dr. Michael Schnedler[1], Dr. Qianqian Lan[1], Dr. Philipp Ebert[1], Prof. Dr. Rafal E. Dunin-Borkowski[1]

[1]Ernst Ruska-Centre for Microscopy and Spectroscopy with Electrons (ER-C-1), Forschungszentrum Jülich GmbH, Jülich, Germany

1185

# Quantification of Potential Drops Across Semiconductor Heterointerfaces Using 4D-STEM: prospects and pitfalls

Prof. Dr. Kerstin Volz

PS-03 (1), Lecture Theater 2, august 29, 2024, 14:00 - 16:00

233

# In situ TEM study of phase and electronic structure transformations in amorphous Ga2O3

Dr JIJUN ZHANG[1], Mr. Thilo Remmele[1], Miss. Wenshan Chen[2], Mr. Hans Tornatzky[2], Mr. Oliver Bierwagen[2], Dr. Dan Zhou[1], Mr. Martin Albrecht[1]
[1]Leibniz-Institut für Kristallzüchtung, Max-Born-Straße 2, 12489 Berlin, Germany, [2]Paul-Drude-Institut für Festkörperelektronik, Leibniz-Institut im Forschungsverbund Berlin e.V., Hausvogteiplatz 5-7, 10117, Berlin, Germany

PS-03 (2), Lecture Theater 2, august 30, 2024, 10:30 - 12:30

Background
Amorphous semiconductors have ignited considerable interest in technological explorations owing to their distinctive electrical and optical properties stemming from their disordered structure and thermodynamic metastability. Thermal treatments have the potential to enhance or activate certain unique properties by reorganizing their atomic and electronic structures. Establishing precise correlations between thermal processes, structure evolutions, and electrical properties is essential for understanding fundamental mechanisms and achieving high-performance semiconductor materials. Gallium oxide (Ga2O3) is an advanced semiconductor material characterized by an exceptionally wide bandgap ranging from approximately 4.5 to 4.9 eV, depending on its concrete crystal phase and doping level. This wide gap renders Ga2O3 well-suited for high-power and high-frequency electronic devices.
Herein, we will present our in situ TEM work in this scenario by visualizing the atomic and electronic structure evolutions of amorphous Ga2O3 annealed in an O2 atmosphere.
Methods
High-quality morphous Ga2O3 films, ranging in thickness from 100 to 200 nm, were deposited on gas cell chips from Protochips using molecular beam epitaxy (MBE). Under the ambient pressure of an O2 environment, the as-grown films were heated from room temperature to 1000 °C at a heating rate from 1 to 1000 °C/s. Time series of selected area electron diffractions (SAED) and images were acquired with an image aberration-corrected TEM of FEI Titan 80-300 during the heating process. Furthermore, in situ STEM images and electron energy loss spectra (EELS) were collected on a probe aberration-corrected Thermo Fischer Spectra Ultra equipped with GIF Tridem 863 from Gatan to elucidate the atomic and band structure changes.
Results
Figure (a) and (b) depict the bright field (BF) TEM images and corresponding SAED patterns at four typical stages during the heating process of the amorphous Ga2O3 from room temperature to 1000 °C at a heating rate of 1 °C/s. Figure (c) were SAED patterns processed by CrysTBox software with background eliminated, direct beam removed, and intensity averaged. Gold and red arcs are superposed in SAED patterns to represent Debye-Scherrer rings referred to {$hk$l} reflections of the cubic spinel and monoclinic phases, respectively.
As shown in the figure, a circular cubic spinel phase of Ga2O3 (γ-Ga2O3) with a size of approximately 100 nm is formed at the initial stage. Subsequently, these structures evolve into dendritic morphology, accompanied by the generation of the monoclinic phase (β-Ga2O3) and finally undergoing a full transformation to a polycrystalline monoclinic phase.
This transition can be identified as a reconstructive disorder-to-order phase transition mediated by the exchange of cations to the next nearest neighbor sites, as shown in Figure (d). The figure provides a schematic description of the atomic structural evolution and energy barriers needed to overcome for disordered to ordered phase transition upon heating [1].
Further results, such as the complete time-series of BF images and SAEDs, the in situ low loss EELS reveling the band gap shift, and more, will be presented on site.

Conclusion

Our in situ TEM work provides a correlated perspective on the thermal treatments, phase transformations, and band gap shifts involved in the pure Ga2O3. These findings have significant implications for understanding the fundamental mechanisms and are pivotal for the design and engineering of wide bandgap semiconductors in photoelectric applications.

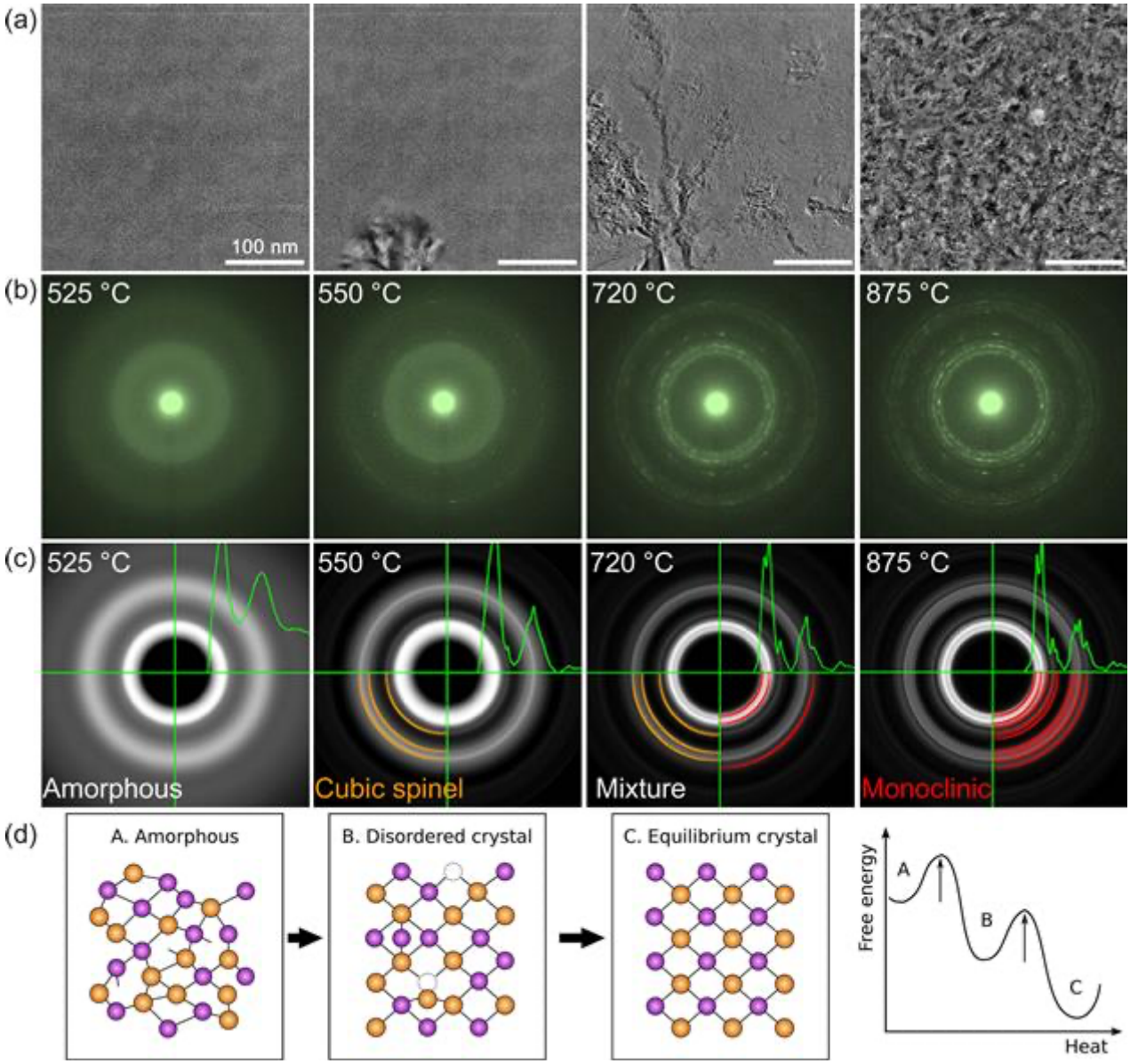


**Keywords:**

Amorphous Ga2O3, in situ TEM

**Reference:**

[1] Wouters, C., Nofal, M., Mazzolini, P., Zhang, J., Remmele, T., Kwasniewski, A., ... & Albrecht, M. (2024). Unraveling the atomic mechanism of the disorder–order phase transition from γ-Ga2O3 to β-Ga2O3. APL Materials, 12(1).

149

# Strain Sensitivity of STEM-GPA-based Strain Map

Bumsu Park[1], Minsik Kim[1], Jiwon Jeong[1], Sungho Lee[1]
[1]Samsung Electronics Advanced Analysis Science & Engineering Team, Hwaseong-si/Samnsungjeonja-ro, Republic of Korea

PS-03 (1), Lecture Theater 2, august 29, 2024, 14:00 - 16:00

Background
Strain engineering, one way to improve the performance of semiconductor devices is to apply strain intentionally to improve device characteristics. In addition, as the size of semiconductor devices decreases to improve the integration density, it has become important to analyze the strain distribution in localized areas that directly affect device performance. The GPA-based strain analysis method is widely used to analyze the strain, but there has been no clear numerical verification of the strain detection limit. In this study, we clarified the empirical limitations of the GPA method and proposed optimal experimental conditions for its application to real devices.

Methods
We used artificial STEM-ADF images with in-plane strains of 1%, 0.1%, and 0.05% to compare the strain values detected by changing the pixel resolution of each image with the actual strain values. Each image was tested up to a data binning factor of 2n (n = 1 to 6) in the original image. In addition, we considered Poisson noise to mimic the real STEM imaging conditions. Finally, we used STEM-ADF images obtained from a silicon device with various pixel resolutions and compared the strain mapping results.

Results and Conclusions
The strain analysis results using images containing 1%, 0.1%, and 0.05% strain without considering Poisson noise showed that the detected strain is 1 ± 0.001%, 0.1 ± 0.002%, and 0.05 ± 0.01% respectively for images with a pixel resolution of 22 pm or less. When considering Poisson noise, a comparison of the standard deviation (SD) of the strain values showed that for spatial resolutions of 22 pm/px or higher, strains of 1% and 0.1% can be detected with a reliability lower than 0.02% of SD. In the case of 0.05%, the strain value is detectable up to a spatial resolution of 22 pm/px, but the strain precision deteriorates from 0.04% to 0.7%. Interestingly, as the binning factor increases, a periodically repeating local strain undulation was observed on the strain map. This is due to the difference in distance between atoms and periodicity between pixels, resulting in a Moiré pattern that degrades the accuracy of the strain map. In this presentation, I will additionally share the results of strain maps obtained through GPA on real devices and will compare strain maps obtained by 4D-STEM.

Figure1. (a) Simulated Si (Z.A = [110]) STEM-ADF images containing 0.05% in-plane strain with various binning factors. Corresponding in-plane strain maps (b) without and (c) with Poisson noise.

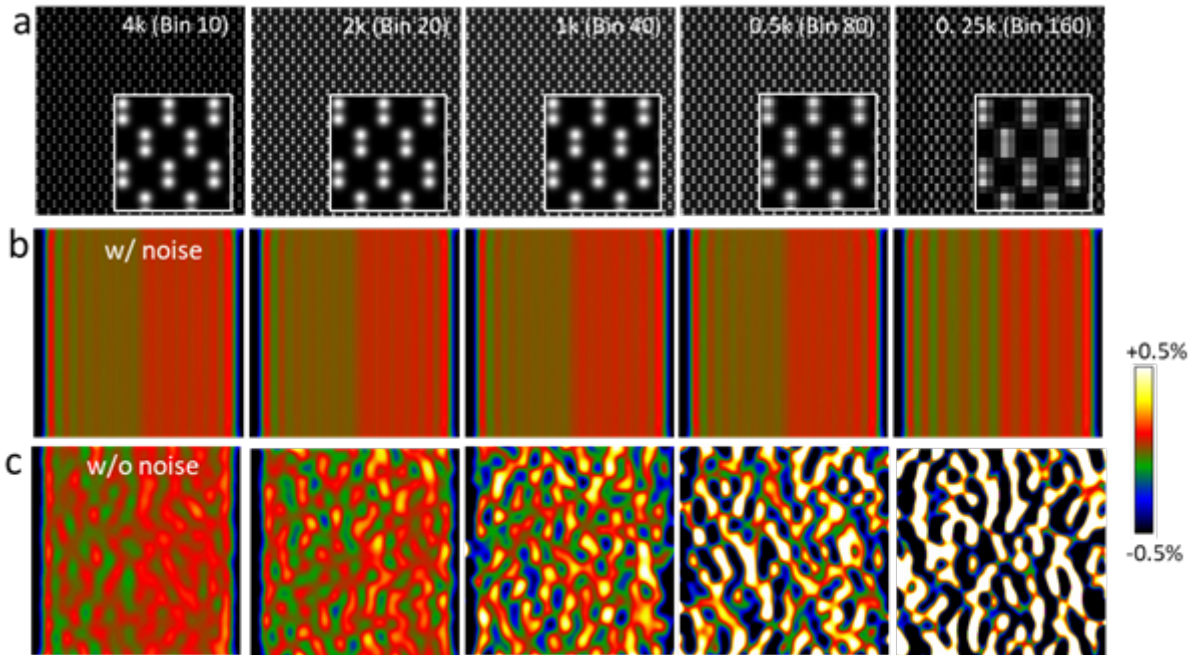


**Keywords:**

GPA, strain sensitivity, strain limit

198

# Advanced EELS spectroscopy characterization of AlGaN/GaN materials

Mr Esteve Drouillas[1,2], Mrs. Bénédicte Warot-Fonrose[2], Mr. Jean-Gabriel Mattei[1]
[1]STMicroelectronics Crolles 2, Crolles, FRANCE, [2]CEMES-CNRS, Toulouse, FRANCE

PS-03 (1), Lecture Theater 2, august 29, 2024, 14:00 - 16:00

Background incl. aims
The combination of STEM with electron energy-loss spectroscopy (EELS) and Electron-Loss Near-Edge Structure (ELNES) has gained great interest in the microelectronics industry. Indeed, ELNES can provide additional information on local atomic and electronic structures of materials compared to the already commonly used XEDS method for chemical quantification. This project intends to investigate High-Electron Mobility Transistor (HEMT) devices based on AlxGa(1-x)N semiconductors for high-power and high-frequency applications.
Methods
The HEMT device presented in this work [See Fig.1 (a) and (b)] is composed of a GaN channel and an AlGaN barrier structure separated by a few-nanometer AlN spacer grown to improve the performance of the 2-Dimensional Electron Gas (2DEG) formed at the interface [2]. The wider bandgap and stronger polarization of AlN compared to AlGaN provides higher breakdown fields and enhances the electron mobility and sheet density in the 2DEG while limiting alloy scattering. Due to significant lattice mismatch between GaN and Si, an AlN nucleation layer is grown first on 300 mm Si wafers. Successive AlxGa(1-x)N buffer layers with decreasing amounts of Al are then needed to accommodate stress in the structure. This buffer stack allows the growth of an ideally crack-free GaN channel as shown in Fig. 1 (a), assuring optimal electron mobility in the device. Layers are grown using MOCVD deposition method on Si (111) wafers. The main goal of this project is to investigate the comportment of materials in this device, especially at the active AlGaN/AlN/GaN interface through EELS analysis with “ultimate” resolution. TEM experiments are performed on a probe Cs-corrected JEOL Neo-ARM 200F equipped with a Cold-FEG and a GIF (Gatan Image Filter) Continuum spectrometer.
Results
Preliminary work has been conducted to investigate the variation of the plasmon peak in the low-loss region (≈ 10-30 eV) along the buffer stack which demonstrated a linear dependency between the plasmon energy peak (Ep), and the fraction of Al in the ternary alloys, xAl [Fig. 2 (a)]. Likewise, the acquisition of the N K-edge ELNES structure along the buffer layer stack has been conducted at 200 kV, highlighting the transition between layers [Fig.2 (b)]. The most significant difference is observed for the first 3 peaks of the spectra (≈ 400-410 eV) where the first and third peaks gradually gain in intensity over the second as the AlN mole fraction increases in the ternary alloys. According to literature [3], these peaks should result from N-cation anti-bonding interactions and the intensity re-distributions is mostly due to the valence d-electrons of the GaN. These experimental N K-edges are consistent with calculated wurtzite AlxGa(1-x)N spectra obtained in the previous studies [4,5].
Conclusion
Based on these first results, additional work has been carried out to optimize TEM sample preparation for EELS analysis, especially using Plasma-FIB Xe and PIPS II Ar ion polishing to successfully prevent Ga implantation experienced with standard Ga FIB thinning as illustrated by Fig.3 (a) and (b). Further experiments will be performed to investigate electron beam irradiation as well as the contribution of lower acceleration voltage (i.e. 80 and 60 kV) on the N K-edge ELNES analysis.

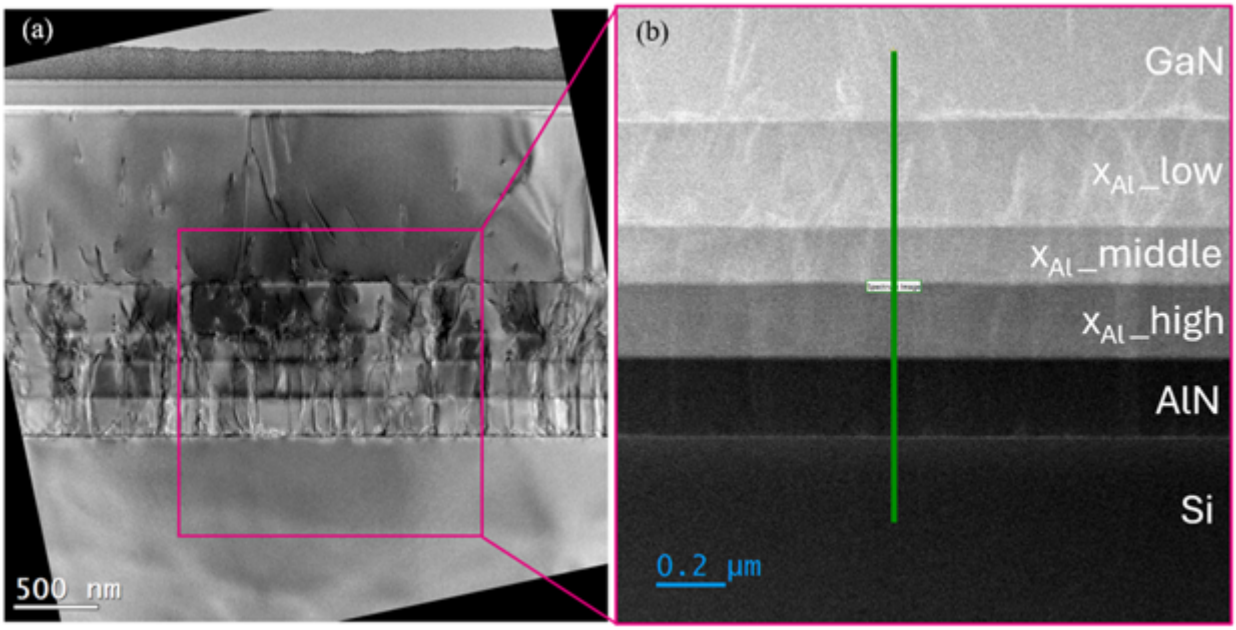


**Figure 1.** (a) TEM micrograph of HEMT device, (b) STEM-HAADF image of the $Al_xGa_{1-x}N$ buffer layer stack

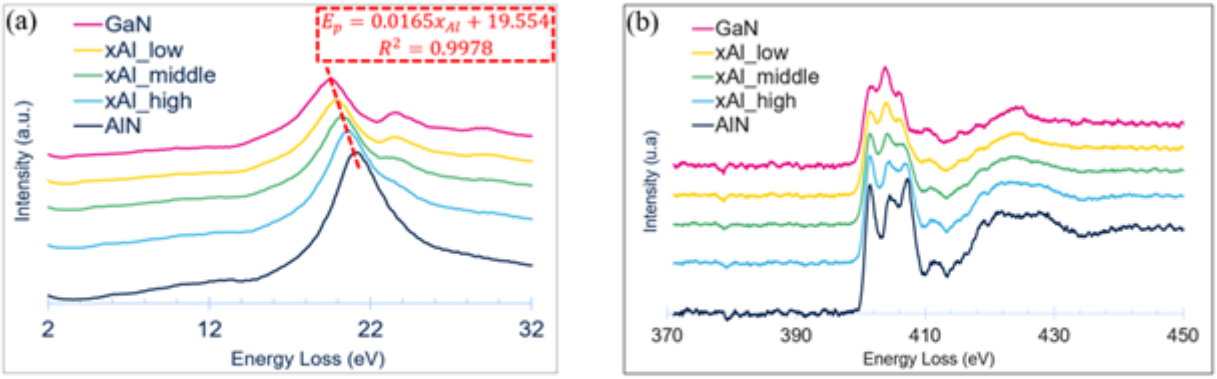


**Figure 2.** (a) plasmon peak analysis along $Al_xGa_{1-x}N$ buffer layer stack and linear dependency of the Ep depending on AlN mole fraction xAl (b) ELNES spectra of N K edge in GaN, $Al_xGa_{1-x}N$ buffer layers and AlN nucleation layer.

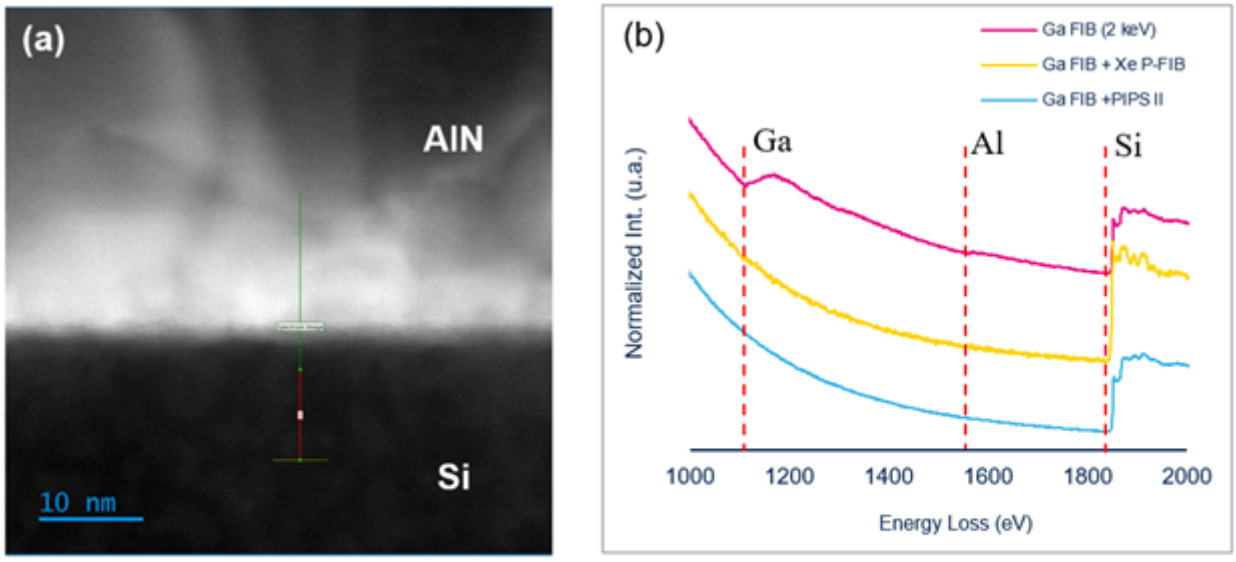


**Figure 3.** (a) STEM-HAADF image of the Si substrate and AlN nucleation layer interface (b) EELS spectra highlighting the presence of Ga and Al in Si substrate for the Ga FIB prepared sample whereas neither Ga nor Al is observed after Xe P-FIB or PIPS II polishing.

**Keywords:**

EELS, ELNES, AlGaN/AlN/GaN, HEMT

**Reference:**

[1] T.N. Nguyen, 2013. https://theses.hal.science/tel-00934655.
[2] R. Ramesh et al., 2021 Mater. Chem. Phys. Vol. 259 124003.
[3] T. Mizoguchi, 2009 J. Phys.: Condens. Matter, 21 104215.
[4] D. Holec et al., 2011 Phys. Rev., B 83, 165122
[5] M. Petrov et al., 2011 J. Phys.: Conf. Ser. 326 012016

245

# Investigating All-Inorganic Halide Perovskite Phase Transformations via in-situ 4D STEM Heating Experiments

Mr Tom Warwick[1], Mr. Paul Smeets[2,3], Mr. Roberto dos Reis[2,3]
[1]Gatan, Inc., Pleasanton, United States, [2]Department of Materials Science and Engineering, Northwestern University, Evanston, United States, [3]Northwestern University Atomic and Nanoscale Characterization Experimental (NUANCE) Center, Northwestern University, Evanston, United States

PS-03 (1), Lecture Theater 2, august 29, 2024, 14:00 - 16:00

Background incl. aims
Halide perovskite materials, in particular Cesium lead-based halides (CsPbX3, where X = Br or Cl), are known in the halide perovskite family due to their promising optoelectronic properties. Understanding any phase transitions in CsPbX3 that would occur under typical device operating conditions is crucial for assessing device thermal stability and structural integrity [1, 2]. This work focuses on elucidating phase transitions in CsPbX3 that occur as a result of thermal variations by utilizing in-situ four-dimensional scanning transmission electron microscopy (4D STEM). This approach captures their structural evolution across a temperature range from sub-ambient to the melting point.
Methods
Energy-filtered 4D STEM data were acquired using a JEOL ARM300F microscope outfitted with a GIF Continuum® and post-GIF K3® detector from Gatan. DigitalMicrograph® version 3.6 and eaSI™ technology were used for in-situ 4D STEM data acquisition. Digital Temperature modulation of the samples was achieved using a DENSsolutions heating holder controlled within DigitalMicrograph and a Gatan LN2 holder for cooling.
Results
The phase diagram of CsPbBr3 predicts multiple phase transformations as the material is heated from room temperature until its melting point at 500°C. The material begins in an orthorhombic (Pnma) phase and begins a phase transformation to a tetragonal (Cmcm) phase at 88°C, followed by a 2nd transformation to a cubic (P4/mbm) phase at 130°C that persists until the melting point. CsPbBr3 was heated from room temperature until its melting point and initial in-situ 4D STEM data shows temperature-dependent variation in the averaged diffraction patterns, seen in Figure 1. Furthermore, virtual bright field images derived from the in-situ 4D STEM data show dynamic reaction interfaces and evolving contrast during heating. These results emphasize the presence of structural evolution of CsPbBr3 about 60°C, 130°C, and above 500°C.
Conclusion
In-situ 4D STEM data acquisition of CsPbX3 during heating is a powerful methodology for quantitative analysis of the phase evolution of halide perovskites from ambient temperature until their melting point. The data collection tools available with in DigitalMicrograph link 4D STEM data with the experimental temperature profile from the heating holder, providing a detailed chronology of the phase evolution. This allows for a more concrete understanding of the stability ranges of the observed intermediate phases during heating and deeper insight into the material behavior under simulated operational temperatures. Adding complementary techniques such as in-situ electron energy loss spectroscopy (EELS) should provide important chemical information to further assess the structural behavior of CsPbX3 and its consequences on optoelectronic properties.

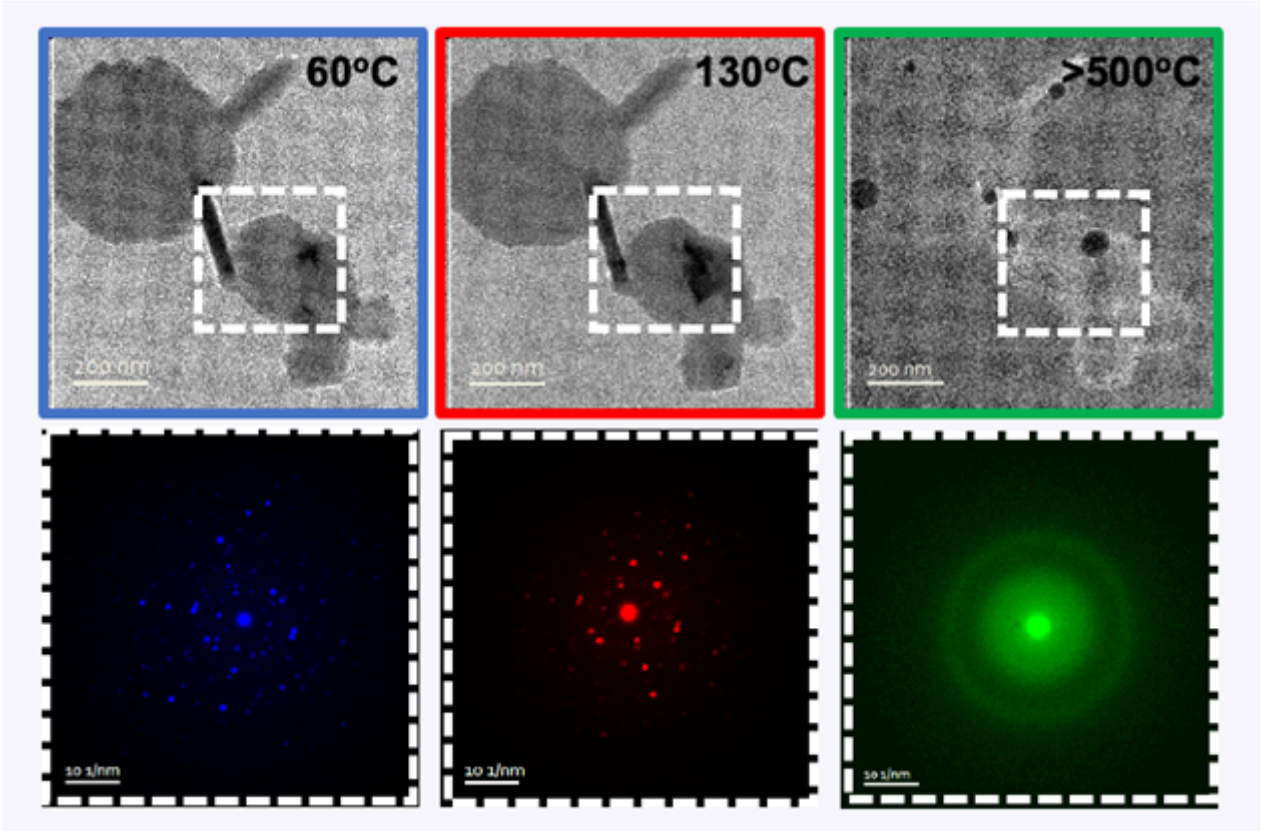


**Keywords:**

Halide perovskites, in-situ, 4D STEM

**Reference:**

1. M. Keshavarz et al., Tracking Structural Phase Transitions in Lead-Halide Perovskites by Means of Thermal Expansion. Adv. Mater. 2019, 31, 1900521. https://doi.org/10.1002/adma.201900521

2. Erik Fransson, J. Magnus Rahm, Julia Wiktor, and Paul Erhart. Chemistry of Materials 2023 35 (19), 8229-8238. DOI: 10.1021/acs.chemmater.3c01740

257

# Mapping electric fields in real nanodevices by operando electron holography

Dr Christophe Gatel[1], Dr Leigeng Zhang[2], Dr Kilian Gruel[2], Dr Frédéric Lorut[3], Dr Martin Hÿtch[2]
[1]CEMES-CNRS, University Toulouse III - Paul Sabatier, Toulouse, France, [2]CEMES-CNRS, Toulouse, France, [3]STMicroelectronics, Crolles, France

PS-03 (1), Lecture Theater 2, august 29, 2024, 14:00 - 16:00

Background
The development of nanometer-scaled electronic devices with reduced dimensions, involving new materials or new architectures such as Magnetic Random Access Memories (MRAM), memristors or Phase Change Memories (PCM)1, requires a deeper understanding of their operating properties. While electrical and physical characterizations are widely used to monitor and evaluate both the device performance and the quality of the layer stack, there is a lack of knowledge on how the electromagnetic fields are precisely mediated along devices at the nanoscale level. Correlating electric fields mapped at the nanoscale across a chosen device with its structural properties and chemical composition would give new insights on the local electrical properties such as resistivity, polarisation, and charge traps.
Off-axis Electron Holography (EH) is an interferometric technique that allows quantitative mapping of electrical potentials inside and around the specimen, as well as the measurement of charge distributions2. However, operando EH has been rarely used, in particular on real devices3,4, because of key issues such as specimen preparation, surface damage layers, stray field and electron radiation. We will present the methodology that we have been developing for mapping the electrical properties of nano-electronic devices extracted directly from production lines without using a probe-based approach. Taking the example of phase change memory cell, we will show how electron holography can be used to measure in situ the resistivity distribution within the active layer after changing its state.

Methods
Phase-change materials exhibit a huge change of electrical resistivity between the amorphous (high resistance) and crystalline phase (low resistance). The electrical resistivity encodes the state of the bit, denoted SET for the crystalline state (low resistance) and RESET for the amorphous state (high resistance). To read the device, the resistance is measured by biasing the top and bottom electrode connected to a thin metallic filament called the “heater”. To write, a high-amplitude current pulse is injected, whose exact form depends on whether the operation is to stabilize the crystalline phase (SET) or the amorphous state (RESET). Current passing through the heater and GST layer causes localised Joule heating; the associated rise in temperature in turn causes the phase change. To SET, a relatively long pulse allows gradual crystallisation of the amorphous state whilst for RESET, a short pulse induces rapid melt-quench of the crystalline to amorphous state.
In situ biasing TEM experiments necessitate a specific and complex sample preparation that minimizes preparation artifacts whilst ensuring the electrical functionality of the nanodevice itself. The specimen-device was extracted from production lines before being thinned by focused ion-beam (FIB) and contacted to a chip with predefined electrical contacts, similarly to our previous work on electrostatic fields.5 An important part of the preparation was to preserve the encapsulation layer of insulating material all around the heater and GST layer. Special care was also taken to avoid any electrical discharges which would destroy the device. Holograms were recorded during long exposure time using dynamical automation for compensating instabilities under bias, and while measuring the total current. Experimental phase images were then compared to additional numerical simulations

using finite element modelling (FEM) including factors such as specimen geometry, stray fields and local resistivity.

Results

The GST layer within the device is initially crystalline (Initial state) and holograms were first recorded under a DC bias as if the memory was to be read. The layer was then switched to an amorphous state (Final state) by sending a sequence of pulses. Remarkably, the thin lamella survived the injection of peak currents of several hundreds of µA during the pulse. The overall resistance, measured under a biasing of 0.5 V during the holography experiments, changed radically between the initial and final states, increasing 5-fold after switching.

The corresponding phase images in initial and final states are presented in Figure b and e, respectively. We can clearly see the difference of the potential distribution between both states, with a dome-like shape in spanning the GST layer in the final state after amorphisation. The electrical information, in the form of isophase contours, has also been superimposed onto the conventional TEM images (Figure a and d) to help visualise the region involved. We can see, notably, that the phase contours seem to radiate outwards from the tip of the heater into the GST layer.

We obtained a very good agreement between experimental and simulated phase images using finite element modeling (Figure b and Figure e). This agreement gives access to the distribution of the electric potential within the device, and therefore to the local resistivity with the Ohm's law. From the reasonable assumption that the conductivity is radially symmetric around the heater tip and using the experimentally measured total current flowing through the device in situ, we determined the local map of the conductivity. A small seed of highly resistive material around the heater tip was revealed in the initial crystalline state and for the final state, the crystalline to amorphous transformation occurred at a certain radius, about 10 nm, from the heater tip.

Figure. Conventional bright-field TEM image, Initial state (a), Final state (d) with isophase contours (values on the right) extracted from experimental phase maps, Initial (b), Final (e). Simulated phase maps, Initial (c), Final (f). In dotted line the dome-like shape where the phase change occurs. Scale bars are 20 nm.

Conclusion

We developed a new methodology to map the local resistivity across the active area of an individual device in operation. This method, based on operando electron holography, has been applied on a PCM cell and directly highlights unexpected features. On switching the device by electrical pulses, we demonstrated that electrical resistance is inhomogeneous near the heater. This study shows the power of our methodology for studying the local electrical properties of active devices and can be applied in a general way.

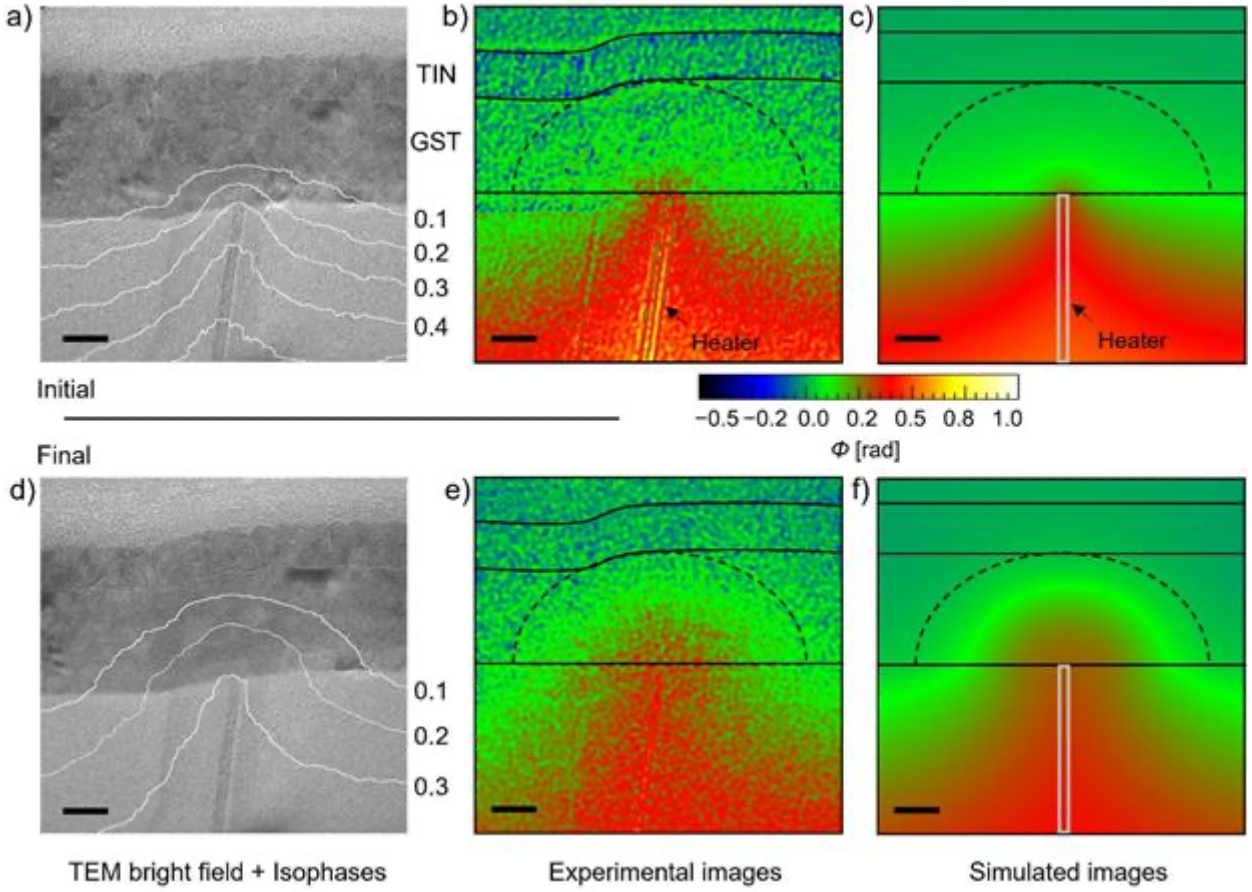


**Keywords:**

Phase change materials, in situ

**Reference:**

(1) S. Raoux et al. IBM J. Res. Dev. 52, 465 (2008).
(2) P.A. Midgley and R. Dunin-Borkowski, Nat. Mater. 8, 271–280 (2009)
(3) T. Goto et al. Microscopy 62, 383 (2013)
(4) N. Ikarash et al. Appl. Phys. Lett. 100 , 143508 (2012)
(5) C. Gatel et al., Phys. Rev. Lett. 129, 137701 (2022)

353

# Unveiling Strain Fields and Plastic Relaxation in Narrow-Core GaAs/In(Al,Ga)As Nanowires with High-Resolution Electron Microscopy

Mrs Polyxeni Chatzopoulou[1], Dr Isaak Vasileiadis[1], Mr Donovan Hillard[2,3], Dr Nikoletta Florini[1], Dr Vivek Devulapalli[4], Dr Christian Liebscher[4], Assoc. Prof. Liverios Lymperakis[5], Prof. Thomas Kehagias[1], Prof. Philomela Komninou[1], Dr. Emmanouil Dimakis[2], Professor George Dimitrakopulos[1]
[1]Physics Department, Aristotle University of Thessaloniki, Thessaloniki, Greece, [2]Helmholtz-Zentrum Dresden-Rossendorf, Dresden, Germany, [3]TUD Dresden University of Technology, Dresden, Germany, [4]Max-Planck Institut für Eisenforschung GmbH, Düsseldorf, Germany, [5]Physics Department, University of Crete, Heraklion, Greece

PS-03 (1), Lecture Theater 2, august 29, 2024, 14:00 - 16:00

Background incl. aims
Narrow GaAs nanowires (radius in the range of 10 nm) can undergo extreme elastic stretching when overgrown by much thicker, highly mismatched In(Al,Ga)As shells. Subsequently, GaAs in such core/shell heterostructures has demonstrated up to 40% bandgap reduction [1] and 30-50% boost in electron mobility [2]. Compared to planar epilayers, such nanowires offer superior flexibility by facilitating elastic relief along the side facets and strain partitioning between the core and the shell. This effectively reduces the strain energy and expands the coherency limits. However, plastic relaxation ensues once the lattice mismatch surpasses a critical threshold. This critical limit is determined by the intricate 3D strain distribution within the nanowires and the plastic relaxation mechanisms involved. In this contribution, we determine experimentally the critical misfit of such core/shell GaAs/In(Al,Ga)As nanowires featuring narrow cores and thick shells, using (scanning) transmission electron microscopy ((S)TEM) methods. Additionally, we utilize high-resolution (S)TEM (HR(S)TEM) combined with theoretical calculations, to obtain the 3D strain fields. Finally, we employ topological analysis with HR(S)TEM to identify the operating plastic relaxation mechanisms.

Methods
The [111]-oriented GaAs/Inx(Al,Ga)1-xAs core/shell nanowires were epitaxially grown on Si(111) substrates in the self-catalysed vapour-liquid-solid mode by molecular beam epitaxy. The shell composition was varied systematically from x = 0.2 to 1, while the core radius and shell thickness were fixed at 10 nm and 80 nm, respectively. (S)TEM and HR(S)TEM observations, as well as energy dispersive X-ray spectroscopy, were performed in a 300 kV probe-corrected ThermoFisher Scientific Titan Themis 60/300 microscope and a 200 kV JEOL JEM F200 CFEG microscope. Samples were prepared along <1-10> and <11-2> zone axes by ion-thinning, as well as along [111] with cross-sections prepared by ultramicrotomy. The 3D strain fields were directly determined from the HR(S)TEM observations, using geometrical phase analysis (GPA). The experimentally-extracted strain fields were compared to theoretical ones obtained by finite element analysis, performed using thermal expansivity to model the lattice mismatch, and with atomistic energetical calculations, employing the Tersoff interatomic potential [3]. Plastic relaxation mechanisms were investigated by employing diffraction contrast TEM and HR(S)TEM observations.

Results
Experimental observations showed the axial strains to be uniformly distributed. In contrast, the elastic relaxation along the free facets, combined with the hexagonal geometry of the core, resulted in opposite radial and tangential strain gradients in the core and shell as determined by GPA on (111) cross-sections of the nanowires. Even the plastically-relaxed nanowires retained radial and tangential elastic relaxation. These results were consistent with the theoretical continuum and atomistic calculations. The critical indium content for the initiation of plastic relaxation was determined

through the onset of defect introduction. In order to determine the residual elastic strain along the nanowire axis, analysis of Moiré fringe patterns was employed. Shells in plastically relaxed nanowires exhibited extended defects relieving the misfit, such as lattice and partial dislocations whose density varied with the lattice mismatch. Nanowire bending was found to influence the plastic relaxation process. Circuit mapping [4] around interfacial defects unveiled their Burgers vectors and, subsequently, the plastic relaxation nano-mechanisms, which involved both dislocation glide and stacking fault formation.

Conclusions

An integrated methodology, combining atomic resolution electron microscopy with continuum and atomistic calculations, has been employed to achieve a comprehensive understanding of the intricate strain relaxation in GaAs/Inx(Al,Ga)1-xAs core/shell nanowires featuring narrow cores. The 3D strain field distribution in such nanowires has been determined experimentally for the first time along with the maximum sustainable elastic strain in the core, the critical lattice mismatch for plastic relaxation, and the associated mechanisms of defect introduction. These insights can be employed for further straining the core while mitigating the formation of defects that impede electron mobility and internal quantum efficiency.

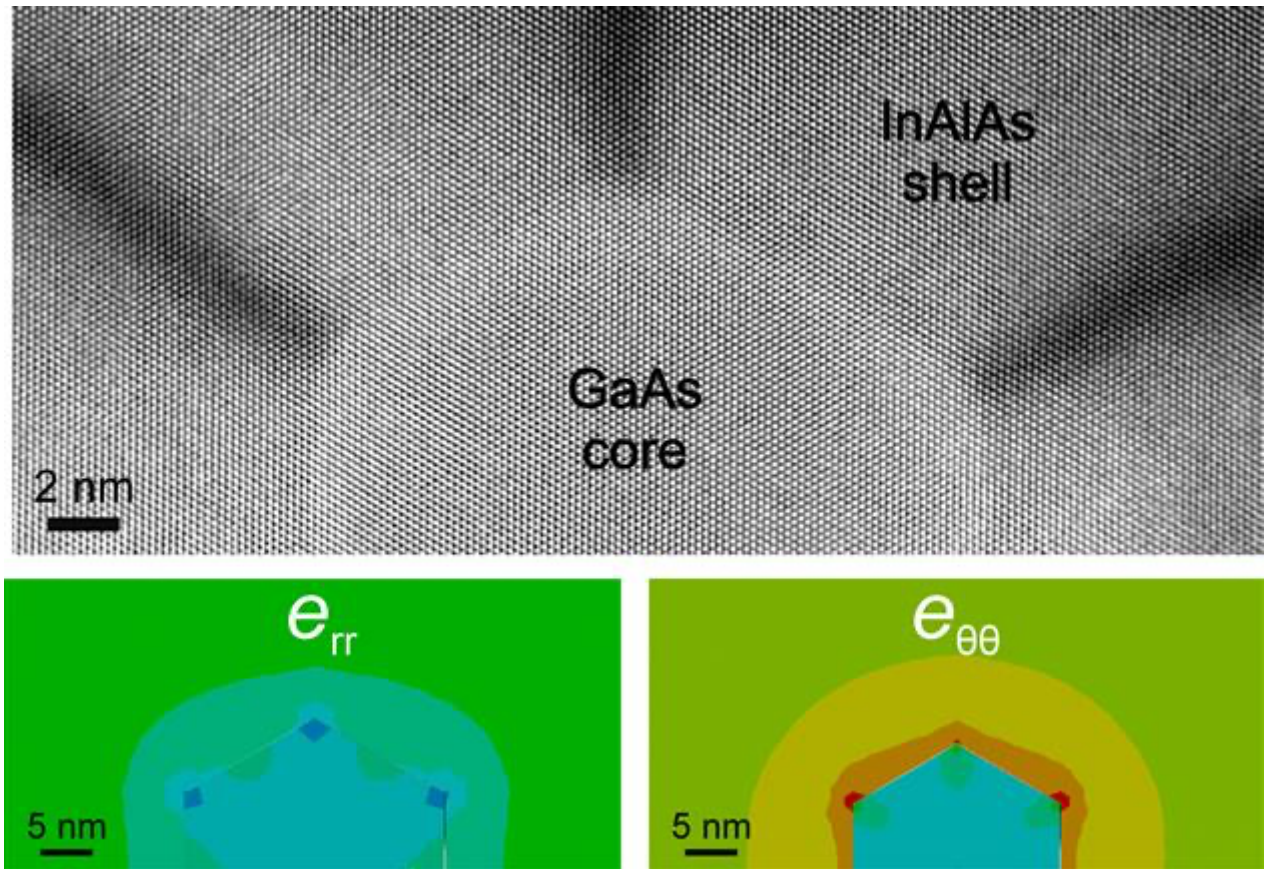


**Keywords:**

nanowires, III-arsenides, strain, dislocations, HR(S)TEM

**Reference:**

[1] L. Balaghi, G. Bussone, R. Grifone, R. Hübner, J. Grenzer, M. Ghorbani-Asl, A. V. Krasheninnikov, H. Schneider, M. Helm and E. Dimakis, Nature Communications 10, 2793 (2019).
[2] L. Balaghi, S. Shan, I. Fotev, F. Moebus, R. Rana, T. Venanzi, R. Hübner, Th. Mikolajick, H. Schneider, M. Helm, A. Pashkin and E. Dimakis, Nature Communications 12, 6642 (2021).
[3] H. Detz and G. Strasser, Semicond. Sci. Technol. 28, 085011 (2013).
[4] R. C. Pond and J. P. Hirth, Defects at surfaces and interfaces, Solid State Phys. 47, 287 (1994).

578

# Controlling heterostructures with atomic precision in III-V nanowires using microheaters in an in-situ TEM

Mr. Christopher Røhl Yskes Andersen[1,2], Mr. Marcus Tornberg[3,4,5], Mr. Sebastian Lehmann[4,5], Mr. Daniel Jacobsson[3,4], Prof. Jonas Johansson[4,5], Prof. Kimberly A. Dick[3,4,5], Prof. Kristian S. Mølhave[1]
[1]DTU Nanolab, Technical University of Denmark, Kgs. Lyngby, Denmark, [2]Quantum DTU, Technical University of Denmark, Kgs. Lyngby, Denmark, [3]nCHREM, Lund University, Lund, Sweden, [4]NanoLund, Lund University, Lund, Sweden, [5]Solid State Physics, Lund Uni., Lund, , Lund, Sweden

PS-03 (1), Lecture Theater 2, august 29, 2024, 14:00 - 16:00

Precision in heterostructure control within III-V nanowires is essential for the advancement of future technologies, especially quantum computing and quantum internet. The ability to embed one crystal phase, e.g., zincblende, within another, e.g., wurtzite, can be used to determine the optical and electrical properties of so-called crystal phase quantum dots. This crystal phase engineering offers a sharp transition between phases, superior to compositional quantum dots, but its control remains challenging within traditional ex-situ growth environments. Integrated electron microscopy with gas handling capabilities offers a unique in-situ perspective, revealing the dynamics of crystal phase formation and the parameters influencing it. Our research study is focused on how changing the growth conditions can be used to enable atomically precise crystal phase control. We also look into the growth dynamics and the commonly assumed control parameter: the contact angle, to unravel its actual impact on crystal phase determination in GaAs nanowires.
We use a cantilever based microheater system for GaAs Metalorganic Vapor Phase Epitaxy (MOVPE) growth within a Transmission Electron Microscope (TEM) as depicted in the figure to the left. This setup enables us to map the crystal phase formation at different growth conditions, specifically varying temperature and group V precursor flow. Instantaneous adjustments in temperature and precursor flow allow for the real-time analysis of the dependencies between these growth parameters and the phase transitions as illustrated in the figure to the right. Additionally, we introduce a field perturbation technique to the catalytic droplet to decouple its shape from the underlying growth conditions, further investigating the mechanisms driving the phase formation.
Our findings reveal that crystal phase transitions can be controlled with atomic precision using temperature shift in-situ. The cantilever-based microheaters offer rapid temperature changes, achieving 100$^{o}$C variations within milliseconds, significantly outperforming the slower response of precursor flow adjustments, taking tens of seconds. This rapid temperature control is instrumental in creating atomically precise crystal phase quantum dots. We conduct an in-depth study of droplet geometry during these phase transitions, revealing critical insights into the growth dynamics. Furthermore, by applying an external electric field, we successfully deform the catalytic droplet, effectively decoupling the contact angle from the crystal phase formation process. This experimental approach underscores the complex interplay between physical conditions and nanowire growth mechanisms.
In conclusion, using microheaters within a TEM with an integrated gas handling system has enabled a detailed study of the growth dynamics and heterostructure formation in III-V nanowires. By having the advantage of instantaneous temperature changes, we have demonstrated the ability to form crystal phase quantum dots with atomic precision. Furthermore, our findings challenge the traditional coupling of the contact angle as a driving force for the crystal phase formation. This research paves the way for new methodologies in nanowire synthesis, potentially revolutionizing the approach to designing materials for quantum and nanotechnological applications.

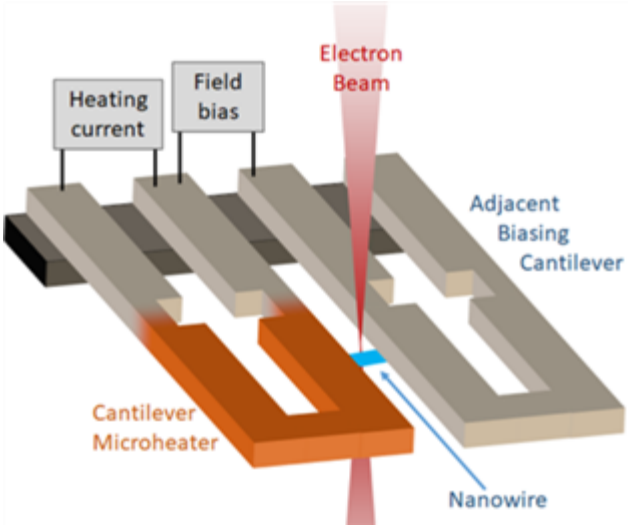


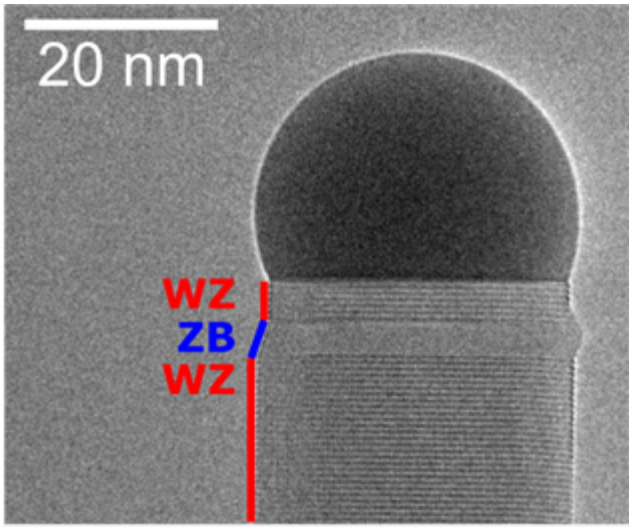


**Keywords:**

MEMS chips, III-V-Nanowires, Contact angle

**Reference:**

Hastrup et al. Sci. Rep. 10, 14911 (2020)
N. Akopian et al. Nano Lett. 10, 1198–1201 (2010)
F. Panciera et al., Nature Comm. 7, 12271 (2016)
K. Molhave et al. Small 4, 1741 (2008)
M. Tornberg et al. Microscopy and Microanalysis 20, 1484-1492 (2022)

83

# Inversion of the Internal Electric Field in GaN/AlN Heterostructures Studied by Off-Axis Electron Holography

Lou Denaix[1], Dr Florian Castioni[1], Dr Matthew Bryan[1], Dr David Cooper[1], Dr Eva Monroy[2]
[1]Univ. Grenoble Alpes, CEA, Leti, Grenoble, France, [2]Univ. Grenoble Alpes, CEA, Grenoble INP, Irig, Pheliqs, Grenoble, France

PS-03 (2), Lecture Theater 2, august 30, 2024, 10:30 - 12:30

Background incl. aims
Wurtzite III-nitride semiconductor are renowned for their applications in light emitting devices, due to their wide bandgap and doping capabilities. One of the main challenges of these materials is managing their intense spontaneous and piezoelectric polarization fields. In order to enhance the efficiency of GaN-based emitters, it is important to design new architectures to engineer the electric field in these materials. In addition, validation of these new designs requires the development of characterization methods capable of mapping the electric fields with nanometer resolution.
In this work, we study the effect of n-type delta doping on the potential profile of AlN/GaN and AlGaN/GaN superlattice using off-axis electron holography for the quantification of the electrostatic potentials. In addition, the sample composition, and the concentration and localization of dopants are determined using correlative techniques: high-resolution electron dispersive X-Ray spectroscopy (EDX), secondary ion mass spectroscopy (SIMS) and Nextnano simulations.

Methods
The samples under study consist of 10-periods of AlN/GaN (20 nm/20 nm) (1st series: samples S1 and S2) or 12 periods of AlN0.3Ga0.7N/GaN (15nm/15nm) (2nd series: samples S3, S4 and S5) grown by plasma-assisted molecular beam epitaxy. In the first series, S1 is non-intentionally doped and S2 is heavily doped with Ge in the GaN layers, at a nominal concentration [Ge] = 2.0±0.2 × 1021 cm−3, which is close to the solubility limit. In the second series, S3 is non-intentionally doped and S4 and S5 have a delta doping of Ge ([Ge] = 1020 cm-3) and Si ([Si] = 1019 cm-3), respectively, localized in the AlGaN layers. The dopant concentrations are measured by SIMS.
The electrostatic potential of the samples are measured by off-axis electron holography performed in a double-corrected FEI Titan Ultimate TEM operating at 200 kV. The electron holograms were recorded on a Gatan OneView 4k camera. EDX-spectroscopy was performed in a probe-corrected FEI Titan Themis microscope operated at 200 kV and equipped with a Super X detector system. EDX spectra quantification was done using the Cliff-Lorimer method.

Results
Using electron holography in undoped AlN/GaN and AlGaN/GaN samples (S1, S3), we confirm the presence of internal electric fields in the GaN and AlN layers, with a sign that is consistent with Schrödinger-Poisson simulations performed with the Nextnano software. Then, comparing S1 and S2, we are able to demonstrate the effect of carrier screening due to Ge doping. However, we also observed an inversion of the internal electric field in some of the AlN layers in S2. A correlative study involving holography, EDX and theoretical calculations of the band diagram demonstrate that this inversion can be attributed to Ge accumulation at the heterointerfaces in the AlN layers [1]. These result pave the way to the use of delta doping as a design tool to modulate and even invert the electric field in polar heterostructures.
The second sample series (S3, S4 and S5) presents our attempt to reproduce intentionally the inversion of potential observed in S2 by designing AlGaN/GaN heterostructures using delta doping with silicon and germanium. In this case, we observe a systematic inversion of the internal electric field using Si doping. However, this inversion was not observed for Ge delta-doping. Further analysis

using SIMS showed a migration of Ge in the GaN layer that explain this absence of inversion. This migration is consistent with our observations of a higher solubility limit of Ge in AlGaN compared with GaN [2], and is coherent with the Ge clustering observed in S2.

Conclusion

We show here that electron holography is a very powerful tool that allow the measurement of electrostatic potential with a nanometer resolution. It is particularly useful to study III-nitride materials that present peculiar electrostatic properties. We apply it here to study first the efficiency of germanium doping to screen the polarization-induced internal electric field in AlN/GaN superlattices. In addition, our identification of electric field inversion domains associated with Ge inhomogeneities paves the way for the use of delta doping as a tool in the design of heterostructures, to modulate and even invert the electric field in polar heterostructures. We have also addressed the effect of delta-doping in AlGaN/GaN, showing that inversion of the electric field is also possible using Si delta-doping, with improved reproducibility. Our studies show that the incorporation of germanium in III-nitride heterostructures remains challenging, with issues such as dopant segregation and dopant migration, but silicon delta-doping is also a very promising tool for fine-tuning of the internal electric fields in these materials.

This work, carried out on the Platform for Nanocharacterisation (PFNC), was supported by the “Recherche Technologique de Base” and "France 2030 - ANR-22-PEEL-0014" programs of the French National Research Agency (ANR).

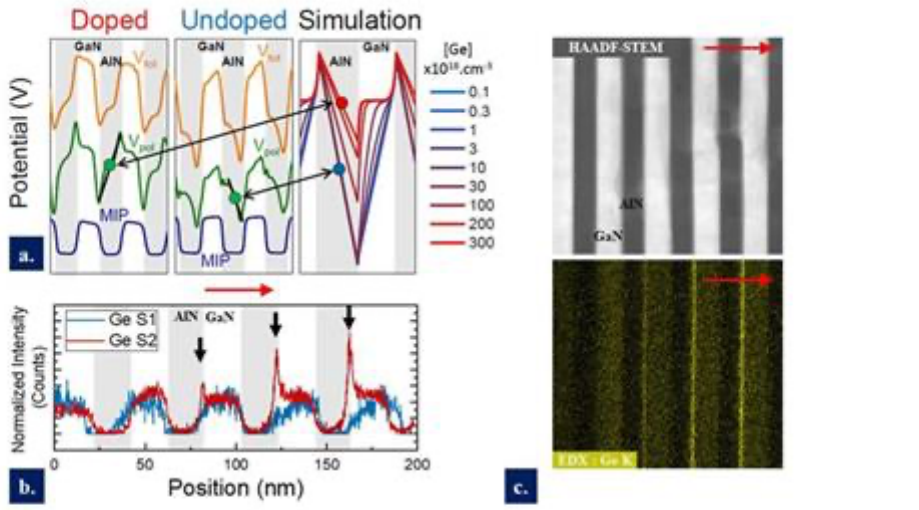


Fig.2: The red arrow represents the [0001] growth direction. [a] Comparison of the potential profiles for the doped (S2) and undoped (S1) potential with simulations (nextnano3 software), showing an inversion of the electric field in the AlN layer for the doped sample. [b] EDX profile of the germanium for S1 and S2. The signal observed for S1 is an artefact due to the proximity of Kα energy band for Ga and Ge. The black arrows highlight the Ge peak at AlN/GaN interfaces. [c] HAADF-STEM image of the AlN/GaN superlattice and EDX map of the Ge, showing the accumulation of Ge at interfaces.

**Keywords:**

Electron holography, III-nitride semiconductors, doping

**Reference:**

[1] L. Denaix, et al., ACS Appl. Mater. Interfaces 15, 11208 (2023)
[2] C. Bougerol, et al., ACS Appl. Mater. Interfaces 13, 4165 (2021)

258

# Detection limits of electric field characterization at a p-n junction by 4D-STEM

Bruno Cesar da Silva[1], Yiran Lu[1], Alexis Wartelle[1], Eva Monroy[2], Jean-Luc Rouviere[3], David Cooper[4], Dr Martien den Hertog[1]
[1]Univ. Grenoble Alpes, CNRS, Grenoble INP, Institut Néel, 38000 Grenoble, France, Grenoble, France, [2]Univ. Grenoble-Alpes, CEA, Grenoble INP, IRIG, PHELIQS, Grenoble, France, Grenoble, France, [3]Univ. Grenoble-Alpes, CEA-IRIG, MEM, Grenoble, France, Grenoble, France, [4]CEA, LETI, MINATEC, Grenoble, France, Grenoble, France

PS-03 (2), Lecture Theater 2, august 30, 2024, 10:30 - 12:30

The emergence of fast pixelated direct electron detectors over the last years is allowing experiments in four-dimensional scanning transmission electron microscopy (4D-STEM) that would previously be too slow or noisy to be feasible, for example enabling the assessment of internal electric fields with high spatial resolution and precision[1–4] However, the electric field strength of long range built-in electric fields present in semiconductor devices, for example those associated with p-n junctions, is typically three orders of magnitude smaller than atomic electric fields, making 4D-STEM experiments in such systems challenging. It is therefore interesting to assess the detection limit and signal to noise that can be expected depending on the TEM operation conditions.

In this presentation, we describe how the quantification, sensitivity and spatial resolution of electric field mapping in a silicon p-n junction are influenced by the acquisition parameters in a momentum-resolved 4D-STEM experiment [3,5] comparing two different TEM setups differing in brand and in age by 10 years: the first setup, a TFS Titan Ultimate, was installed in 2012; the second, a Jeol Neo Arm in 2022. Both instruments provide 4D STEM capabilities using a Merlin camera based on medipix technology from Quantum Detectors. We have used the center-of-mass approach to analyze the diffraction patterns, obtained on a focused ion beam prepared silicon sample containing a p-n junction.

It will be shown that the success of the quantitative measurements depends not only on the correct estimation of the dead layer, but also on the acquisition conditions, most importantly the electron beam convergence angle.

The detection limit, defined as the three-sigma standard deviation of the field value away from the field containing region, was evaluated both as a function of beam semi-convergence angle as well as TEM setup. It was observed that the electric field precision improves by decreasing the semi-convergence angle [5]. For example, at a convergence angle of about 200 µrad, the detection limit was as good as 0.01 MV/cm, and it can even be lowered to 0.007 MV/cm in the more recent TEM setup. While such a low convergence angle setting gives the best detection limit and signal to noise ratio of the electric field (SNR 10 and 20, respectively), the increased probe size (estimated around 10 nm) can lead to an underestimation of the electric field value if the field containing region is of similar size as the electron probe. This was the case in the sample under study, where the field containing region was about 50 nm wide. Increasing the convergence angle to about 1 mrad avoids the underestimation of the field since the probe size is smaller (3-4 nm), at the expense of an increased detection limit. With about 1 mrad convergence angle a precision of 0.087 and 0.030 MV/cm with SNR 1.8 and 4.7 were achieved, respectively. As an example, maps of the modulus of the electric field are shown in Fig. 1 together with electric field profiles integrating either over 12 or 90 nm at three different convergence angles, where the Jeol Neo Arm is operated in Lorentz STEM mode.

The effect of electron dose is an important parameter, in particular in relation to beam sensitive materials. The influence of dose was evaluated and invariable electric field profiles were obtained using an electron dose as low as 24 e-/Å. Of course, the precision of the measurement does depend

on dose. It was shown that for an average electron count of about 25 -75 counts per px, the detection limit does not further decrease for increased exposure times. Above this number of counts, the detection limit seems no longer limited by statistical Poisson noise on the detector, but by experimental instabilities, such as fluctuations on the high tension or lens currents or irregularities on the sample such as surface roughness.
In addition, in-situ electrical biasing coupled to momentum-resolved 4D-STEM measurements were performed, investigating the study of the degree of ideality of the junction abruptness, allowing the detection of phenomena like dopant segregation or interdiffusion [4].

This work paves the way for the development of advanced STEM based techniques able to provide imaging and quantification of built-in electric fields, potentials and charge densities in semiconductor devices with high spatial resolution, providing crucial feedback to improve growth/device fabrication processes.

Figure 1: 4D STEM maps at different convergence angle: The local modulus of the electric field is represented using three different Lorentz STEM modes of the Jeol Neo Arm, with three different convergence angles. Profiles are made along 12 nm, top row, and along 90 nm, bottom row.

Acknowledgements: This project received funding from the European Research Council under the European Union's H2020 Research and Innovation programme via the e-See project (Grant No. 758385). Experiments have been performed at the Nanocharacterisation platform PFNC in Minatec, Grenoble as well as at TEM facility JEOL NEOARM co-financed by the European Union under the European Regional Development Fund (ERDF, contract n° RA0023813).

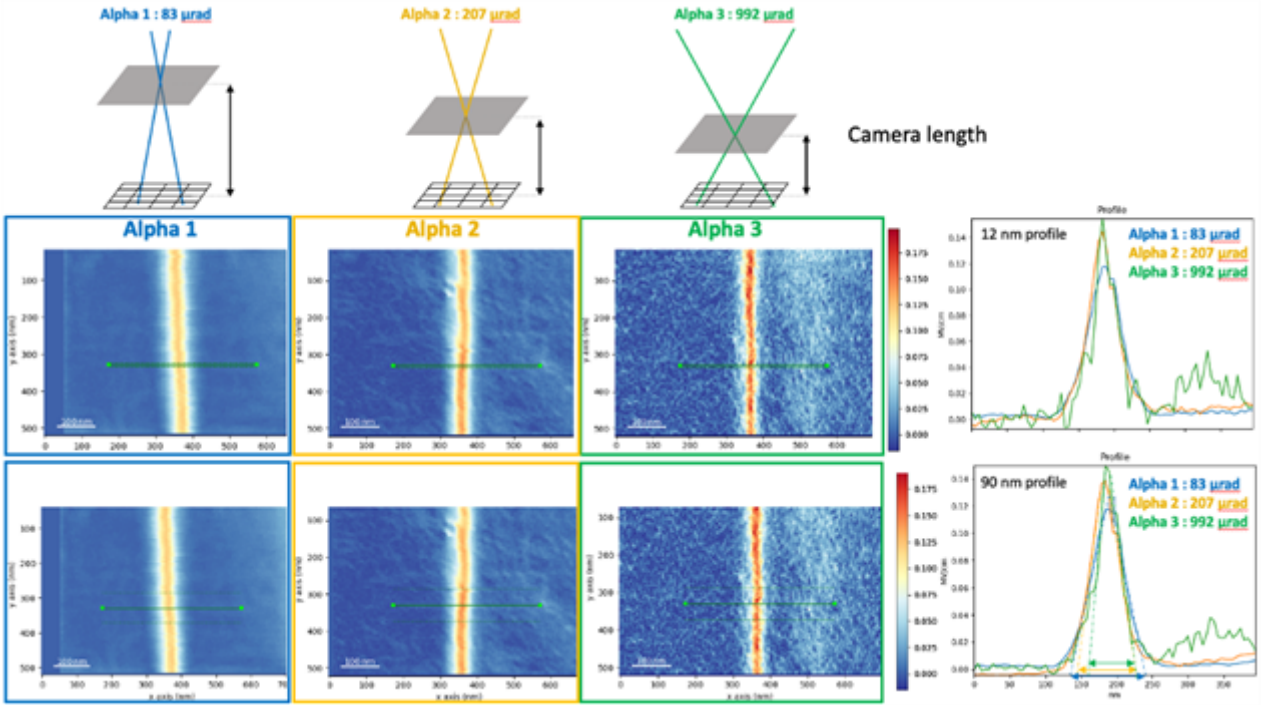


**Keywords:**

4D-STEM, electric field characterization, biasing

**Reference:**

[1] L. Bruas, et al, J. Appl. Phys. 2020, 127, 205703.
[2] A. Beyer, et al, Nano Lett. 2021, 21, 2018–2025.
[3] B. C. da Silva, et al, Appl. Phys. Lett. 2022, 121, 123503.
[4] B. C. da Silva, et al, Nano Lett. 2022, 22, 9544–9550.
[5] S. Pöllath, et al, Ultramicroscopy 2021, 228, 113342.

399

# Low-Dose 4D-STEM Investigations of the Octahedral Network Structure in Formamidinium Lead Bromide Nanocrystals

Nadine Schrenker[1,2], Mr. Tom Braeckevelt[3], Mrs. Annick De Backer[1,2], Mr. Nikolaos Livakas[4], Mr. Chu-Ping Yu[1,2], Mr. Thomas Friedrich[1,2], Mr. Daen Jannis[1,2], Mr. Armand Béché[1,2], Mr. Maarten Roeffaers[5], Mr. Johan Hofkens[6], Mr. Johan Verbeeck[1,2], Mr. Liberato Manna[4], Mrs. Veronique Van Speybroeck[3], Mrs. Sandra Van Aert[1,2], Mrs. Sara Bals[1,2]
[1]Electron Microscopy for Materials Science (EMAT), University of Antwerp, Antwerp, Belgium, [2]NANOlab Center of Excellence, University of Antwerp, Antwerp, Belgium, [3]Center for Molecular Modeling, Ghent University, , Belgium, [4]Department of Nanochemistry, Istituto Italiano di Tecnologia (IIT), Genova, Italy, [5]cMACS, Department of Microbial and Molecular Systems, KU Leuven, Leuven, Belgium, [6]Department of Chemistry, KU Leuven, Leuven, Belgium

PS-03 (2), Lecture Theater 2, august 30, 2024, 10:30 - 12:30

Background incl. aims
Hybrid organic-inorganic metal halide perovskites have shown great potential as semiconductors for new optoelectronic devices, such as photovoltaics, light-emitting diodes, and X-ray detectors. Their outstanding optoelectronic properties, including a tunable bandgap, high charge carrier mobility, high photoluminescence quantum yield, and low recombination rate of photogenerated carriers, have contributed to their rapid development.(Dey et al. 2021) The structure of metal halide perovskites (MHP) is described by the chemical formula ABX3, where A is a monovalent organic cation (e.g. formamidinium (FA+) [CH(NH2)2+] or methylammonium (MA+) [CH3NH3+]) or a metal cation (e.g. Cs+), B is a divalent metal cation (typically Pb2+or Sn2+), and X is a halide anion (X = Cl-, Br-, I-). The perovskite structure consists of [BX6]4-octahedra that are connected through the corner halides. The octahedral network structure is closely linked with the polymorphic nature of MHPs, which is of great importance since phase instability is still one of the major roadblocks for long-term applications of MHPs. Only the “black” phase demonstrates photoactive properties, which dramatically decrease once the MHPs convert to the “yellow” phase. From the high-symmetry cubic phase, the transition to the lower symmetry phases can be described by rotation or shearing of the octahedra. It is crucial to understand the role of the octahedral network to unravel the structure-property connection and correlate it to transformations during degradation. Transmission electron microscopy (TEM) is an excellent method for investigating the local structure of nanocrystals (NCs), even down to the atomic level. Nevertheless, when applied to MHPs, their sensitivity to the electron beam is highly challenging. Irradiation with the electron beam easily causes degradation of the MHP NCs with PbX2 and Pb as resulting products.
Methods
In this study we utilize four dimensional scanning transmission electron microscopy (4D-STEM) to obtain phase contrast image reconstructions to investigate the local structure of colloidal FAPbBr3 NCs, which were synthesized following a hot injection method. Phase contrast imaging is beneficial for materials in which both heavy and light elements are simultaneously present, such as organic cations and lead in perovskites. Moreover, 4D-STEM is superior with respect to information-richness and dose-efficiency as compared to high-angle annular dark-field (HAADF) STEM, where only electrons scattered to relatively high angles are used. The 4D-STEM datasets were acquired with a custom-made Timepix3 detector, which is an event driven hybrid pixelated direct electron detector. To retrieve the phase information from the recorded 4D datacube, we applied a recently developed convolutional neural network (CNN).(Friedrich et al. 2023) The CNN was trained based on a large synthetic dataset, using atomic structures extracted from the materials project database. Moreover, to analyze the local structure we fitted the shape of the projected atomic columns. For this purpose, a parametric model was used which consists of a sum of two-dimensional elliptical Gaussians, each

centered on the atomic column positions. Additionally, the experimental STEM results were compared with a series of molecular dynamics (MD) simulations at constant temperature and pressure, which were performed using a machine learning potential trained on underlying Density Functional Theory energies and forces.

Results

The high dose efficiency of the CNN reconstruction enables to study these beam-sensitive NCs with an electron dose that is sufficiently low to avoid the formation of Pb-rich clusters due to electron beam irradiation while maintaining a high signal-to-noise ratio. It is noteworthy that at a total electron dose below 50 e-/A2, all atomic columns, including the light formamidinium cations and Br anions can be clearly detected in the CNN reconstructions (see panel (a) in Figure 1). Moreover, a close inspection of the projected Br columns revealed deviations from perfect round projections. A possible reason are alternations in the position of the Br atoms along the viewing direction. The ellipticity ratio for the projected Br atomic columns was obtained by fitting elliptical Gaussians. In panel (b) the arrows illustrate the ellipticity ratio of the projected Br atomic columns and the overlay represents the different atomic columns ((Br = purple, Pb-Br = blue, FA = orange). This indicates that the Br atoms have a small flexibility in the octahedral network structure and can be displaced perpendicular to the Pb-Br-Pb bond, which is schematically illustrated by the red arrows in panel (c) in Figure 1. Furthermore, the performed MD simulations confirmed the displacement of the Br atomic columns. This observation is also in good agreement with previous synchrotron XRD measurements of FAPbBr3 NC, where the measured Pb-Br-Pb bond angles deviate up to 15 ° from the ideal 180 ° angle due to local disorder caused by displacement of Br anions.(Yazdani et al. 2023)

Conclusion

Thus, our approach via low-dose phase image reconstructions enables to study the local octahedral network structure of perovskites and could be transferred to in situ experiments in the future to investigate degradation mechanisms under environmental triggers.

.

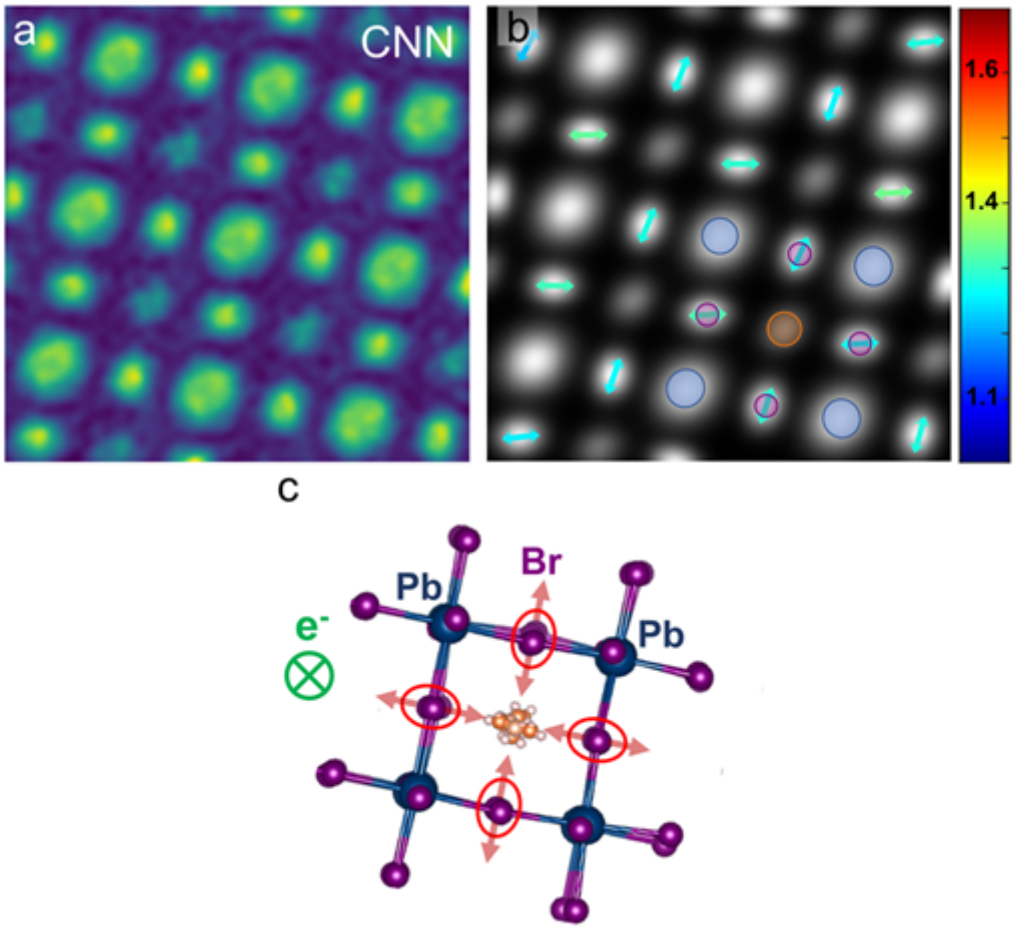

**Keywords:**

perovskite, 4D-STEM, phase contrast imaging

**Reference:**

1. Dey, A. et al. ACS Nano 15, 10775–10981 (2021).
2. Friedrich, T., Yu, C.-P., Verbeeck, J. & Van Aert, S. Microscopy and Microanalysis 29, 395–407 (2023).
3. Yazdani, N. et al. Nature Physics 2023 1–7 (2023)

439

# Picoseconds and nanometers; time and spatially resolved cathodoluminescence spectroscopy to characterise nonradiative defects in semiconductors.

Dr. Gunnar Kusch[1], Dr. Thomas Weatherley[2], Dr. Frank Mehnke[3], Dr. Eamon T. Hughes[4], Dr. Tim Wernicke[3], Dr. Justin Norman[4], Prof. John E. Bowers[4], Prof. Kunal Mukherjee[5], Prof. Michael Kneissl[3], Prof. Nicolas Grandjean[2], Prof. Rachel A. Oliver[1]
[1]University of Cambridge, Cambridge, United Kingdom, [2]Ecole Polytechnique Fédérale de Lausanne, Lausanne, Switzerland, [3]Technische Universität Berlin, Berlin, Germany, [4]University of California Santa Barbara, Santa Barbara, USA, [5]Stanford University, Stanford, USA

PS-03 (2), Lecture Theater 2, august 30, 2024, 10:30 - 12:30

The drive for miniaturization in the ever evolving field of semiconductor technology has pushed the ability to provide in depth material and device characterization to its limit. This is particularly strongly felt in the characterization of the opto-electronic properties, as the established techniques (such as photoluminescence) are inherently limited in their achievable spatial resolution. Nevertheless, being able to characterize not only the steady state optical properties on the nanoscale but also time dependent properties is paramount for further scientific and engineering progress. Especially as nanoscale features such as point and extended defects can significantly influence material and device properties.
While cathodoluminescence spectroscopy for characterization of steady state properties on the nanoscale has been available for quite some time, reports on (hyperspectral) time-resolved characterization with picosecond resolution have been much more limited (1), (2), (3). This work demonstrates hyperspectral time-resolved cathodoluminescence (TR-CL) spectroscopy for the analysis of the interplay between extended defect and point defects in UV-C light emitting AlGaN quantum wells (QWs), single nonradiative point defects in an InGaN/GaN QW and extended defects in InAs QDs on Si substrates.

We are using an Attolight Chronos dedicated TR-CL scanning electron microscope with laser pulsing system. We have achieved time-resolved measurements with 7 ps resolution in point and shoot mode, and 100 ps time resolution when recording hyperspectral TR-CL maps. All investigated samples were grown by MOVPE. Sample analysis has been performed using the open source Python packages Hyperspy and Lumispy.

We have successfully measured the carrier lifetime in AlGaN-based, UV-C light emitting, QWs with emission wavelengths ranging from 260 nm to 220 nm (with QW composition varying from 56% to 82%) at temperatures from 80 K to 300 K. We found, that the carrier lifetime decreases strongly with increasing QW Al mole fraction, indicating a significant increase in the point defect density. Further, spatially resolved, investigation of the interplay between threading dislocations and point defects show no evidence for a significant influence of the local threading dislocation density on the carrier lifetime, indicating that the optoelectronic properties of these materials are being controlled by their point defect density.
Observation of decay dynamics in InAs QD systems using hyperspectral TR-CL reveals changes in the carrier lifetime in and around misfit dislocations. In contrast to our observations in AlGaN we can observe a significant decrease in carrier lifetime, when compared to the surrounding material, at the extended defect. This does highlight both the strong effect extended defects can have on carrier dynamics and that differences in the point defect density and carrier localization can significantly impact local recombination channels. We also observed a lack of impact of the misfit dislocation on the lifetime on the material immediately surrounding the dislocation which we attributed to a short

carrier diffusion length, preventing carriers from reaching the non-radiative recombination centre. This in turn causes the observed high tolerance of the internal quantum efficiency for defects in this system (4).
Lastly, hyperspectral TR-CL has been carried out on a carefully designed InGaN/GaN QW system for the investigation of isolated point defects. The system contains an ultrathin QW ( 3 ~bilayers thick) on a low dislocation density template (~106 cm-2) with a point defect filtering layer, resulting in a point defect density of about 109 cm-2 . The low density allowed us to first find isolated point defects and then measure hyperspectral TR-CL maps containing these isolated point defects. Extracting spatially resolved carrier lifetimes from the hyperspectral dataset then allowed us to not only compare and analyse decay times across the mapped area but also to visualize carrier diffusion within the system. Our findings in this system reveal the direct influence of isolated nonradiative point defects on carrier recombination dynamics and open the pathway for indepth studies of the optoelectronic properties of point defects.

We have demonstrated the unparalleled ability of TR-CL to characterize the opto-electronic properties of defects in a wide range of materials systems on the nanoscale. Further development of TR-CL capabilities will only strengthen this research capability and provide future research on nanoscale devices and objects with an invaluable tool for the characterization of spatially resolved carrier dynamics.

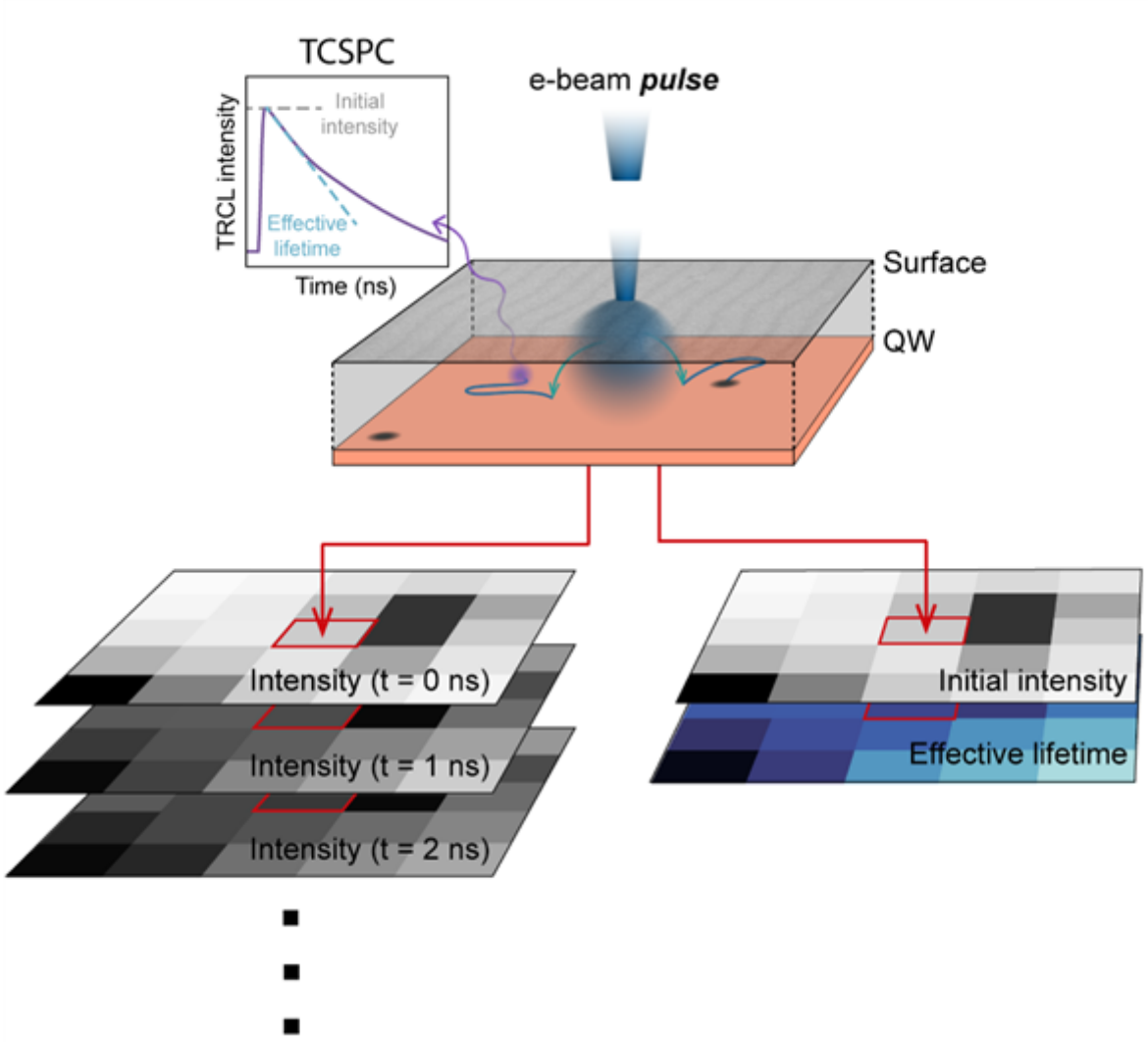


**Keywords:**

Cathodoluminescence, Time-resolved, Hyperspectral, Nitrides, Arsenides

**Reference:**

1. Probing carrier dynamics in nanostructures by picosecond cathodoluminescence. Merano, M. 7067, s.l. : Nature, 2005, Vol. 438, pp. 479-482.
2. Photon bunching in cathodoluminescence. Meuret, S. 19, 2015, Physical review letters, Vol. 114, p. 197401.
3. Lifetime measurements well below the optical diffraction limit. Meuret, S. 7, s.l. : ACS photonics, 2016, Vol. 3, pp. 1157-1163.
4. Dislocation-Induced Structural and Luminescence Degradation in InAs Quantum Dot Emitters on Silicon. Hughes, E. T. 14, s.l. : physica status solidi(a), 2023, Vol. 220, p. 2300114.

471

# In situ TEM thermal study of MBE and CVD GeSn layers: cross-section and plan-view geometries

Karí Martínez[1], Alexey Minenkov[1], Johannes Aberl[2], Moritz Brehm[2], Heiko Groiss[1]
[1]Christian Doppler Laboratory for Nanoscale Phase Transformations, Center for Surface and Nanoanalytics, Johannes Kepler University Linz, 4040 Linz, Austria, [2]Institute of Semiconductor and Solid-State Physics, Johannes Kepler University Linz, 4040 Linz, Austria

PS-03 (2), Lecture Theater 2, august 30, 2024, 10:30 - 12:30

Introduction

Direct band gap GeSn epilayers have great potential in high-performance Si-based electronics and optoelectronics. A transition to a direct band gap can be achieved in GeSn layers when the Sn concentration exceeds 6 at% [1], a value well above the solubility limit. Therefore, these non-equilibrium GeSn alloys with the desired materials concentrations are unstable at high temperatures, resulting in phase separation and decomposition processes [2]. Two main epitaxial methods used for the material synthesis are molecular beam epitaxy (MBE) and chemical vapor deposition (CVD). Depending on the method, the properties of the GeSn can vary strongly. For example, the CVD GeSn films exhibit better optical properties and, to the best of our knowledge, all GeSn-based lasers were grown via this technique. Thermal stability is another property that can vary. The excess of Sn and its possible segregation that, can occur during material growth, has a major influence on thermal stability. Understanding this is important for predicting the thermal budget that a Ge1-xSnx layer can be exposed to during device fabrication.

Methods

We use the powerful technique of in situ transmission electron microscopy (TEM) to study the dynamic process during thermal annealing experiments. We analyze how the Sn concentration and the presence of dislocations affect the thermal stability. In this regard, samples grown by CVD and MBE, 50 nm thick epilayers with 6-14 at% Sn on Ge substrate, were analyzed in cross-section and plan-view geometries. The cross-sectional lamellae were cut and installed on micro-electro-mechanical system (MEMS) heating chips with a Ga+ focused ion beam (FIB). In the case of the plan-view, first, the samples were prepared by wedge polishing technique, and then with FIB transferred to the MEMS chip and finally thinned [3]. The experiments were performed by heating-cooling-cycles with an increasing maximum temperature up to 750°C, investigating the sample via complementary HRTEM and STEM EDXS. In cross-section geometry, we can trace precipitation in relation to present interfaces and surfaces, while in plan-view geometry we can gain information about the morphological changes and particle size distribution on the surface of interest.

Results

For the MBE samples, two different concentrations of 10 and 14 at% Sn were investigated. The cross-section specimen with 10 at% Sn is stable up to 500°C. At 500°C, Sn-based precipitates are formed in the GeSn epilayer. HRTEM Fast Fourier transform (FFT) analysis of these inhomogeneities reveals a pattern well-fitted with the β-Sn crystal structure [4]. At the same temperature, we monitored the formation of Sn drops in the plan-view sample. In the case of a cross-section sample with 14 at% Sn, the start of the precipitation process is found at a lower temperature of 350°C. For a CVD GeSn layer with 11.5 at% Sn, the specimen shows stability up to 450°C where also β-Sn precipitates appeared. However, to achieve these results the cross-section specimen had to be prepared by the wedge polishing technique, reducing the FIB processing and Ga contamination. Without this measure, the CVD-grown sample decomposes already at 200°C under the influence of Ga impurities implanted during FIB-assisted specimen preparation. To better understand the present Ga contamination

effects and the relation with defects, we analyzed CVD samples with different growth and buffer qualities, which influence the density of threading dislocations. However, all samples were highly susceptible to Ga contamination during the standard lamella preparation. Applying our optimized wedge polishing technique, we analyzed additionally a CVD sample with 6 at% Sn, which demonstrated stability up to 650°C during the in situ TEM experiment.

Conclusion

The measured Sn segregation temperature for cross-sectional and plan-view geometries correlate well, however, there are differences in the precipitate densities which are attributed to the free surface diffusion of Sn for the plan-view specimen compared to the suppressed one for the capped cross-section. Regarding the two MBE specimens, since no formation of liquid phases was observed, a solid-state diffusion and precipitation mechanism is believed to occur. Ga contamination during preparation can lead to the formation of a GaSn liquid phase during annealing [4], leading to a fast decomposition of the GeSn layer. CVD GeSn layers are more susceptible to this effect, which we believe is due to the presence of point defects induced by the CVD method. Nevertheless, using the wedge polishing approach it was possible to overcome this challenge. The obtained results show the highest stability for the sample with 6 at% Sn and the lowest for the sample with 14 at% Sn. The gained results indicate a strong dependence of the decomposition temperature on the Sn content, which is summarized in the figure presented.

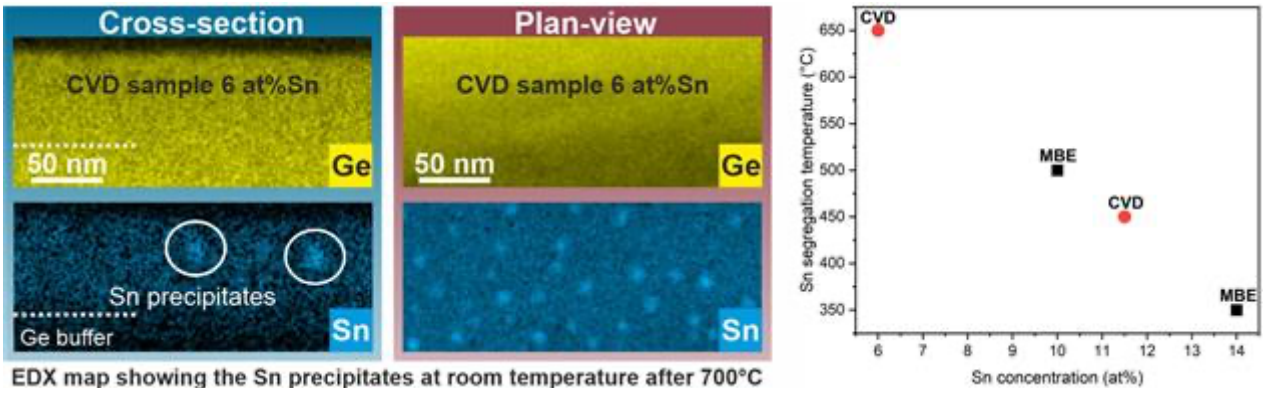


EDX map showing the Sn precipitates at room temperature after 700°C

**Keywords:**

In-situ TEM, GeSn, MBE, CVD

**Reference:**

[1] J. Doherty et al., “Progress on Germanium-Tin Nanoscale Alloys,” Chem. Mater., vol. 32, no. 11, pp. 4383–4408, 2020, doi: 10.1021/acs.chemmater.9b04136.

[2] A. Minenkov and H. Groiss, “Evolution of phases and their thermal stability in Ge–Sn nanofilms: a comprehensive in situ TEM investigation,” J. Alloys Compd., vol. 859, p. 157763, 2021, doi: 10.1016/j.jallcom.2020.157763.

[3] A. Minenkov et al., “Advanced preparation of plan-view specimens on a MEMS chip for in situ TEM heating experiments,” MRS Bull., vol. 47, no. 4, pp. 359–370, 2022.

[4] K. Martínez, A. Minenkov, J. Aberl, D. Buca, M. Brehm, and H. Groiss, “In situ TEM heating experiments on thin epitaxial GeSn layers: Modes of phase separation,” APL Mater., vol. 11, no. 10, 2023, doi: 10.1063/5.0167407.

503

# Sn Alloying Impact on Structural and Electronic Properties of Core-Shell Ge-GeSn Nanowires: A TEM Study

Milenka Andelic[1], Dr. Alexandre Pofelski[1,4], Dr. Isobel Bicket[1,2,3], Dr. Simone Assali[5], Dr. Sebastian Koelling[5], Dr Lo Luo[5], Dr. Oussama Moutanabbir[5], Dr. Gianluigi Botton[1,6]
[1]McMaster University, Hamilton, Canada, [2]Atominstitut, TU Wien, Vienna, Austria, [3]University Service Centre for Transmission Electron Microscopy, TU Wien, Vienna, Austria, [4]Brookhaven National Laboratory, Upton, USA, [5]Ecole Polytechnique Montreal, Montreal, Canada, [6]Diamond Light Source, Oxfordshire, UK

PS-03 (2), Lecture Theater 2, august 30, 2024, 10:30 - 12:30

Background incl. aims
Alloying group IV elements in out-of-equilibrium conditions when there is a significantly different atomic size between the atoms of the host lattice (Ge) and the alloying element (Sn) results in peculiar modifications of the structure and electronic properties of the parent phases. Growing alloys in the form of core-shell Ge-GeSn heterostructures adds an additional degree of freedom for strain accommodation. Moreover, such core-shell configuration induces changes in their morphological, chemical, electronic, and optical properties. Investigating these heterostructures, where Ge acts as the core and GeSn as the shell in hexagonally faceted nanowires with a diameter in a range of 80-100 nm and length exceeding tens of µm, poses significant challenges. While there are challenges, these heterostructures offer numerous opportunities for developing silicon-compatible devices with enhanced capabilities in the mid-infrared wavelength range (5-20µm). These capabilities include, among others, CMOS and MOSFET devices, night-vision devices, and lasers [1], owing to their advanced band-to-band transitions and enhanced carrier mobility. Consequently, a thorough investigation and precise characterization, at the atomic level, are crucial for these heterostructures, requiring a high degree of sensitivity and high-spatial resolution. The introduction of Sn to Ge, a high carrier mobility element, will undoubtedly have a profound impact on its bandgap characteristics, influencing transitions within the bandgap [2]. We observe and extract information locally and detect features using the Scanning Transmission Electron Microscopy (STEM) technique, employing an extremely narrow electron probe directed at the sample to obtain detailed insights into the structure and chemical composition of these intriguing core-shell structures. The initial Sn content ranges from below 8 at. % to above 14 at. % representing a substantial amount of Sn. It has been predicted that the transition from an indirect to a direct bandgap will occur at approximately 8 at. % Sn [3], a hypothesis we aim to experimentally confirm and deepen further.

Methods
To study such core-shell heterostructures, we utilize a High-Resolution (HR) STEM with the High-Angle Annular Dark Field (HAADF) detector and Energy-Dispersive X-Ray Spectrometer (EDS). For such purpose we employ the ThermoFisher Scientific Spectra Ultra double-corrected TEM operated at 300 kV with a segmented Ultra-X EDS detector enabling atomic-resolved EDS maps. Additionally, we implement electron energy-loss spectroscopy (EELS) in STEM mode using the Nion HERMES 100 instrument operated at 60 kV, with optimal energy resolution of 4.8 meV for detailed examination of electronic and optical properties.

Results
The results of this investigation unveil a substantial impact of increased Sn content in the core-shell Ge-GeSn nanowires on their structural, electronic, and optical characteristics. The performed EDS analysis validates the distinctive core-shell configuration, highlighting a region depleted of Sn in the core, alongside a discernible degree of its uniformity in the shell (Figure 1a). Additionally, findings

show that the notable segregation of Sn adatoms along the hexagonal facets promotes the generation of complex defects and that their complexity is more prominent with the elevated Sn content and incorporated strain. The presence of twinning may contribute to the growth of supplementary structures such as nanobelts (NB) with unique non-hexagonal cross-sectional shapes. Moreover, the coexistence of both diamond cubic (DC) and hexagonal-wurtzite (WZ) structures (Figure 1b) or polytypism, results in notable changes in the polarity of these initially presumed non-polar elements (i.e. we alloy within the same group IV elements), enhancing the complexity and interest in the ordered nature of these structures. The investigation of electronic transitions at a high level of locality with high-energy resolution EELS confirms that the increase of the Sn content from 8 at.% up to 18 at.% leads to a transition from an indirect bandgap of Ge (measured 0.67 eV) to a direct bandgap of GeSn, and a shift from 0.56 eV for 8 at.% Sn to approximately 0.3 eV for 18 at.% Sn (Figure 1c).

Conclusion

In summary, our findings demonstrate that core-shell Ge-GeSn nanowires exhibit a unique morphology and crystalline structure ascribed to the Sn content within the GeSn shell. Furthermore, an in-depth investigation of high-spatial resolution HAADF data unveils that the presence of Sn segregation, occurring with higher Sn concentrations in the shell, significantly impacts the occurrence of intricate defects like twinning. As evidenced by the EELS data, the transition of the bandgap from indirect to direct concomitant with a reduced value (measuring below 0.67 eV for Ge), was confirmed with higher Sn concentrations surpassing approximately 8 at.%.

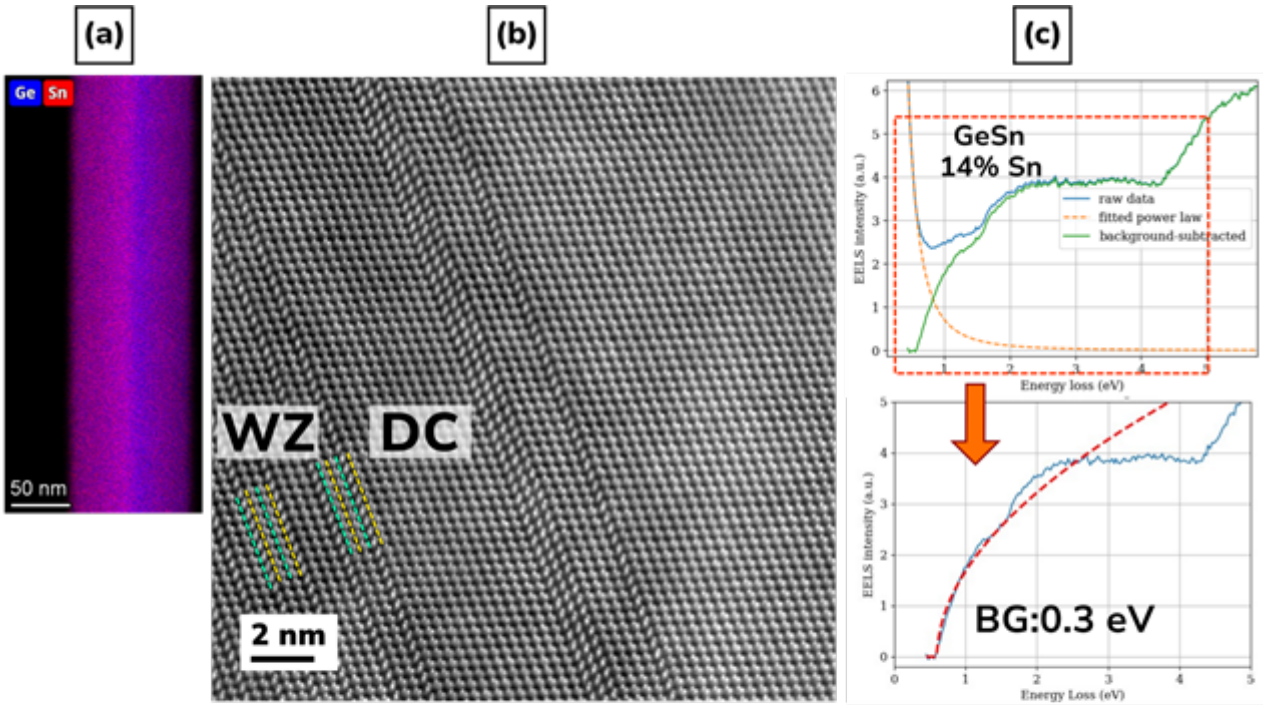


Figure 1: (a) EDS map illustrating the dominant core-shell structure with the Ge-rich area (blue region) in the core, and uniform Sn distribution in the GeSn shell (b) Atomically resolved HAADF image revealing the presence of the polytype crystal structures consisting of transitions between diamond cubic (DC) and wurtzite (WZ) through the emergence of stacking faults and twins; (c) EELS data extraction showing the bandgap energy onset of approximately 0.3 eV for 14 at. % of Sn.

**Keywords:**

GeSn core-shell nanowires, bandgap, STEM/EELS

**Reference:**

[1] Du, Wei, and Shui-Qing Yu. Mid-infrared Optoelectronics. Woodhead Publishing, 2020. 493-538.
[2] Fadaly, Elham MT, et al. Nature 580.7802 (2020): 205-209.
[3] Gupta, Suyog, et al. Journal of Applied Physics 113.7 (2013).

228

# Study on local indium concentration in Ga(1-x)InxN quantum wells using quantitative scanning transmission electron microscopy

Daesung Park[1,3], Jannik Guckel[1,3], Philipp Horenburg[2], Heiko Bremers[2,3], Uwe Rossow[2], Andreas Hangleiter[2,3], Harald Bosse[1,3]
[1]Physikalisch-Technische Bundesanstalt (PTB), Braunschweig,, Germany, [2]Institute of Applied Physics (IAP), Technische Universität Braunschweig, Braunschweig,, Germany, [3]Laboratory for Emerging Nanometrology (LENA), Braunschweig,, Germany

PS-03 (3), Lecture Theater 2, august 30, 2024, 14:00 - 16:00

Background incl. aims
Multiple quantum wells (MQW) and single quantum wells (SQW) of Ga(1-x)InxN on GaN are promising candidates for nanooptical light emitters due to their high quantum efficiency. The band gap of Ga(1-x)InxN can be controlled over a wide wavelength range by tailoring the variation of the indium concentration [1]. In addition, the epitaxially grown quantum well structures can be easily modified using chemical etching for the formation of a pyramid containing a quasi quantum dot structure. As the dimension of the quantum structure shrinks, the variation of the local indium concentration impairs the optical properties. Therefore, a robust characterization technique is required to understand and optimize such complex structures on the atomic scale.
Methods
In this study, an ultra-thin single quantum well of Ga(1-x)InxN between GaN layers on an Al2O3 substrate was grown using metal organic vapor phase epitaxy (Fig. 1). The cross-sectional specimen was prepared using focused ion beam, including the final low kV milling. The prepared specimen was characterized using a double-aberration corrected JEOL NeoARM 200F equipped with a cold field emission gun. For a precise intensity and local lattice parameter analysis, sequential high-angle annular dark-field (HAADF) imaging was utilized with a reasonably short acquisition time (1 sec/frame). The entire image stack was aligned by the rigid registration algorithm and averaged out to obtain a single drift-corrected HAADF image (Fig. 2(a)).
Results
The fractional intensity (normalized by the incident electron beam intensity) of the HAADF image was analyzed based on frozen phonon multi-slice calculation results [2]. The local thickness was determined by the mean intensity of the Ga atomic columns in the GaN layers and additionally verified by the acquired position averaged convergent beam electron diffraction (PACBED) pattern (Fig. 2(e,f)) [3]. The local indium concentration of the single quantum well of Ga(1-x)InxN was finally derived from the fractional intensity of the HAADF image (Fig. 2 (d)), showing the mean indium concentration of 13 at.% within the single quantum well. In addition, the local lattice parameters were analyzed based on the individual atomic column positions obtained from the drift-corrected HAADF image (Fig. 2(g)). The local indium concentration was then derived using a modified Vegard's law including biaxial elastic strain effects (Fig. 2(h)). The mean indium concentration within the single quantum well from this analysis was 10 at.%. This result was reasonably comparable with the local indium concentration obtained from the quantitative HAADF intensity analysis. Moreover, this local composition information was supported by the quantitative electron energy-loss (EEL) spectroscopy analysis at the unit cell level, confirming the mean indium concentration of about 16 at. % (Fig. 3).
Conclusion
The combination of HAADF imaging, PACBED, and spatially resolved EEL spectroscopy techniques provided detailed structural and chemical information of Ga(1-x)InxN quantum well structure. The relationship between atomic structure and composition could be thoroughly studied. These robust combined scanning transmission electron microscopy (STEM) techniques will ultimately reveal the effect of altering indium concentration on complex quantum dot structures.

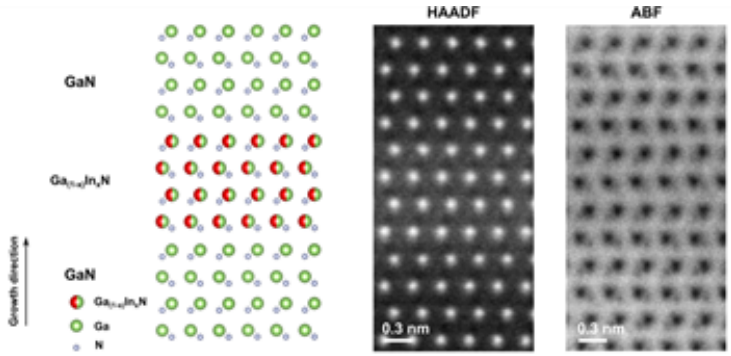


**Fig. 1: Atomic structure of the ultrathin single quantum well of Ga(1-x)InxN between GaN layers with corresponding HAADF and annular bright-field (ABF) image.**

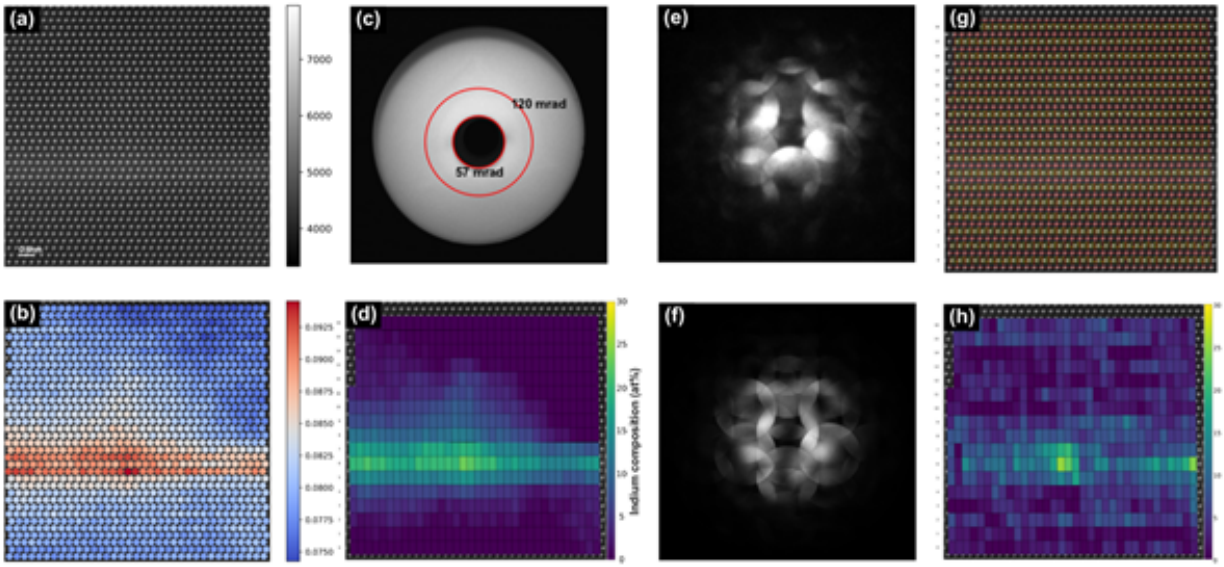


**Fig. 2: Quantitative HAADF image analysis of the single quantum well of Ga(1-x)InxN between GaN layers. (a) raw HAADF image, (b) mean normalized intensity within a finite mask size, (c) the ADF detector image, (d) the local indium concentration map from the HAADF intensity analysis, (e) experimental PACBED, (f) PACBED simulation for ~ 30 nm, (g) the local lattice parameter analysis, and (h) the local indium concentration map from the lattice parameter analysis.**

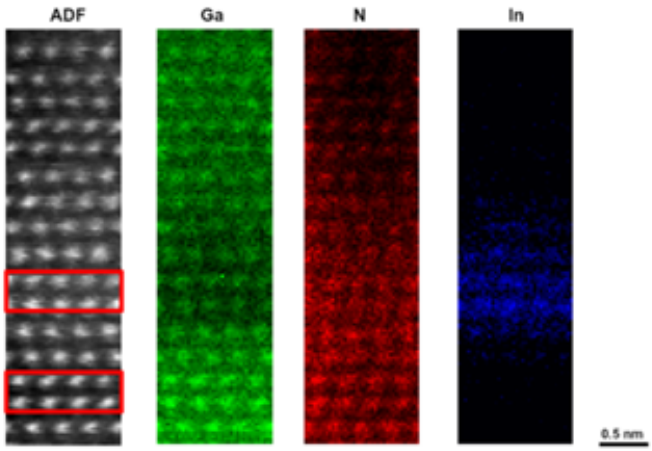


**Figure 3: Atomic resolution EELS elemental map and the quantification for spatially resolved EEL spectra. Ga(1-x)InxN = Ga0.84In0.16N (~ 16 at.% of indium).**

**Keywords:**

GaInN, Quantitative STEM, PACBED, EELS

**Reference:**

[1] U. Rossow et. al., Phys. Status Solidi B, 258, (2021)
[2] J. LeBeau et. al., Physical review Letters, 100, (2008)

[3] J. LeBeau et. al., Ultramicroscopy, 110(2), (2010)
[4] This work was supported by the Deutsche Forschungsgemeinschaft under Germany's Excellence Strategy – EXC-2123 QuantumFrontiers – 390837967

332

# Growth of Au-seeded GaAs-GaSb nanowires explored in environmental TEM

Phd Candidate Mikelis Marnauza[1,2], Dr. Robin Sjökvist[1,2], Ms. Azemina Kraina[1,2], Dr. Daniel Jacobsson[1,2,3], Prof. Kimberly Dick-Thelander[1,2]
[1]Centre for Analysis and Synthesis, Lund University, Lund, Sweden, [2]NanoLund, Lund University, Lund, Sweden, [3]National Centre for High Resolution Electron Microscopy, Lund University, Lund, Sweden, [4]Solid State Physics, Lund University, Lund, Sweden

PS-03 (3), Lecture Theater 2, august 30, 2024, 14:00 - 16:00

Background incl. aims
Group III-Sb semiconductor nanowires are an important material system with potential uses in applications such as quantum electronics, optoelectronics, and sensing. This is due to their excellent electrical properties, including high carrier mobility and narrow band gap. However, current device development is slowed down by the difficulty to control the growth of Sb-based nanowires, as compared to the more common III-As materials. To a large extent this is caused by the complex growth conditions of antimonides, as elemental antimony exhibits low vapour pressure and surfactant effect.[1,2] In order to understand the limits and possibilities of the III-Sb nanowire system, a thorough investigation of the growth behaviour is therefore needed. Since atomic scale dynamics and liquid catalyst composition are parameters that are not readily accessible during conventional nanowire growth, in-situ investigations are crucial to develop a comprehensive understanding of the nanowire growth.

Methods
Herein we utilize a Hitachi HF-3300S environmental transmission electron microscope (ETEM) to grow and analyze Au-seeded GaAs and GaSb containing nanowire heterostructures in-situ as demonstrated in Figure 1 (a). This allows us to acquire high frame rate videos of nanowires using a Gatan OneView IS camera in addition to acquiring X-ray energy dispersive spectroscopy (XEDS) compositional data using an Oxford Instruments SDD X-MaxN 80T system. In order to conduct the in-situ growth studies Norcada MEMS chips with ex-situ aerosol deposited Au particles were used.[3] To perform the growth of GaSb nanowires trimethylgallium (TMGa) and trimethlyantimony (TMSb) were used as precursors.

Results
When conducting in-situ XEDS measurements during the growth of Au-seeded GaSb segments we have shown that the Ga concentration in the particle is in the range of 66 – 94 at.%, while the Sb concentration is in the range of 3-4 at.% depending on the used V/III ratio between precursors. The particle composition had a significant impact on the particle volume, which in turn affected the nanowire diameter as shown in Figure 1 (b-c). We observed that steady-state axial growth of GaSb nanowires with diameters in the range of 50-100 nm can be achieved (for the lowest and highest Ga concentration, respectively).[4] Varying the vapor phase composition and particle composition had a further effect on the growth dynamics. We examined the growth process by extracting incubation and step-flow process times from the nanowire growth videos at different V/III ratios. These processes describe the time it takes for a new layer to nucleate and subsequently the time it takes the layer to cover the liquid-solid interface, respectively. Our experimental observations and Monte-Carlo modelling of the growth revealed both processes to be predominantly affected by Sb atom abundance (in vapor and liquid phase). Lastly, we examined GaSb-GaAs heterostructure formation dynamics. Here we were able to show qualitative analysis of the kinking mechanism often found in these and similar high lattice mismatch heterostructures. Furthermore, we were able to demonstrate

that the growth of these highly lattice mismatched heterostructures can be attained via ternary GaAsxSb1-x segments.

Conclusions

In this study we offer a thorough in-situ analysis of the Au-seeded GaSb nanowires. Firstly, we demonstrate how the precursor flows affect the seed particle composition, which in turn affects the seed particle volume subsequently leading to dramatic changes in nanowire morphology. Furthermore, we examine in close detail the layer-by-layer growth dynamics revealing how precursor flows affect the step-flow and incubation processes revealing the growth to be mainly Sb limited. Lastly, we demonstrate how GaSb-GaAs heterostructures can be attained without nanowire kinking which offer insight into high lattice mismatch nanowire heterostructure growth strategies.

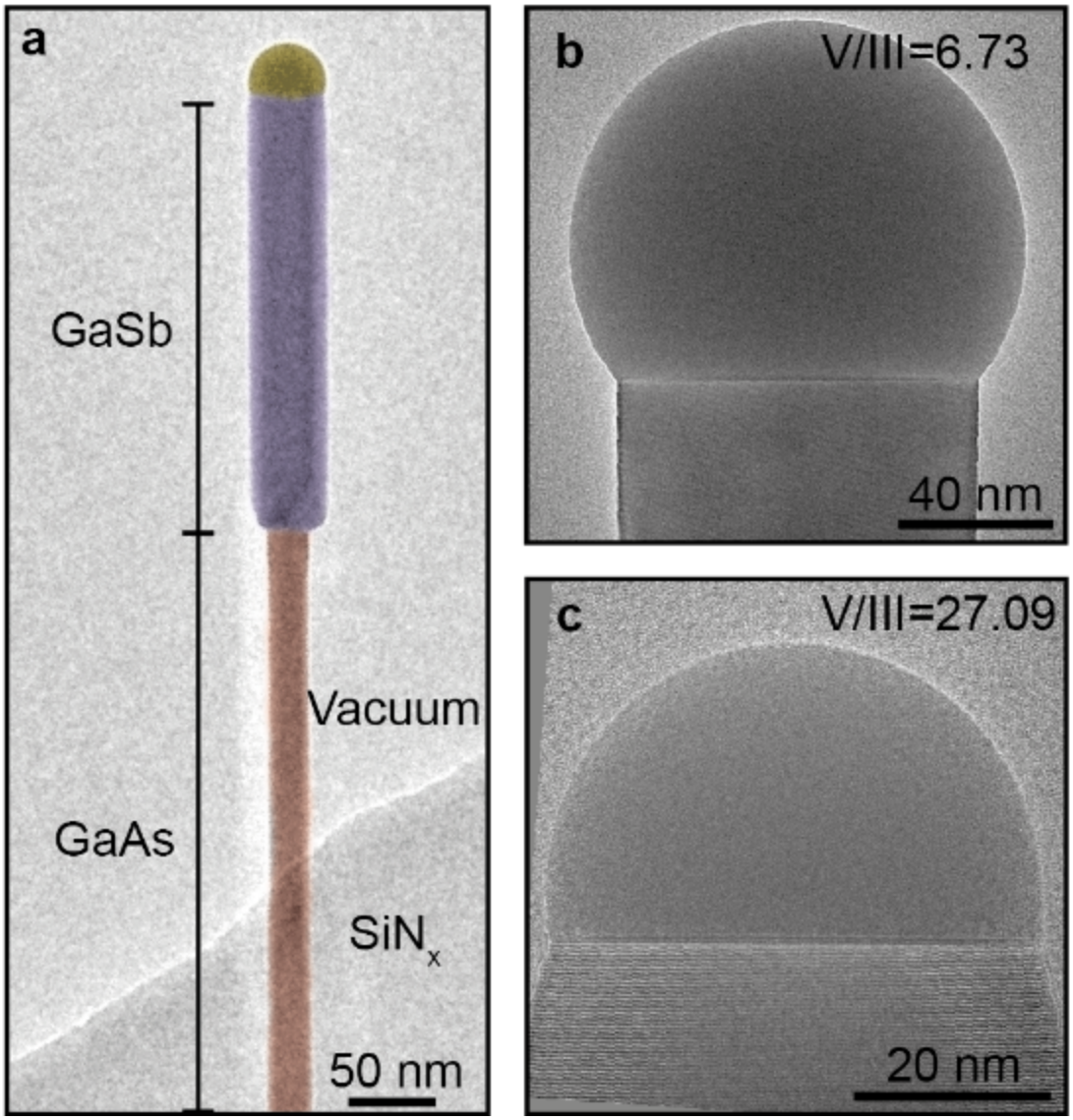


**Keywords:**

In-situ, MOCVD, nanowires, GaSb, VLS

**Reference:**

[1] Mattias Borg, B.; Wernersson, L.-E. E. Synthesis and Properties of Antimonide Nanowires. Nanotechnology 2013, 24 (20), 202001. https://doi.org/10.1088/0957-4484/24/20/202001.

[2] Jeppsson, M.; Dick, K. A.; Wagner, J. B.; Caroff, P.; Deppert, K.; Samuelson, L.; Wernersson, L. E. GaAs/GaSb Nanowire Heterostructures Grown by MOVPE. J. Cryst. Growth 2008, 310 (18), 4115–4121. https://doi.org/10.1016/j.jcrysgro.2008.06.066.

[3] Magnusson, M. H.; Deppert, K.; Malm, J. O.; Bovin, J. O.; Samuelson, L. Size-Selected Gold Nanoparticles by Aerosol Technology. Nanostructured Mater. 1999, 12 (1), 45–48. https://doi.org/10.1016/S0965-9773(99)00063-X.

[4] Marnauza, M.; Sjökvist, R.; Lehmann, S.; Dick, K. A. Diameter Control of GaSb Nanowires Revealed by In Situ Environmental Transmission Electron Microscopy. J. Phys. Chem. Lett. 2023, 7404–7410. https://doi.org/10.1021/acs.jpclett.3c01928.

514

# Understanding phase and chemical transitions in Ge-rich GeSbTe based phase change memory: a (S)TEM tribute

Sijia RAN[1], Minh-Anh LUONG[1], Eloïse RAHIER[1], Elisa PETRONI[2], Daniel BENOIT[3], Alain CLAVERIE[1]
[1]CEMES-CNRS and University of Toulouse, Toulouse, France, [2]STMicroelectronics, Agrate Brianza, Italy, [3]STMicroelectronics, Crolles, France

PS-03 (3), Lecture Theater 2, august 30, 2024, 14:00 - 16:00

Background incl. aims
Phase change memory (PCM) has demonstrated potentials to become the mainstream of the non-volatile memory technique at 28 nm node and below and is promising for applications in future computing hierarchy [1]. The data storage of PCM relies on the reversible phase transition of its active material, which exhibits distinct electrical resistances between crystalline (high conductivity, logic “1”) and amorphous (low conductivity, logic “0”) states.
To meet high-temperature data retention requirements, compositional optimized Ge-rich GeSbTe (GGST) alloys are used by the industry for fabricating PCM for embedded applications [2]. While being the key for the improved thermal stability, GGST alloys undergo chemical phase separation during thermal annealing [3]. The crystallized GGST has been found to be a “composite” material, resulting from the formation of multiple crystalline phases, such as GeTe, Ge, GST-225, and Sb2, at different crystallization stages [4].
In PCM cells, GGST alloys experience different kinds of thermal cycles after deposition. In particular, to allow for the switching between 2 logic states, the GGST layer is locally heated by Joule heating generated by applied current pulses, which provide adequate temperatures either to melt-quench or to crystallize it. Owning to the off-stoichiometry nature of the as-deposited GGST, these heating processes may result in different microstructures and elemental distributions within the cell.
While understanding the evolution of GGST materials is critical for building up the physics behind the functionality of such devices, experimental observations are challenging due to the confinement of the active material to the nanometer scale in integrated PCM. We have thus worked at developing a methodology combining various (scanning) transmission electron microscopy ((S)TEM) techniques to identify grains of different phases that define the cells’ microstructure and the structural and chemical transitions that affect them during electrical programming.

Methods
The studied devices were integrated PCM with a “wall architecture”. The cell consists of a GGST active layer of a few tens of nanometers thick, which is deposited on top of the heater and encapsulated by a metallic top electrode. Extremely thin (<30 nm) TEM lamellas were prepared using focused-ion beam (FIB) from cells after electrical programming. The active region of PCM is a dome which can be amorphous (RESET state, see Fig. a) or crystalline.
TEM samples were characterized by various (S)TEM-based techniques: dark-field (DF) and high-resolution (HR) imaging to access crystallographic information, and high-angle annular dark-field (HAADF) imaging and electron-energy loss spectroscopy (EELS) for chemical mapping. In-situ TEM heating was conducted on cells in RESET state under DF imaging conditions using a furnace-type holder. Results were cross-compared with samples after ex-situ baking.

Results
Fig. b shows a typical (S)TEM analysis of the GGST cell for a region near the heater. The cell was programmed by a forming pulse, which is used to activate the material by melting it followed by slow cooling during which the melt recrystallizes [5]. The STEM HAADF image and associated EELS maps show chemical segregation near the heater: the material is separated into an outer Ge-rich region

surrounding a core made of a Sb-rich (left) and a Te-rich (right) regions. TEM HR images of 2 regions in the core show quite similar crystalline lattices. However, when compared using geometric phase analysis (GPA), the corresponding “strain” map indicates the lattice spacing in the Sb-rich region is ~4% larger than found in the Te-rich region. A clear interface is seen which matches with the boundary evidenced in chemical maps. In the SAED pattern, diffraction spots from 2 sets of slightly different lattices are found and show a good match with rhombohedral Sb (ZA 44$\bar{1}$) and face-center-cubic GST (ZA 111), respectively. By selecting the spot arising from one or the other, DF images of Sb and GST grains can be obtained separately. This demonstrates our ability to identify and distinguish main crystalline phases (Ge, GST, and Sb2) in GGST cells using combined chemical and crystallographic analysis.
Fig. c shows a GGST cell after being programmed by a melt-quench pulse (RESET). An amorphous dome can be evidenced in the BF and DF images. Beyond that, composite “BF & DF” images can be generated by superimposing the BF and several different DF images of either the Ge or the GST phase. A very peculiar characteristic of the polycrystalline region surrounding the dome is evidenced by DF images and the EELS map: Ge crystals preferentially accumulate at the lateral sides of the dome while GST grains are mainly located above it.
The thermal stability of PCM, notably of their RESET state, is a key factor for device reliability. Fig. d shows a GGST cell programmed to the RESET state and subjected to annealing in-situ in the TEM. DF imaging shows a GST crystal located above the amorphous dome. When heating to temperatures at which RESET resistance decreases (250 to 300 ˚C), DF images show that this grain progressively regrows by epitaxy into the amorphous region until it occupies almost the entire dome. EELS maps of the RESET state and after partial-crystallization (by ex-situ annealing) show that while the amorphous dome is initially chemically homogeneous, phase separation is observed after recrystallization (Fig. c and d): Sb segregates inside the crystallized region while the remaining amorphous material becomes more enriched in Ge.

## Conclusion

In this work, we have set up a (S)TEM-based methodology to study complicated phase and chemical transitions that occur when programming GGST-based PCM cells. By combining chemical and crystallographic analyses, grain distributions of crystalline phases formed during programming can be revealed. A specific polycrystalline environment, involving two Ge “walls” and a “roof” of GST grains, has been identified. Using in-situ and ex-situ TEM, the thermal recrystallization behavior of the amorphous dome has been revealed: the growth of GST crystals from top of the dome is the mechanism dominating the crystallization. Further chemical analysis has evidenced the phase separation inside the dome, which limits the crystallization process.
Such complete (S)TEM-based analysis provides important experimental results for setting up physical models describing electrical conduction in PCM cells and to guide the process optimization.

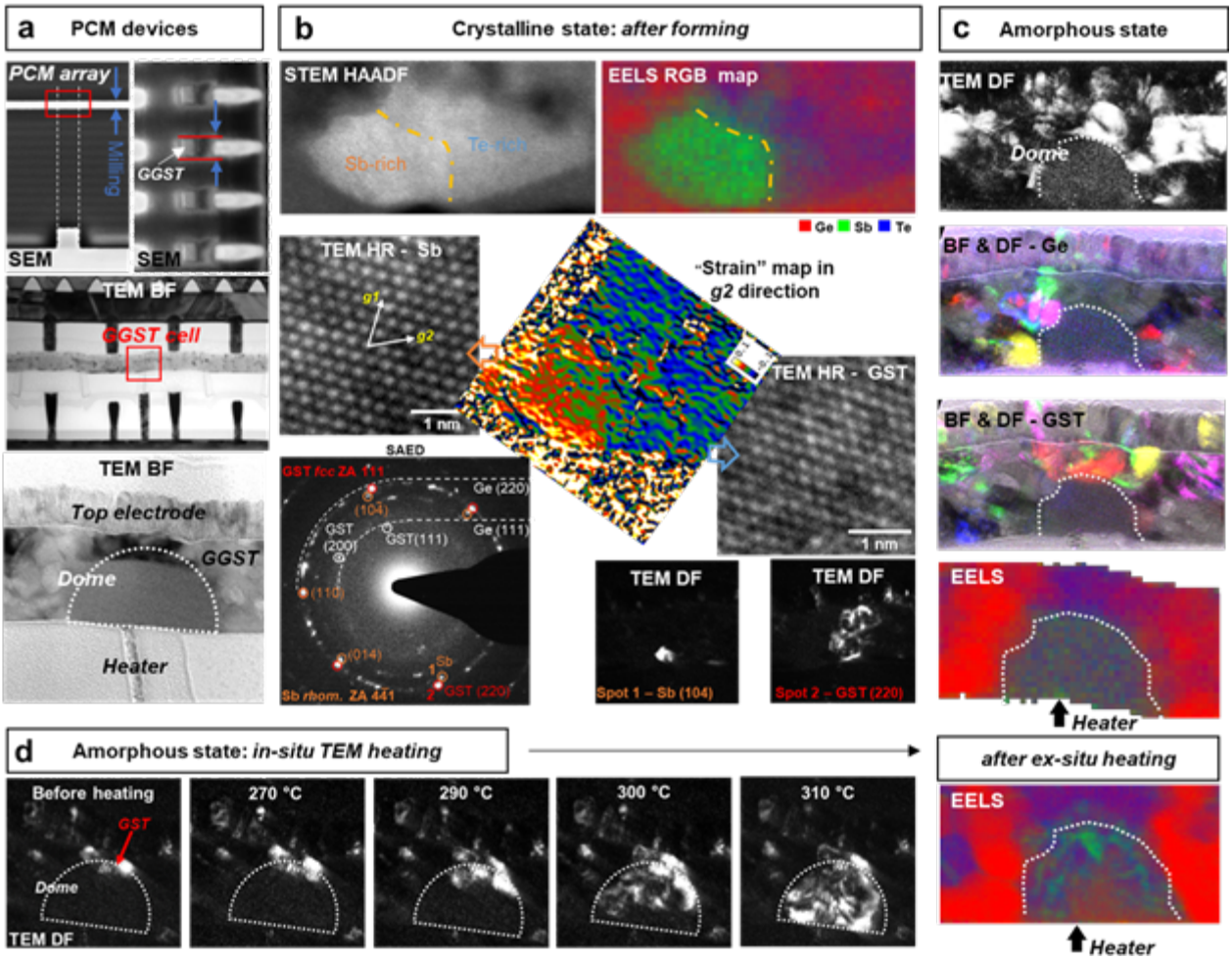


**Keywords:**

phase-change-memory, chalcogenide, in-situ TEM, crystallization

**Reference:**

[1] P. Cappelletti, et al. J. Phys. D: Appl. Phys. 53 (2020) 193002.
[2] F. Arnaud, et al. 2020 IEDM (2020) 24.2.1-24.2.4.
[3] E. Rahier, et al. ACS Appl. Electron. Mater. 4 (2022) 2682-2688.
[4] E. Rahier, et al. Phys. Status Solidi – Rapid Res. Lett. (2023) 2200450.
[5] S. Ran and E. Petroni, et al. ‘‘Phase transitions and chemical segregation in Ge-rich GeSbTe based phase-change memory cells (tentative)’’, in preparation.

530

# Momentum resolved band gap measurement by high energy resolution electron energy loss spectroscopy

Dr Dileep Krishnan[1], Dr. Ioannis Iatrakkis
[1]Thermofisher Scientific, Eindhoven, Netherlands

PS-03 (3), Lecture Theater 2, august 30, 2024, 14:00 - 16:00

Techniques based on light optics have been traditionally used for studying optical properties of semiconductors. But there are 2 fundamental limitations of photon sources – 1. Its spatial resolutions are limited to µm range and 2. Photons cannot transfer any momentum (q) to the material. Electron energy loss spectroscopy (EELS) has been used to measure optical band gap for a few decades which compensates the aforementioned two shortcomings of UV-visible spectroscopy with nanometer range resolution and momentum transfer. But the limitation of EELS has been the energy resolution of the electron source; an X-FEG without mono was only 1 eV of resolution. With improvements of monochromator design on Thermo Fisher Scientific Spectra platform microscopes, energy resolution < 20 meV is now possible. Also, the 3-condensor lens system allows for a large range of momentum resolution possible with an upper limit <200 µrad in STEM mode.

In this report, momentum resolved band gap measurement has been performed with an excited monochromator (energy resolution < 25 meV) with a momentum resolution of < 800 µrad using the Thermofisher Scientific EELS filter and spectrometer. Effort is put to automate the acquisition of EELS across the momentum space. In the literature, the modelling of EELS in the low-loss region has been commonly done by simplistic free electron gas model [1 ].We are developing an effective tight binding model approach to approximate the band gap and extract the low loss spectral function. The final state in the double differential scattering cross section formula has been described suing mixed dynamic form factor (MDFF) [2].

Figure caption: Figure 1. (a) The CBED pattern and the positions where the low-loss EELS measurements have been made. (b) The corresponding EELS spectra.

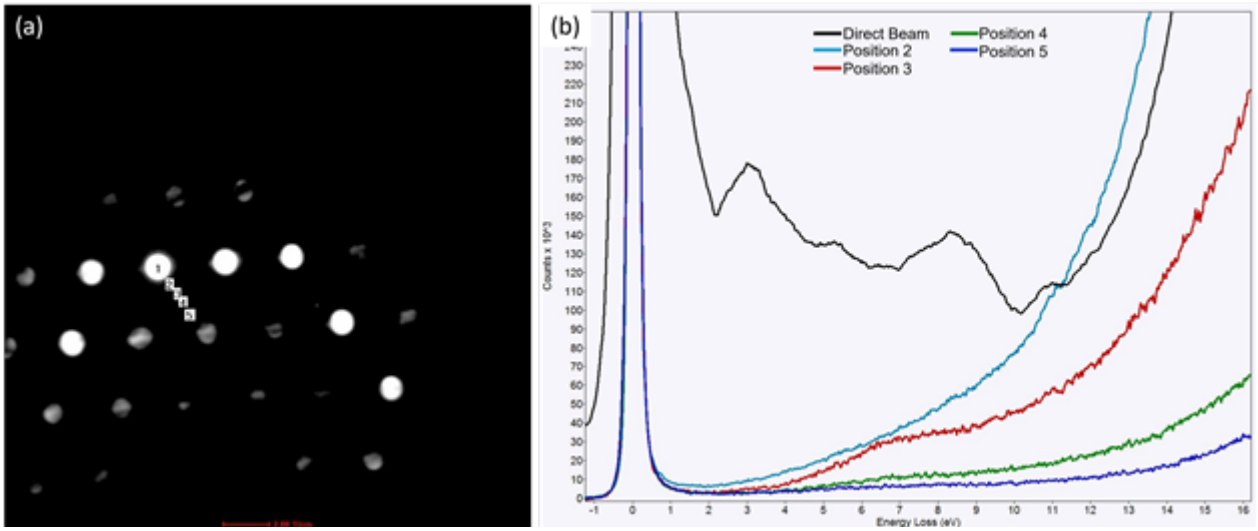


**Keywords:**

Extreme low-loss, band gap, q-resolved-EELS

**Reference:**

[1] Korneychuk, S., Guzzinati, G. & Verbeeck, J., Phys. Status Solidi A 215, 1800318 (2018).
[2] Schattschneider, P., Nelhiebel, M., Souchay, H., Jouffrey, B., Micron 31, 333 (2000)

640

# Probing photonic resonant modes in InAs semiconductor nanostructures by STEM-EELS

Yajie Wang[1], Qingnan Cai[1], Zifan Huo[2], Yanhui Zhang[2], Pingping Chen[2], Kun Ding[1], Changlin Zheng[1]
[1]State Key Laboratory of Surface Physics and Department of Physics, Fudan University, Shanghai, China, [2]State Key Laboratory of Infrared Physics, Shanghai Institute of Technology Physics，Chinese Academy of Sciences, Shanghai, China

PS-03 (3), Lecture Theater 2, august 30, 2024, 14:00 - 16:00

Background incl. aims
Dielectric and semiconductor nanostructures are garnering increased interest due to their low radiative loss properties. This makes them a promising alternative to metal plasmonic structures for manipulating light fields at the nanoscale. The flexibility to manipulate optical resonance can be further enhanced by electrically doping and gating the mobile carrier density in semiconductors. In this study, we present the experimental observation of distinct optical resonances in one-dimensional InAs nanostructures, achieved through high-energy electron excitation.
Methods
The nanowires were grown with molecular beam epitaxy (MBE) system. Their length and width were fined tuned by modifying the growth conditions. The STEM-EELS investigation was conducted using a double-aberration corrected microscope (Thermo Fisher Scientific Themis Z) fitted with a high-resolution monochromator and a Gatan 1066 continuum spectrometer. The energy resolution is approximately 200 meV.
Results
Figure 1 presents the two-dimensional EELS mapping of an individual InAs nanowire across various energy windows. It's evident that as the energy loss increases from 0.94 eV to 1.17 eV and further to 1.43 eV, the EELS intensity distributions display different nodal patterns. These patterns correspond to resonant modes from m = 2 to 4 and can be recognized as standing wave Fabry–Perot type resonances. Figure 1(b) shows the intensity line profiles along the direction of the nanowire's growth, taken from the central area. To fully understand the experimetnal observation, we applied the quasi-normal mode theory and boundary element methods to simulate the resonate excitations in siminar geometric structures. The simulated results succssfully interprate the subtle changes in the EELS reponse across different energy windows within a given geometric confinment.
Conclusion
Our STEM EELS investigation and simulation show that InAs nanostructures are a promising candidate for local light field manipulation covering the near infrared-visible-ultraviolet (NIR-vis-UV) spectral range.

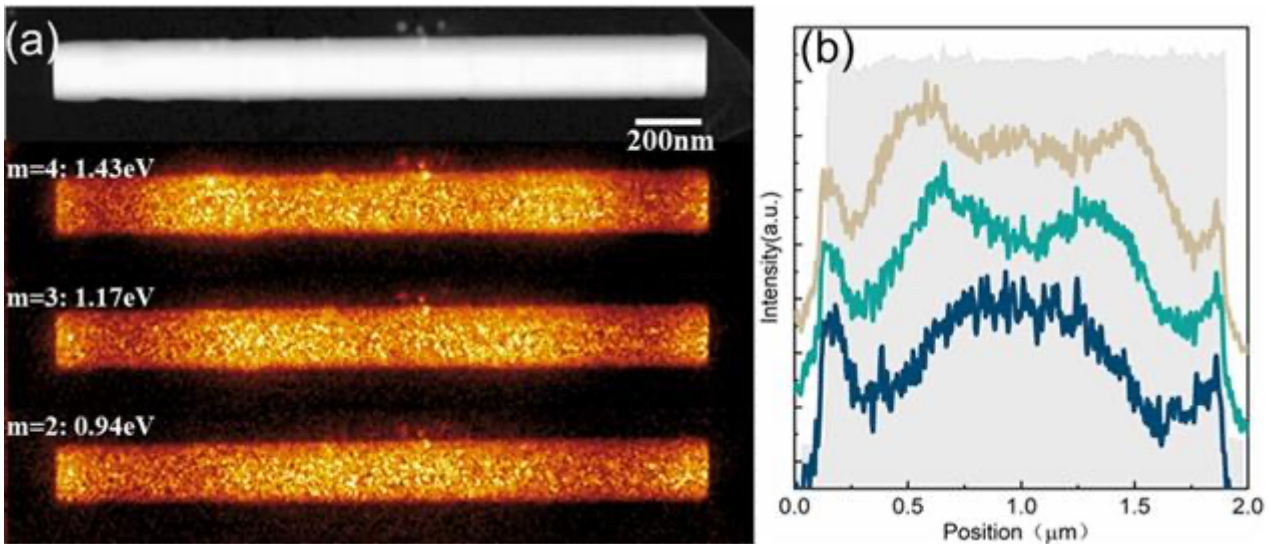


**Keywords:**

Optical resonance, InAs nanowire, STEM-EELS

**Reference:**

Duncan T. L. Alexander, Valentin Flauraud, and Frank Demming-Janssen, Near-Field Mapping of Photonic Eigenmodes in Patterned Silicon Nanocavities by Electron Energy-Loss Spectroscopy, ACS Nano 15 (10) (2021) 16501-16514. DOI: 10.1021/acsnano.1c06065.

656

# Structural and optoelectronic properties of layered halide perovskites

Dr Giorgio Divitini[1], Dr Andrea Griesi[1], Mr Andrea Cicconardi[1], Dr Sirous Khabbazabkenar[1], Dr Yurii Ivanov[1], Dr Gunnar Kusch[2], Prof Rachel A Oliver[2]
[1]Istituto Italiano di Tecnologia, Genoa, Italy, [2]Department of Materials Science, University of Cambridge, Cambridge, UK

PS-03 (3), Lecture Theater 2, august 30, 2024, 14:00 - 16:00

Background incl. aims
Halide perovskites have recently risen into the spotlight due to their exceptional optoelectronic properties and compositional flexibility, enabling a wide range of choices for each component in the archetypical ABX3 formulation (A: cation, B: typically Pb or Sn, X: halide anion). The basic structural unit is the [BX6]4- octahedron, sharing corners in a 3D lattice. A new class of perovskites, featuring layers of corner-sharing octahedra alternating with layers of organic spacers, has been demonstrated to have enhanced fluorescent emission compared to their 3D counterparts. Understanding local composition, crystallography and optoelectronic properties is fundamental to develop an understanding of these materials and their engineering.
In this work we showcase the combination of various electron microscopy techniques (EDX, cathodoluminescence, 4DSTEM, monochromated EELS) to unravel the interplay between local compositional, structural and optoelectronic properties in layered halide perovskites. We also study systems where the halide component is replaced, obtaining a lateral heterostructure.
Methods
Materials (PEA2PbBr4, PEA2PbI4, PEA2MA2Pb3I10) were synthesised using a wet chemistry route described in [1]. The resulting materials were dispersed on silicon for CL measurements and lacey carbon or silicon nitride grids (20 nm thick) for STEM measurements. SEM-EDX was carried out in a ZEISS GeminiSEM 560 using an Oxford Instruments detector. SEM-CL was done in an Attolight Allalin 4027 Chronos SEM-CL. Spectra were acquired with an iHR320 spectrometer (focal length of 320 mm, 150 gratings per mm blazed at 500 nm, 700 µm entrance slit) and an Andor 1024-pixel charge-coupled device (acquisition time 100 ms/pixel). All the measurements were performed at room temperature under high vacuum (<10 – 7 mbar) with acceleration voltage of 10 kV and a pulsed beam with a frequency of 80 MHz, a pulse duration of ~7ps, at a current of ~100 pA as measured by a Faraday cup. STEM measurements were done in a ThermoFisher Spectra300 with probe and image correctors, a monochromated source and a dual-X EDX detector (1.7 sr total solid angle).
Results
We considered layered perovskites with different thicknesses and composition. Thick flakes were used for CL measurements. In PEA2PbBr4 and PEA2PbI4, a multivariate analysis decomposition highlights the presence of an emission originating from the bulk of the material and a blue-shifted emission visible along the edges in the CL hyperspectral maps. The analysis was extended to lateral PEA2PbBr4 - PEA2PbI4 heterostructures (for which the elemental distribution is shown in the figure), identifying emission from both the phase in the bulk (original phase of the flake) and the one along the edge (dominated by the replaced halide). The emissions were correlated with local compositional changes.
Furthermore, we have carried out a 4DSTEM analysis to verify local crystallinity in thin PEA2MA2Pb3I10 flakes at low electron doses. The flakes were good single crystals, with loss of crystallinity observed at the edges. The monochromated EELS signal was integrated over large areas to minimise dose and used to calculate optoelectronic properties, finding good agreement of the calculated bandgap with optical measurements.
Conclusion

We were able to obtain spatially resolved CL measurements on layered halide perovskites, identifying emission heterogeneities. We also characterised local crystallinity and demonstrated the ability of measuring the local bandgap in individual flakes using EELS. These approaches will enable tailoring of the material engineering, leading to better light emitting and management devices.

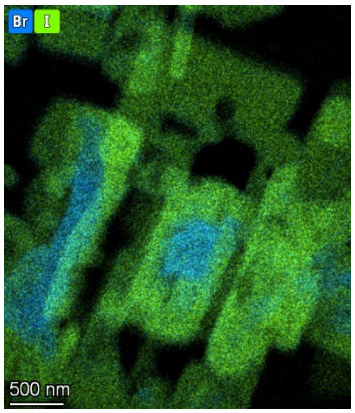


**Keywords:**

Cathodoluminescence EELS halides perovskites

**Reference:**

[1] Andrea Griesi et al 2024 Nanotechnology 35 105204, DOI 10.1088/1361-6528/ad12ec

705

# In-Situ Charging and Charging Map for Characterization of Electronic Materials

Dr. Wen-Shan Zhang[1], Dr. Nikolai Hippchen[1], Prof. Dr. Rasmus R. Schröder[2], Prof. Dr. Uwe H. F. Bunz[1]
[1]Institute of Organic Chemistry, Ruprecht-Karls-University Heidelberg, Im Neuenheimer Feld 270, Heidelberg, Germany, [2]Bioquant, Ruprecht-Karls-University Heidelberg, Im Neuenheimer Feld 267, Heidelberg, Germany

PS-03 (3), Lecture Theater 2, august 30, 2024, 14:00 - 16:00

Background incl. aims
Electronic materials have garnered significant interest due to their potential applications in a wide array of important electronic devices, including transistors, sensors, solar cells, and more. Achieving high-performance devices and developing new electronic materials for future technologies relies fundamentally on understanding electronic processes through advanced characterization techniques. Currently, the characterization of the active layer in a device can offer either global functional information, such as with the most current-potential methods, which only demonstrate the impact of defects on performance without detailing the quantity and distribution of defects, or provide localized details, as seen with techniques like atomic force microscopy and conventional scanning electron microscopy (SEM), which may not capture the entirety of the case. Therefore, we present a novel characterization method capable of acquiring both kinds of information from the active layer, which would be highly beneficial for comprehending the structure-morphology-performance relationship.

Methods
The use of Ultra-low voltage (ULV) SEM has become increasingly crucial for investigating beam-sensitive materials, particularly organic molecules and polymers, due to its ability to significantly suppress beam damage. Additionally, the charging behavior under ULV conditions becomes more material-characteristic compared to conventionally used beam energies (e.g., < 500 eV). Fine-tuning the beam energy within the range of 10-200 eV can result in either negative or positive surface charging [ref.1], depending on factors such as beam energy, beam current, charging density, and the conductivity of the materials. This capability allows us to simulate the working state of a p- or n-type transistor by in-situ generating the required charge type. Moreover, the surface potential resulting from charge flow anomalies enables us to visualize morphological defects along the pathways. Through post-imaging processing, we can calculate the real working pathway for charge-carrier transport, subsequently correcting the charge-carrier mobility [ref. 2].
Furthermore, under ULV conditions, we can collect the energy distribution spectrum of emitted electrons, which can be transformed into a surface charging map. The gradient of the charging attenuation provides structural information within (poly)crystalline domains [ref. 3].

Results
Utilizing the first method mentioned above, we successfully corrected 11 organic thin-film transistor devices, resulting in highly reliable mobility values that accurately reflect the material's charge transport capability. With the latter method, we can estimate the charge-carrier mobility from polycrystalline thin films, which align well with the calculated values. Of particular interest is our ability to distinguish between various crystalline domains with different molecular orientations. Furthermore, we can determine molecular orientation by observing the gradient of the charging attenuation, a technique which, to the best of our knowledge, represents the first application of SEM for this purpose.

Conclusion

By employing in-situ charging and charging maps via ULV-SEM, we can gather information regarding various morphological phenomena. This enables us to directly correlate device performance with the chemical structure of the active material and its morphology, thereby facilitating the design of novel structures and the optimization of the active layer in electronic devices.

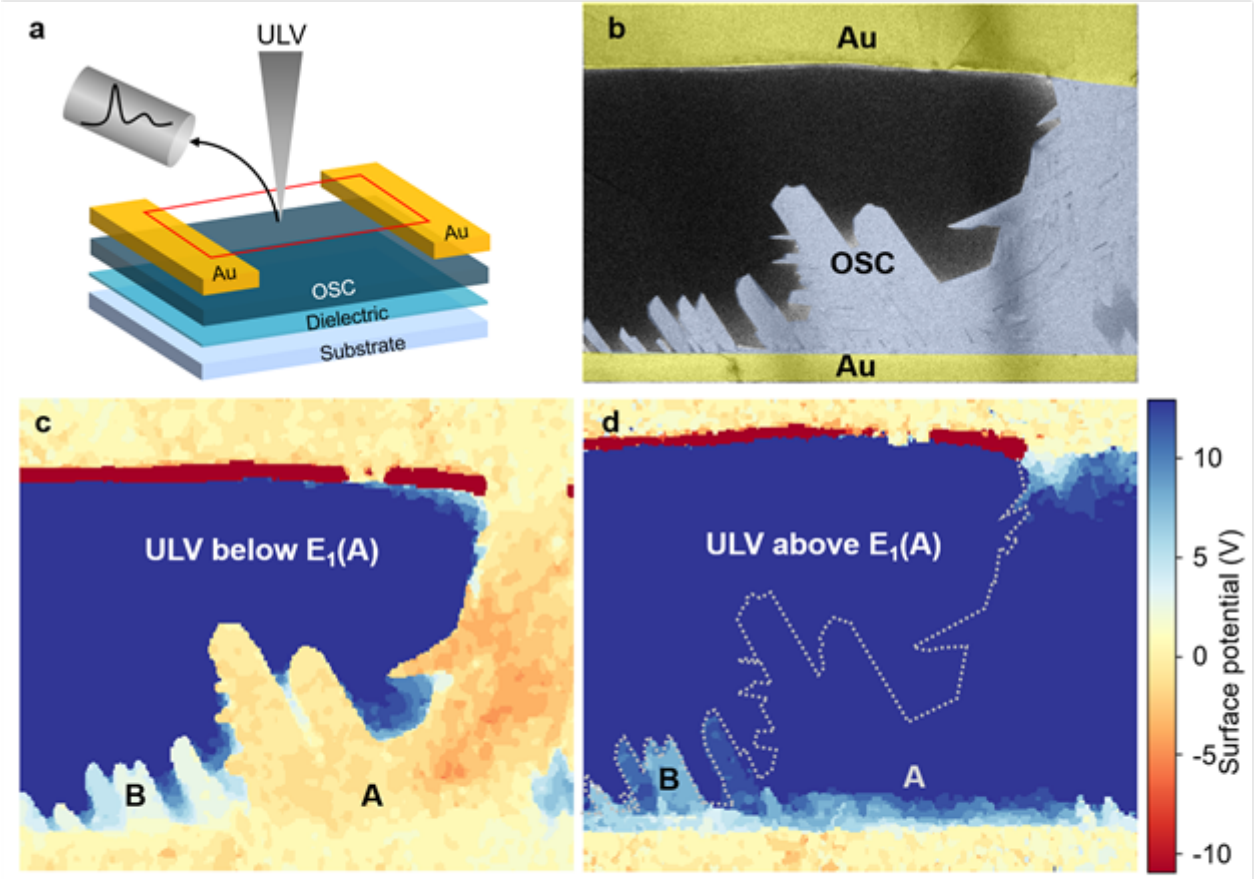


**Figure 1.** Electron Spectroscopic Characterization of an Organic Thin-Film Transistor Using Ultra-Low Voltage (ULV) Scanning Electron Microscopy (SEM).(a) Working principle (OSC stands for organic semiconductor).(b) False-colored SEM image of a channel section of a transistor.(c) and (d) In-situ charging maps of the channel section as shown in (b). A and B represent two different molecular orientations in the crystalline OSC thin-film.

**Keywords:**

charging map, molecular orientation, mobility

**Reference:**

[1] L. Reimer, Image Formation in Low-Voltage Scanning Electron Microscopy, TT 12, SPIE, Washington 1993.
[2] W.-S. Zhang, M. Matthiesen, B. Günther, J. Wensorra, D. Fischer, L. H. Gade, J. Zaumseil, R. R. Schröder, Adv. Electron. Mater. 2021, 7, 2100400.
[3] Manuscript in preparation.

738

# Band gap measurements of aluminum and indium doped Ga2O3 multilayers

Dr. Annett Thøgersen[1], Professor Lasse Vines[2], Dr. Georg Muntingh[1], Professor Øystein Prytz[2], Professor Holger von Wenckstern[3], Dr. Ingvild Julie Thue Jensen[1]
[1]SINTEF, Oslo, Norway, [2]UiO, Oslo, Norway, [3]University of Leipzig, Leipzig, Germany

PS-03 (3), Lecture Theater 2, august 30, 2024, 14:00 - 16:00

Background incl. aims
Power electronics (PE) are integral to the acquisition, distribution, and storage of energy, serving as a pivotal facilitator for enhancing energy efficiency, leveraging renewable resources, and advancing smart grid technologies. While silicon-based PE components have reached a peak in optimization, further enhancements are constrained by intrinsic material properties. This limitation underscores the appeal of wide bandgap semiconductors in PE applications, offering the potential for superior speed, compactness, and energy efficiency compared to their silicon counterparts [1]. One promising avenue lies in the development of High-Electron-Mobility Transistors (HEMTs) based on novel (MxGa1-x)2O3 thin film heterostructures (where M represents Al or In), which exhibit the promise of heightened operational speeds, reduced footprint, and increased power capabilities owing to their ultra-high breakdown field [2]. Ga2O3, capable of existing in various polymorphs such as α, β, γ, δ, and ε phases, boasts a bandgap ranging from 4.5 to 4.9 eV depending on crystallographic orientation [3]. κ-Ga2O3, notably, demonstrates a substantial polarization effect (23 µC/cm2), indicative of its potential to harbor an interface-localized two-dimensional electron gas (2DEG), making it a viable candidate for HEMTs [4, 5]. Through controlled alloying with group III metals, (MxGa1-x)2O3 presents a tunable framework for adjusting critical properties like bandgap and carrier concentrations, thereby tailoring its suitability for specific applications. The band gap range obtained by using Al and In is spanned out by In2O3 (Eg= 2.9 eV) [6] and Al2O3 (Eg= 8.8 eV) [3], and the values can be calculated by eq1: Eg = 4.91 + 2.10x for κ-(AlxGa1-x)2O3 and eq2: Eg = 4.90 – 1.95y for κ-(InyGa1-y)2O3.

Methods
In this work we have investigated (MxGa1-x)2O3 thin film heterostructures (M = Al, In) with various doping concentrations, thickness of layers, and substrate deposition, made using pulsed laser deposition (PLD) and vertical (quasi-) continuous composition spread (VCCS) PLD. The morphology, crystal structure, element composition and band gaps have been measured by transmission electron microscopy (TEM) for three types of samples. For the analysis, we have used a FEI Titan G2 operated at 60 kV with a monochromator, DCOR Cs probe corrector, Super-X EDS detector, and Gatan GIF Quantum 965 electron energy loss (EELS) Spectrometer. The analysis of the EELS spectrum images (SI) and individual spectra (such as the band gap fitting) are performed by our own python-based EELS fitting program combined with Gatan Digital Micrograph and Hyperspy.

Results
Scanning TEM (STEM) image of one type of sample is shown in Figure 1A. Where the top layer is (Al0.3Ga0.7)2O3, second layer is (In1.8Ga0.82)2O3, and the third layer Ga2O3, where the substrate is indium tin oxide (ITO). The band gap has been fitted for each spectrum in the spectrum image (SI) in Figure 1B. The average band gap for each row with the variations (in gray) is plotted in Figure 1C. The band gaps have been fitted to be 5.1 eV, 4.3 eV, and 4.8 eV, for (Al0.3Ga0.7)2O3, (In1.8Ga0.82)2O3, and Ga2O3 respectively. The band gap value for (Al0.3Ga0.7)2O3 and (In1.8Ga0.82)2O3is lower than what can be estimated theoretically, which is 5.54 eV and 4.45 eV respectively. We also observe a decreasing band gap across the interfaces. Is this due to a decrease in band gap or because of the delocalization of the electron beam? The data has then been analyzed in detail and compared to the

structural properties across the interface and compared with two other samples of (MxGa1-x)2O3 deposited on ZnO substrates with different compositions and thinner layer thicknesses.

Conclusion

The results have shown that the reduced band gap values are most likely due to strain in the layers and was not found in layers with high amounts of defects. The decrease in band gap across the interface is a real decrease in value, probably due to lattice mismatch-strain.

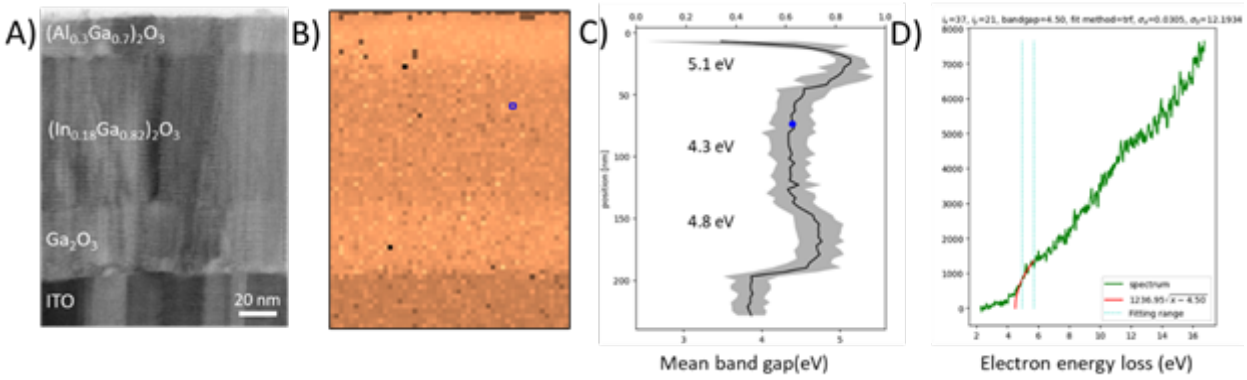


**Keywords:**

Band gap, Ga2O3, TEM

**Reference:**

[1]: Iacopi et al. MRS Bulletin 40 (2015) 390
[2]: Pearton et al. J. Appl. Phys. 124 (2018) 220901
[3]: von Wenckstern, Adv. Electron. Mater. 3 (2017) 1600350
[4]: Maccioni and Fiorentini, Appl. Phys. Express 9 (2016) 041102
[5]: Dingle, IEEE Trans. Electron devices 31 (1984) 1662
[6]: Walsh et al. Phys. Rev. Lett. 100 (2008) 167402

82

# Optimizing FIB-based sample preparation for quantitative in-situ biasing studies of semiconductors using 4D-STEM

Vitalii Lider[1], Franziska Hüppe[1], Saleh Firoozabadi[1], Shamail Ahmed[1], Jürgen Belz[1], Andreas Beyer[1], Kerstin Volz[1]
[1]Materials Science Centre and Department of Physics, Philipps University Marburg, Marburg, Germany

Poster Group 2

Background incl. aims
Recent advancements in four-dimensional scanning transmission electron microscopy (4D-STEM) technology have facilitated the precise quantification of electric fields and potential differences at the nanometer scale.[1] To comprehend the operational dynamics of semiconductor devices under applied voltage, operando TEM represents a logical progression. However, measurements require the sample to be properly mounted and brought into contact with the electrical chip. Since the necessary microcontacts are created by focused ion beam (FIB), a systematic study must be carried out on how the sample must be prepared, protected, contacted and thinned consequently. This creates guidelines for quantitative measurements of the amount and path of currents that must flow through the circuit. Once properly quantified, the procedure will help carry out in-situ biasing studies of semiconductor materials and simultaneously measure the built-in potential. Furthermore, this will also help do in situ breakdown study of semiconductors quantitatively.

Methods
In this study, we used a pn junction with doping concentrations and corresponding built-in potential known from electrochemical capacitance-voltage (ECV) measurements. For the characterization within the TEM, the Protochips Fusion holder was used. As a comparison criterion, we chose the IV characteristic curve for different lamella geometries, bulk material and theoretical calculations. Sample preparation leverages the combined advantages of two FIB microscopes: The Helios 5 Hydra CX PFIB and the Jeol JIB-4601F. The former has xenon plasma source which enables faster chuncking. Thanks to the advanced manipulator needle control and appropriate geometry, this microscope provides the solution for lifting out the TEM lamella and attaching it to the biasing chip without complicated intermediate steps. However, it is known that thinning of the lamella with Xe-Beam can cause curtaining.[2] In our case this would be undesirable as it could result in electrical short circuit channels. We can avoid this problem by using the second FIB microscope mentioned above with a gallium-ion source. For the electrical contacts and the protective layer tungsten is used.

Results
The electrical experiments require the smallest possible resistance between the sample and the metal contacts. It is already known from the literature that ion beam induced deposition (IBID) leads to a significantly lower resistance compared to electron beam induced deposition (EBID).[3] Accordingly, the contacts here were made using FIB.
In the following we compare different geometries of the lamellas. Graphic A shows the 'H' shape lamella. This geometry would have the advantage that the same potential can be applied to the entire p-side. However, the distance between the positive and negative contacts is very short, which leads to a short circuit due to undesirable contamination of the chip surface. This can also be clearly seen in the IV characteristic curve. In graphic B the 'S' shape lamella is shown. This form has the advantage that the positive and negative contacts are at a significantly greater distance from each other. Contamination of the chip surface can also be neglected with this geometry, as the potential drops from the right to the left side across a cut in the chip. This geometry leads to a significant

improvement in the behaviour of the IV characteristic, as can be seen in the plot. Graphic C shows the same lamella as B with additional cuts to prevent current flow to the tungsten layer on top. Although the 'S' shape geometry has an improved IV characteristic, it is more similar to a Schottky diode than a pn diode. However, this is not surprising, because the contacts are on the same size scale as the lamella. This must be considered in the theoretical calculations in order to be able to quantify what proportion of the externally applied voltage drops at the pn junction.

Conclusion

This study highlights the importance of careful sample preparation techniques for in-situ biasing studies of semiconductor materials using 4D-STEM. By optimizing the FIB-based preparation and lamella geometries, we have achieved improved IV characteristic behaviour and a lower amount of short circuits. However, the metal-semiconductor contacts must be carefully considered in the descriptive models. These results will provide practical insights for improving measurement accuracy and reproducibility in operando TEM studies of semiconductor devices and may contribute to advances in electronic device development.

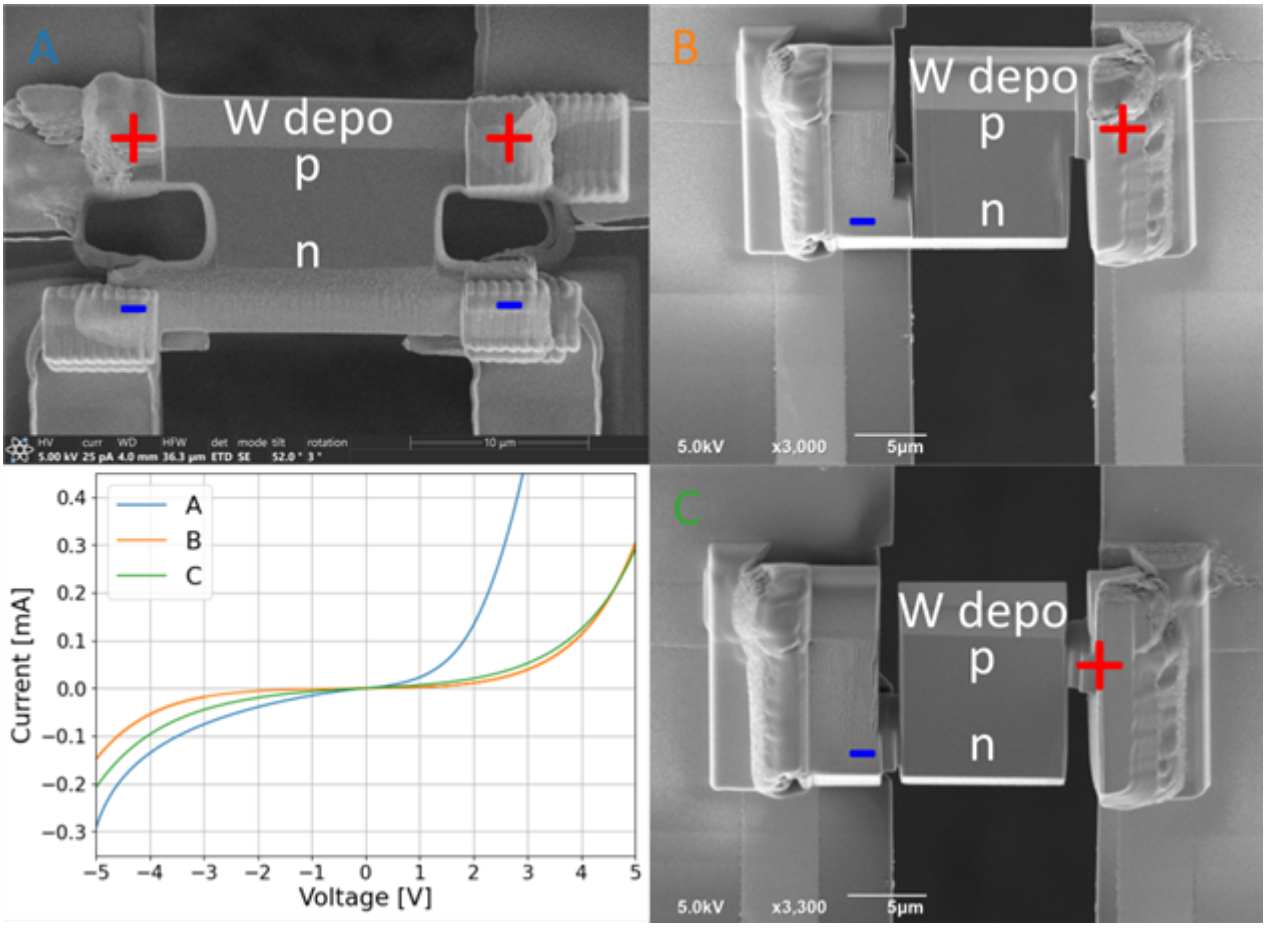


**Keywords:**

electric_fields, pn_junction, in-situ_biasing, 4D-STEM, sample_preparation

**Reference:**

[1] A. Beyer, et al., Nano Letters 21 (2021) 2018.
[2] S. M. Vitale and J. D. Sugar, Microscopy and Microanalysis 28 (2022) 1.
[3] M. Hammad Fawey, et al., Microscopy Research and Technique 79 (2016) 615.

109

# Enhancing quantifiability of S/TEM-based composition mappings through correlative techniques

Kai-luis Jakob[1], Mr. Frederik Otto[1], Dr. Dirk Berger[2], Dr. Tore Niermann[1], Prof. Dr. Michael Lehmann[1]
[1]Technische Universität Berlin, Institute of Optics and Atomic Physics, Berlin, Germany, [2]Technische Universität Berlin, Zentraleinrichtung Elektronenmikroskopie (ZELMI), Berlin, Germany

Poster Group 2

Background incl. aims
In the realm of semiconductor physics and material engineering, the precise quantification of alloy concentrations is imperative as slight variations in the concentration can have far-reaching implications for the optical and electrical properties of semiconductor devices, e.g. InGaAsN near-infrared lasers [1]. As humanity continuously advances the frontiers of nanotechnology and device sizes shrink to just a few atomic layers, material's analysis must keep up and provide sufficient precision in the determination of alloy concentrations as well as the necessary spatial resolution to resolve these tiny devices. While S/TEM based approaches provide this necessary spatial resolution, each method used to determine elemental concentrations in STEM presents its own challenges, especially when it comes to quantifiability. To reliably determine concentrations, STEM-EDX for example, relies on proper reference samples and detailed knowledge of the systems x-ray signature [2]. Diffraction based techniques, such as dark-field imaging of a chemically sensitive beam, exhibits strong dependencies on the specimen's thickness and bending, as these influence dynamic diffraction conditions [3].
The study aims to improve the accuracy of compositions mappings by leveraging the individual challenges and advantages of EDX and diffraction-based techniques against each other.

Methods
We prepare a TEM-lamella, incorporating InGaAs layers (with known In concentration) near the [100] foil normal, employing classical cross-section preparation. This specific zone axis, characterized by 4 {002} reflections, exhibits chemical sensitivity as the structure factors of these {002} reflections hinge on the difference in atomic scattering factors within the unit cell of constituent materials. To exploit this chemical sensitivity optimally, we strategically tilt the specimen, predominantly exciting one of these reflections. This minimizes dynamic diffraction effects while concurrently enhancing the relative intensity of the respective reflection.
Employing an ultrafast pixelated detector, we systematically scan the tilted specimen, capturing 2D diffraction patterns. In a complementary set of measurements, STEM-EDX signals from the layer are acquired for a comparative analysis. STEM-EDX measurements and 4D-STEM mappings are conducted on a JEOL ARM300F2 at 300kV with a 2.2 sr EDX-system. The integration of these measurements is achieved through 2D cross-correlation of the simultaneously acquired signals on the HAADF detector. Subsequently, virtual dark-field image of the (002) reflection is computed, facilitating a direct correlation with the structure factor and, consequently, revealing the corresponding Indium concentration within the layer. Results are compared to Bloch waves simulations to account for dynamic diffraction effects for the respective lamella thickness. Further investigations of the Indium segregation are conducted in high-resolution conditions analyzing the geometric phase.

Results
From a dark-field image of the (002) reflection, a segregation profile for the Indium concentration within a 5 nm layer of InGaAs, nominally possessing a 20% indium concentration, can be extracted. It's noteworthy that, for the specified indium concentration and under strong-beam conditions, no

significant disparity in indium levels, attributable to dynamic diffraction, is noticeable when comparing the (020) and (002) reflections. In Fig. 1 a segregation profile of the Indium concentration with a Muraki-Fit [4] is shown. Furthermore, for small Indium concentrations, the dependency of the concentration determined by this dark-field imaging on the specimen thickness seems to be negligible. This assertion finds support in Blochwave simulations, analyzing dynamic diffraction. For larger Indium concentrations, strain effects play an increasingly important role in the analysis of concentrations through dark-field imaging. Here, we explore the possibilities of determining concentration profiles from strain analysis, taking into consideration strain relaxation at the lamella surfaces. The obtained results are compared to STEM-EDX mappings of the same quantum well layer. Our comprehensive discussion covvers the results and their implications for the interplay with specimen thickness, Indium segregation, and how these factors collectively impact spatial resolution and quantifiability in STEM-EDX. In further investigations, we replicate the study using a set of TEM specimens prepared through a FIB TEM-lamella preparation. This replication aims to scrutinize the influence of FIB Ga-ions on the composition determination in Ga-based heterostructures, the changes to the In-distribution and amorphized layers.

Conclusion

Among the multitude of interaction possibilities of the high-energy electron beam, traditional approaches often focus on a single interaction, such as analyzing the corresponding x-ray signature of the specimen. However, scanning transmission electron microscopy techniques provide a broader perspective, as the transmitted electrons carry additional information for each scan position. This interplay becomes particularly valuable dealing with diverse measurement conditions, including specimen thickness and orientation, providing an opportunity to enhance the quantifiability of composition mappings. Importantly, this methodology transcends the limitations of individual techniques, leveraging the improved signal-to-noise ratio for thicker specimen in EDX over diffraction-based techniques, which are more effective with thin specimens. The resulting versatility not only enables precise composition determinations across a wider range of specimen parameters but also reveals additional synergies. For instance, it aids in resolving the indium concentration degeneracy in a pure analysis of the local form factor for InGaAs quantum devices. These insights not only amplify the quantifiability of S/TEM-based composition mappings but also harmonize well with novel approaches of composition determination, such as the analysis of stress relaxation for thin TEM-lamellas.

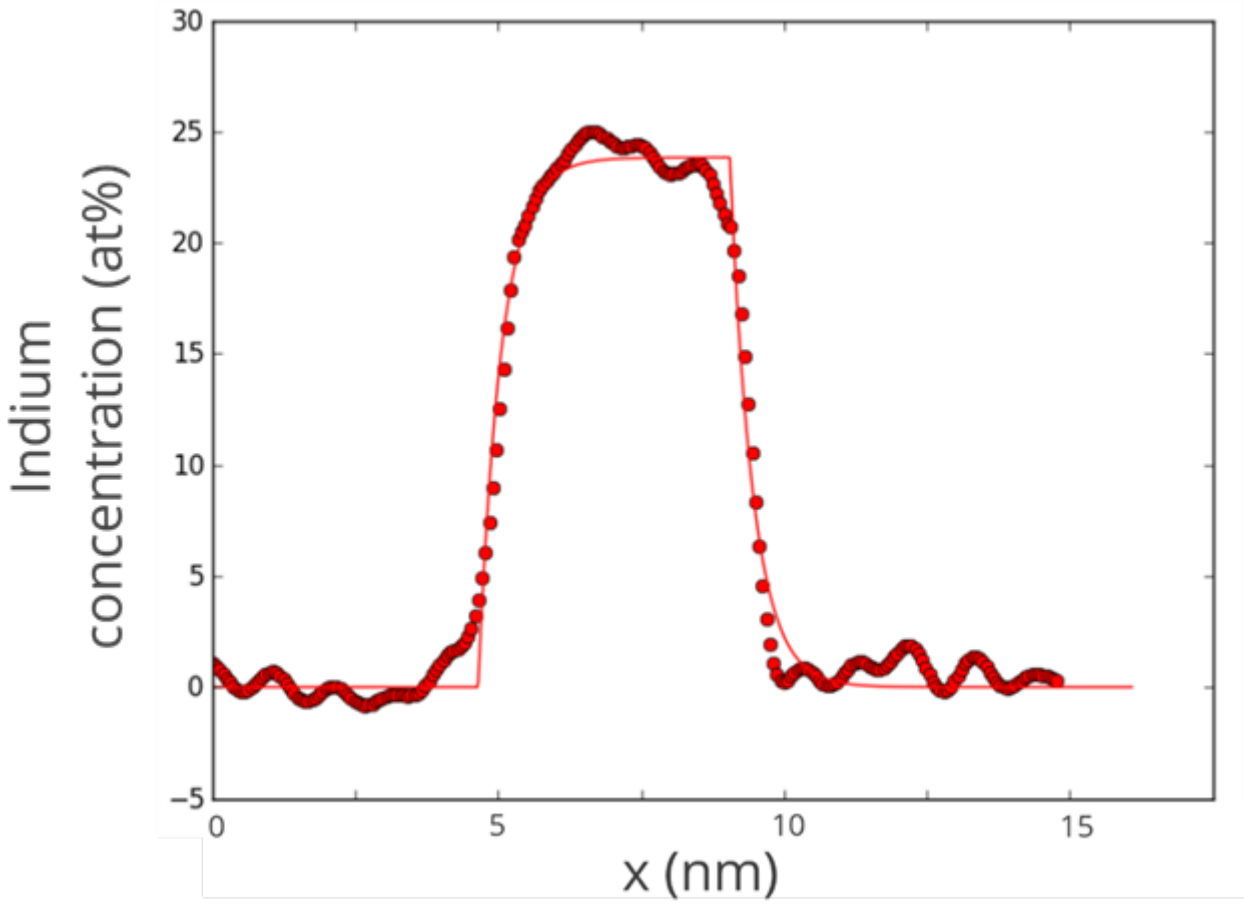


**Keywords:**

InGaAs, composition-mapping, Alloy-distribution, STEM-EDX, 4D-STEM

**Reference:**

[1] N. V. Kryzhanovskaya et. al. Semicond. Sci. Technol. 20, 961 (2005).
[2] J. S. Nilsen et. al. Microscopy and Microanalysis, 28, 61 (2022)
[3] T. Niermann et. al. Nat Commun, 15, 1356 (2024).
[4] K. Muraki et. al. Appl. Phys. Lett. 3, 61 (5), 557 (1992).

114

# Electronic properties of W' twin domain walls in ferroelastic BiVO4

Yuwen Xu[1], Dr. Pankaj Sharma[2,3,4], Mr. Haotian Wen[1], Mr. Dawei Zhang[1,2], Dr. Charlie Kong[5], Dr. Zewu Yan[6], A/Prof. Shery L.Y. Chang[1,5], Prof. Jan Seidel[1,2]
[1]School of Materials Science and Engineering, UNSW Sydney, Sydney, Australia, [2]ARC Centre of Excellence in Future Low-Energy Electronics Technologies (FLEET), UNSW Sydney, Sydney, Australia, [3]College of Science and Engineering, Flinders University, Bedford Park, Australia, [4]Flinders Institute for Nanoscale Science and Technology, Flinders University, Adelaide, Australia, [5]Electron Microscope Unit, Mark Wainwright Analytical Centre, UNSW Sydney, Sydney, Australia, [6]Laboratorium für Festkörperphysik, ETH Hönggerberg, Zürich, Switzerland

Poster Group 2

Background incl. aims
Topological defects in ferroic materials are important in solid state physics since they can exhibit different intrinsic properties from the bulk and act as active sites in device engineering.[1] Investigation of those defects in terms of their structural variations and relevant properties in special materials systems opens a new path for improving materials' performance and developing novel devices. Here, we aim to investigate the structural and electronic properties of the ferroelastic domain wall in a well-known visible-light catalytic material,[2] monoclinic scheelite $BiVO_4$ (ms-BVO), which may be interesting for photochemistry-relevant applications.

Methods
The BF-TEM image and SAED were obtained using a JEOL JEM-F200 S/TEM operated at 200 kV for domain wall determination. HAADF-STEM images and electron energy loss spectroscopy (EELS) were obtained using a JEOL Grand ARM300F2 double-corrected S/TEM operated at 300 kV, for atomic resolution crystallographic structure and electronic structure demonstration. A Digital Instruments Nanoscope-IV Multimode atomic force microscope equipped with a c-AFM application module (TUNA) was used for nanoscale conductivity measurement.

Results
Highly dense twin walls are found in ms-BVO single crystal and identified as ferroelastic W' wall forming along the strain direction.[3] Opposite shear strain is seen in ferroelastic twin domains (A and B) and released at the wall. The W' wall has a kink configuration, and the overall wall width (d) is approximately ~2 unit cells. The W' walls show clear electrical conductivity by c-AFM under a DC tip voltage of −9.8 V while the domains show no obvious current signal. Subsequent STEM-EELS analysis shows that the V eg state of the W' wall shifts downward of 0.12 eV, indicating a lower conduction band minimum (CBM) compared to twin domains. The larger energy splitting at V $L_3$ and $L_2$ peaks at the W' wall is consistent with the symmetry of the topological defects. The higher V $L_3/L_2$ peak ratio indicates a lower oxidation state of vanadium, i.e., a higher density of oxygen vacancies at the W' wall. The higher shoulder peak at ca. 517 eV (compared to V eg state) indicates the possible accumulation of small polarons at the W' wall. The lower conduction band minimum, increased amount of oxygen vacancies and small polarons may be the reasons for the ferroelastic W' wall conductivity.

Conclusions
The present work investigates the structures and electronic properties of the ferroelastic W' wall in ms-BVO bulk crystals. The W' wall is atomically sharp in a zig-zag shape. Compared to non-conductive domains, the W' walls show conductivity in c-AFM measurement under negative bias. The electronic structures revealed by EELS spectra show that the wall has a relatively lowered conduction band

minimum, a higher density of oxygen vacancies and possible accumulation of small polarons compared to the domains, which may contribute to the increased wall conductivity. Since the photocatalytic performance of a semiconductor is highly related to its conductivity,[4] the investigation of W' wall conductivity of ms-BVO crystals may help in designing highly efficient catalytic materials.

**Keywords:**

ferroelastic domain walls, electronic properties

**Reference:**

1. G. Catalan, J. Seidel, R. Ramesh, J.F. Scott, Rev. Mod. Phys., 2012, 84.
2. S. Tokunaga, H. Kato, A. Kudo, Chem. Mater., 2001, 13.
3. J. Sapriel, Phys. Rev. B, 1975, 12.
4. P. Dong, G. Hou, X. Xi, R. Shao, F. Dong, Environ. Sci. Nano, 2014, 4.

141

# Development and characterization of N2O-plasma oxide layers for high-temperature passivating contacts solar cells

Mrs Sofia Libraro[1], Mr Lars Bannenberg[2], Mr Theodosios Famprikis[2], Mr David Reyes[3], Mr Julien Hurni[1], Mr Christophe Ballif[1,4], Mr Franz-Josef Haug[1], Mrs Audrey Morisset[1], Aïcha Hessler-Wyser[1]
[1]Photovoltaics and thin-film electronics laboratory (PV-Lab), Institute of Electrical and Micro Engineering (IEM), École Polytechnique Fédérale de Lausanne (EPFL), 2000 Neuchâtel, Switzerland, [2]Department of Radiation Science and Technology, Faculty of Applied Sciences, DUT, Delft, the Netherlands, [3]Interdisciplinary Centre for Electron Microscopy, EPFL, 1015 Lausanne, Switzerland, [4]CSEM Sustainable Energy Center, 2000 Neuchâtel, Switzerland

Poster Group 2

Full-area passivating contacts solar cells based on SiOx/poly-Si stacks represent the key elements for the fast growing new generation of industrial silicon solar cells substituting the passivated emitter and rear cell (PERC) technology. The utilization of n-type wafers with an n-type contact at the back and a p-type diffused boron emitter has become the industry standard in 2024.
In this work, variations of this technology are explored, considering p-type passivating contacts formed via a rapid thermal processing (RTP) step on p-type wafers, which could be useful in conjunction with n-type contacts for realizing solar cells with passivating contacts on both sides. Here, a particular focus is set on investigating the influence of the applied thermal treatment on the interfacial oxide layer. Thin SiOx layers formed via UV-$O_3$ exposure of the wafer are compared with layers obtained through a plasma treatment with nitrous oxide ($N_2O$). The different steps for sample fabrication are depicted in Figure 1(a).
For both oxide types, the influence of the RTP thermal budget on passivation quality and contact resistivity is investigated, as presented in Figure 1(b). The $N_2O$ oxide exhibits an excellent passivation quality (i.e. high implied open circuit voltage iVoc) in the range of high thermal budget, whereas the UV-$O_3$ oxide shows a pronounced degradation under these conditions. Simultaneously, the contact resistivity achieved with the $N_2O$ oxide layer is comparable to that yielded by the UV-$O_3$ oxide. Prior research emphasised the importance of employing a higher thermal budget for contacts formed by RTP to ensure both sufficient lateral conductivity of the poly-Si layers and compatibility with localized metal contacts [1]. These results demonstrate that fabrication of the thin SiOx by $N_2O$ oxidation can be a viable solution to obtain high passivation quality in the high thermal budget range.
To unravel the mechanisms behind the improved performance obtained with the $N_2O$ oxide at high thermal budget, high resolution TEM is conducted on layer stacks featuring both $N_2O$ and UV-$O_3$ oxides after RTP at T=860°C, as presented in Figure 2. A break-up of the UV-$O_3$ oxide at high thermal budget is observed, whereas the $N_2O$ oxide is found to maintain its structural integrity along the interface. The differences are shown in higher magnification in the STEM-HAADF micrographs in Figure 2(e,f). The superposition between a region displaying contrast from SiOx and a region with a pinhole in Figure 2(f) indicates that the UV-$O_3$ layer is only partially disrupted.
Characterization of the same samples by X-Ray reflectometry (XRR) was also used to study the differences in the two oxide layers on a larger scale, confirming the HR-TEM results. Furthermore, chemical analysis conducted by depth-dependent X-Ray photoelectron spectroscopy (XPS) reveals that the $N_2O$ oxide is richer in oxygen and contains a higher amount of nitrogen compared to the UV-$O_3$ one, as shown in Figure 3. These distinguishing characteristics can be directly linked to the enhanced stability exhibited by the $N_2O$ oxide under higher annealing temperatures and extended dwell times, in agreement with previous research [2], [3].
This study highlights the effectiveness of the employed characterization techniques as a robust method for analyzing multi-layer stacks, particularly well-suited for nanoscale thin films. By integrating more invasive techniques such as TEM and XPS depth-profiling with the non-destructive

approach of XRR, it is possible to characterize large sample areas while also resolving layers at the atomic scale. This combined approach allows the analysis of full c-Si/SiOx/poly-Si stacks after RTP, closely resembling structures used in solar cell applications, thereby providing valuable insight for further development and application of such contacts. This approach differs from the majority of similar studies in literature that primarily focus on characterization of as-deposited oxide layers [3]–[5].

Figures captions:
Figure 1. a) Sample fabrication process. (b) Implied open-circuit voltage (iVoc) after hydrogenation and contact resistivity (ρC) as a function of the RTP temperature for contacts with UV-$O_3$ and $N_2O$ oxides.

Figure 2. (a,b) High resolution TEM micrographs of the c-Si/poly-Si(p) interface for the two samples with $N_2O$ and UV-$O_3$ oxide layers, respectively, after RTP at 860°C. Higher magnification of the interface is shown in (c) and (d). (e,f) High resolution STEM-HAADF micrographs of the samples with the two oxide types. White arrows in (d) and (f) indicate the crystalline protrusions at the position of the SiOx for the UV-$O_3$ oxide.

Figure 3. XPS contour plots of signal intensity versus etching time and binding energy for Si 2p, O 1s, and N 1s spectral ranges at processing T=860°C. The intensity scale remains consistent across plots within the same spectral range for both samples.

Figure 1:

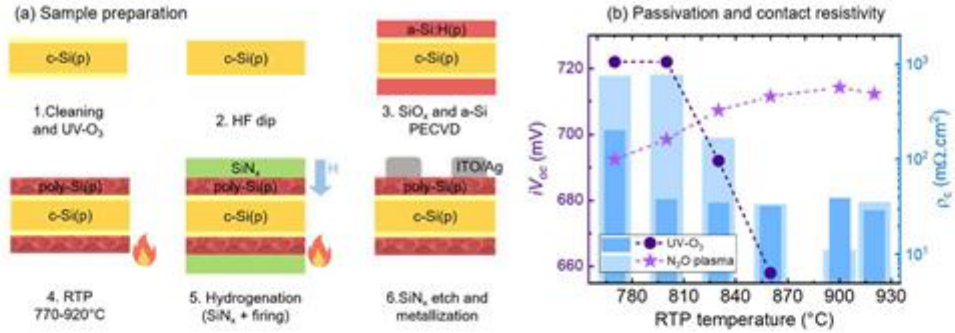


Figure 2:

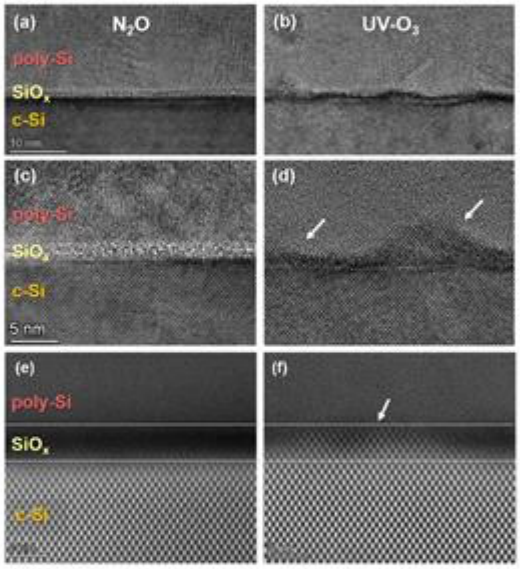


Figure 3:

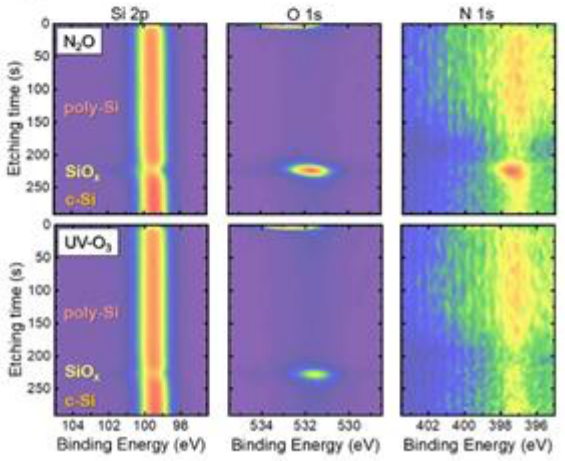


**Keywords:**

Photovoltaics, Passivating-contacts, Silicon oxide, Polysilicon

**Reference:**

[1] J. I. Polzin et al., Sol. Energy Mater. Sol. Cells, vol. 218, no. July, p. 110713, 2020.
[2] A. Moldovan et al., Energy Procedia, vol. 55, pp. 834–844, 2014.
[3] H. Xing et al., Sol. Energy Mater. Sol. Cells, vol. 257, no. December 2022, p. 112354, 2023.
[4] Z. Yao et al., Sol. RRL, 2023.

142

# Characterization of aluminium diffusion in high-temperature passivating contacts by in situ scanning transmission electron microscopy

Mrs Sofia Libraro[1], Mr Janghyun Jo[2], Mr Maximilian Kruth[2], Mr Rafal Dunin-Borkowski[2], Mr Saul Estandia Rodrigez[3], Mr Pierpaolo Ranieri[3], Mr Christophe Ballif[1,4], Mrs Audrey Morisset[1], Mr Franz-Josef Haug[1], Aïcha Hessler-Wyser[1]
[1]Photovoltaics and thin-film electronics laboratory (PV-Lab), Institute of Electrical and Micro Engineering (IEM), École Polytechnique Fédérale de Lausanne (EPFL), Neuchâtel, Switzerland, [2]Ernst Ruska Center for Microscopy and Spectroscopy with Electrons, Jülich, Germany, [3]Institute of materials, École Polytechnique Fédérale de Lausanne (EPFL), Lausanne, Switzerland, [4]CSEM sustainable energy center, Neuchâtel, Switzerland

Poster Group 2

Full-area passivating contacts utilizing SiOx/poly-Si stacks are a critical component for the coming generations of high-efficiency industrial silicon solar cells, replacing the previous mainstream technology called passivated emitter and rear cell (PERC). In this work, the metallization of p-type passivating contacts formed via a rapid thermal processing (RTP) step is investigated. Metallization of poly-Si layers typically involves silver-based pastes for both sides of the cell, leading to higher production costs compared to PERC, which use Ag only on one side. Moreover, concerns over the long-term availability of silver prompt the search for more abundant alternatives to reduce costs and ensure sustainability in solar cell production [1].

The formation of Al-Si contacts, which results in the creation of µm-deep spikes within the c-Si wafer, has been well-documented in the context of PERC cells [2], but it has not been investigated thoroughly for poly-Si layers. The feasibility of utilizing aluminium pastes to establish contact with p-type poly-Si layers was explored in a prior study [3]. Characterization of the microstructure of the contacts after firing at different temperatures highlighted the numerous interactions taking place between the aluminium and the different layers in the stack (SiNx, poly-Si, SiOx and the c-Si wafer), which create a challenging trade-off between achieving a good electrical contact while retaining high passivation quality. Moreover, it was demonstrated that, for more fundamental studies, it is possible to replace the paste with evaporated Al, simplifying the analysis [3].

To gain further insight into the reaction mechanisms, this works focuses on characterization of the samples during in situ heating by scanning transmission electron microscopy and energy dispersive X-ray spectroscopy (STEM/EDX) for temperatures below 650°C. The sample fabrication steps, structure and the heating profile applied during characterization are depicted in Figure 1. The reactions observed during the heating process are represented schematically in Figure 2. The initial phase involves Si out-diffusion into the Al from the underlying layers (Figure 2(b)), followed by Al diffusion at higher temperatures. The latter appears to occur initially vertically through regions with reduced density or thickness in the parasitic SiOx layers present at the various interfaces, and subsequently laterally within the SiNx and poly-Si layers (Figure 2(c)). Here, the oxide layers at the interfaces function as diffusion barriers, promoting lateral rather than vertical Al diffusion. The nc-Si(i) layer exhibits similar behaviour, showing no discernible reaction with Al at this stage (T < 500°C), as visible in Figure 3. This is likely due to the enhanced crystallinity of the nc-Si(i) compared to the poly-Si(p) layer, which has been reported to hinder reactions with Al [4]. In the final stages of the process (Figure 2(d) and Figure 4), Al diffuses into the nc-Si(i) layer, eventually reaching the wafer interface where it accumulates at the thin SiOx and creates pinholes within the SiOx layer. These observations can explain the passivation degradation observed in previous work at relatively low temperature (500-600°C), well below the threshold for formation of the µm-deep Al spikes. Furthermore, this study provides insights into potential avenues for improvement, such as enhancing the crystallinity of the poly-Si layer or substituting the SiOx with a layer less reactive with Al.

Figures captions:
Figure 1. (a) Fabrication process for the studied SiOx/poly-Si contacts. (b) Structure of the studied sample. (c) Temperature profile applied during in situ heating.

Figure 2. Schematic representation of a possible reaction sequence: (a) beginning of the heating process, and (b) diffusion of Si from the various layers into the Al contact. (c) Diffusion of Al through pinholes in the oxide layers, and lateral diffusion in the channel provided by the parasitic oxide layers or the nc-Si(i) region. (d) Complete reaction of the different layers with Al, and changes to the SiOx layer.

Figure 3. STEM-ADF micrograph acquired after heating up to 500°C and successive rapid cooling to room temperature, and corresponding elemental maps for Al (orange) and Si (green) (overlaid onto ADF micrograph). The different layers are indicated by the colour bar on the left side. The white arrows highlight the nc-Si(i) at the interface with the Si wafer.

Figure 4. (a) STEM-HAADF and (b) ADF micrographs of the layer stack after heating to 650°C and subsequent rapid cooling. The colour bar on the left side indicates the different layers. Elemental maps for aluminium (orange), silicon (green), nitrogen (blue) and oxygen (pink) correspond to the areas highlighted by the white rectangles in (a) and (b). The white arrows highlight the regions where epitaxy from the c-Si occurs.

Figure 1 :

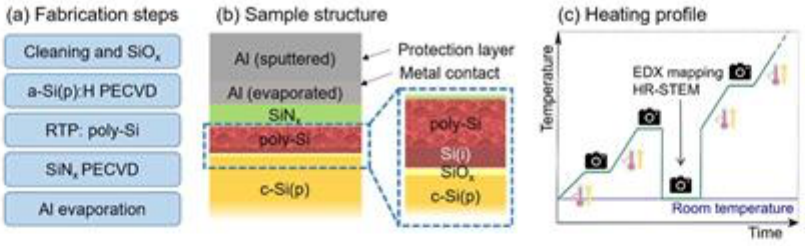


Figure 2 :

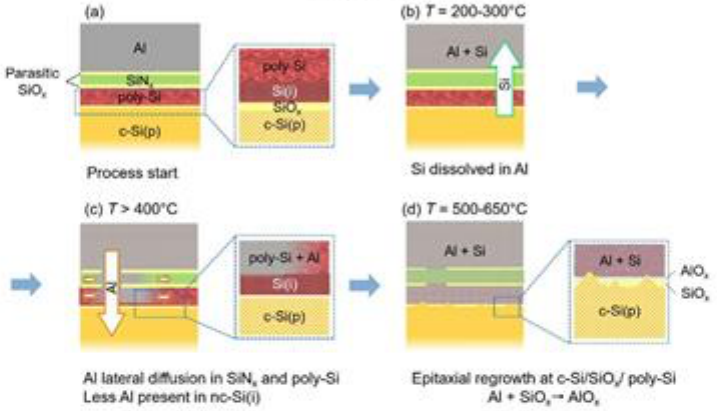


Figure 3 :

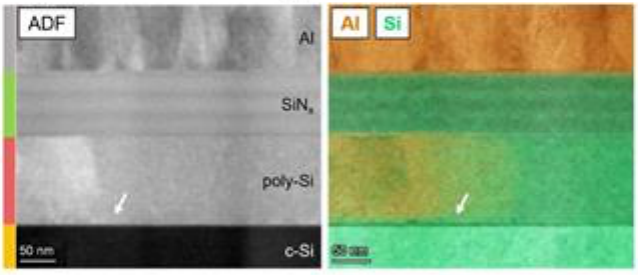


Figure 4 :

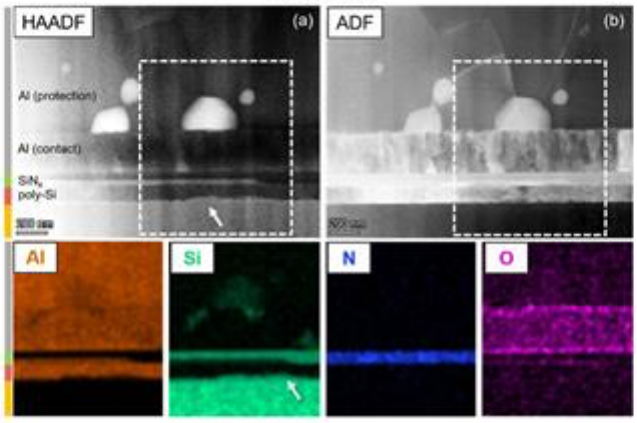


**Keywords:**

photovoltaics
thin-films
in situ STEM

**Reference:**

[1] B. Hallam et al., Prog. Photovoltaics Res. Appl., no. June, pp. 1–9, 2022.
[2] T. Lauermann et al., Prog. photovoltaics, vol. 20, no. 6, pp. 1114–1129, 2013.
[3] S. Libraro et al., Sol. Energy Mater. Sol. Cells, vol. 249, no. 112051, 2023.
[4] M. S. Haque et al., J. Appl. Phys., vol. 79, no. 10, pp. 7529–7536, 1996.

271

# Polar Discontinuity Governs Surface Segregation and Interface Termination: a case study of LaInO3/BaSnO3

Dr Martin Albrecht[1]
[1]Leibniz-Institut für Kristallzüchtung, Berlin, Germany, [2]Humboldt-Universität zu Berlin, Berlin, Germany, [3]ThermoFisher Scientific, Eindhoven, Netherlands, [4]Paul-Drude-Institut, Berlin, Germany

Poster Group 2

Background and aims.
Interfacial polar discontinuities are a unique way to manipulate charge states at interfaces and to create novel two-dimensional electron states. The polar-nonpolar interface between ABO3 perovskite oxides offers new degrees of freedom to tune interface states by the accessibility of mixed-valence states. The commonly accepted model for the formation of a two-dimensional electron gas (2DEG) is based on the concept of charge transfer between the layers terminating the polar-nonpolar interface. To realize a 2DEG or a two-dimensional hole gas (2DHG), control of the interface is a prerequisite. When growing the heterostructures, it is commonly assumed that the surface termination of the non-polar layer controls the interface. In this work, we provide experimental evidence that polar discontinuity compensation can drive surface segregation and thus control the interface

Methods.
We study the surface termination of BaSnO3 and the interface formation between the cubic wide bandgap semiconductor BaSnO3, and orthorhombic LaInO3, by negative cs imaging and direct spectral imaging of the LaInO3-BaSnO3 interface using Scanning Transmission Electron Microscopy Energy Dispersive X-Ray Spectroscopy (STEM-EDS) with the Thermo Fisher Spectra Ultra electron microscope equipped with Ultra X EDS detector. In parallel we perform Integrated Differential Phase Contrast STEM (iDPC-STEM) technique to study the oxygen octahedral tilt at the interface, providing further insights into the compensation of polar charges at that interface. Density functional theory (DFT) calculations are used to rationalize our experimental results. The samples were grown by plasma assisted molecular beam epitaxy on DyScO3 substrates at 835°C using a mixture of Sn and SnO2 as a SnO source.

Results.
While TEM experiments of BaSnO3 bulk crystals and DFT agree that BaO is the most stable surface termination of BaSnO3 over wide range of chemical potentials, we find by EDX spectral imaging the interface between BaSnO3 and LaInO3 is terminated by SnO2 (Fig. 1). This is consistent with the presence of a 2DEG but also with our DFT calculations which show this interface to be the most energetically favorable. STEM EDX shows the presence of BaO on the surface of thin LaInO3 films indicating Ba surface segregation. Based on our DFT calculations we find that the driving force for Ba segregation is the compensation of the polar discontinuity at the interface. This compensation is an effect the gradual reduction of the octahedral tilt from the orthorhombic LaInO3 to the cubic BaSnO3 and the polar and non-polar distortions at the interface as evidenced by the evaluation of iDPC images (Fig. 2). In the case of the n-type SnO2 interface, this leads to an expansion of the out-of-plane lattice spacing at the interface which most efficiently compensates for the discontinuity. At the BaO terminated p-type interface it leads to non-polar distortions in the BaSnO3, while polar distortions remain mainly in the LaInO3 which compensate the polar discontinuity less efficiently. This shows that in Perovskites in addition to surface energy and strain, the response of the system to compensate for the polar discontinuity must be considered as an additional driving force for segregation which may control the interface termination.

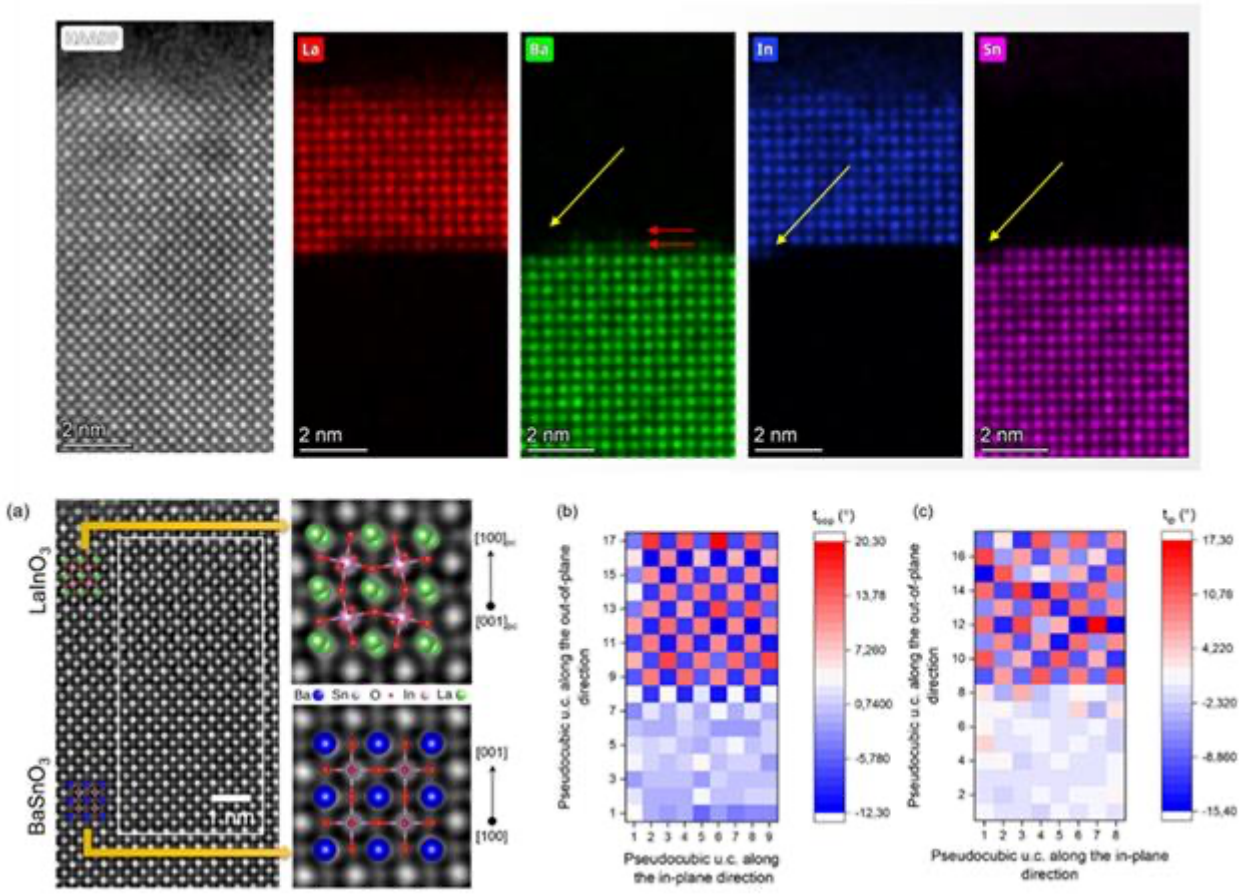


**Keywords:**

EDX, EELS, iDPC, Perovskites, 2DEG

279

# Effect of Oxygen-Doping in Ferroelectric Wurtzite-type Al0.73Sc0.27N

Md Redwanul Islam[1], Dr. Niklas Wolff[1], Mr. Georg Schoenweger[2,4], Dr. Simon Fichtner[3,4], Dr. Lorenz Kienle[1]
[1]Synthesis and Real structure, Department of Material Science (Kiel University), Kiel, Germany, [2]Nanoelectronics, Institute of Electrical and Information Engineering (Kiel University), Kiel, Germany, Kiel, Germany, [3]Microsystem and technology transfer, Department of Material Science (Kiel University), Kiel, Germany, [4]Fraunhofer Institute for Silicon Technology, Itzehoe, Germany

Poster Group 2

Background and aim

Al1-xScxN is a group III-N based wide-bandgap wurtzite (w)-type ferroelectric. The material has been proven to be highly temperature stable as well as thickness scalable towards ultra-thin range.[1], [2] Most importantly, it is also compatible to both CMOS and GaN technologies. Therefore, ferroelectricity in Al1-xScxN is highly promising for applications such as non-volatile memory devices, neuromorphic computing, high-electron mobility transistors and even harsh environment electronics.[3], [4] However, ferroelectricity in w-Al1-xScxN is affected by high-leakage current which can become a limiting factor for its successful integration into devices.[5] In the past, standard approaches such as doping or strain was used in semiconductors to alter their properties, especially conductivitiy. Therefore, in this work we address this issue via elemental doping with Oxygen (O). During sputtering of 200 nm thin Al0.73Sc0.27N on Pt/Si templates, we introduced O via gas source into. This allowed us to tune the overall O-content in the bulk thin-film and study its underlying effect on the material structure and the ferroelectric properties of Al0.73Sc0.27N.

Methods

The structure of the doped samples was examined using X-ray diffraction, scanning transmission electron microscopy (STEM). The surface imaging and topography was performed via scanning electron microscopy and atomic force microscopy.

Results

Our results show that all the O-doped Al0.73Sc0.27N films have an overall lower leakage current density compared to the undoped films. This applies to the films even with significantly high O-concentrations ≥ 8 at.%. STEM analysis showed that the columnar Al0.73Sc0.27N crystalline grains remained unhampered with no local phase or O segregation in the bulk. In addition, as O-dopant increases, the overall polarity of the film gradually changes from entirely nitrogen to metal polarity. This modification has no significant impact on the overall (0002) crystalline texture of the film, hence allowing for better control of the as-deposited polarization state of the material.

Conclusion

Our study shows that O-doping could be a viable remedy for the leakage current compensation in w-Al1-xScxN and possibly for all other wurtzite-type ferroelectrics as well.

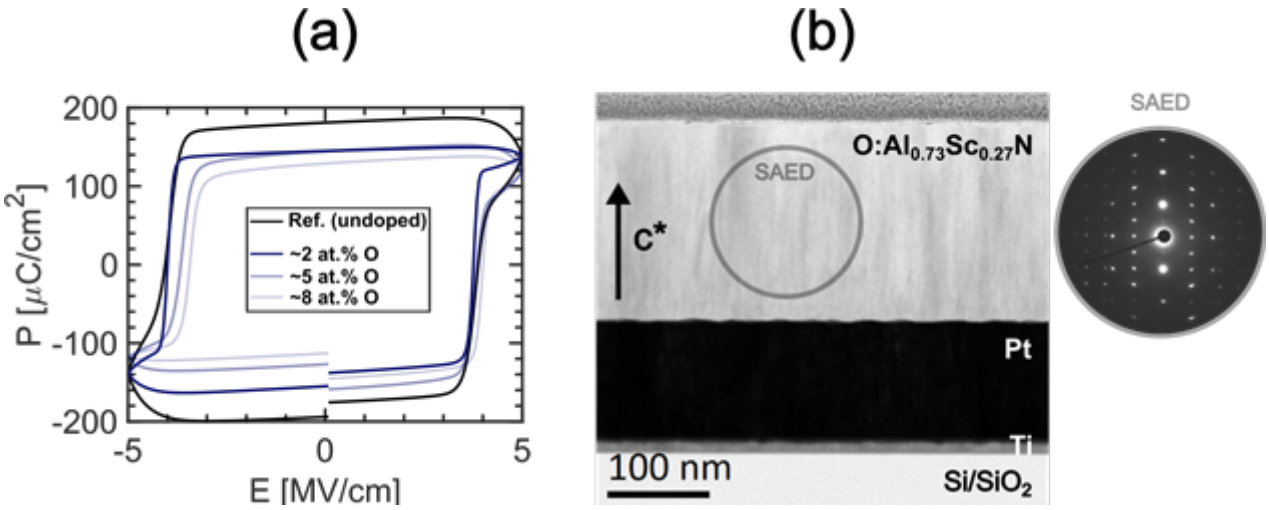


**Keywords:**

Wurtzite-type, Ferroelectric, doping, Oxygen

**Reference:**

[1] G. Schönweger et al., Advanced Science 10.25 (2023): 2302296.
[2] M. R. Islam et al., Applied Physics Letters 118.23 (2021).
[3] S. Fichtner et al., Journal of Applied Physics 125.11 (2019)..
[4] D. Drury et al., Micromachines 13.6 (2022): 887.
[5] M. R. Islam et al., ACS Applied Materials & Interfaces 15.35 (2023): 41606-41613.

285

# Fast and local determination of phases in (V1-xCrx)2O3 Mott materials

Mr Seyed-Mohammad Dolatabadi-Hamedi[1], Mr Eric Gautron[1], Mr Chris Leroux[1], Mohammed Haydoura[1], Mr Julien Tranchant[1], Mr Benoit Corraze[1], Mr Laurent Cario[1], Mr Etienne Janod[1], Seyed Mohammad Dolatabadi Hamedi[1]
[1]Nantes Université, CNRS, Institut des Matériaux de Nantes Jean Rouxel, NANTES, FRANCE

Poster Group 2

Background incl. aims
The Flash memory technology is getting close to its limit of downscaling and many researches have focused on alternative non-volatile memory technologies [1]. Mott memories, a special case of the broader class of resistive memories, are characterized by localization of their valence electrons owing to strong electronic correlations [2]. An electric field well above the avalanche threshold creates a nonvolatile conductive filament within the Mott insulator such as $(V1\text{-}xCrx)_2O_3$ [3]. Recent µ-XRD analysis of this filament shows that it is made of the same material but with smaller cell volume [4]. With the desired miniaturization of devices, the question of the actual and minimum size of this filament is vivid and requires techniques with nanometer scale resolution. Such resolution is achievable in STEM providing that a spectroscopic technique sensitive to the conductive state of the compound is used. The objective of this communication is to demonstrate that STEM-VEELS, by carefully studying the conditions and limits of the technique, indeed fulfils these requirements.
Methods
Measurements were performed using a Themis Z 80-300 kV (S)TEM equipped with a Gatan 969 EELS spectrometer. TEM lamella were prepared with a Focused Ion Beam (ZEISS, Crossbeam 550L) on $V_2O_3$ and $(V0.95Cr0.05)_2O_3$ single crystals (Figure a). In order to obtain data on the AFI phase appearing at low temperature in $(V1\text{-}xCrx)_2O_3$ compounds, a cryo sample-holder was used and data acquired at 95 K.
EELS spectra in the low-loss region were acquired at 300 kV with 2-10 nm pixel sizes and 0.2 ms per pixel.
The STEM-VEELS-SI were Fourier-Log deconvolved, carefully processed with PCA and the plasmon peak at around 27 eV was fitted on a limited energy range with a Drude-Lorentz model (Figure b). The precision of the method (<0.1 eV) was checked with respect to the influence of the local thickness, the crystal orientation and the possibility of presence of ice at low temperature.
Results
Our numerous experiments carried out on $V_2O_3$ single crystals showed that the use of the plasmon peak energy was precise enough to distinguish between the room temperature paramagnetic metal (PM) and the low temperature antiferromagnetic (AFI) phases (Figure c-d). The paramagnetic insulator (PI) and AFI phases of (V0.95Cr0.05)2O3 can also be analyzed with this method. The shift of the plasmon peak can be at least partially explained by the change in the volume density of electrons consecutive to the increase of the cell parameter in the AFI phase at low temperature. The existence/absence of a gap in the electronic structure is proven to have a minor influence on the measurement.
Other experiments on MIM devices show that the plasmon peak energy can be determined at a 5 nm resolution establishing this technique as very suitable to the visualization of (conducting) nanofilaments suggested to explain the resistive transition in these Mott-insulators.
Polycrystalline thin films and MIM devices were also studied before/after resistive switching to gain a better knowledge of the phenomenon when applied to technology relevant systems. The analysis of the considerable changes observed at the local scale will be presented.
Conclusion

By carefully setting-up parameters and experimental conditions, we demonstrated the usefulness of STEM-VEELS spectrum imaging to distinguish, at the nanometer scale, PM, PI, AFI phases in $(V_{1-x}Cr_x)_2O_3$ compounds. These temperature dependent and the ex situ characterizations of the electrical switching are prerequisites to assess which changes to expect for future in situ measurements and consequently progress on this still partly elusive mechanism.

Acknowledgments.
TEM measurements in Nantes were performed using the IMN's characterization platform PLASSMAT, CIMEN TEM Microscope having been funded by the French Contrat Plan Etat-Région (CPER), the European Regional Development Fund of Pays de la Loire (FEDER), the Région Pays de la Loire, Nantes Métropole and CNRS.

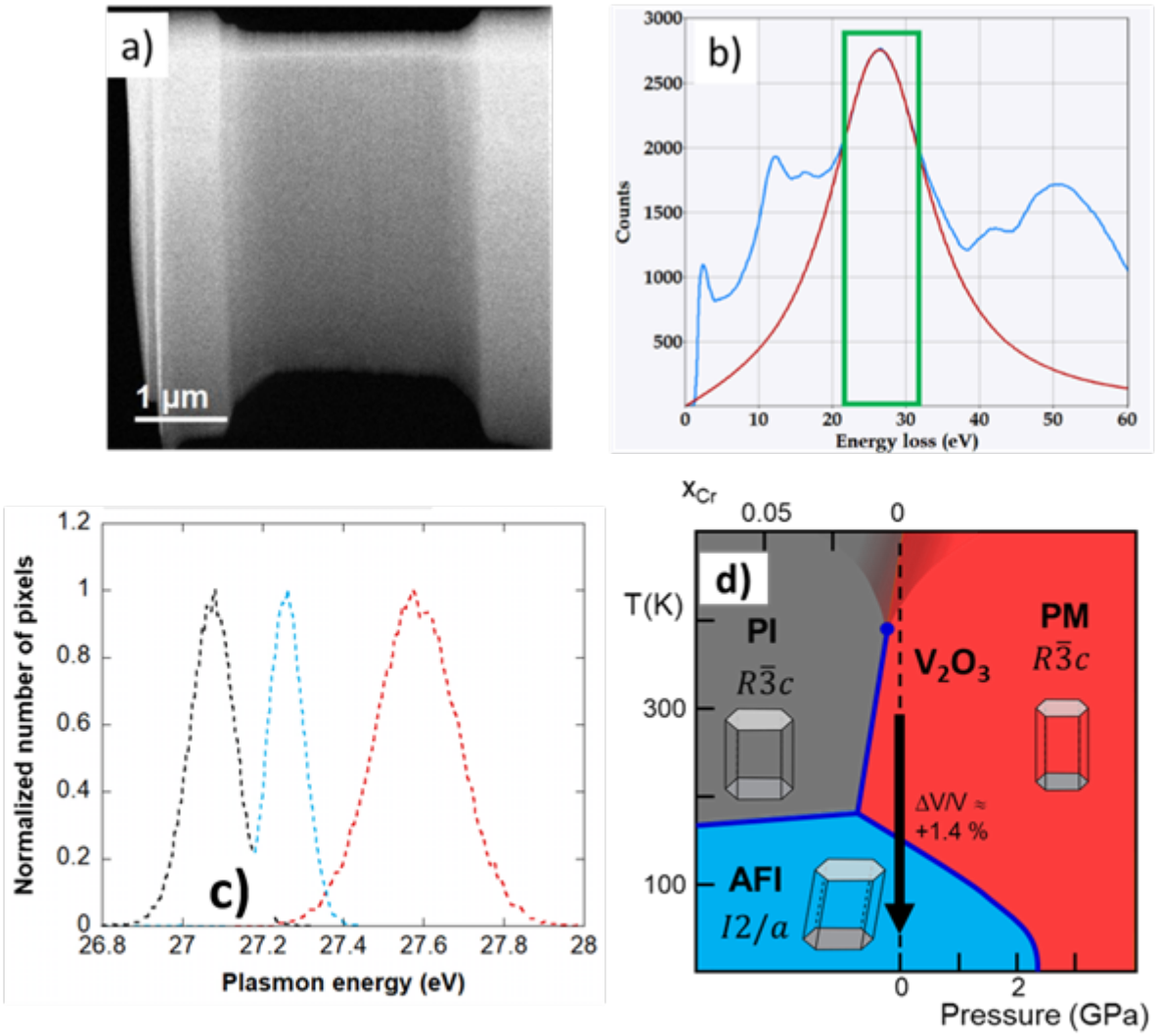


**Figure:** (a) STEM-HAADF micrograph of a $V_2O_3$ lamella prepared by FIB. (b) Low-loss Electron Energy spectrum fitted with a Drude-Lorentz model to extract the plasmon energy. (c) Plasmon energy distribution (over a 1 µm² area) for $V_2O_3$ at room temperature in the PM phase (red curve), at 95 K in the AFI phase (blue curve). The black curve corresponds to $(V_{0.95}Cr_{0.05})_2O_3$ at room temperature in the PI phase. (a) Phase diagram Temperature *vs.* composition x and pressure of the $(V_{1-x}Cr_x)_2O_3$ system, composed of paramagnetic metal (PM), paramagnetic insulator (PI) and antiferromagnetic insulator (AFI) phases. In pure $V_2O_3$, a volume increase $\Delta V/V$ of +1.4 % occurs at the PM to AFI transition.

**Keywords:**

Mott-insulators, Resistive transition, STEM-VEELS, plasmon

**Reference:**

[1] F. Zahoor, T. et al., Nanoscale Res. Lett., vol. 15, no 1, p. 90, 2020.
[2] M. Imada, et al., Rev. Mod. Phys., vol. 70, no 4, p. 1039, 1998
[3] L. Cario, et al., Adv. Mater., vol. 22, no 45, p. 5193, 2010.
[4] D. Babich et al., ArXiv210505093 Cond-Mat, oct. 2022

302

# Microstructure characterization of CIGS/GaP/Si tandem solar cells

Dr Eric Gautron[1], Mr. Eugène Bertin[2], Mr. Ludovic Arzel[1], Mr. Léo Choubrac[1], Mr. Antoine Létoublon[2], Mrs. Rozenn Gautheron[2], Mr. Charles Cornet[2], Mrs. Maud Jullien[2], Mrs. Sylvie Harel[1], Mr. Emmanuel Cadel[3], Mr. Olivier Durand[2], Mr. Nicolas Barreau[1]
[1]Nantes Université, CNRS, Institut des Matériaux de Nantes Jean Rouxel, IMN, Nantes, France, [2]INSA Rennes, CNRS, Institut Foton – UMR 6082, University of Rennes, Rennes, France, [3]Univ Rouen Normandie, INSA Rouen Normandie, CNRS, Normandie Univ, GPM UMR 6634, Rouen, France

Poster Group 2

Background incl. aims
The conversion efficiencies of single-junction solar cells have reached values very close to the theoretical Schockley-Queisser limit (~33%). One strategy for exceeding this value is to use tandem solar cells [1] combining a top cell optimized to absorb solar radiation in the UV/visible range with a bottom cell optimized for IR absorption. As part of the ANR EPCIS project [2], we have developed this type of cell using a Cu(In,Ga)S2 (CIGS) layer (with a band gap of 1.65-1.70 eV) deposited at low cost by co-evaporation on a Si substrate (band gap of 1.1 eV). However, the adhesion of a CIGS layer to Si is very poor, so an intermediate layer is needed to improve adhesion. The GaP material was chosen for 3 main reasons : 1) its cubic symmetry with a lattice parameter close to that of Si and also to that of CIGS, for a GGI close to 20% (chalcopyrite material with pseudo-cubic quadratic symmetry with c~2a) can promote epitaxy growth of the CIGS film, 2) such layer can act as a diffusion barrier to prevent diffusion of species between layers during the growth process, and 3) its low absorption coefficient (2.26 eV indirect bandgap) coupled with an electron affinity around 3.8 eV make it an ideal selective contact for holes. Despite the above-mentioned advantages, electrical performances of our synthesized tandem solar cells are still very low. We combined different characterization techniques including S/TEM to try understanding the relation between microstructure and optoelectonic performances.

Methods
Growth parameters including temperature, GGI=[Ga]/([Ga]+[In]) and CGI=[Cu]/([Ga]+[In]) can be adjusted during the co-evaporation process to deposit the CIGS layer on the GaP/Si substrate. When CGI is greater (less) than 1, the film is described as "Cu-rich" ("Cu-poor"). Various S/TEM techniques (ACOM-TEM, probe-corrected S/TEM imaging, spectroscopies) were used to study the 'Cu-rich' and 'Cu-poor' CIGS films: the epitaxial growth of the chalcopyrite CIGS layer, the presence of other crystalline phases and their orientation, and the identification of certain intragranular defects. The interdiffusion of elements and the possible presence of an additional layer between the CIGS and the GaP were characterised by atom probe tomography (APT).

Results
In the Cu-poor sample, the existence of a CuIn5S8 thiospinelle phase (TS) was demonstrated in addition to the CIGS chalcopyrite phase (CH) with this epitaxial relationship: CH[100](001)//TS[100](001)//GaP[100](001)//Si[100](001). In the case of Cu-rich sample, the epitaxial relationship is the same, except that there is no TS phase (Figure). However, the interface between GaP and CIGS layer is much more abrupt in the Cu-poor case than in the Cu-rich case where a few nanometers thick layer made of Cu and P is detected.
Despite the presence of TS phase and interface layers, the desired chalcopyrite phase is the most present. Unexplained contrast in HAADF-STEM images for both kind of samples led us to consider defects such as cation antiphase boundaries. On the basis of these contrasts, three types of CAPB were conceptualized.

Conclusion

Combined with other more macroscopic techniques, S/TEM and APT have enabled us to show that the growth of a CIGS layer on a GaP/Si pseudo-substrate for the application of tandem solar cells is far from ideal. Differences in Cu stoichiometry in the CIGS film were also highlighted.

Acknowledgments :

TEM measurements in Nantes were performed using the IMN's characterisation platform PLASSMAT, CIMEN TEM Microscope having been funded by the French Contrat Plan Etat-Région (CPER), the European Regional Development Fund of Pays de la Loire (FEDER), the Région Pays de la Loire, Nantes Métropole and CNRS.

The authors acknowledge financial support from the CNRS-CEA ''METSA'' French network (FR CNRS 3507)

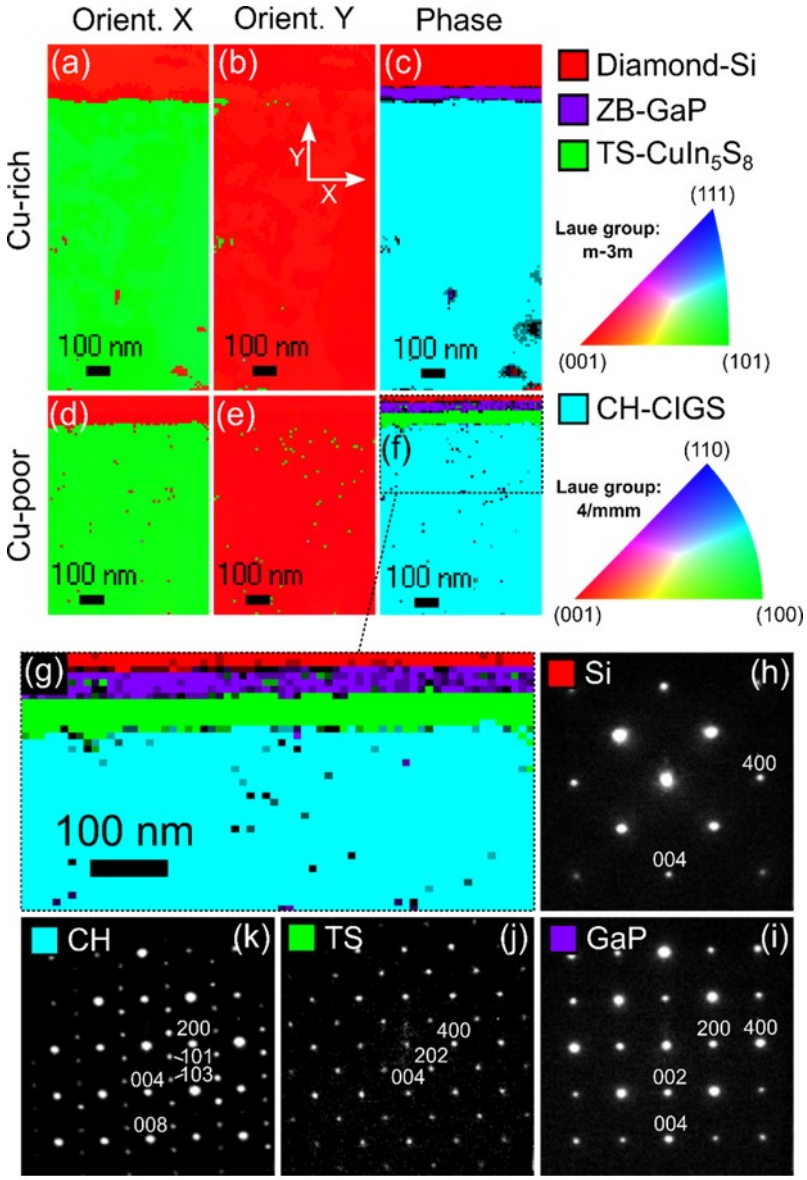


Figure : Orientation map a,d) along X, b,e) along Y, and c,f) phase map for the d–f) Cu-poor and a–c) Cu-rich sample. g) Zoom around the GaP layer for the Cu-poor sample. Electron diffraction patterns of h) the Si, i) the GaP, j) the TS, and k) the CH phases.

**Keywords:**

Tandem-solar-cell, epitaxy, secondary phases, interdiffusion

**Reference:**

[1] F. Martinho, Challenges for the future of tandem photovoltaics on the path to terawatt levels: A technology review, (2021).
[2] This research was supported by the French National Research Agency EPCIS Project (Grant No. ANR-20-CE05-0038)

308

# In-situ electrical characterization of MOSFET transistors using AFM-in-SEM solution

Ondrej Novotny[1], Libor Strakos[2], Marek Patocka[1], Vojtech Schanilec[1], Veronika Hegrova[1], Umberto Celano[3], Tomas Vystavel[2], Dr. Jan Neuman[1]
[1]NenoVision s. r. o., Brno, Czech Republic, [2]Thermo Fisher Scientific, Brno, Czech Republic, [3]Arizona State University, Tempe, USA

Poster Group 2

Background incl. aims
The semiconductor industry is continuously working on improving the performance of modern electronics and new components development. Key physical parameters like dopant concentration levels, carrier types, and crystalline defect densities are fundamental factors that influence the electrical performance of semiconductor devices. To improve device performance, novel methodologies, instrumentation, and workflows are being developed. The key requirement is the ability to investigate samples with nanoscale features to characterize device reliability or failure root cause. One example of a progressive approach for characterizing complex physical and electrical properties of semiconductor materials is correlative in-situ microscopy. A combination of different imaging systems provides a comprehensive understanding of the sample properties without the need to move the sample between multiple instruments.
Methods
The AFM-in-SEM approach, combining Atomic Force Microscopy (AFM)-based techniques with Scanning Electron Microscopy (SEM)-based or Focused Ion Beam (FIB)/SEM-based techniques, provides means to integrated correlative approach for studying semiconductor materials and devices. This solution allows for non-destructive mapping of diverse electrical properties of trenches, measuring gate dimensions, or localizing defects, which could help to understand the device processes. This approach provides the advantages of combining the benefits of capabilities of site-specific sample preparation by FIB, and ultra-high resolution imaging by SEM and AFM techniques. This integration helps in revealing the structures below the sample surface and measuring various properties at the exact location under in-situ conditions. Additionally, it provides quantitative 3D information while avoiding sample or environmental changes such as differential pressure or sample contamination.
Using the AFM module LiteScope, integrated inside the FIB/SEM, it is possible to measure high-resolution topography, and various electrical properties using techniques such as Conductive Atomic Force Microscopy (C-AFM), Scanning Spreading Resistance Microscopy (SSRM) and Kelvin Probe Force Microscopy (KPFM). C-AFM enables electrical conductivity measurement with nanoscale resolution, while SSRM can provide valuable information on dopant concentration profiles in semiconductors. KPFM is a non-destructive technique that measures surface potential, giving insight into electronic properties.
Results
With such an instrumentation, the samples are either in-situ lifted-out, or bulk x-sectioned. First we calibrated the probe measuring SSRM resistance on p- and n-doped silicon substrate, reference samples for dopant concentration measurement in SEM. Then, we analyzed MOSFET high power transistor by SSRM, showing the resistance of different components of the sample, see Fig. 1. The resistance can then be calculated to the dopant concentrations, using the calibration data from reference samples. This workflow proves that the dopant concentration steps of transistors can be safely measured under in-situ conditions in SEM, thus, enabling quality control and failure analysis of semiconductor components.
Conclusion

In summary, integrated AFM-in-FIB/SEM is a valuable instrumental combination for studying semiconductor materials or devices in order to improve device performance and enhance failure analysis success.

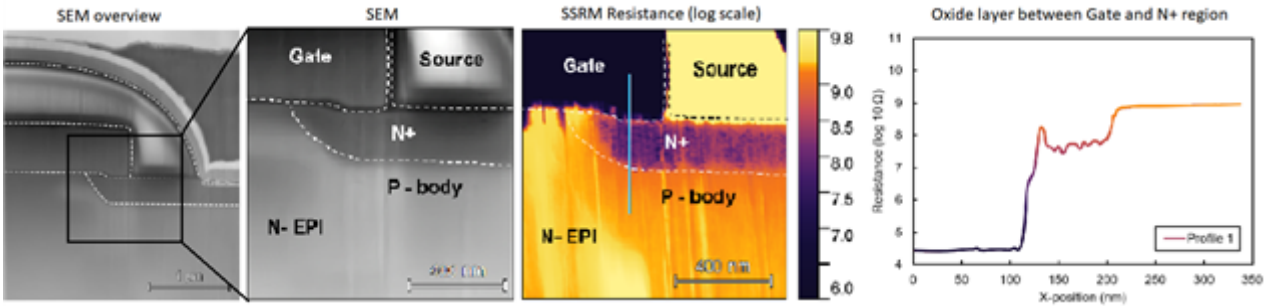


**Keywords:**

in-situ, semiconductors, SSRM, AFM, SEM

320

# Unraveling the composition of monolayer-thick InGaN/GaN quantum wells: A quantitative analysis via probe-corrected HRSTEM

Mr. Isaak G. Vasileiadis[1], Mr. Liverios Lymperakis[2], Mr. Adam Adikimenakis[3,4], Mr. Athanasios Gkotinakos[1], Mr. Vivek Devulapalli[2], Mr. Christian H. Liebscher[2], Mrs. Maria Androulidaki[3,4], Mr. Rene Hübner[5], Mr. Alexandros Georgakilas[3,4], Mr. Theodoros Karakostas[1], Professor Philomela Komninou[1], Mr. Emmanouil Dimakis[5], Mr. George P. Dimitrakopulos[1]
[1]School of Physics, Aristotle University of Thessaloniki, Thessaloniki, Greece, [2]Max-Planck Institut für Eisenforschung GmbH, Düsseldorf, Germany, [3]Microelectronics Research Group (MRG), IESL, FORTH, Heraklion, Greece, [4]Department of Physics, University of Crete, Heraklion, Greece, [5]Institute of Ion Beam Physics & Materials Research, Helmholtz-Zentrum Dresden-Rossendorf, Dresden, Germany

Poster Group 2

Short-period superlattices comprising ultra-thin InGaN/GaN quantum wells (QWs) with thicknesses of a few (0002) monolayers (MLs) have attracted considerable interest within the field of advanced optoelectronics. These nano-heterostructures offer the potential to manipulate the bandgap through precise control over both the QW and GaN barrier thicknesses [1]. Furthermore, their potential applications in quantum computing and spintronics have been spurred by the possibility of topological insulator behavior [2]. These crucial properties are intricately linked to the indium content within the QWs. Growth efforts strive to achieve high-quality heterostructures with high indium content and QW thickness of less than 5 MLs. This study aimed to determine the impact of growth temperature on indium incorporation and minimum QW thickness down to a single ML, by employing a methodological approach utilizing quantitative analysis of probe-corrected HRSTEM observations.

Methods
Multi-quantum-well (MQW) samples were grown by plasma-assisted molecular beam epitaxy under highly indium-rich conditions. These conditions included In:N flux ratios of 3:1 or 6:1 and InN growth rates of 0.25 or 0.15 ML/s. The objective was to kinetically stabilize QWs with nominal thicknesses of only 1 or 2 MLs. The MQWs were fabricated with either 3 or 5 periods. The thickness of the GaN barriers was maintained at 10 nm. Both the QW and GaN barrier growth temperatures were systematically varied. An integrated characterization approach was implemented to comprehensively analyze these nano-heterostructures. This approach encompassed quantitative analysis of probe-corrected HAADF HRSTEM observations. A peak finding algorithm utilizing 2D Gaussians was implemented to determine the atomic column positions within the experimental HRSTEM images with sub-Angstrom precision. These positions were subsequently used for nanoscale strain mapping and measurement of the atomic column intensities via a 2D Voronoi tessellation applied to each image. For Z-contrast quantification of the atomic column intensities, comparison to frozen-phonon HRSTEM image simulations was employed. The latter were generated from supercells relaxed using either density functional theory or empirical potential calculations with a modified embedded atom method interatomic potential [3-5].

Results
HAADF HRSTEM observations along the <11-20> zone axis of the wurtzite structure were employed for quantitative Z-contrast and strain analysis. Empirical potential calculations were conducted to determine the strain behavior of QWs with thicknesses of 1 and 2 MLs. A significant number of InxGa1-xN/GaN QW supercells spanning the entire compositional range, including both ordered and random alloy configurations, were constructed, and relaxed under biaxial strain conditions. These calculations yielded composition-dependent strain profiles. Subsequently, the relaxed supercells

served as input for the multislice HRSTEM image simulations. Consequently, graphs of InxGa1-xN/GaN column intensity ratios versus TEM foil thickness were generated, facilitating the correlation between QW composition and average column intensity. The analysis explicitly considered the effects of thin foil relaxation, the presence of amorphous surface layers and the cross-scattering phenomenon. The latter was identified as leading to an artificial intensity enhancement of the adjacent GaN MLs of the QWs, particularly at large foil thicknesses. The HAADF HRSTEM observations were then compared to the strain and intensity calculations in order to determine the indium contents within the QW MLs. The evaluation of the results allowed the elucidation of the crucial role of growth temperature in governing the indium incorporation and the QW thickness. A synthesis model explaining the nanoscale processes occurring during epitaxial growth was subsequently proposed.

## Conclusion

This work emphasized the importance of an HRSTEM-based methodology for determining the composition of ultra-thin InGaN/GaN QWs. The indium content was determined directly through quantification of Z-contrast and indirectly through measurements of lattice strain. Quantification of Z-contrast utilized thickness-composition-intensity ratio maps obtained from image simulations. Similarly, lattice strain measurements were translated to indium composition by employing the theoretically derived strain-composition coupling of such thin nano-heterostructures. The development and application of this integrated approach were necessitated by the requirement for sub-nanometer accuracy in compositional and strain analysis of low-dimensional materials. This accuracy is crucial for defining their structure-composition-properties relationship.

## Acknowledgments

The work was supported by the project “INNOVATION-EL” (MIS 5002772). I.G.V. acknowledges support by the State Scholarships Foundation (IKY) project “Strengthening Human Resources Research Potential via Doctorate Research” (MIS-5000432). We would like to thank the Aristotle University of Thessaloniki HPC infrastructure for the provision of computing resources.

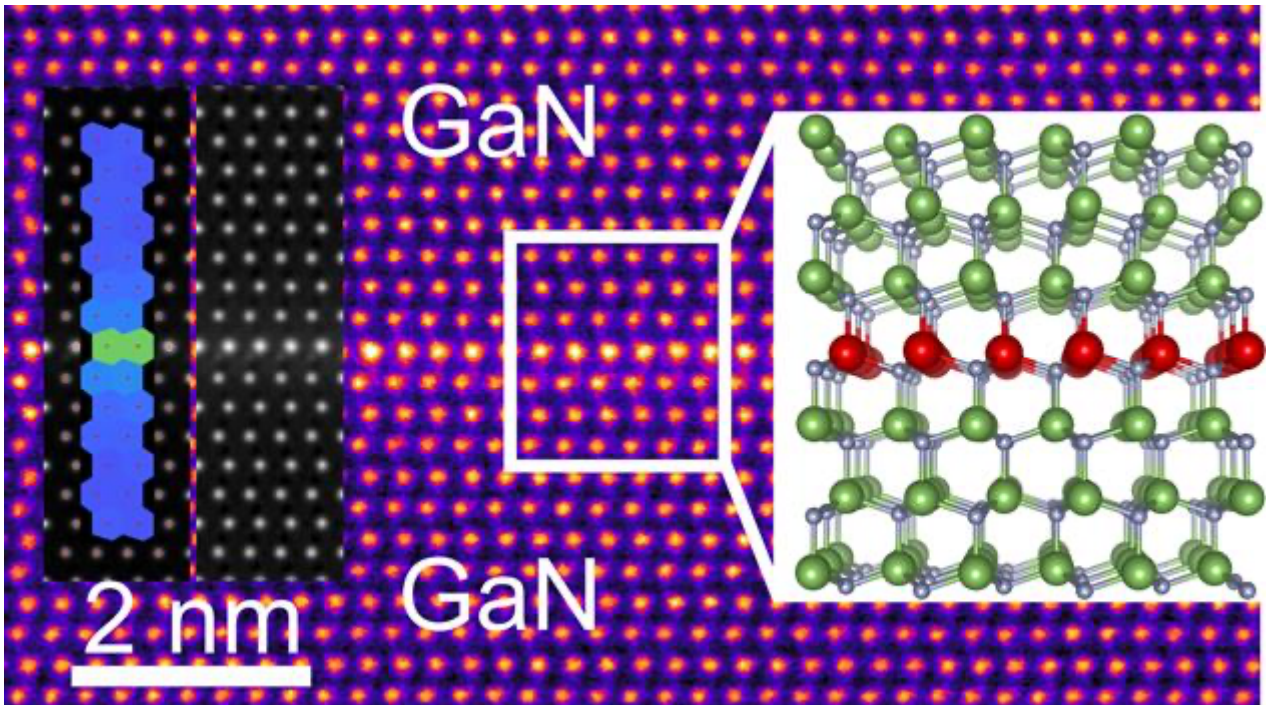


**Keywords:**

III-nitrides, Monolayers, Strain, Z-contrast quantification

**Reference:**

[1] Gorczyca et. al, J. Phys. Condens. Matter 30, 063001 (2018).
[2] Pan et. al, Appl. Phys. Lett. 105, 213503 (2014).
[3] Dimitrakopulos et. al, Appl. Phys. 123, 024304 (2018).
[4] Vasileiadis et. al, Sci. Rep. 11, 20606 (2021).
[5] Chatzopoulou et. al, Crystals 13, 700 (2023).

345

# Strain analysis comparison in complementary and nanosheet field-effect transistor devices: nanobeam vs Bessel electron diffraction

Paola Favia[1], Anabela Veloso[1], Geert Eneman[1], Ankit Nalin Mehta[1], Xiuju Zhou[1], Olivier Richard[1], Jef Geypen[1], Eva Grieten[1]
[1]Imec, Leuven, Belgium

Poster Group 2

Complementary Field-Effect Transistors (CFETs) represent a significant innovation in semiconductor technology currently drawing a lot of interest as they can be a potential solution for extending Moore's law by allowing considerably higher density compared to conventional CMOS. The novelty of these devices lies in the possibility to integrate different polarity transistors within a single structure, stacking nmos on top of pmos or vice-versa. That allows substantial density scaling benefits with enhanced performance and reduced power consumption. [1] CFETs represent an evolutionary step from the nanosheet transistors (NSFETs) which consist of several vertically stacked lateral nanosheets per device and where pmos and nmos devices are positioned next to each other on the same horizontal plane in the wafer instead of vertically atop one another as in CFETs. In both architectures, unlike finFET-based CMOS, in order to reduce their parasitics, inner spacers are introduced in-between the vertically stacked NS and prior to the source/drain (S/D) epitaxial growth, a flow addition which will also impact the S/D epi process. [2]

Strain engineering is a crucial technique for enhancing the mobility of conventional semiconductor devices. In general, channel strain, induced by the S/D in both conventional and novel CMOS, depends on the epitaxial layer composition used for the S/D (with SiGe typically used for pmos), its geometry and defectivity. Understanding the strain distribution within these structures is important for optimizing device characteristics. Previous studies on NSFET devices [2] demonstrated that the presence of inner spacers impacts S/D growth and, by consequence, the strain distribution induced in the channels. In this work, we evaluate and compare the channel strain distribution in aggressively scaled (CFET-NS) relative to more relaxed (NSFET) gate pitches, employing nanobeam electron diffraction (NBD) and Bessel diffraction [4] to discern the most apt technique for studying strain in these novel architectures.

TEM samples are prepared by focused ion beam lift-out technique. Strain analysis is performed by NBD and Bessel in a double corrected Titan3 G2 60-300 transmission electron microscope operating at 200kV. CFET and NSFET samples consist of fin-shaped structures of Si/SiGe layers. The sacrificial SiGe layers, destined later for etching to release the NS, are also recessed post-S/D recess to accommodate inner spacer deposition. CFET samples feature a single pmos Si channel sandwiched between SiGe50 S/D at the bottom and one nmos Si channel at the top, while the NSFET sample consists of a dual Si-channel pmos. Notable, the main difference between NSFET and CFET devices in this study lies in the gate pitch dimensions, with NSFET at 100nm and CFET at 50nm.

Strain profiles along the Si channels (indicated by blue arrows in Figure 1a and b) in double Si-channel NSFET (Figure 1a) and single Si-channel CFET (Figure 1b) devices, processed until after epitaxial SiGe S/D growth, are depicted in Fig1c and Fig.1d, respectively. Both single-level NSFETs and bottom NS of CFET exhibit tensile channel strains, a significant departure from traditional finFETs characterized by compressive strain. [3] This tensile strain originates from the lattice mismatch of the SiGe/Si multilayer stack in the fins, which persists after fin patterning. The introduction of inner spacers further amplifies tensile strain in the channels. Inner spacers lead to separate SiGe epitaxial growth from the bottom and lateral fronts, resulting in defects or air gaps at the interface where the three

growing fronts converge. In addition, CFET exhibits lower strain compared to NSFET likely due to their smaller S/D and gate pitch than in NSFETs. TCAD simulations could offer additional insight into local strain behavior in these devices. Furthermore, we perform a comparison between the NBD and Bessel techniques for assessing strain in CFET devices. As shown in Figure 1d, while the NBD technique reveals minimal or no strain, the Bessel method (dotted curves) enables measurable strain detection. As previously observed [5], the Bessel technique demonstrates superior sensitivity compared to NBD, becoming the preferred technique for strain evaluation in such innovative architecture devices.

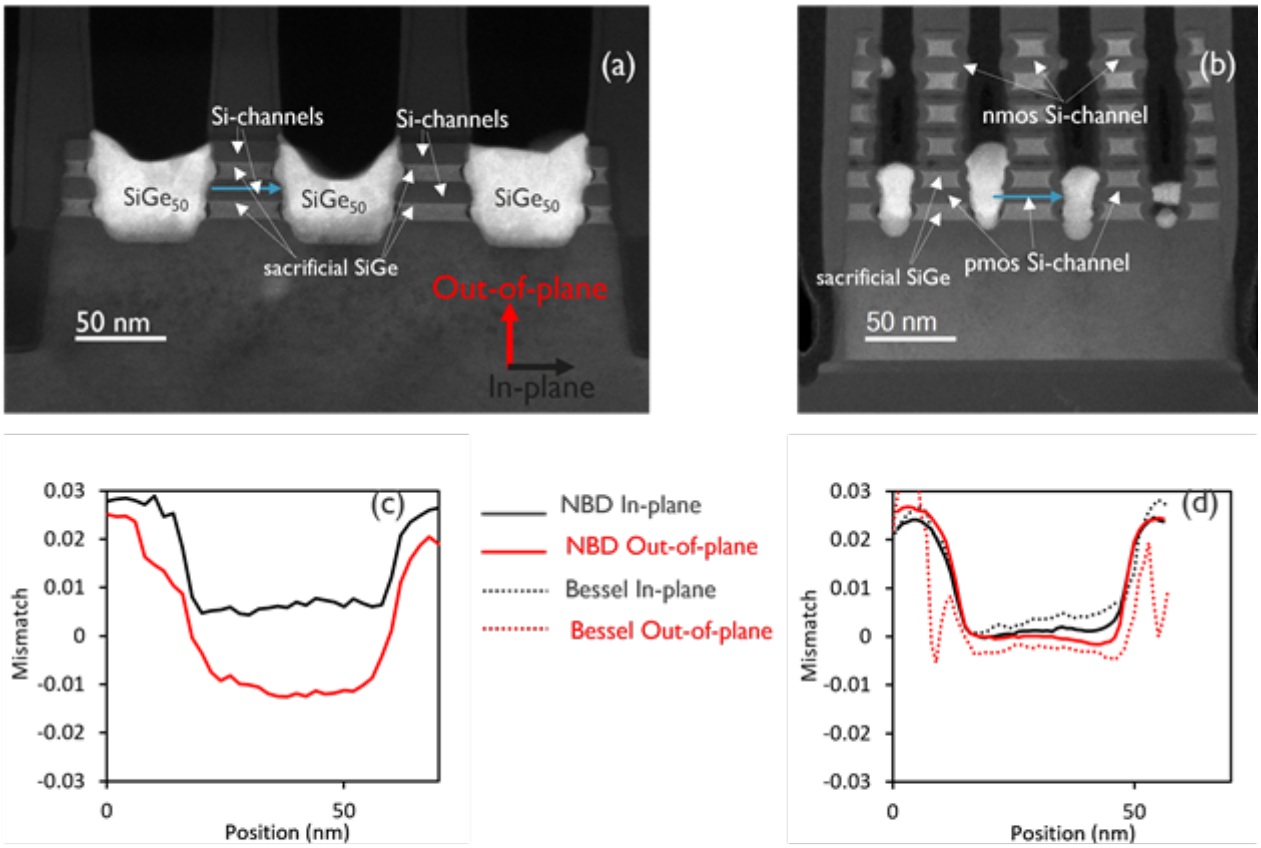


Figure 1 HAADF-STEM images of nanosheets (NSFET) with gate pitch of 100nm (a) and CFET-NS with gate pitch of 50nm (b). Corresponding mismatch along the Si channel (blue lines in a and b) for NS (c) and CFETs (d). NBD and Bessel are compared in case of CFET (d)

**Keywords:**

Strain, CFET, nanosheet-FET, NBD, Bessel

**Reference:**

1. J. Ryckaert et al., VLSI Tech. Dig., 2018, 141
2. A. Veloso et al., ICICDT, 2022
3. A. Veloso et al., IWJT023, 2023,
4. G. Guzzinati et al., Applied Physics Letters, 2019, 114/24
5. P. Favia et al., IMC20, 2023

382

# Atomic-scale Defects Critical to the Performance of Perovskite Solar Cells

Dr Weilun Li[1], Dr Mengmeng Hao[2,3], Dr Shanshan Ding[2,3], Mr Qimu Yuan[4], Prof. Michael Johnston[4], Prof. Lianzhou Wang[2,3], Prof. Joanne Etheridge[1,5,6]
[1]School of Physics and Astronomy, Monash University, Melbourne, Australia, [2]Nanomaterials Centre, Australian Institute for Bioengineering and Nanotechnology, The University of Queensland, St Lucia, Australia, [3]School of Chemical Engineering, The University of Queensland, St Lucia, Australia, [4]Department of Physics, University of Oxford, Clarendon Laboratory, United Kingdom, [5]Monash Centre for Electron Microscopy, Melbourne, Australia, [6]Department of Materials Science and Engineering, Monash University, Melbourne, Australia

Poster Group 2

Background
Metal halide perovskite semiconductors have emerged as a focal point of research due to their potential applications in solar cells, characterized by exceptional power conversion efficiencies, extended carrier lifetimes, reduced recombination rates, and cost-effective manufacturing techniques. Despite their considerable potential, challenges such as structural instability, ion migration, hysteresis, and defect intolerance are impeding their practical application. There is a critical need for a detailed atomic-scale understanding of the processes that control these properties and performance, however, atomic-scale electron microscopy studies have been relatively limited due to the extreme sensitivity of these materials to the electron beam. Here we develop and apply low dose electron microscopy methods to provide new insights into the structure-property relationships of these materials, including the role of nanoscale heterostructures, octahedral tilts, and point and planar defects, that are critical to their distinctive properties.

Methods
Transmission Electron Microscopy (TEM) offers valuable insights into the local atomic structure of materials. The application of TEM in the study of perovskite solar cells is extremely challenging due to their extreme sensitivity to electron irradiation, which can lead to rapid changes to their pristine structures with doses as little as a few electrons per Å2, far below conventional techniques, including STEM, EDX and EELS. To circumvent this limitation, we have developed and applied a suite of specialized TEM protocols encompassing specimen preparation, inert atmosphere transfer, diffraction pattern and image acquisition, and data interpretation.

Results
Our study reveals the sequence of subtle, atomic-level structural transformations leading to the degradation of mixed-cation Cs1-xFAxPbI3, beginning with the formation and ordering of ion vacancies and followed by a composition-dependent octahedral tilt. Additionally, we elucidate the atomic configurations of planar defects, including twins and Ruddlesden-Popper phases, and establish a correlation between these defects and solar cell performance. Our findings indicate that certain types of twin defects adversely affect solar cell efficiency, and their removal markedly enhances device performance.

Conclusion
The insights gained from our study into ion loss, ion migration, octahedral tilt modes, and the influence of A-cations shed light on the atomic-scale structural mechanisms responsible for the instability of perovskite solar cells. By correlating specific atomic defect structures, including planar defects, with optoelectronic properties, we outline strategies for the amelioration of perovskite solar cells through defect engineering, paving the way for their improved performance and stability.

**Keywords:**

Low-dose TEM, perovskite solar cells

**Reference:**

Reference
[1] Rothmann et al., Advanced Energy Materials 7.23 (2017): 1700912.
[2] Rothmann et al., Science 370.6516 (2020): eabb5940.
[3] Chen et al., Nature Communications 13.1 (2021): 5516.
[4] Li et al., Nature Communications 14.1 (2023): 8523.

This work was supported by Australian Research Council (ARC) grants DP200103070, FL220100202, FL190100139; EPSRC grants EP/T025077/1, EP/V010840/1, EP/W007975/1, ACAP and ARENA and used the Titan3 80-300 FEG-TEM (ARC LE0454166) & Spectra ϕ FEG-TEM (ARC LE170100118) in the Monash Centre for Electron Microscopy, a node of Microscopy Australia.

408

# NBED investigations of coaxial (Al,In,Ga)As nanowires

Alina Friemel[1], Dr. Tore Niermann[1], Dr. Laura Niermann[1], Dr. Paul Schmiedeke[2], Dr. Gregor Koblmüller[2], Prof. Dr. Michael Lehmann[1]
[1]Technische Universität Berlin, Berlin, Germany, [2]Technische Universität München, Munic, Germany

Poster Group 2

Background incl. aims
GaAs-based semiconductor nanowire (NW) lasers exhibit many advantageous properties for telecom-band data communications and sensing applications, like e.g. their ultra-compact size and their compatibility to Si-based photonics. In comparison to other III-V semiconductors, GaAs allows a fairly mature Au-free NW growth on Si. However, within the coaxially grown multiple quantum wells (MQW) the strain resulting from lattice mismatch accumulates during the growth. This problem can be mitigated by the introduction of an InAlGaAs buffer layer in between the GaAs core and the active region of the MQW-stack [1].
For process control and further engineering of NW laser structures, the strain in the resulting devices must be monitored. We report on strain investigation by means nanobeam electron diffraction (NBED) for such structures.

Methods
GaAs NW cores were grown via a vapor-liquid-solid growth mechanism on pre-patterned Si substrates along the [111] direction. Subsequently, an In0.3Al0.3Ga0.4As buffer layer, followed by an In0.3Ga0.7As QW, an In0.23Al0.23Ga0.54As barrier layer, and a GaAs cap layer were grown coaxially onto the side walls of the GaAs core. A cross-sectional lamella was prepared from the NW using focused ion beams.
HAADF, EDX and eventually NBED measurements were performed using a JEOL GrandArmF2 microscope, operated at 300kV. The NBED data was recorded using the Quantum Detector's Merlin detector.

Results
We applied a custom algorithm to determine the base vectors for the reciprocal lattice visible in the individual diffraction patterns for each scan point. Starting with an initial guess for the base vectors and the origin of the pattern, the algorithm consists of several steps: (i) for each lattice point spawned by the base vectors, a sub-region of the diffraction pattern is extracted; (ii) within each subregion the position of the reflection is determined with sub-pixel projection; (iii) a new set of base vectors is calculated by weighted linear regression, using the inverse precision from step (ii) as weights; (iv) unless the resulting set of base vectors has converged to a predefined precision, the algorithm is repeated from step (i) again. From the resulting base vectors of the reciprocal lattice observable in the diffraction patterns, the strain components can be calculated in reference to the GaAs core.
In comparison of the resulting strain data with finite element calculations short-scaled variations of the determined strain components are observed in areas where smooth strain components are expected. We attribute these variations to dynamical diffraction effects stemming from small specimen inhomogeneities created during preparation, for example from thickness variations. We discuss the influence of experimental and evaluation parameters, like the convergence angle or the method used to determine the reflection position, on the precision of the obtained strain components.

Conclusion

NBED generally allows the evaluation of strain data with nanometer precision. However, the resulting strain maps suffer from dynamical diffraction effects, which can be further mitigated by optimized experimental parameters and optimized evaluation procedures.

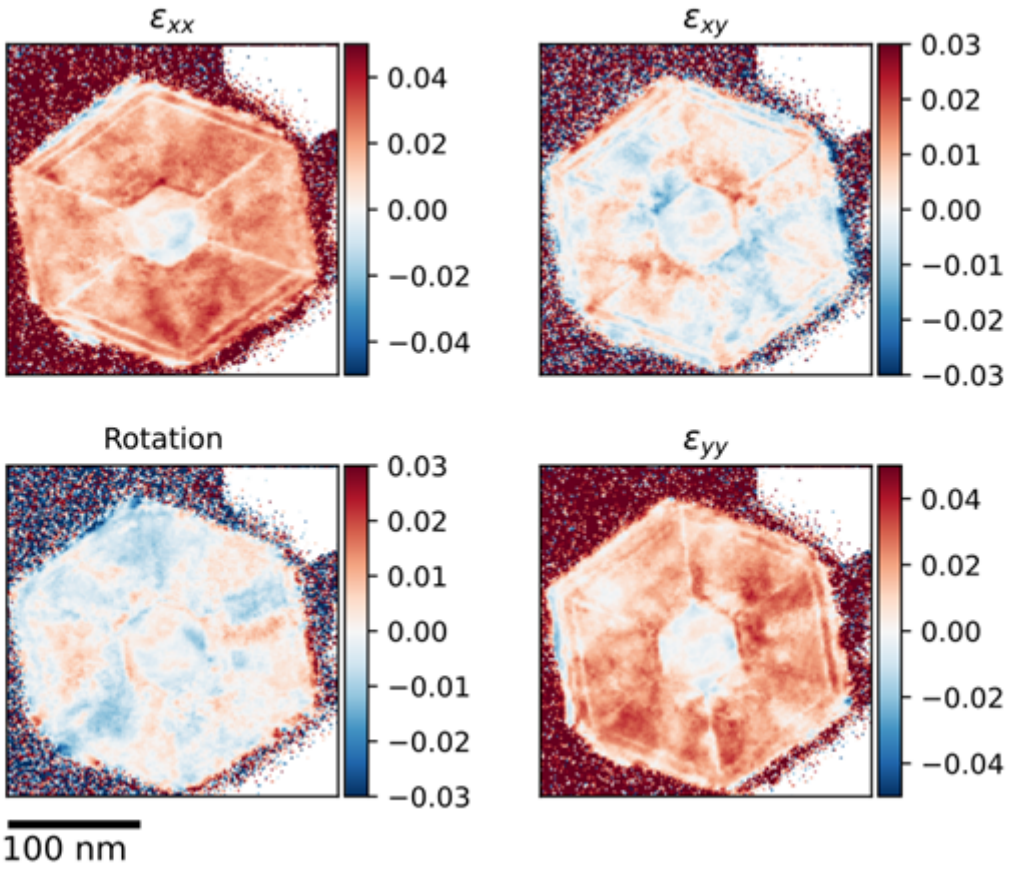


**Keywords:**

4D-STEM, NBED, Strain

**Reference:**

[1] P. Schmiedeke, A. Thurn, S. Matich, M. Döblinger, J. J. Finley, G. Koblmüller; Appl. Phys. Lett. 118, 221103 (2021)

446

# Electron microscopic investigation of photothermal laser printed ZnO nanoarchitectures

Kristian Kraft[1], Dr. Lukas Grünewald[1], Dr. Aina Quintilla[1], Dr. Erich Müller[1], Mr. Matthias Steurer[2,3,4,5], Dr. Paul Somers[3], Mr. Steven Kraus[2,3], Dr. Florian Feist[3], Dr. Bastian Weinert[3], Dr. Ben Breitung[3], Dr. Gabriel C. Marques[3], Prof. Dr. Stefanie Dehnen[3], Prof. Dr. Claus Feldmann[4], Prof. Dr. Christopher Barner Kowollik[3,5], Prof. Dr. Martin Wegener[2,3], Prof. Dr. Jasmin Aghassi[3], TT-Prof. Dr. Yolita Eggeler[1]
[1]Karlsruhe Institute of Technology (KIT), Laboratory for Electron Microscopy (LEM), Karlsruhe, Germany, [2]Karlsruhe Institute of Technology (KIT), Institute of Applied Physics (APH), Karlsruhe, Germany, [3]Karlsruhe Institute of Technology (KIT), Institute of Nanotechnology (INT), Karlsruhe, Germany, [4]Karlsruhe Institute of Technology (KIT), Institute of Inorganic Chemistry (AOC), Karlsruhe, Germany, [5]Queensland University of Technology (QUT), School of Chemistry and Physics, Brisbane, Australia

Poster Group 2

Background incl. aims
Multi-photon 3D laser printing of polymers can be used to create complex structures on the micro- and nanoscale [1,2]. This technique involves focusing a laser into a liquid ink, initiating a reaction that solidifies the material at the laser focus. While this technology has primarily been employed with polymers, recent developments aim to extend its capabilities to inorganic materials. However, these materials often need post-processing at elevated temperatures, facing challenges for multi-material architectures due to the potential impact on polymer structure [3]. Recent advances in the direct printing of semiconducting ZnO through hydrothermal synthesis offer a promising alternative since no post-processing step is needed [3]. This enables the direct laser printing of functional microelectronic devices, possibly combined with polymers. Using electron microscopy, we demonstrate that single crystalline ZnO can be printed on amorphous substrates, opening the possibility of new applications, e.g., non-linear properties for devices in optics. However, a deeper understanding of the growth of the ZnO crystals and the crystal rotation is necessary for further applications in microelectronic devices.

Methods
The ZnO structures are photothermally printed from a liquid ink (zinc formate and sodium citrate in dimethyl sulfoxide) onto a glass substrate using a focused continuous-wave laser (532 nm wavelength).
An FEI Helios G4 FX combined focused ion beam (FIB) and scanning electron microscopy (SEM) dual-beam system was used to characterize the crystallinity and crystal orientation of the printed ZnO with electron backscatter diffraction (EBSD) with a Bruker eFlash detector. EBSD requires a polished sample surface, for which we used FIB milling since the ZnO structure sizes are in the µm range. First, a Pt protection layer is deposited using the FIB. Then, the sample is tilted so that the sample surface is aligned at an angle of 10° relative to the Ga+-ion incidence. After polishing, the sample is tilted to a 70° effective sample tilt relative to the electron beam incidence for EBSD data acquisition. The Bruker Esprit software was used for the collection of the EBSD patterns, data processing, and indexing using the Hough transformation of EBSD patterns to detect the Kikuchi lines . Subsequent orientation analysis was performed using the MTEX toolbox for MATLAB [4], providing, e.g., inverse pole figure (IPF) maps.
Cross-section samples for scanning transmission electron microscopy (STEM) were prepared using the in-situ lift-out technique in an FEI Strata 400S Ga+-ion FIB/SEM instrument. A Pt protection layer was deposited by FIB to protect the underlying material during FIB milling. High-resolution high-angle annular dark-field (HAADF-) STEM images were acquired on an FEI Titan³ 80-300 at 300 keV. An FEI

Tecnai Osiris operated at 200 keV and equipped with ChemiSTEM technology was used for chemical analyses with energy-dispersive x-ray spectroscopy (EDXS). The EDXS data was processed using Bruker Esprit.

## Results

The continuous laser is focused at the interface of ink and substrate, resulting in the deposition of crystalline ZnO. Residual ink is removed by a solvent and the ZnO line is left (Fig. 1g).
SEM -EBSD was applied to analyze the crystallinity of ZnO (Fig. 1a). Single crystalline ZnO with the wurtzite crystal structure (P63mc) grows on the amorphous substrate for a 1 µm/s printing speed and a laser power of approximately 0.8 mW. The initial ZnO orientation is likely random since different lines show different initial orientations (not shown). In the IPF maps, one large ZnO single-crystal can be identified due to one single general color in each IPF map (Fig. 1b-d). However, a gradient of the color in all IPF maps indicates that the orientation of the crystal varies along the printed line, which means the crystal rotates along the printing direction. The corresponding color legend is presented in a triangle color legend (Fig. 1e). The orientation of the hexagonal lattice of ZnO at the start and the end of the printing is schematically shown (Fig. 1f). Earlier works have reported rotating lattice crystals in Sb-S-I glass system, by using different materials and laser printing parameters [5]. A total misorientation of 20° over the entire printed line (7.9 µm) is observed, corresponding to a linearly changing rotation rate of 2.6°/µm.
STEM-EDXS is used for chemical analysis of a cross-section TEM sample, which shows porous ZnO formed on silica (Fig. 1h). Nanometer-sized pores in the ZnO layer are visible as dark regions in the HAADF-STEM image result from the printing process (marked with arrows) . The Pt layer on the ZnO is deposited by FIB and acts as a protection layer during TEM lamella preparation. Also chemical analysis shows that the substrate layer below ZnO consists of 20 nm $SiO_2$ and the layer below is a 250 nm Si layer. The silica glass under the Si contains Ti. The atomic resolution image shows a small region of the single crystalline laser-printed ZnO, here viewed along the ZnO<2-1-10> zone axis orientation (Fig. 1i). The Zn atomic columns appear bright and the O columns are not visible due to the HAADF-STEM Z-contrast.

## Conclusion

To conclude, we provide an extensive electron microscopic examination of ZnO single crystals produced by photothermal laser printing at relatively low printing speed and laser power on an amorphous substrate. EBSD confirms the single crystallinity of ZnO with a rotating lattice over a distance of 7.9 µm. We will explore different printed geometries for a better understanding of the rotating lattice ZnO single crystals and the growth process regarding laser printing parameters. The aim will be to use such laser-printed semiconductor devices in microelectronics applications [3].

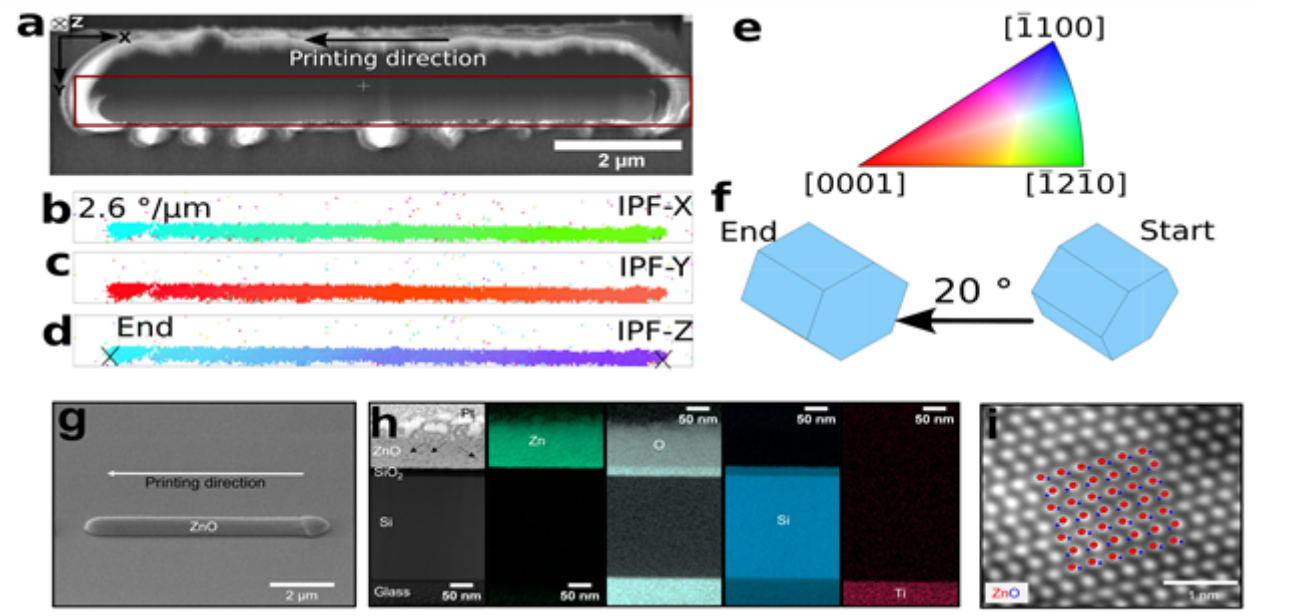


**Keywords:**

Electron microscopy
EBSD
laser-printing
ZnO

**Reference:**

1. L. Yang, Light: Advanced Manufacturing 2 (2021), 296–312. https://doi.org/10.37188/lam.2021.017
2. P. Mainik, C. A. Spiegel, and E. Blasco, Advanced Materials (2023), 2310100. https://doi.org/10.1002/adma.202310100
3. L. Yang et al., Nature Communications 14 (2023), 1103. https://doi.org/10.1038/s41467-023-36722-7.
4. F. Bachmann et al., Solid State Phenomena 160 (2010), 63-68. https://doi.org/10.4028/www.scientific.net/SSP.160.63
5. D. Savytskii et al., Science Reports 6 (2016), 36449. https://doi.org/10.1038/srep36449.

495

# Identification of the phases resulting from the thermal crystallization of Ge-rich GeSbTe alloys using EELS

Dr. Minh Anh Luong[1], Dr. Eloïse Rahier[1], Dr. Sijia Ran[1], Dr. Alain Claverie[1]
[1]CEMES-CNRS and University of Toulouse, 29 Rue Jeanne Marvig, 31055 Toulouse, France

Poster Group 2

Background incl. aims
Among many phase change materials, Ge-rich GeSbTe (GGST) alloys are of considerable interest due to their high thermal stability, a specification required for the next generation of embedded digital memories. This stability results from the fact that these alloys do not crystallize congruently but experience phase separation and finally form a polycrystalline material in which small grains of Ge and of several GeSbTe (GST) cubic phases coexist [1-3]. As all these phases, which have different chemical compositions, have almost the same lattice parameters, they cannot be differentiated by X-ray diffraction. On the other hand, as the grains are much smaller than the thickness of the lamella, the compositions measured by energy-dispersive X-ray spectroscopy (EDX) or electron energy loss spectroscopy (EELS) in the transmission electron microscope result from the overlapping of many small grains and do not give access to their individual stoichiometry (Figure 1). Herein, we report an efficient method to deduce the stoichiometry of the different phases of the grains which overlap by exploiting “pixel by pixel” EELS data and by extracting their characteristic Sb/Te ratio. Using this method, we show that the crystallization of the GST phase proceeds through the initial formation of cubic GeTe and its progressive enrichment in Sb during thermal annealing, ultimately leading to the formation of the well-known stable GST-225 phase.

Methods
A 100 nm-thick GGST layer was deposited by physical vapor deposition (PVD) onto a naturally oxidized 300 mm Si(100) wafer and covered by a 20 nm-thick TiN cap layer. The samples were annealed in a conventional furnace under nitrogen flux. Cross-sectional specimens were prepared by focus ion beam (FIB) technique operating with a 30 keV Ga ion beam and finally polished and cleaned at 2 keV–3 pA. High-angle annular dark-field (HAADF)-STEM and dual-EELS data were acquired on a probe corrected ARM JEM JEOL 200F microscope, operated at 200 kV. The convergence and collection angles for EELS were 29.6 and 75.9 mrad, respectively. The quantification process was carried out through the following steps: 1) the zero-loss spectrum is used to subtract the background and plural scattering signals caused by the specimen thickness, 2) high-loss elemental peaks are fitted using the Hartree-Slater model, after exclusion of the ELNES edges (about 50eV width) and 3), the Ge, Sb and Te ratios are normalized and the result obtained at each pixel is plotted in a ternary diagram for visualization.

Results
Figure 2 shows HAADF STEM images and corresponding plotted Sb/Te ratio for GGST samples, annealed at different temperatures and time durations. After 320°C/8h annealing, when the first GeSbTe cubic phase forms, the compositional data points spread along an almost horizontal line (Sb/Te = 0.05). The alignment of the pixels on such a horizontal line indicates that the compositions which are measured result from the superposition of pure Ge and almost pure GeTe grains in varying proportions, depending on the overall composition of the layer and statistical fluctuations. The vertical shift of this horizontal line upwards reflects the homogeneous distribution of Sb in the material and should be interpreted as being due to the presence of a third highly dispersed "phase" containing all the Sb. When annealing for longer times or at higher temperatures (320°C/16h, 400°C/30min and 400°C/3h), the Sb/Te ratio characteristic of the GST phase which is formed slowly

and progressively increases, from 0.05 (horizontal line) to 0.4, the signature of the well-known stable GST-225 phase. In the meantime, the horizontal shift due to dispersed Sb decreases. This shows that Sb, which was initially diluted in the matrix, progressively incorporates into the GeTe crystals during annealing (by substitution, necessarily on Ge sites). Moreover, some pixels point toward Sb-rich GST phases. Complementary TEM analysis shows these phases have the hexagonal structure, the most common being Sb2Te3. Pure Sb2 lamellas can also be identified by HAADF STEM imaging and EELS mapping, as shown in Figure 1.

Conclusions

We have thoroughly investigated the phases resulting from the thermal crystallization a GGST alloy using advanced transmission electron microscopy based techniques. While X-ray diffraction cannot differentiate the various phases found in the polycrystalline material due to their “close” lattice parameters, the careful analysis of the Sb/Te ratio obtained from pixelated EELS data gives access to the stoichiometry of the GST phases in the samples. Based on such analysis, we demonstrate that the thermal crystallization of GGST alloys proceeds through the initial formation of GeTe and Sb-poor GST grains which get progressively enriched in Sb during annealing until forming GST-326 (Sb/Te=0.33) and GST-225 (Sb/Te=0.4) grains. Moreover, excess of Sb and Te can be accommodated within Sb2 lamellas and Sb2Te3 hexagonal grains.

**Figure 1**

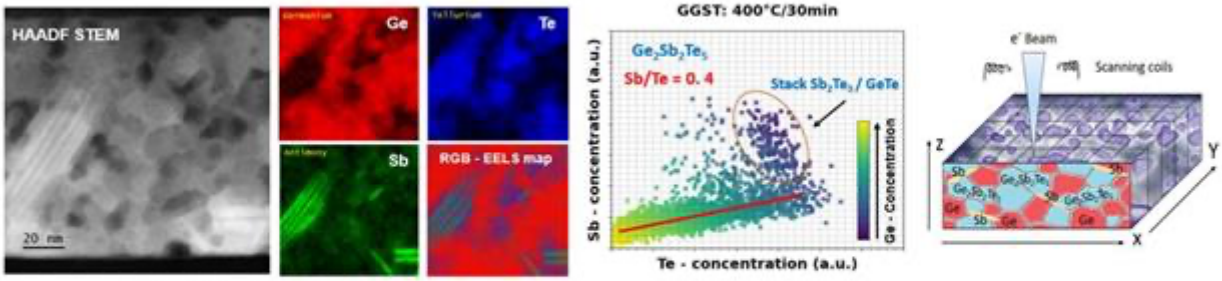


**Figure 2**

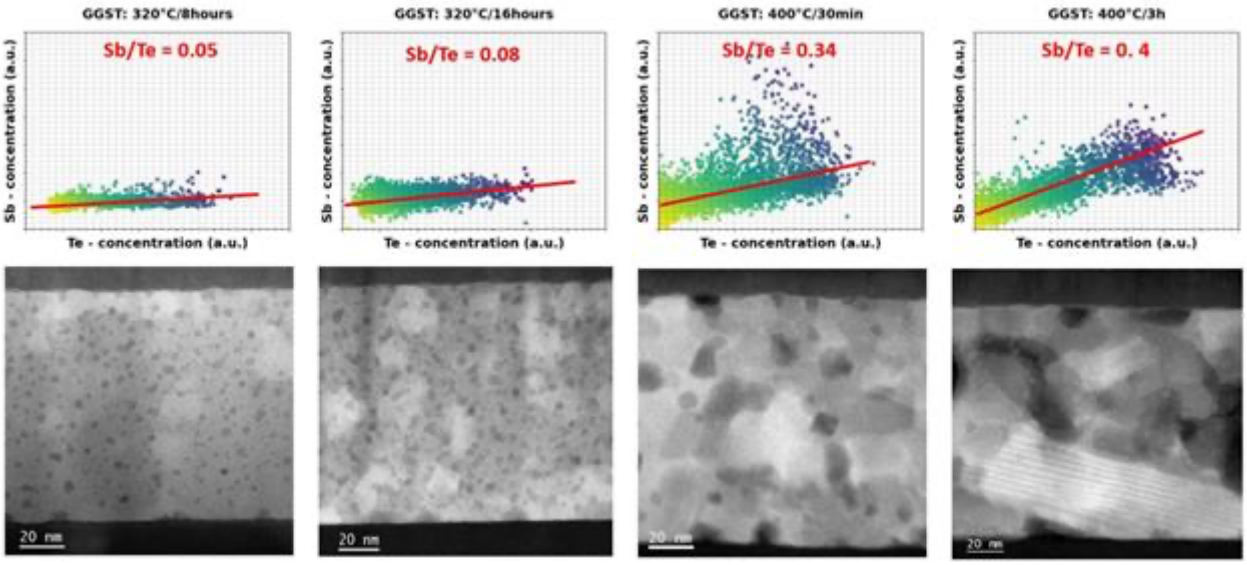


**Keywords:**

PCMs, GeSbTe, crystallization, EELS, TEM

**Reference:**

(1) Rahier et al. ACS Appl. Electron. Mater. 2022, 4 (6), 2682–2688.
(2) Rahier et al. Physica Rapid Research Ltrs 2023, 17 (8), 2200450.
(3) Luong et al. Physica Rapid Research Ltrs 2024, 2300421.

506

# Strain mapping and simulation of transistor structures in a 22nm FDSOI technology

Dirk Utess[1], Dominik Martin Kleimaier[1], Etienne Billan[1], Tashfain Youssuf[1], Zhixing Zhao[1], Thorgund Nemec[1], Dr. Moritz Andreas Meyer[1], Dr. Jochen Rinderknecht[1]
[1]GlobalFoundries, Dresden, Germany

Poster Group 2

Background & aims
With the advent of the AI/ML and 5G/Satellite internet era, modern electronic devices need to be operated with low energy consumption, high performance, radiation hardness and manufactured at low cost. One of the technologies is 22FDX offered by GlobalFoundries® which utilizes a fully depleted silicon-on-insulator (FDSOI) technique. Speed and power consumption of devices are improved accordingly. Introducing mechanical strain to transistor channels e.g. by epitaxial growth or process-induced pre-stressed overlayers or periphery layouts alters the crystal lattice and thus also the band structure of the semiconducting channel. As different requirements of strain for N- or P-type transistors e.g., along the direction of the channel, the characterization of strain in electronic devices is necessary, both for monitoring the intended engineered strain but also the unintended strain states. However, for verification as well as enhancing strain, FEM Simulation of Strain is crucial. The second part of this study focuses on the simulation of transistors. A detailed model is developed that includes mechanical and structural parameters. [1, 3]

Methods
Precession Electron Diffraction (PED) is a specialized technique in Transmission Electron Microscopy (TEM) employed to gather electron diffraction patterns while scanning across the designated region of interest. During the scanning process, the electron beam rotates around the central axis, while the beam itself is tilted at a specific angle. This results in a quasi-kinematical diffraction pattern, which facilitates the use of a more sophisticated algorithm for crystal structure determination. The strain simulation, based on the finite element method, started with a basic structural model and mechanical parameters. After validating this fundamental model with corresponding structures at the transistor size level, increasingly complex models were developed and subsequently verified. [2, 4]

Results
In this study, strain maps and graphs will be presented obtained from both experimental data using PED and simulated data from various transistor devices. These strain maps exhibit excellent agreement with each other as well as with electrical measurements. Furthermore, they enable the verification and identification of new stress elements, highlighting potential areas for improvement by adjusting structural dimensions and addressing distinct stress elements.

Conclusion
This holistic approach—combining simulation and measurement—enables a comprehensive understanding and optimization of strain effects in electronic components. It also promotes the progression of 22FDSOI technologies and beyond. Finally highlighting the Significance of Advanced TEM Techniques in the Semiconductor industry.

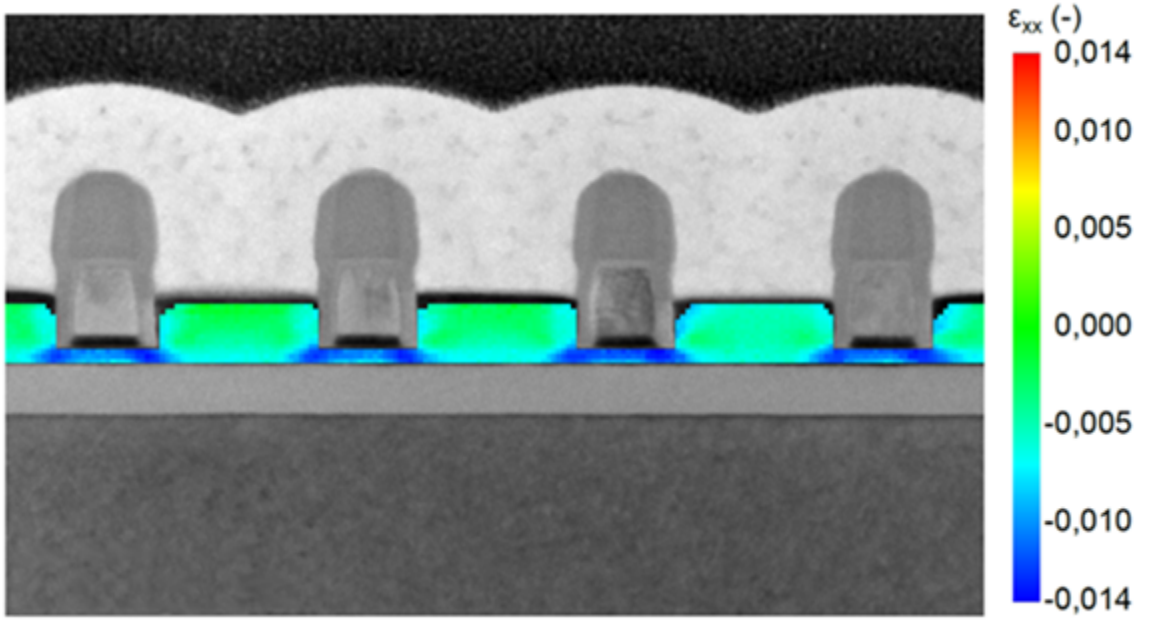


**Keywords:**

Strain, FDSOI, Transistor, Simulation, PED

**Reference:**

[1] D. Kleimaier, Z. Zhao, D. Utess, I. Saadat, F. Ravaux, K. Sloyan (2019). Strain mapping of transistor structures in a 22nm Fully Depleted Silicon-On-Insulator technology. CARAC 2019 -Advanced Material Characterization Workshop, Grenoble
[2] T. Yousuf: Impact of Strain Produced by Diverse Structures and Si1-xCx as Source/Drain Material on Electron Mobility in FDSOI Transistors using COMSOL Simulations and TEM Analysis of Real Models, Masterarbeit, TU Dresden, 2020
[3] J. Hoentschel, L. Pirro, R. Carter, M. Horstmann: 22FDX® Technologies for Ultra-Low Power IoT, RF and mmWave Applications. ISTE Science Publishing, London, 2019.
[4] NanoMEGAS SPRL: Precession Electron Diffraction Applications. Online resource. https://nanomegas.com/precession-electron-diffractionand-applications/
[5] R. Thomas, D. Benoit, L. Clement, P. Morin, D. Cooper. F. Bertin: Characterization of stress transmission from silicon nitride layer to transistor channel. Journal of Physics: Conference Series 326 (2011) 012058

558

# STEM-EELS unveils atomic stacking in 2D MoSe2 ECM memristors.

Dr Khalil El Hajraoui[1,2], Dr Andrea Capasso[3], Mr Guilherme Araújo[3], Dr Demie Kepaptsoglou[1,2], Prof Quentin. M Ramasse[1,4]
[1]SuperSTEM Laboratory, SciTech Daresbury, Daresbury, United Kingdom, [2]School of Physics, Engineering and Technology, University of York, York, United Kingdom, [3]International Iberian Nanotechnology Laboratory, Braga, Portugal, [4]School of Chemical and Process Engineering & School of Physics and Astronomy, University of Leeds, Leeds, United Kingdom

Poster Group 2

Background incl. aims
Memristors, short for 'memory resistors', are two-terminal electronic devices whose resistance can be modulated by previous voltage and current inputs. As such, memristors can act as both processing and storage units, enabling computation within the memory subsystem itself, with high-speed switching and low power consumption [1],[2]. An electro-chemical metallization (ECM) memristor consists of a solid electrolyte layer (acting as an ion conductor) sandwiched between an electrochemically active electrode (usually Cu or Ag) and an inert electrode (such as Au or Pt) [3]. The device switches to an ON state when a positive voltage induces the formation of a metallic filament between the electrodes (SET), maintaining this state until a negative voltage dissolves the filament (RESET) [4]. Recently, 2D materials such as hexagonal boron nitride (h-BN) and transition metal dichalcogenides (TMDs, e.g.,MoSe2 ) have been integrated into memristor designs [5]. With their atomic thickness and suitable electrical/electronic properties, these materials have the potential to enable ultra-low switching voltages, a critical feature for neuromorphic computing and artificial synapses. In this work, we study a vertical ECM cell composed of chemical vapor deposited (CVD) few-layers MoSe2 sandwiched between a Au bottom electrode (BE) and a Cu top electrode (TE) in a cross-bar configuration (5×5 µm2). The metallic electrodes were patterned by ultra-violet (UV) lithography, while the MoSe2 film was transferred to the device and selectively etched by O2 plasma prior to the TE deposition. I-V measurements, performed using a two-terminal configuration, demonstrated bipolar resistive switching with SET and RESET voltages of 0.75V and - 0.95V, respectively, corresponding to the low and high resistive states (LRS, HRS) (see Fig. 1a). This macroscopic observation suggests the successful formation of conductive filaments (CFs) between the two electrodes.

Methods
To visualise the CFs formed in the cross-bar device, focused ion beam (FIB) lamellae were prepared from the operated devices (that demonstrated electrical switching) in a Hitachi Ethos NX5000 dual FIB-SEM instrument. Standard FIB protocol for low-kV STEM observations was followed to prepare these lamellae with extra care on reducing the ion milling time at 30kV to limit Ga+ damage on the MoSe2 film. Final 1kV argon (Ar+) polishing was applied for 4 min directly within the FIB-SEM instrument using a dedicated 'third beam' Ar+ source to remove remnant surface damage from the low-kV milling. These lamellae were investigated at atomic resolution in an aberration-corrected Nion UltraSTEM100 dedicated Scanning Transmission Electron Microscope (STEM) operated at 60kV. The instrument is equipped with a cold field emission source with a nominal energy spread of 0.3 eV. STEM High-angle annular dark field (HAADF) images were acquired by rastering a 1Å corrected probe with a beam convergence half-angle of 30 mrad across the interfaces. The EELS spectrum images (SI) were acquired with a collection half-angle of 44 mrad using an Enfina EEL spectrometer retro-fitted with a MerlinEM direct electron detector optimized for EELS acquisition at low acceleration voltages.

Results

The HAADF images of the devices confirmed the presence of clean Cu/MoSe2/Au interfaces in most of the investigated regions, as displayed in Fig. 1b-d, where the atomic-scale crystalline structure of each material is apparent. This confirms the successful fabrication process and the absence of residues at the interfaces, resulting in the expected electrical contact between the layers [5]. Furthermore, the HAADF image in Fig. 1d shows the hexagonal order confirming the semiconducting character of the CVD-grown MoSe2 film, essential for a good ohmic-contact at the TE/MoSe2 interface in HRS. However, a number of sections of the interface between the MoSe2 and the respective BE and TE showed a non-perfect adhesion, resulting in 'gaps' seen as darker contrast along the interface between the materials (see Fig. 1b-d). EELS maps were acquired across the interfaces to clarify their chemistry at the atomic scale, and to identify the location of Cu after the biasing cycles undergone by the devices. The Cu and Se EELS maps in Fig. 1f, obtained from integration of the Cu and Se L2,3 edges, show that Cu appears to have diffused into the MoSe2 layers and beyond. A continuous Cu layer is observed at the BE surface, filling the 'gap' between the MoSe2 and the BE. The presence of Cu in MoSe2 layer could be linked to the formation of Cu CFs during the HRS and LRS cycles, while the Cu layer at the BE surface might be ascribed to the fabrication process. For the latter, the presence of discontinuities in the MoSe2 film (possibly connected to its morphology and/or transfer process) could allow the infiltration of Cu during the TE sputtering process.

Conclusion

Cu diffusivity is a big hurdle in device fabrication. Our results highlight its presence at the atomic scale, even in macroscopically functional devices. A number of solutions could be proposed to limit its effect starting by using a less energetic deposition process such as electron-beam deposition process, a low-cost process compatible with industrial large production. Furthermore, our findings show that atomic STEM-EELS characterisation of 'real-life' 2D MoSe2 based memristor devices is possible, providing new insights and paving the way towards a better understanding of memristor's working mechanisms and a potential optimisation in the device fabrication process.

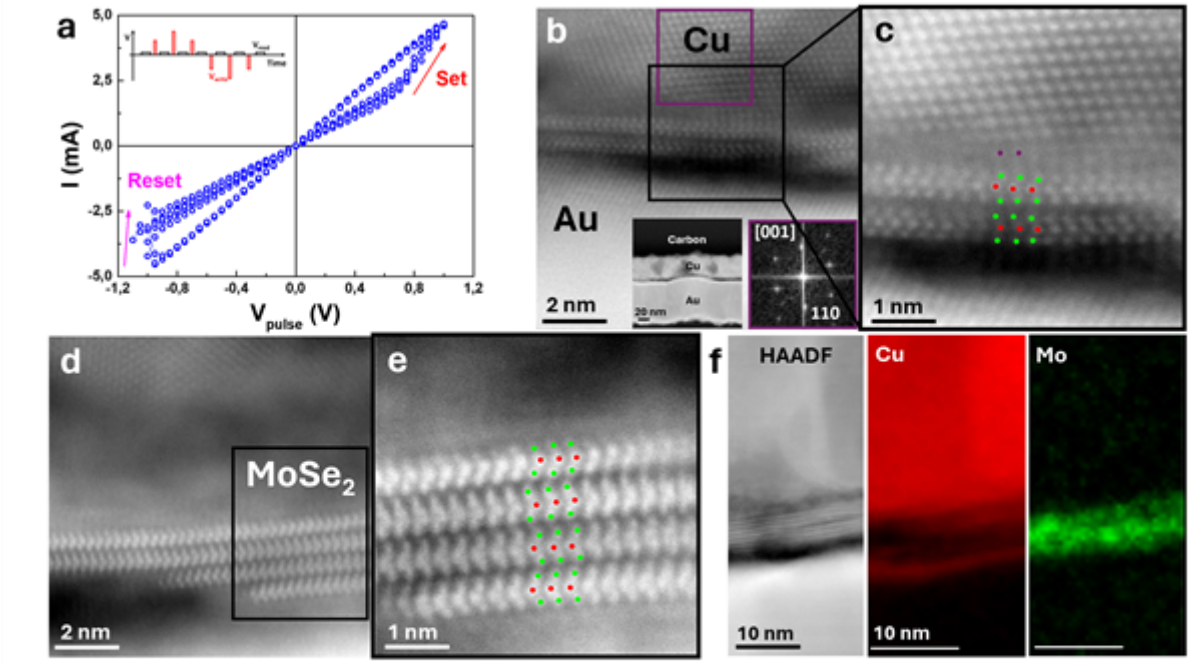


Fig.1: (a) Representative I–V curve of the device (5 DC sweeps). The curve clearly shows the bipolar resistive switching with a set voltage at ~ 0.75 V and a reset voltage at ~ −0.95 V. The inset shows the schematic of the pulsed IV measurements with the 1 ms write pulses (red), intercalated by 10 ms/50 mV read pulses (black) (b) HAADF image of the Cu/$MoSe_2$/Au interface showing a Cu grain along [001] zone axis as confirmed by the diffractogram (FFT), inset. (c) A magnified image of the highlighted region with a black square in *(a)* showing the transition from the Cu grain to the 2H-$MoSe_2$. (d),(e) HAADF images of the Cu/$MoSe_2$/Au interface showing the 2H-$MoSe_2$ stacking between the two metal contacts. (f) HAADF image and EELS maps of Cu and Se showing the diffuse interface at the TE/$MoSe_2$ interface and the presence of Cu layer above the Au BE.

**Keywords:**

EELS, Memristors, 2D materials, Semiconductor

**Reference:**

[1] W. Huh, D. Lee, and C.-H. Lee, “Memristors Based on 2D Materials as an Artificial Synapse for Neuromorphic Electronics,” Adv. Mater., vol. 32, no. 51, p. 2002092, Dec. 2020, doi: https://doi.org/10.1002/adma.202002092.

[2] G. Cao et al., “2D Material Based Synaptic Devices for Neuromorphic Computing,” Adv. Funct. Mater., vol. 31, no. 4, p. 2005443, Jan. 2021, doi: https://doi.org/10.1002/adfm.202005443.

[3] D. Ielmini, “Modeling the Universal Set/Reset Characteristics of Bipolar RRAM by Field- and Temperature-Driven Filament Growth,” IEEE Trans. Electron Devices, vol. 58, pp. 4309–4317, 2011, [Online]. Available: https://api.semanticscholar.org/CorpusID:31394956.

[4] I. Valov, R. Waser, J. R. Jameson, and M. N. Kozicki, “Electrochemical metallization memories—fundamentals, applications, prospects,” Nanotechnology, vol. 22, no. 28, p. 289502, 2011, doi: 10.1088/0957-4484/22/28/289502.

[5] J. Fernandes et al., “Bipolar Resistive Switching in 2D MoSe2 Grown by Atmospheric Pressure Chemical Vapor Deposition,” ACS Appl. Mater. Interfaces, vol. 16, no. 1, pp. 1767–1778, Jan. 2024, doi: 10.1021/acsami.3c14215.

647

# Effects of electron cascade and lamella preparation on InGaN quantum well recombination dynamics

Nika van Nielen[1], Delphine Lagard[2], Cleo Santini[3], Florian Castioni[4], Robin Cours[3], Andrea Balocchi[2], Teresa Hungria[5], Andrey Tsatsulnikov[6], Alexei Sakharov[6], Andrey Nikolaiev[6], Nikolay Cherkashin[3], Luiz Tizei[4], Albert Polman[1], Sophie Meuret[3]
[1]AMOLF, NWO, Amsterdam, Netherlands, [2]LPCNO, CNRS, Toulouse, France, [3]CEMES, CNRS, Toulouse, France, [4]Laboratoire de Physique des Solides, CNRS, Orsay, France, [5]Centre de Microcaracterisation Raimond Castaing, CNRS, Toulouse, France, [6]Ioffe Institute, , Russia

Poster Group 2

Background: InGaN/GaN quantum wells (QWs) have garnered significant attention for LED applications due to their high quantum efficiencies in the ultraviolet/visible range and emission tunability with indium content, among other factors. However, the growth of QWs with high indium content encounters issues with indium phase separation, resulting in structural changes and inhomogeneous light properties. This can be controlled via growth stopping, forming quantum dot like islands that behave as localized emitters [1,2]. Furthermore, subsequent etching reduces the strain-induced quantum Stark effect present in majority of such structures. Due to its deep subwavelength spatial resolution and broadband frequency components enabling coupling to high-energy optical transitions, cathodoluminescence nanoscopy (CL) has emerged as the ideal tool to study such high-bandgap semiconductor systems [3] and characterize their nm-scale features and defects. Despite it being a popular characterisation technique, the impact of the electron cascade on the sample, as well as the optoelectronic effects of thinning bulk samples into lamella, as is commonly performed for studies in a transmission electron microscope (TEM), have hitherto not been studied systematically. In this work we aim to confront this using a comprehensive study comparing time-resolved (TR) scanning electron microscope- (SEM) based CL, TEM-CL, and TR-photoluminescence (PL) measurements.

Methods: We utilized CL imaging with both 5 and 150 keV electron beams to acquire hyperspectral maps on InGaN/GaN QWs. Additionally, employing a beam blanked SEM with pulse lengths ranging between 30 – 100 ps, we conducted time correlated single photon counting and extracted luminescence decay maps as a function of position, temperature, and wavelength. The samples subsequently underwent preparation as lamella using Ga-based focused ion beam milling, after which the same measurements were performed. These measurements were compared to the decay maps obtained via an ultrafast photoemission TEM, along with decay traces from analogous samples acquired using TR- PL at liquid helium to room temperatures.

Results and Conclusions: We show that despite the energy density deposited by a 5 keV electron beam being an order of magnitude larger than that deposited by a 150 keV beam, the probability of exciting higher energy localized emitters, seen in the RGB fitted hyperspectral map in the graphic, is reduced due to the size of the electron cascade. The recombination dynamics of carriers, however, are comparable, with two major lifetime components of around 100 ps and 1.5 ns, as well as a delay in the rise time of the lower energy component of the emission. Interestingly, the TR-PL results indicate shorter lifetime components of 30 and 120 ps, when usually lifetimes in PL are reportedly longer than in CL. We present a model describing the recombination dynamics measured and the nuances between the different experimental techniques and respective results.

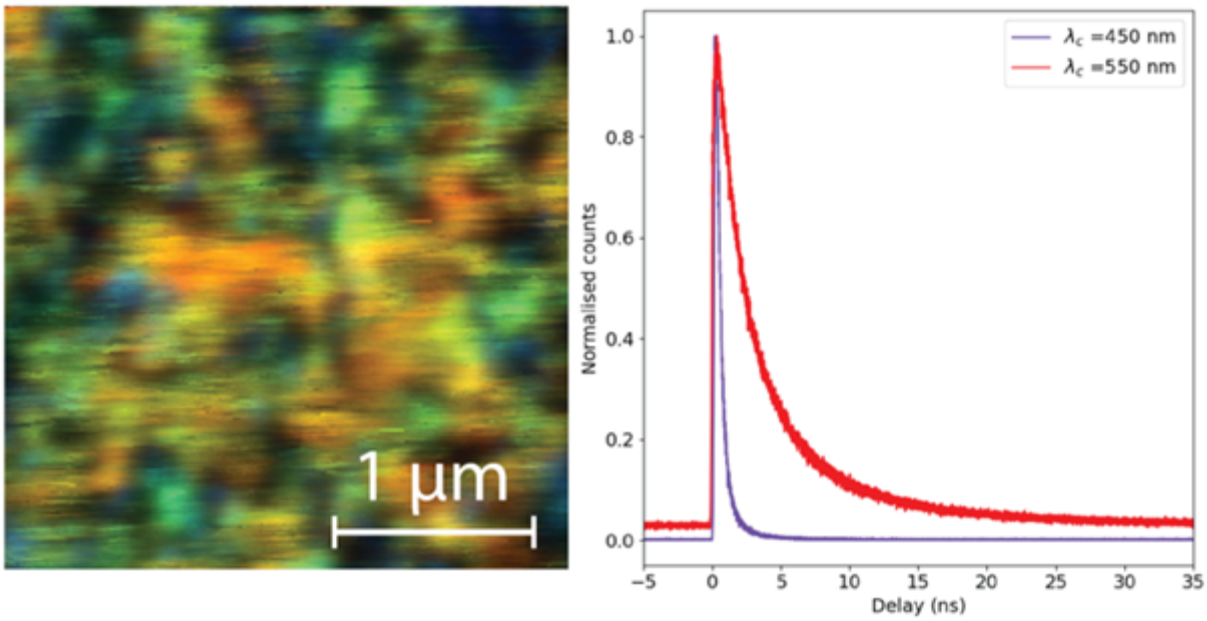


Left: plane-view hyperspectral CL map of the QW structure at 5 keV, fitted to RGB values in the window $\lambda = 500 \Delta 75$ nm.
Right: averaged and normalized TR-CL decay traces filtered at 450 Δ 40 nm and 550 Δ 40 nm.

**Keywords:**

InGaN heterostructure, recombination dynamics, cathodoluminescence

**Reference:**

[1] A. F. Tsatsulnikov. Science of Adv. Mater., 2015, 7 (8), 1629-1635
[2] D. Barettin. Nanomaterials 2023, 13, 1367
[3] S. Meuret. Ultramicroscopy 2019, 197, 28-38

679

# The effects of solution processing methods on halide perovskite nanostructure

Dr Alexandra Sheader[1], Dr Ryley Ratnasingham[2], Dr Nakita Noel[1]
[1]University of Oxford, Oxford, UK, [2]Eindhoven University of Technology TU/e, Eindhoven, Netherlands

Poster Group 2

Background:
Over the last decade, hybrid lead halide perovskite (LHP) materials have emerged as auspicious candidates for next-generation thin-film photovoltaics. This is largely due to both impressive optoelectronic properties and photovoltaic power conversion efficiencies, making them ideal for next-generation solar applications. Within this class of materials, formamidinium lead triiodide ($FAPbI_3$)-based perovskites are of particular interest due to their near-ideal bandgaps and improved thermal stability [1]. However, the photoactive (α-) phase of $FAPbI_3$ is only meta-stable at room temperature, and a variety of compositional tuning and additive-based approaches have therefore been employed to stabilise this phase.

While a range of methods can be used to fabricate LHP thin films, the most common of these is one-step spin coating. Precursor salts may be dissolved in a range of solvents to form a precursor ink, into which additives that improve film properties and stability may be incorporated. However, little is known about the effect of both solvent choice and additives on film nanostructure. This ultimately limits the practical application of LHPs in devices, as higher performance materials tend to be less stable. Understanding how precursor ink chemistry affects thin film crystallisation can thus inform improvements in long-term stability of films and devices, and is pivotal to improving this technology moving forward.

Methods:
In this work, we examine 'neat' $FAPbI_3$ films prepared via different solution processed routes including films prepared from the conventional precursor salts formamidinium iodide and $PbI_2$ and single-crystal precursors in solutions of 4:1 DMF/DMSO and 4:1 DMF/NMP, both with and without the addition of a 40% MACl additive.

High-resolution transmission electron microscopy (HRTEM) is used to elucidate the nanoscale structure of these films at the atomic scale. However, $FAPbI_3$ is highly susceptible to electron beam-induced damage; doses in excess of 100e-/Å$^2$ induce degradation into $PbI_2$ indistinguishable from that natively present in the film [2]. Here, all HRTEM is performed at doses below this critical threshold to ensure beam-induced effects are minimised.

Results:
While bulk characterisation data suggests that these varied approaches to $FAPbI_3$ film formation result in structurally the same material (albeit with varying levels of electronic defects and morphological film changes) [3], HRTEM shows at the nanoscale these films exhibit significant structural and compositional differences. Figure 1(a) shows a typical low-dose HRTEM image of a $FAPbI_3$film prepared from conventional precursor salts in DMF/DMSO. The FFT of this image (Figure 1(b)) shows poor agreement with spacings expected for α-$FAPbI_3$(red rings) and the 2H-polytype of $PbI_2$ (blue rings). In comparison, the HRTEM image of a single-crystal precursor sample in the same solvent system and the corresponding FFT (Figure 1c,d) shows good agreement with the spacings

expected for the photoactive perovskite phase. We attribute these differences to the presence of unreacted precursor material and the presence of non-photoactive $FAPbI_3$ polytypes.

It has been previously suggested that in some more structurally stable compositions, degradation in these materials occurs as a result of the inclusion of various unwanted $FAPbI_3$ polytypes during crystallisation [4]. Our HRTEM images show direct evidence of these phases, and in combination with other characterisation techniques support the suggestion that the inclusion of these undesirable phases can be controlled and ultimately eliminated through careful modulation of the precursor ink chemistry. By using a single crystal precursor we have been able to achieve better precursor ink purity, which results in films with significantly reduced structural disorder (evidenced by lower Urbach energies, as shown in Figure 1e,f). In this work, we link these observations directly to nanostructural changes visible in the HRTEM data.

Conclusions:
Precursor ink chemistry undoubtably affects LHP thin-film composition and structure. We show a direct link between these properties and laboratory-based results through the use of low-dose HRTEM. These links provide an important stepping stone on the path to truly understanding precursor ink chemistry, which ultimately may be the key to perfecting the crystallisation of LHPs.

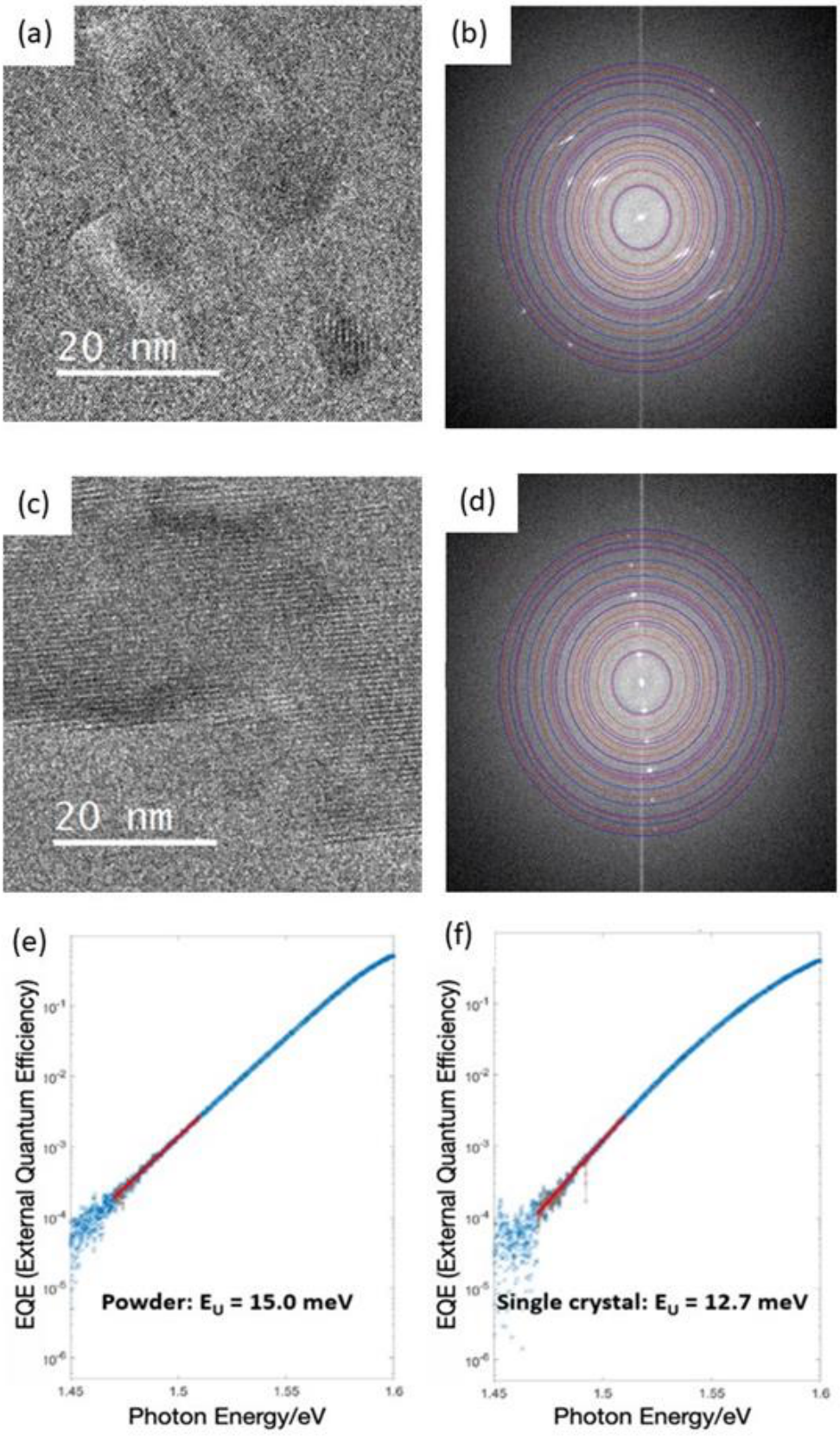
(a)
20 nm
(b)
(c)
20 nm
(d)
(e)
EQE (External Quantum Efficiency)
Powder: $E_U$ = 15.0 meV
Photon Energy/eV
(f)
EQE (External Quantum Efficiency)
Single crystal: $E_U$ = 12.7 meV
Photon Energy/eV

**Keywords:**

perovskites, photovoltaics, low-dose, HRTEM, STEM

**Reference:**

[1] G. E. Eperon et al., Energy Environ. Sci. 2014, 7 (3), 982–988
[2] M. Rothmann et al., Science 2020, 370, eabb5940
[3] K. A. Elmestekawy et al., ACS Energy Lett. 2023, 2543–2551
[4] S. MacPherson et al., Nature 2022, 607

730

# Analysis of molecular packing and nanoscale atomic variation in polymer semiconductors

Sang Pham[1], Sean Collins[1,2]
[1]Bragg Centre for Materials Research & School of Chemical and Process Engineering, University of Leeds, Leeds, United Kingdom, [2]School of Chemistry, University of Leeds, Leeds, United Kingdom

Poster Group 2

Background incl. aims
Conjugated polymers are an important class of organic light emitting diodes (OLEDs) and organic solar cells (OSCs). These materials are predominantly semi-crystalline or amorphous with intricate molecular packing and mixed variety of structural orders and disorders [1]. The susceptibility of these materials to 'burn-in degradation' [2] can induce blend-demixing and photo-induced ordering/disordering [3], thereby resulting in the performance losses of the devices [4]. Controlling this performance degradation during operation necessitates an understanding in changes in chemical structures and structural disorders at the nanoscale – the length scale commensurate with the transport of charge carriers. Yet direct nanoscale characterisation is limited for polymer semiconductors and their associated devices due to the irreversible changes in these materials structure when exposed to high-energy ion and electron beam conditions [5]. Here, we advance the structural characterisation of polymer semiconductors, whether in the form of free-standing films or cross-sectioned lamella, using low-dose four-dimesion scanning transmission electron microscopy (4D-STEM), enabling the analysis of the molecular packing, crystallinity, and atomic arrangement in the polymer semiconductors in response to temperature and ion milling-induced damage.

Methods
Low-dose 4D-STEM analysis was conducted using established nanobeam scanning electron diffraction alignment at electron Physical Science Imaging Centre (ePSIC), Diamond Light Source. In particular, Merlin-Medipix detector and <1 mrad convergence semi-angle with 1-2 pA in probe current at 300 kV were used to minimize radiolytic damage. We obtained data at a range of camera lengths to enable both mapping of crystalline domains from Bragg scattering as well as reciprocal space (variance measures) and real space electron Pair Distribution Function (ePDF) analysis of disordered and amorphous regions. The materials under examination were free-standing polymer films (F8:F8BT, 1:1), prepared by spin-coating onto PDOT:PSS/ITO/Glass substrates. Subsequently, the multi-layered sample was submerged in deionized water, and the F8:F8BT films were floated onto carbon support films for 4D-STEM analysis. Additionally, we developed cryo-Focused Ion Beam (cryo-FIB) protocols to facilitate the structural examination of the cross-sectioned device model, Glass/ITO/PDOT:PSS/F8:F8BT (1:1).

Results
The developed techniques reveal the formation of nano-crystalline domains in the F8:F8BT films after heat treatment. These domains are attributed to the crystallisation of F8 polymers, as evidenced by indexing some diffraction patterns aligning along the zone axis. Additionally, ePDF analysis allows us to characterise the atomic structures in amorphous areas with varying contrast. The analysis indicates that there were no chemical changes in the F8:F8BT blends induced by temperature. However, partial phase segregation occurred, as also supported by low-dose EELS analysis. We extended these analyses to a cross-sectioned device model prepared by cryo-FIB, and the findings demonstrate that our cryo-FIB protocol preserves the crystalinity of the polymer blends. ePDF shows that cryo-FIB milling does not alter the chemical structures of the films, i.e. intramolecular structure, but does affect the intermolecular arrangement.

Conclusion

The developed electron microscopy techniques enable the characterisation of microstructures and nanoscale atomic arrangements in beam-sensitive polymer semiconductors, paving a pathway for examining phase segregation and chemical changes resulting from the burn-in degradation. By doing so, effective strategies can be developed to minimise structural degradation in polymer semiconductors, thereby preventing performance losses during operation.

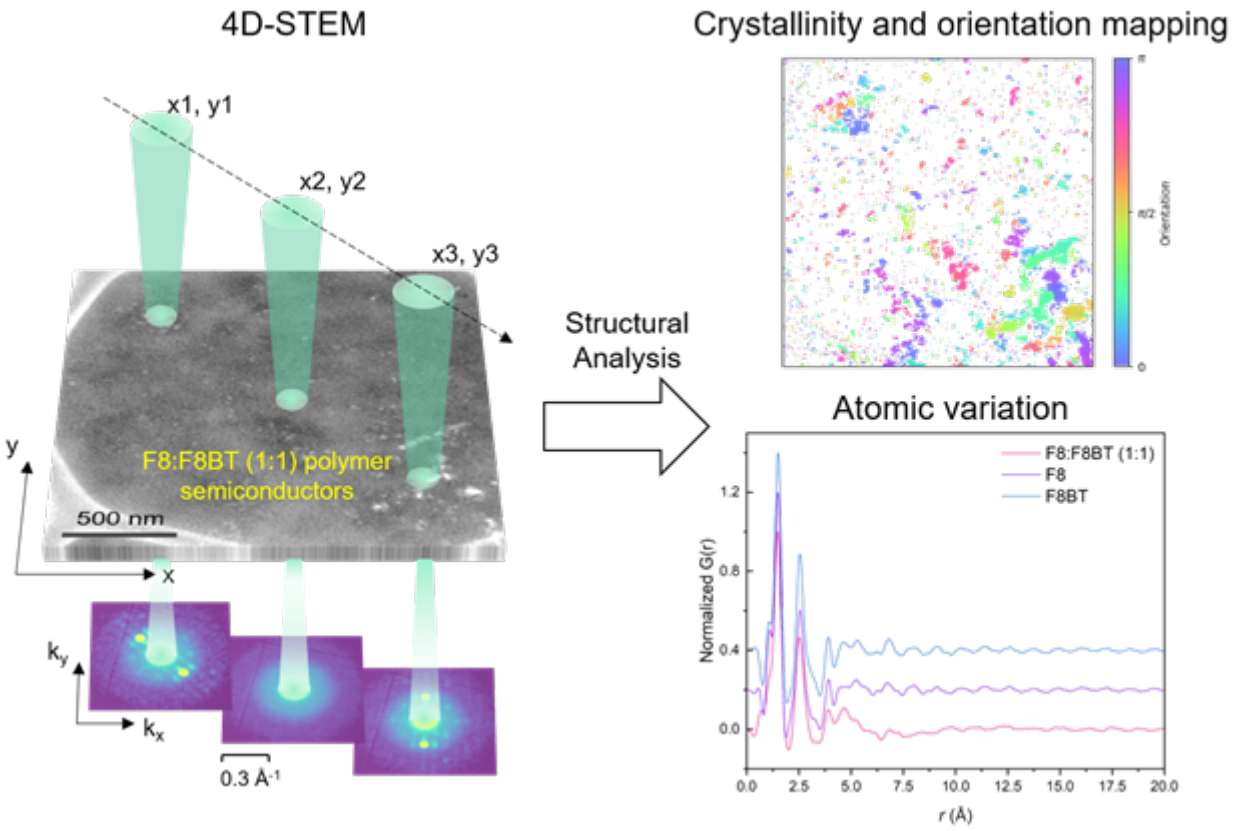


**Keywords:**

Polymer semiconductors, 4D-STEM, ePDF, cryo-FIB

**Reference:**

[1] L. Ding et al. Chemical Reviews. 2023, 123, 12, 7421–7497; [2] L. Duan et al., ACS Appl. Mater. Interfaces 2020, 12, 24, 27433–27442; [3] N. Li et al., Nat. Commun. 2017, 8, 14541; [4] L. G. Kaake et al. J. Phys. Chem. Lett. 2010, 1, 3, 628–635; [5] J. Donohue et al. iScience, 2022, 25, 103882.

741

# Characterization of 2DEG on WG semiconductors through sub-sampled 4DSTEM

Dr Giuseppe Nicotra[1], Dr Gianfranco Sfuncia[1], Dr Alex Robinson W[2], Dr Daniel Nicholls[3], Mr Jack Wells[2,3], Dr Antonio Mio M[1], Mr Corrado Bongiorno[1], Dr Cettina Bottari[5], Dr Salvatore Adamo[5], Dr Alfio Russo[5], Dr Santi Alessandrino[5], Prof. Nigel Browning D[4], Dr Corrado Spinella[1]
[1]CNR-IMM zona industriale strada VIII n.5, Catania, Italia, [2]SenseAI Innovations Ltd, Liverpool, UK, [3]Distributed Algorithms Centre for Doctoral Training, Liverpool, UK, [4]University of Liverpool, Liverpool, UK, [5]STMicroelectronics, Catania, Italy

Poster Group 2

Wide-bandgap (WBG) materials such as gallium nitride (GaN) are better candidates for fabricating power switches and high-frequency transistors than conventional Silicon-based technology. At the interfaces of a high mobility transistor heterojunction (HEMTs) such as that between AlGaN/GaN, in addition to the formation of a strained zone which increases the electronic mobility of the charges located there, a strong polarization effect is created as well. Such polarization causes band bending, including the Fermi level, at the AlGaN/GaN interface resulting in the accumulation of electric charges and the formation of a very electron-rich two-dimensional gas (2DEG). 2DEG contributes to the outstanding performance of AlGaN/GaN based HEMTs and can achieve a sheet carrier concentration close to the interface, well in excess of those observed in other III – V material systems.[1]. The ability to reveal the 2DEG in real space by TEM's conventional techniques would be desirable, but up to now has been very challenging to accomplish due to an unavoidable strong diffraction contrast formation at the heterointerfaces. [2]. Recently a new microscopy technique called 4D scanning transmission electron microscopy (4D-STEM) is gaining momentum for probing materials at sub-Angstrom resolution with the full electron−atom scattering interactions recorded in a convergent beam electron diffraction pattern (CBED) [3]. The 4DSTEM has been demonstrated that sub-Å measurements of electric fields and electrostatic potentials in materials is feasible [4].

In this work we studied a AlGaN/GaN based device where the 2DEG has been kept on and off in two different regions of the device, the latter obtained by means a p-GaN structure. In our opinion, this is the best system to test this technique to directly visualize the 2DEG in real space. The acquisition of a full set of CBED on the entire field of view could be very time and data consuming. For this reason, in this study, we acquired a sub-sampled 4DSTEM dataset by sampling only the 10% of the entire field of views [5]. As for the detector we used a QD MerlinEM Direct Electron Detector (DED) 256x256 and with 2x12bit count depth able to work as fast as 2000fps. The experiments have been carried out on a probe corrected ARM200F operated at 200keV. Data analysis was performed by center of mass (CoM) field shift data analysis method.

The 2DEG has been revealed in the regions in the proximity of the interface between GaN/AlGaN and in both regions. We discovered that where we expect 2DEG to be off it appears still visible instead but shifted far away by the interface due probably to the counter field of the p-GaN located at the opposite interface.

In this work we have shown that 4DSTEM through its analysis methods, such as CoM, can show the exact location of 2DEG as a function of interface electric fields.
The localization of 2DEG in the real space is essential for understanding its properties and to improve device designs aimed at optimizing both properties and miniaturization.

**Keywords:**

WBS, HEMT, 4DSTEM, sub-sampling

**Reference:**

[1] Ambacher, O. et al. Two dimensional electron gases induced by spontaneous and piezoelectric polarization in undoped and doped AlGaN/GaN heterostructures. J. Appl. Phys. 87, 334–344 (2000).
[2]Toyama, S., Seki, T., Kanitani, Y. et al. Real-space observation of a two-dimensional electron gas at semiconductor heterointerfaces. Nat. Nanotechnol. 18, 521–528 (2023). https://doi.org/10.1038/s41565-023-01349-8]
[3] Fang, S., Wen, Y., Allen, C.S. et al. Atomic electrostatic maps of 1D channels in 2D semiconductors using 4D scanning transmission electron microscopy. Nat Commun 10, 1127 (2019). https://doi.org/10.1038/s41467-019-08904-9]
[4] Hachtel, J.A., Idrobo, J.C. & Chi, M. Sub-Ångstrom electric field measurements on a universal detector in a scanning transmission electron microscope. Adv Struct Chem Imag 4, 10 (2018). https://doi.org/10.1186/s40679-018-0059-4
[5] Daniel Nicholls, Jack Wells, Andrew Stevens, Yalin Zheng, Jony Castagna, Nigel D. Browning, Sub-Sampled Imaging for STEM: Maximising Image Speed, Resolution and Precision Through Reconstruction Parameter Refinement, Ultramicroscopy, Volume 233, 2022, 113451, ISSN 0304-3991

751

# Structural and spectroscopic studies of Cu-doped NiO thin films

Mr Ahmad Althumali[1,2], Mr Ibrahim Aldawood[1], Mr Umit Dogan[3], Dr Adam Kerrigan[4], Dr Leonardo Lari[1,4], Dr Fahrettin Sarcan[3], Prof Ayse Erol[3], Prof Lidija Šiller[5], Prof Vlado K. Lazarov[1,4]
[1]School of Physics, Engineering and Technology, University of York, York , United Kingdom, [2]Department of Physics, Faculty of Science, Taif University, Taif , Saudi Arabia, [3]Department of Physics, Faculty of Science, Istanbul University, Istanbul, Turkey, [4]The York-JEOL Nanocentre, University of York, York, United Kingdom, [5]School of Engineering, Newcastle University, Newcastle upon Tyne , United Kingdom

Poster Group 2

Background
Nickel oxide (NiO) is a wide-band gap p-type oxide semiconductor with good optical transparency and high chemical stability [1, 2]. These properties have been exploited for applications in photovoltaics and light-emitting diodes as a hole-transporting layer [1, 2]. Doping NiO with other metal elements, such as Cu, is an effective way to adjust its grain size, crystallinity, transmittance, and ultimately its conductivity for wider use in optoelectronic devices [2-4]. Polycrystalline Cu-doped NiO films have been fabricated with different techniques using mainly glass substrates. However, studies on single-crystal thin films are lacking, even though they are fundamental to understanding the interplay between structure and functionality of doped NiO films. In this work, we have employed electron microscopy methods in conjunction with photon spectroscopies to gain insight into the role of Cu concentration on the structural, optical, and electronic properties of NiO films grown by Molecular Beam Epitaxy (MBE) as a function of doping/alloying concentrations.

Methods
A series of Ni1-xCuxO thin films with five different Cu nominal concentrations (x = 0, 3, 6, 10, 24, and 42 at.%) were grown on (001)-oriented MgO substrates by MBE. The structural, optical, and electronic properties of the grown films were characterised by in-situ reflection high-energy electron diffraction (RHEED), X-ray diffraction (XRD), ultraviolet-visible spectroscopy (UV-Vis), energy dispersive x-ray spectroscopy (EDX), X-ray photoemission spectra (XPS), atomic force microscopy (AFM), scanning transmission electron microscopy (STEM), electron energy loss spectroscopy (EELS), and current-voltage (I-V) and hot probe measurements.

Results
The in-situ RHEED analysis of the grown films shows the presence of diffraction spots along modulated RHEED streaks for undoped and 3 at.% Cu-doped NiO (indicative of layer-by-layer growth) and distinctive transmission spots (indicative of 3D island growth) for higher Cu concentration doping, with segregation of the Cu metallic phase as the Cu content reaches 10 at.%. XRD results and diffractogram patterns from cross-sectional HAADF-STEM images show the structure of the grown films remains a single crystal cubic with [001] as the preferred growth orientation, with polycrystallinity developing as Cu content exceeds 10 at.%, with observation of the Cu metallic phase in 42% Cu:NiO films (Figure 1a–c). An increase in Cu concentration also results in increased surface roughness, as confirmed by AFM and cross-sectional HAADF-STEM images. The STEM-EDX maps show a uniform distribution of the Cu in 3 at.% Cu-doped NiO film, Cu ions are likely to be substituted for Ni ions, and a segregation of Cu grains as Cu concentration increases (Figure 1d-f), which is further confirmation of Cu-phase segregation. The correlation between EELS and XPS indicates the existence of a mixture of oxidation states of Cu (Cu0, Cu+, and Cu2+) up to 10 at.% of Cu, with Cu0 becoming dominant as its concentration increases. The UV-vis absorption spectra show that an increase in Cu content results in a redshift of the absorption edges, leading to a decrease in the band

gap of the grown films as Cu concentrations increase. The band gap measurements by EELS were correlated to UV-VIS measurements and were found to be in good agreement. The electrical measurements show the conductivity of NiO films increases from 2.8×10^-5 (Ω.cm)^-1 for un-doped NiO thin film and reaches the highest value of 4.1×10^-1 (Ω.cm)^-1 for NiO film with 42 at.% Cu.

Conclusion

Undoped NiO and low Cu-doped NiO films are grown as a single crystal film, and as Cu exceeds 10 at.%, it starts segregation and forms secondary phases within the NiO film. The Cu doping increases the surface roughness, as confirmed by RHEED, AFM, and STEM. The band gap of the grown films decreases as a function of Cu concentration. The characterization techniques indicate that at the lowest Cu concentration (3 at.%), Cu ions seem to be substituted for Ni ions, and as Cu concentrations increase, Cu likely starts segregating and forming Cu grains within the films. Cu phase segregation is very likely responsible for the conductivity transition from p-type to n-type properties of NiO film with increasing Cu concentrations. This result could open the door for new applications where Cu-doped NiO can be applied as p-type, n-type, or both layers in the same devices.

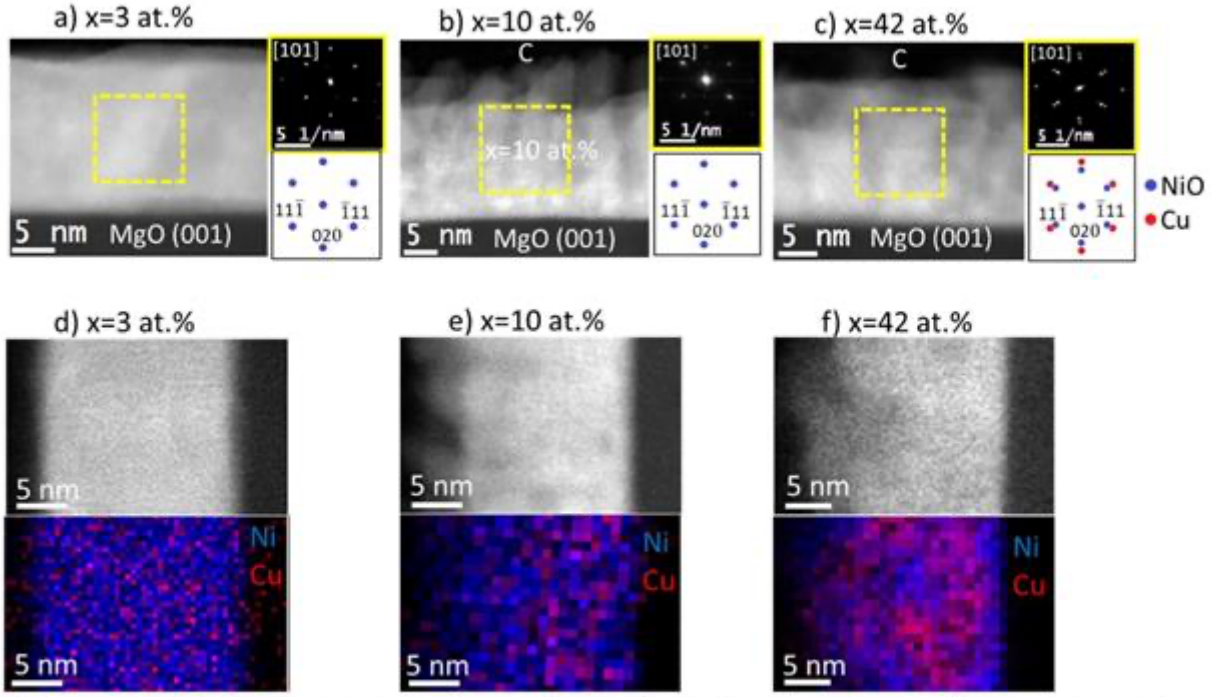


Figure 1 a-c) HAADF-STEM images of $Ni_{1-x}Cu_xO$ thin films with corresponding diffractogram patterns representing the grown film phase, and d-f) STEM-EDX maps of $Ni_{1-x}Cu_xO$ thin films, Ni and Cu in blue and red colour, respectively.

**Keywords:**

STEM, AFM, EELS, NiO, doping

**Reference:**

1. Kumar A, Singh S. Advancement in Inorganic Hole Transport Materials for Inverted Perovskite Solar Cells. Journal of Electronic Materials. 2020;49(10):5840-81.
2. Arumugam GM, Karunakaran SK, Liu C, Zhang C, Guo F, Wu S, Mai Y. Inorganic hole transport layers in inverted perovskite solar cells: A review. Nano Select. 2021;2(6):1081-116.
3. Chen W, Wu Y, Fan J, Djurišić AB, Liu F, Tam HW, et al. Understanding the Doping Effect on NiO: Toward High-Performance Inverted Perovskite Solar Cells. Advanced Energy Materials. 2018;8(19).
4. Kim KH, Takahashi C, Abe Y, Kawamura M. Effects of Cu doping on nickel oxide thin film prepared by sol–gel solution process. Optik. 2014;125(12):2899-901.

774

# Observation of logic states of HfO2-based ferroelectric FETs using STEM-DPC

Thorgund Nemec[1,2], Dirk Utess[1], Stefan Duenkel[1], Martin Weisheit[1], Halid Mulaosmanovic[1], Sven Beyer[1], Moritz Andreas Meyer[1]
[1]GlobalFoundries Dresden Module One LLC & Co. KG, Dresden, Germany, [2]Institute of Materials Science, Faculty of Mechanical Science and Engineering, Dresden Technical University, Dresden, Germany

Poster Group 2

Background incl. aims
In recent years, ferroelectric field-effect transistors (FeFETs) have become valuable alternatives to the flash technology for nonvolatile memory applications. Not only do they incorporate ultra-fast and energy-efficient switching as well as radiation hardness, but they also provide high thermal stability of their logic states. [1, 2]
The low-VT and high-VT states have been intensively studied and characterized, e.g., as described in [1], yet the understanding of the exact electrostatic field in the polarized ferroelectric (FE) gate stack is still subject of discussion. While various TCAD simulations aim to analyze these from a theoretical perspective [3], utilizing scanning transmission electron microscopy (STEM) can deliver more direct insights. Recent work [4] has shown the observation of the FE polarization in STEM utilizing the differential phase contrast (DPC) method. In addition, STEM-DPC analysis of FE devices would provide the opportunity to conduct failure analysis, not only of structural defects in single devices, but also of imperfections in the crystallographic phase and the resulting electrostatic field itself.

Methods
DPC is a STEM imaging method which can visualize local electrostatic and magnetic fields in specimens at high resolution. The fields are detected as a shift of the transmitted bright-field disk on a segmented annular or a pixelated detector resulting from the interaction of the local fields with the incident electron beam. Since the FE polarization in FE materials creates electrostatic fields, the DPC method is suitable for the investigation of local polarization effects in the thin FE layers of FeFETs.
In this study, $HfO_2$-based FeFET arrays were programmed in a striped pattern, as described in [2]. The FeFETs consisted of 10 nm FE $HfO_2$, a 1 nm $SiO_2$ interfacial layer, TiN and a top electrode made from polycrystalline Si. For investigation with the DPC method, TEM specimens of the programmed array were prepared by in-situ lift-out utilizing the focused ion beam (FIB). A convergent electron beam was employed to achieve high spatial resolution and thus investigate the FE polarization states in the FE material.

Results
The local charge carrier density was calculated from the DPC data and analyzed for the investigated FeFETs, respectively. The FeFETs programmed in low-VT and high-VT states showed opposing gradients of the charge carrier density in the FE layer. The direction of the electrostatic fields indicated by those gradients was found to be in accordance with the theoretical direction of the electrostatic fields due to the FE polarization of the material.

Conclusion
In future investigations, the use of DPC can provide deeper insights into the properties of FeFETs. Combining DPC with other techniques, such as precession electron diffraction (PED), could yield additional information about these devices. Employing PED would help reduce diffraction-related artifacts in DPC data. Furthermore, PED can identify grains of both FE and non-FE phases within the

material. In addition, observing the in-situ switching behavior of FE devices would contribute significantly to understanding the electric behavior of FeFETs during operation.

**Keywords:**

DPC, STEM, FeFET, logic states

**Reference:**

[1] H. Mulaosmanovic et al. (2021) Ferroelectric field-effect transistors based on $HfO_2$: a review, Nanotechnology, 50(32).
[2] M. Trentzsch et al. (2016) A 28nm HKMG super low power embedded NVM technology based on ferroelectric FETs, in 2016 IEEE IEDM, San Francisco, USA.
[3] S. Müller et al. (2013) Performance investigation and optimization of Si:$HfO_2$ FeFETs on a 28 nm bulk technology, in: 2013 Joint IEEE ISAF/PFM, Prague, CZ.
[4] L. Chen et al. (2023) First direct observation of the built-in electric field and oxygen vacancy migration in ferroelectric Hf0.5Zr0.5O2 film during electrical cycling, Nanoscale, 15.

890

# Analytical TEM of materials for gas sensing

Catalina-Gabriela Mihalcea[1,2], Corneliu Ghica[1], Adelina Stanoiu[1], Cristian-Eugen Simion[1], Daniela Ghica[1], Mariana Stefan[1], Simona Somacescu[3], Ioana-Dorina Vlaicu[1], Alexandra-Corina Iacoban[1]
[1]National Institute of Materials Physics, Atomistilor 405A, 077125, Romania, [2]Faculty of Physics, University of Bucharest, Atomistilor 405, 077125 , Romania, [3]"Ilie Murgulescu" Institute of Physical Chemistry, Romanian Academy, Spl. Independentei 202, 060021, Romania

Poster Group 2

Background incl. aims
Metal-oxide semiconductor (MOX) layers are frequently used as gas sensors since they can detect different types of gases, such as CO, CO2, CH4, NO2, etc. and also due to their increased sensitivity, quick response times and reduced fabrication costs. The main challenge for this type of materials is to improve their selectivity [1].
Morphology and structure play an important role during the interaction between the target gas and the sensing layer since porosity, grain size, grain faceting, crystal phase and elemental composition can influence the sensor signal. All these properties depend on the synthesis route.
Our study is focused on the synthesis and determination of the structure, morphology and electrical properties of different MOX systems, such as NiO (p-type semiconductor), SnO2 and Gd2O3 (n-type semiconductors).

Methods
NiO was synthesized by hydrothermal route followed by calcination at 400 °C and 500 °C [2,3], while SnO2 (doped with different concentrations of Gd: 5%, 10% and 20%) and pure Gd2O3 were synthesized by co-precipitation [4].
The morphology and the structure of these samples were investigated using analytical TEM techniques: CTEM, SAED, HRTEM and STEM-EDS. These results were correlated with X-ray Diffraction (XRD), Electron Paramagnetic Resonance Spectroscopy (EPR) and X-ray Photoelectron Spectroscopy (XPS) data as well as with the electrical response of the fully characterized materials to CO and CO2 target gases.

Results
p-type semiconductors (NiO)
Increasing the calcination temperature induced visible morphological changes, as suggested by XRD patterns and observed by TEM imaging. One notable difference consists in the fact that the calcination temperature increased the nanoparticle size from ~9 nm to ~20 nm, with the formation of intragrain structural defects (e.g. twin boundaries), as revealed by HRTEM imaging (see graphic, [2]).
The electric response was tested in the CO atmosphere. Considering the observed morphological differences, a decrease in the sensor response was expected, but the opposite effect was observed [2].
To understand this phenomenon, an in-depth analysis was performed, using spectroscopic techniques: STEM-EDS, EPR and XPS. The EPR investigations revealed the formation of metallic Ni clusters in the sample calcined at 500 °C and the analytical TEM techniques (SAED, CTEM and STEM-EDS) confirmed their presence. The formation of these metallic clusters, corroborated with the morpho-structural properties, could explain the different sensing properties of the samples calcined at different temperatures [3].
n-type semiconductors (SnO2 doped with Gd, Gd2O3)
The increase in the dopant concentration had a notable effect on the morphology and the structure of the samples. The TEM analyses correlated with the Rietveld refinement of XRD patterns revealed

the formation of SnO2-Gd2O3 nanocomposites. The presence of the two crystallographic phases was analyzed using different analytical TEM techniques: CTEM, SAED and STEM-EDS, which confirmed the formation of the cubic Gd2O3 secondary phase. The electric response was tested in the CO2 atmosphere, at different values of relative humidity, to determine the sensing mechanism of the SnO2-Gd2O3 nanocomposites [4].

Conclusions

Analytical TEM techniques correlated with XRD, EPR, XPS and electrical measurements offered valuable information for understanding the sensing mechanism of metal-oxide semiconductor materials in the presence of different gases, i.e. NiO in the presence of CO and SnO2/Gd2O3 exposed to CO2.

Acknowledgements

This work was supported by the Ministry of Research, Innovation and Digitization CNCS-UEFISCDI through the projects PN-III-P4-PCE-2021-0384 within PNCDI III and the Core Program of the National Institute of Materials Physics, Project PC1-PN23080101.
This work is part of the PhD thesis “Nanostructured materials for gas sensing: correlations between functional, electronic and microstructural properties” supported by CERIC-ERIC.

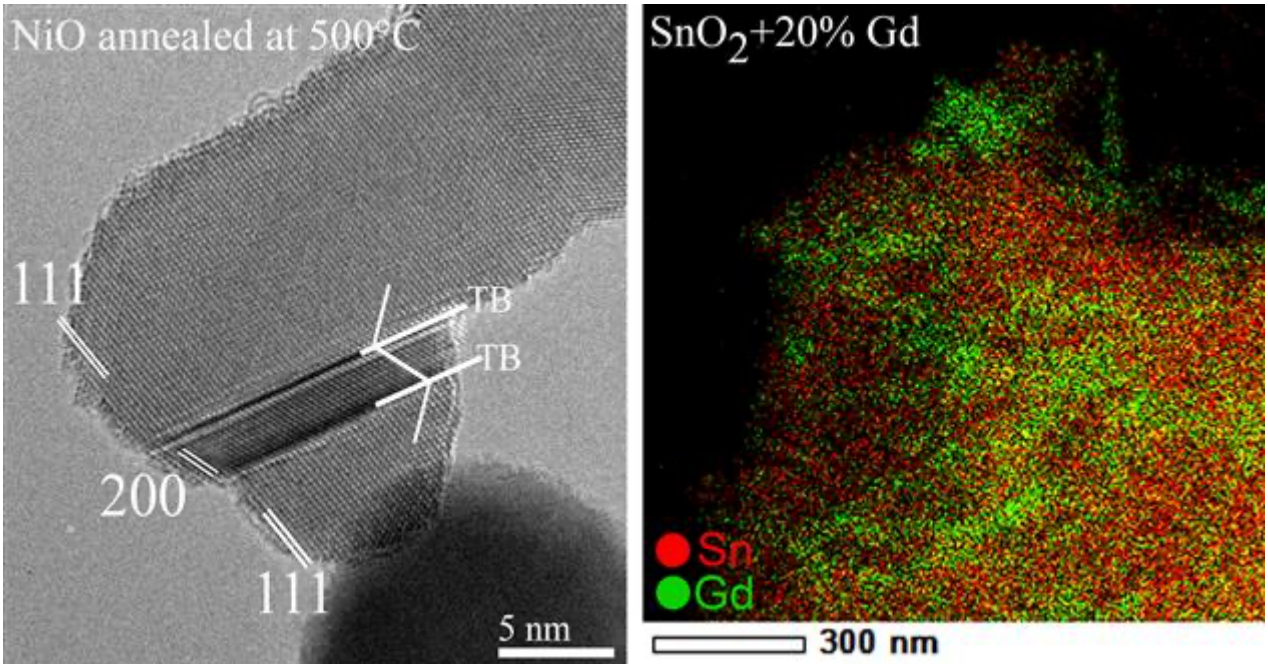


**Keywords:**

Analytical TEM
Metal-oxide semiconductors
Gas-sensing

**Reference:**

[1]. George F. Fine, Leon M. Cavanagh, Ayo Afonja and Russell Binions, Sensors 2010, 10, 5469-5502
[2]. Adelina Stanoiu, Corneliu Ghica, Catalina G. Mihalcea, Daniela Ghica, Simona Somacescu, Ovidiu G. Florea, Cristian E. Simion, Chemosensors 2022, 10, 191
[3]. Catalina G. Mihalcea, Mariana Stefan, Corneliu Ghica, Ovidiu G. Florea, Adelina Stanoiu, Cristian E. Simion, Simona Somacescu, Daniela Ghica, Applied Surface Science 651 (2024) 159252
[4]. Corneliu Ghica, Catalina G. Mihalcea, Cristian E. Simion, Ioana D. Vlaicu, Daniela Ghica, Ion V. Dinu, Ovidiu G. Florea, Adelina Stanoiu, Sensors & Actuators: B. Chemical 368 (2022) 132130

898

# TEM observations of threading dislocations in gallium nitride under external stimuli

Mrs. Eva Kolibalova[1,2], Daniel Citterberg[2], Richard Gazdik[3], Petr Babor[2,3], Tomas Sikola[2,3], Miroslav Kolibal[2,3]
[1]CEITEC Nano, Brno University of Technology, Brno, Czech Republic, [2]CEITEC, Brno University of Technology, Brno, Czech Republic, [3]Institute of Physical Engineering, Brno University of Technology, , Czech Republic

Poster Group 2

Background incl. aims
Gallium nitride becomes increasingly utilized in power electronics and currently competes with silicon carbide for the lead in many power applications. Each of the two materials faces different challenges. In GaN, for example, the effect of threading dislocations in GaN-on-Si epitaxial layers is still an open issue. Despite great effort in research of this material, it is questionable whether the high concentrations of dislocations deteriorate device operation [1]. Additionally, dislocation motion at elevated temperature, under local electric field or passing current could be significant in delayed device failure. Localization, identification and operando observation of dislocations is a highly complex task, requiring a correlative multimodal approach [2]. Here, we present initial attempts which include operando TEM observations of threading dislocations.

Methods
We localize and identify dislocations by means of electron channeling contrast in SEM, conductive AFM and wet etching. Subsequently, dislocation dynamics is observed by TEM on FIB-prepared cross-sectional lamellae on MEMS chips.

Results
We inspect the effect of heat, electrical current and electric field on the dislocation motion. The dislocations are stable at elevated temperatures, and they start to move/unpin if extreme current densities over tens of kA/cm2 are passing through (i.e. much higher than common current densities in GaN devices,). We will also present our first attempts to observe the motion initiated by an extreme electric field, generated by a sharp tip close to the lamella surface.

Conclusion
In this contribution, we demonstrate a correlative approach to dislocation identification, combining SEM, TEM, wet etching and probe microscopy. We show the results of our TEM observations of dislocation motion under external stimuli (heat, electric current and large electric field). The dislocations seem to be immobile until only very extreme conditions are met.

Acknowledgements
The ALL2GaN Project (Grant Agreement No 101111890) is supported by the Chips Joint Undertaking and its members including the top-up funding by Austria, Belgium, Czech Republic, Denmark, Germany, Greece, Netherlands, Norway, Slovakia, Spain, Sweden and Switzerland.
Views and opinions expressed are however those of the author(s) only and do not necessarily reflect those of the European Union or the national granting authorities. Neither the European Union nor the national granting authorities can be held responsible for them.

**Keywords:**

Gallium nitride, dislocations, in-situ TEM

**Reference:**

[1] M. Stabentheiner et al., J. Appl. Phys. 2024, 135, 025703.
[2] Besendörfer, S. et al., Sci Rep 2020, 10, 17252.

926

# TEM investigation of the defect structure in epitaxial corundum thin films

Claudio Bellani[1], Alberto Binetti[2], Wei-Fan Hsu[2], Simon Mellaerts[2], Koen Schouteden[2], Prof. Jean-Pierre Locquet[2], Prof. Jin Won Seo[1]
[1]Department of Materials Engineering, KU Leuven, Leuven, Belgium, [2]Department of Physics and Astronomy, KU Leuven, Leuven, Belgium

Poster Group 2

Metal oxides $M_2O_3$ thin films have extensively been studied as they offer a broad range of functionalities. Sapphire $Al_2O_3$ is the most common substrate for the epitaxial growth of several $M_2O_3$ since it shares the same corundum lattice (R-3c) with several $M_2O_3$ systems. Examples include $Cr_2O_3$, a magnetoelectric antiferromagnet with applications in memory devices, and $V_2O_3$, a popular material to study strong electron correlations. α-Fe2O3 and α-Ga2O3 also present the same corundum structure and have potential applications in catalysis and magnetic devices as well as power electronics, respectively.
A good understanding of the defect formed during the film epitaxial growth is crucial for both fundamental studies and devices. Examples of such defects present in $M_2O_3$ thin films grown on c-cut sapphire include twinning, columnar growth, misfit dislocations, screw dislocations and oxygen vacancies. In this work, the microstructure of $Cr_2O_3$ and $V_2O_3$ thin films are studied systematically. Our results indicate for these two $M_2O_3$ systems significantly different defect mechanisms.

All the thin films are grown by oxygen-assisted molecular beam epitaxy (MBE) on c-cut sapphire substrates at high temperature. $V_2O_3$ samples are grown at 700°C and $Cr_2O_3$ samples at 800°C. Base pressure of the system is 10E-10 Torr, while during the deposition the $O_2$ partial pressure is measured with a residual gas analyzer and kept constant at 2E-6 Torr. Bilayer structures have also been grown with $V_2O_3$ on a $Cr_2O_3$ buffer layer. The epitaxial growth is monitored in-situ in the MBE chamber by reflection high-energy electron diffraction (RHEED). X-ray diffraction (XRD) ϕ-scans are performed ex-situ after growth, and the twinned fraction of the film was estimated.
For transmission electron microscopy (TEM), cross-sectional lamellae are prepared by focused ion beam using DualBeam Nova 600 NanoLab and imaged by means of a cold-FEG JEOL ARM200F microscope equipped with a STEM-Cs corrector, operated at 200kV. Geometric phase analysis (GPA) of STEM images is also performed using the Digital Micrograph plugin developed by Du (Ernst Ruska-Center for Microscopy).

TEM images confirm the epitaxial growth of all the thin films. GPA strain maps highlight the strong lattice deformation at the interface linked to the presence of misfit dislocations, which appear periodically with an average distance of 9.5±1.5 nm at the $V_2O_3/Al_2O_3$ interface, when imaged along the <-2110> zone axis. This is comparable to the value expected when the lattice mismatch is fully compensated by incorporation of misfit dislocations, i.e. 10.2 nm for a 4.2% in-plane lattice mismatch. In contrast, strain maps of $Cr_2O_3/Al_2O_3$ films present strong deformations across the entire thickness of the film, despite having a very similar in-plane mismatch with the substrate (4.4%). In addition to misfit dislocations, the sample contains columnar domains and twinning. Columnar domains are best imaged with HRTEM and bright field STEM, although the grain boundary is not visible in the high-resolution STEM images. A similar bright field contrast is present in the $V_2O_3$ thin films as well, albeit less dense and with irregular shape. The presence of columnar domains in $Cr_2O_3$ thin films has been reported previously, and their origin was explained by an additional strain relaxation mechanism beside the incorporation of dislocations. Secondly, twinning can be observed in the XRD ϕ-scan of the planes {10-110}, as a second set of 3 peaks appears while rotating the sample by 360° introducing an apparent sixfold symmetry instead of the trigonal symmetry of the

corundum structure. However, XRD is unable to detect small, twinned fractions of the film which can be observed by TEM and are always present. Increased twinning is observed for samples grown with a higher Cr-flux rate, indicating that the precise growth parameters affect the formation of the twins. On the other hand, $V_2O_3$ does not present any twinning when grown directly on sapphire. Grown on a twinned $Cr_2O_3$ buffer, $V_2O_3$ shows the ability to recover to the untwinned structure despite the underlying twinned structure. This result is in contrast with other works where twinning in $V_2O_3$ and $Cr_2O_3$ appeared to be comparable. The absence of columnar and twinned domains in $V_2O_3$ thin films indicates a different strain relaxation mechanism in both $M_2O_3$ thin films.

Cross sectional TEM analysis of corundum $M_2O_3$ thin films grown on sapphire substrates indicates an intrinsic difference in the defect structure formed in $Cr_2O_3$ and $V_2O_3$ thin films. The former present misfit dislocations, columnar and twinned domains in agreement with previous studies, while the latter does not present any twinning and compensates the lattice mismatch only by incorporation of misfit dislocations.

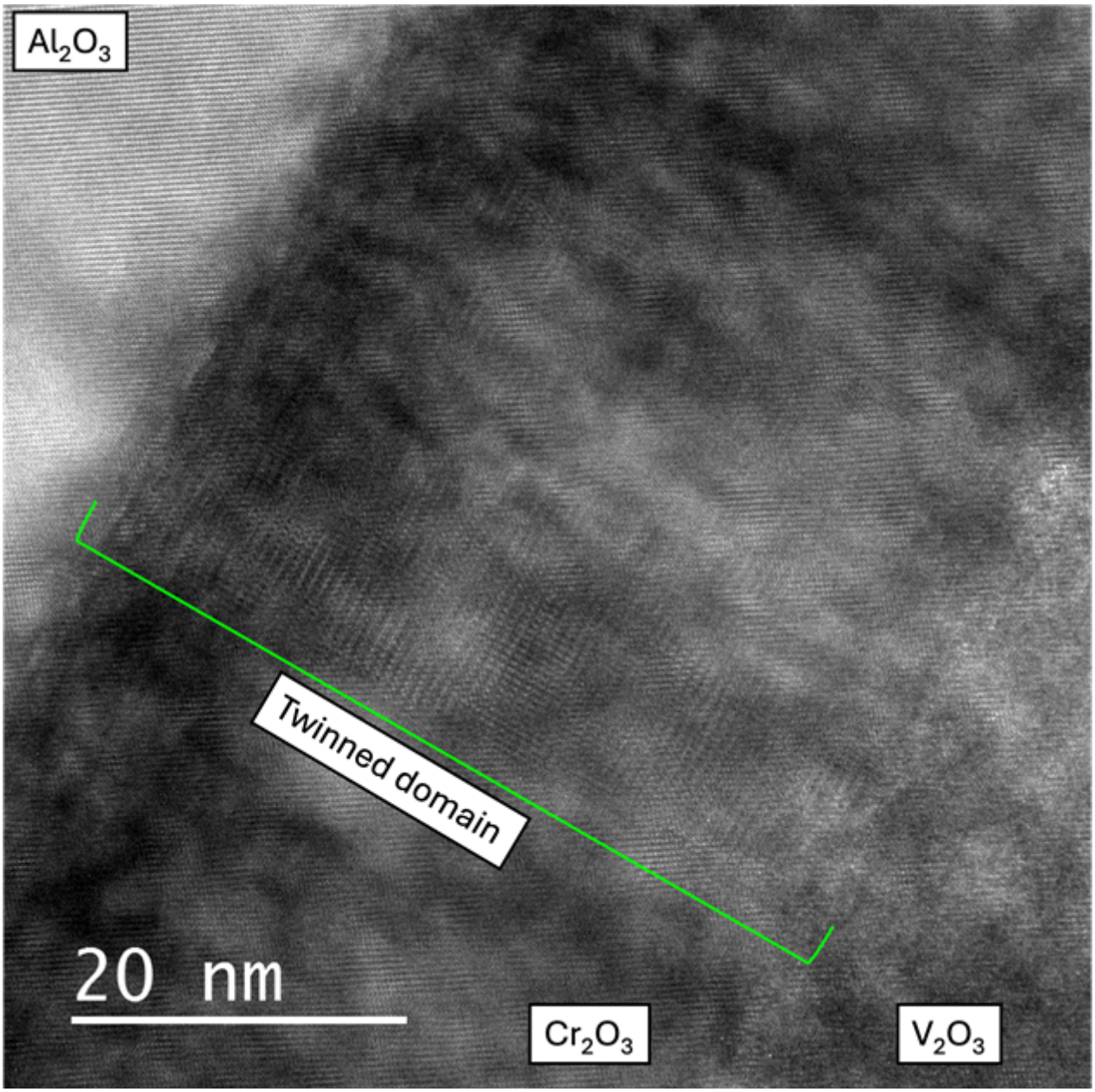


**Keywords:**

Epitaxy
Thin-Films
Defects
Corundum
MBE

**Reference:**

1. Kosub, T., et al. "Purely antiferromagnetic magnetoelectric random access memory." Nature Communications, vol. 8, no. 1, 2017, p. 13985.
2. Makushko, P., et al. "Flexomagnetism and vertically graded Néel temperature of antiferromagnetic Cr2O3 thin films." Nature Communications, vol. 13, 2022, p. 6745.
3. Kaneko, K., et al. "Title of the Article." Journal Abbreviation, vol. 51, no. 020201, 2012.
4. Wang, C-M., et al. "The characteristics of interface misfit dislocations for epitaxial α-Fe2O3 on α-Al2O3 (0001)." Thin Solid Films, vol. 414, no. 1, 2002, pp. 31-38.
5. 5. Du, H. "GPA-geometrical phase analysis software." (2018).

932

# In-situ TEM annealing of vanadium oxide thin films

Claudio Bellani[1], Simon Mellaerts[2], Koen Schouteden[2], Alberto Binetti[2], Wei-Fan Hsu[2], Prof. Jean-Pierre Locquet[2], Prof. Jin Won Seo[1]
[1]Department of Materials Engineering, KU Leuven, Leuven, Belgium, [2]Department of Physics and Astronomy, KU Leuven, Leuven, Belgium

Poster Group 2

The multitude of vanadium oxide phases are traditionally grouped into two families: Magnéli phases (VnO2n-1 where 3 ≤ n ≤ 9) and Wadsley phases (VnO2n+1 where 1 ≤ n ≤ 6). These groups are characterized by the oxidation states V3+/V4+ and V4+/V5+, respectively, separated by the purely V4+ phase, i.e. $VO_2$.
Many of these vanadium oxides present a metal-to-insulator transition (MIT) upon cooling coupled with structural and occasionally magnetic transitions. Of all the VOx phases, $VO_2$ has attracted the greatest attention in terms of technological applications, because the electrical transition occurs close to room temperature at 68°C. The semiconducting monoclinic phase (P21/c) is most stable at room temperature and transitions into the metallic rutile phase (P42/mnm) above the transition temperature. The transition is accompanied by a change in resistivity up to 5 orders of magnitude in single crystals as well as in optical properties. This abrupt change has triggered a broad range of applications: e.g. thermal sensors, electrical switches, smart windows, optical limiting, modulators, bolometers, and Mott field-effect transistors.
The growth of $VO_2$ thin films requires a higher oxygen partial pressure than what is typical for the growth by means of MBE. Therefore, crystalline $VO_2$ thin films have been obtained by growing amorphous VOx and to convert to $VO_2$ through a subsequent annealing process. Very little is known about the structural transition from the amorphous to the crystalline phase, especially how the $VO_2$ phase is established, as well as the structural transition underwent during the MIT.
However, an in-situ transmission electron microscopy (TEM) experiment using an environmental cell experiment provides the possibility to live monitoring of the oxidation and crystallization process of the film by mimicking the annealing process in a furnace-like environment. The structural and chemical information collected during the in-situ annealing can shed light on the complicated mechanism involved in $VO_2$ films as a function of the temperature and the annealing environment.

VOx thin films are deposited directly on the MEMS chips of a closed-cell gas reaction system (Atmosphere, Protochips) by oxygen-assisted molecular beam epitaxy (MBE) at room temperature. The film is directly in contact with the electron transparent membrane of the chip which consists of 30 nm of amorphous $Si_3N_4$. The vanadium flux in the MBE is calibrated to 0.1 Å/s with a quartz crystal microbalance, and the total thickness of the sample is estimated to around 40 nm. Base pressure of the system is 1E-10 Torr, while during the deposition $O_2$ partial pressure is measured with a residual gas analyzer and kept constant at 2E-6 Torr. The sample is then mounted on the TEM sample holder and inserted into a cold-FEG JEOL ARM200F microscope equipped with a STEM-Cs corrector. The MEMS chip is heated up to 500°C in Ar or Ar/$H_2$ mixtures at 760 Torr with a 0.1 sccm flow. Base pressure of the closed-cell is 1 Torr. The sample is imaged both in TEM and STEM mode, with bright field (BF) and high-angle annular dark field (HAADF) detectors. Electron energy loss spectroscopy (EELS) is performed with a Gatan Tridiem detector in STEM mode to evaluate the local oxidation state with the V L edges and O K edge.

The as-grown sample is amorphous and dominated by the V3+ stoichiometry. As temperature increases in the closed cell, the first transformation occurs between 290-310°C for both Ar and Ar/$H_2$ mixtures. Several grains of a few hundred nanometers in size form, with irregular shape and areas

showing different HAADF contrast. Grain boundaries are decorated with dark regions linked to V-deficiency. These areas gradually disappear as the temperature approaches 420°C, where the main crystallization takes place. The morphology of the annealed film shows a great variability with the different gas mixtures applied, while the EELS spectra generally confirm the oxidation of V3+ to V4+ and/or V5+. The residual $O_2$ in the closed-cell gas reaction system is expected to be responsible of the oxidation of the film, and the $H_2$ insertion is intended to counterbalance and to avoid the sample being further oxidized to $V_2O_5$. The fully polycrystalline film is stable until about 500°C when it transforms into $V_2O_5$, which very often forms elongated grains and leaves holes behind between these grains. Electron beam can additionally influence the annealing as it induces local heating of the film, with consequences on the final morphology and oxidation state.

The annealing of vanadium oxide thin films on amorphous substrates has been investigated in several reported works, with the goal of obtaining $VO_2$ polycrystalline films. The outcome is often complex, as the films frequently include additional phases alongside the desired monoclinic $VO_2$ phase, due to under or over-oxidation. The presence of multiple crystalline and amorphous phases, which has a detrimental effect on the electrical transition, complicates the thin film characterization by the most common techniques (e.g. x-ray diffraction, scanning probe microscopies, and x-ray photoemission). A closed-cell experiment in the TEM provides the possibility to mimic the annealing environment and to observe the structural changes as a function of the temperature and the environment. These results can enhance the understanding of the annealing process by combining structural and chemical information at the nanometric scale. In particular, a detailed nano-scale understanding of the oxidation/reduction routes in vanadium oxide films on amorphous substrates can be gained.

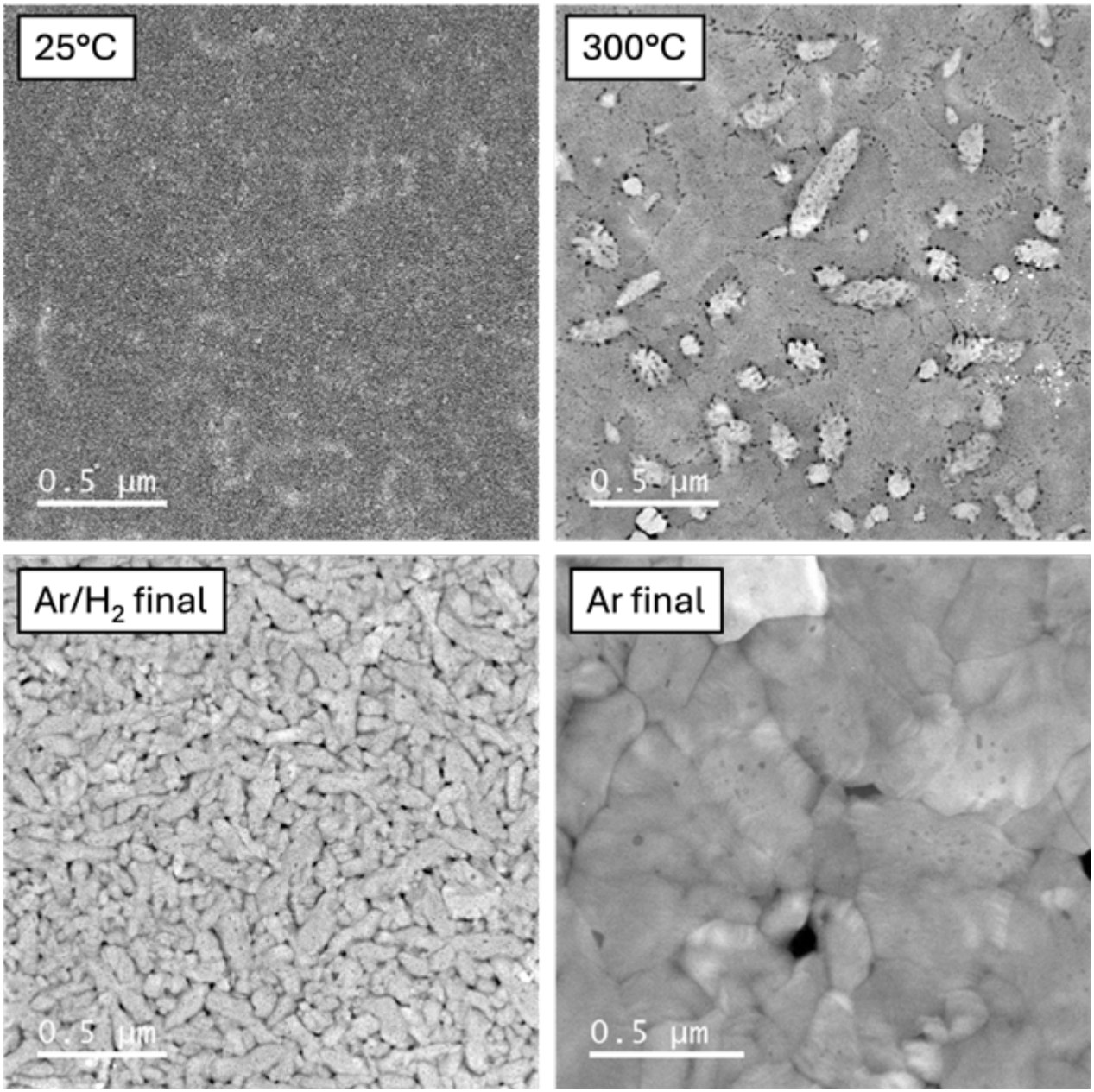


**Keywords:**

In-situ TEM
Thin film
Oxidation

**Reference:**

1. Van Bilzen, B., et al. "Production of VO2 thin films through post-deposition annealing of V2O3 and VOx films." Thin Solid Films, vol. 591, 2015, pp. 143-148.
2. Premkumar, P. A., et al. "Process study and characterization of VO2 thin films synthesized by ALD using TEMAV and O3 precursors." ECS Journal of Solid State Science and Technology, vol. 1, no. 4, 2012, p. P169.
3. Balakrishnan, V., et al. "In situ studies on twinning and cracking proximal to insulator–metal transition in self-supported VO2/Si3N4 membranes." Journal of Materials Research, vol. 27, no. 11, 2012, pp. 1476-1481.
4. Lee, D., et al. "Sharpened VO2 phase transition via controlled release of epitaxial strain." Nano Letters, vol. 17, no. 9, 2017, pp. 5614-5619.
5. Pergament, A. L., et al. "Oxide electronics and vanadium dioxide perspective: A review." Journal on Selected Topics in Nano Electronics and Computing, vol. 1, no. 1, 2013, pp. 24-43.

963

# Robustness evaluation of electric field measurements via template matching in 4D-STEM

Alexis Wartelle[1], Matthew Bryan[2], Yiran Lu[1], David Cooper[2], Jean-Luc Rouvière[3], Martien den Hertog[1]
[1]Institut Néel, CNRS-UGA, Grenoble, France, [2]LETI, CEA, Grenoble, France, [3]MEM, IRIG, CEA, Grenoble, France

Poster Group 2

Background incl. aims
Wave-based Scanning Probe Microscopy (SPM) techniques may provide a wealth of information even down to length scales significantly below the probe's extent. Tapping into it is possible thanks to two-dimensional detectors, which enable access to phase and/or absorption contrasts through the beam's interference patterns. The data analysis may then range from complex, stochastic approaches to simple and deterministic ones. One can take phase retrieval in coherent diffraction imaging [1] and center-of-mass (CoM) in field mapping [2-3] via four-dimensional scanning transmission electron microscopy (4D-STEM) as examples. However, with the dataset's enhanced dimensionality (compared to e.g. differential phase contrast imaging with a segmented detector) comes a broader range of field determination methods from which to choose.

Methods
In this presentation, we address the question of reliability in 4D-STEM electric field mapping by way of a comparison between the conventional CoM method on one hand, and several template matching (TM) approaches on the other hand. Our focus being on methodology, we use data acquired on a well-known silicon p-n junction [2-3] for simplicity. The imaged area is a 128-pixels-side square [see Figure 1(a)], with a step size of 5.4 nm, our detector is a 256x256 pixels Merlin camera based on medipix technology from Quantum Detectors, and the TEM is operated at 200 kV. The lamella's large thickness (326 nm of active material) and the electron beam's semi-convergence angle (992 µrad) allow us to preserve both signal-over-noise ratio and spatial resolution. Most importantly, the small probe size leads to a rigid, lateral shift of the electron beam without intensity redistributions; one may therefore expect good performances from TM.
As a first step, a common reference position (on the detector) for all compared methods is evaluated by averaging the beam's center position over 5120 pixels more than 100 nm away from the junction. We then run a standard CoM analysis along with TM and extract the junction's electric field from the corresponding results, after subtraction of the reference position. It must be noted that the TM algorithm we use (from the liberTEM [4] module) possesses sub-pixel accuracy. Denoting R the estimated beam radius on the detector and r the radial coordinate from the center, the tested, rotation-symmetric templates are: (i) a flat disk with radius R, (ii) the same disk multiplied with r/R, (iii) template (i) with a negative annulus around it, (iv) template (ii) with a negative annulus around it. A final template (v) is created from an actual data frame or the average of several of them.

Results
As can be seen on Figure 1, all templates yield distinct results, and none match the output of CoM. The significant spread in extracted field values suggests high sensitivity to the template's shape, and therefore to user input. That is why we now focus on the template resembling data the most: an acquired detector frame. Since the template (v) was created with a square cropping mask in order to exclude a Kikuchi band from the pattern, we first check whether a disk-shaped cropping mask (with a radius clearly above the beam's) produces different results. Not only is it the case, but we also find out that slightly increasing the mask's radius strongly affects the template matching output, even though the Kikuchi band was still rejected (only background/weak beam tails were included).

This implies that a correlation-based shift determination places too much weight on absolute intensity levels, failing to accurately locate the pattern's edges. In order to alleviate this, we propose to perform template matching using not a raw detector frame, but the corresponding map (still in detector space) of the norm of its gradient [5]. Our goal consists in evaluating the robustness of this approach versus its two free parameters: the smoothing applied before gradient computation, and the threshold applied on the gradient's norm before TM.

Conclusions

With this study, we hope to improve the understanding of TM's limitations and/or biases in the context of quantitative field mapping. In addition to performing a comparison with CoM, we investigate the performance of two pixelated detectors, using direct detection or CMOS with a scintillator respectively. Finally, we develop an analysis which is guided as much as possible by the data themselves, with the objective to restrict the amount of arbitrariness as much as possible.

Acknowledgements

This project received funding from the European Research Council under the European Union's H2020 Research and Innovation programme via the e-See project (Grant No. 758385). Experiments have been performed at the Nanocharacterisation platform PFNC in Minatec, Grenoble as well as at TEM facility JEOL NEOARM, co-financed by the European Union under the European Regional Development Fund (ERDF, contract n° RA0023813).

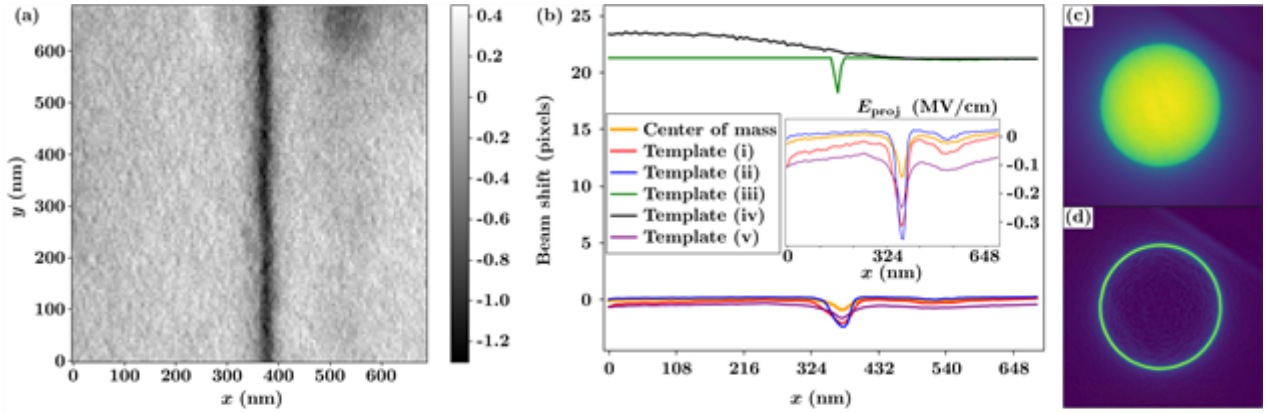


Figure 1: (a) 4D-STEM map of the p-n junction. (b) Extracted average profiles of beam shifts from CoM and template matching; inset: corresponding electric field $E_{proj}$. (c) Template (v) built from 20 data frames. (d) Norm of the gradient of gaussian-smoothed template (v), $\sigma$=1 pixel.

**Keywords:**

4D-STEM, CoM, template matching

**Reference:**

[1] H. N. Chapman et al., J. Opt. Soc. Am. A 2006, 23, 1179-1200.
[2] D. Cooper, L. Bruas, M. Bryan, V. Boureau, Micron 2024, 179, 103594.
[3] B. C. da Silva, Z. S. Momtaz, L. Bruas, J.-L. Rouvière, H. Okuno, D. Cooper, M. I. den-Hertog, Appl. Phys. Lett. 2022, 121, 123503.
[4] A. Clausen, D. Weber, K. Ruzaeva, K. Müller-Caspary, R. E. Dunin-Borkowski, LiberTEM/LiberTEM-blobfinder: 0.5.0. Zenodo 2023.
[5] L. Bruas, V. Boureau, A. P. Conlan, S. Martinie, J.-L. Rouviere, D. Cooper, J. Appl. Phys. 2020, 127, 205703.

999

# Measurement of electrostatic fields in Ge-doped AlGaN structures by off-axis electron holography

Phd Student Alexis Palais[1], Director of Research David Cooper[1], Senior Researcher Eva Monroy[2], Director of Research Bérangère Hyot[1]
[1]CEA-LETI, Grenoble, France, [2]CEA, Grenoble INP, IRIG, PHELIQS, Grenoble, France

Poster Group 2

Background incl. Aims
AlGaN LEDs have been greatly researched these last years for the development of ultraviolet emitters for many applications including disinfection [1]. For that purpose, we need AlGaN alloys with high Al content and high active dopant concentrations. In this presentation, we will discuss the potential of Ge as an alternative n-type dopant instead of Si for AlGaN structures with different Al contents. Indeed, silicon is a widely used n-type dopant but it contributes to edge-type dislocation climb and induces tensile stress. The interest of Ge is that it introduces less strain than silicon in the AlGaN lattice. Moreover, the distribution and activity of the dopants and the location of the electrical junction are very important parameters in the design and optimisation of LED structures. These properties can be measured by off-axis electron holography, which records both the amplitude and the electron phase from an interference pattern. As the change in phase of the electron beam is directly linked to the electrostatic potential, this allows us to measure the potentials across the structures with a nanometer resolution.

Methods
In this study, we examined 6 samples consisting of 675-nm-thick Ge-doped AlGaN grown by plasma-assisted molecular beam epitaxy (PAMBE) on 1µm-thick AlN-on-sapphire templates [2]. The first and the second samples were grown with an Al mole fraction of 12% and varying Ge concentrations (the temperature of Ge cell was 928°C and 1011°C respectively). The third and the fourth samples were grown with 36% Al and varying Ge concentrations (the temperature of Ge cell was 928°C and 840°C respectively). The fifth and the sixth samples were grown with 64% and 66% of aluminum respectively, with a temperature of 1011°C for the Ge cell. Lamellas for transmission electron microscopy (TEM) studies were prepared by in-situ lift-out focused ion beam (FIB) milling in an FEI Strata 400. Each lamella contained areas with different thicknesses to obtain information about the samples such as the inactive thickness and to find the optimum experimental conditions. Electron holography and electron dispersive x-ray (EDX) spectroscopy were then performed using a double-corrected FEI Titan Ultimate TEM operating at 200 kV equipped with a Gatan One View 4k camera.

Results
Using electron holography, we were able to map the electrostatic potential in the specimens. This requires a good sample preparation and optimized experimental parameters during the TEM experiments [3]. The measurement conditions are particularly demanding in the case of AlGaN, since dynamical diffraction is a problem and wide bandgap materials have a tendency to charge during examination. Additionally, the total potential measured in electron holography depends on strong polarisation fields, the mean inner potential (MIP) of our material and additional contributions from dopants. To get reliable measurements, we first deposit a thin carbon layer on the specimen to provide a conductive channel to evacuate the charge. Then, the MIP in the AlGaN is calculated from DFT simulations, which provides values of 15,9 V for bulk AlN and 16,9 V for bulk GaN [4]. Using a linear interpolation, we can estimate the MIP of Al0,12Ga0,88N (16,8 V), Al0,36Ga0,64N (16,5 V) and Al0,66Ga0,34N (16,2 V), so that the MIP contribution can be removed from the total measured phase. Figure 1(a) shows a FIB lamella with several steps of different thicknesses, prepared from the

sample with 36% Al and TGe=928°C. In order to measure accurately the thicknesses of these steps, we use the Convergent Beam Electron Diffraction (CBED) method [5]. Figure 1(b) shows an experimental CBED pattern compared to 1(c) a simulation for a 374nm thick specimen using the JEMS software. Figure 1(d) shows an amplitude image of this specimen. The amplitude image has homogenous contrast, suggesting reduced diffraction contrast, which means that the corresponding phase image can be correctly interpreted. Figures 1(e) and 1(f) show the corresponding phase image before and after carbon coating respectively. The comparison of the images shows the relevance of carbon deposition to reduce charging of the specimen. From Figure 1(f), we can deduce the phase difference across the AlGaN layer (3.2+/-0.1rad), as shown in the profile in Figure 1(g). Finally, it is possible to determine and compare the electrostatic potentials across the AlGaN layer using $\Delta\Phi 0(x,y)=CE.V(x,y).t(x,y)$ where CE = 7,289 × 10^−3 rad/V/nm for 200kV electrons. Thus, a step in electrostatic potential of 1.17+/-0.02 V has been measured in the AlGaN layer.

Conclusion

By optimising the experimental conditions, we will be able to show the effect of Al content on the activity of the dopants in the AlGaN layer. With this study, we also show that the off-axis electron holography is a useful method to measure the electrostatic potential with a nanometer resolution, and thus can be used to optimize the structures grown for the development of UV LEDs. We will couple holography with EDX to determine the dopant concentrations that provide the highest carrier concentrations.

This research was performed on the Platform for Nanocharacterisation (PFNC) at the CEA-LETI of Grenoble and was funded by the French National Research Agency (Grant ANR-22-CE09-0024).

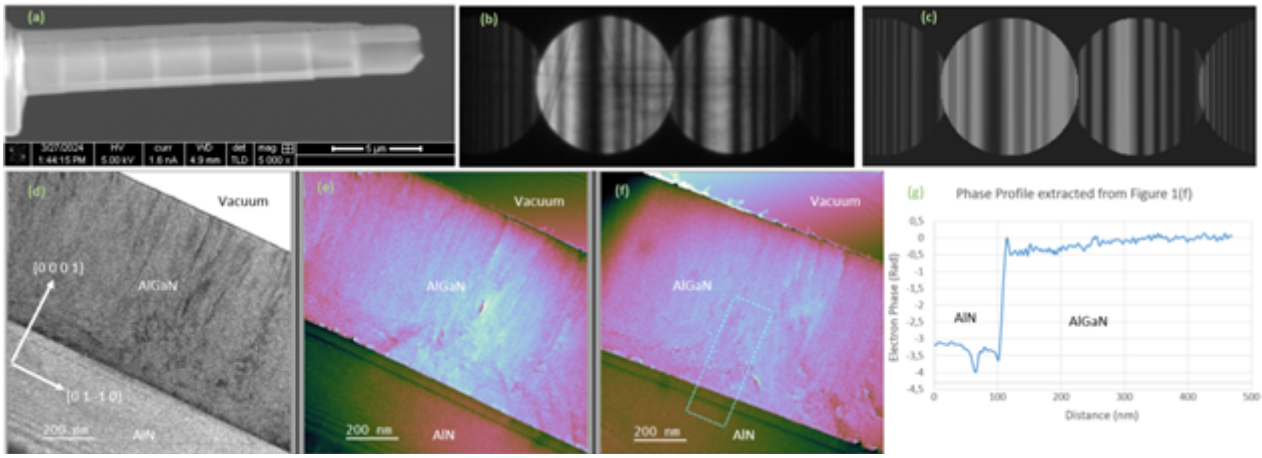


**Keywords:**

Electron holography, AlGaN, Ge doping

**Reference:**

[1] H. Amano, et al., J. Phys. D: Appl. Phys. 53, 503001 (2020).
[2] R. Blasco, et al., J. Phys. D: Appl. Phys. 52, 125101 (2019).
[3] M. R. McCartney et al., Appl. Phys. Lett. 76, 3055 (2000).
[4] M. Schowalter, Appl. Phys. Lett. 88, 232108. (2006).
[5] D.B Williams and C.B. Carter, Transmission Electron Microscopy; Springer US, (2009).

1002

# Structural and Electrical Characterization of $Hf_{0.5}Zr_{0.5}O_2$ Thin Films Crystallized by Rapid Thermal Annealing

Dr Jucheol Park[1], Miss Yeong Gyeong Park[1], Dr Min-Ho Kang[2], Mr Myung-Keun Lee[2], Mr Moon Seop Hyun[2]
[1]Gumi Electronics & Information Technology Research Institute (GERI), Gumi-si, Republic of Korea, [2]Department of Nano-process, National NanoFab Center (NNFC), Daejeon, Republic of Korea

Poster Group 2

Background incl. aims
High-k dielectric thin films such as $HfO_2$, $ZrO_2$ and $Hf_{0.5}Zr_{0.5}O_2$ for semiconducting memory devices was selected as model systems. Metastable orthorhombic phase of $Hf_{0.5}Zr_{0.5}O_2$ (HZO) has ferroelectricity and has been the potential materials to next generation nanoscale electronic devices based on its superior physical scalability. In order to increase the ferroelectricity of HZO, understanding the basic generation mechanism of ferroelectric crystalline phases is crucial and is investigated structurally and electrically in this study.

Methods
10 nm thick $Hf_{0.5}Zr_{0.5}O_2$ films were deposited using atomic layer deposition (ALD) on 200 nm thick TiN electrodes as the top and bottom was crystallized by post-metal rapid thermal annealing (RTA) in the temperature range from 400 to 900℃. The crystalline phase of HZO was determined with high-angle annular dark-field scanning transmission electron microscopy (HAADF-STEM) in TEM (JEOL, ARM-200F). The capacitance-voltage (C-V) characteristics were obtained by Agilent E4980A. Electrostatic Force Microscopy (EFM) and piezoresponse force microscopy (PFM) imaging was performed using NX-10 (Parks systems) on the HZO surface without the top electrode.

Results
From GI-XRD analysis results, the HZO samples annealed at 600 and 700 ℃ showed the higher orthorhombic phase and was consistent with the C-V measurement (Figure 1). The orthorhombic phase is confirmed with HR-STEM. The amplitude and phase images of EFM clearly showed the presence of ferroelectricity at the 600 ℃ RTA-treated sample. The C-V measurement showed that the dielectric constant was 8.8e-18 F/μm for a thickness of 10 nm and an area of $3.14e^4$ $\mu m^2$.

Conclusion
We investigated the basic generation mechanism of ferroelectric hafnia crystalline phases as a function of RTA temperature. We found that the higher ferroelectricity was shown from the samples annealed at 600 and 700 ℃ and that orthorhombic phases were dominant on the sample annealed at 600 ℃.

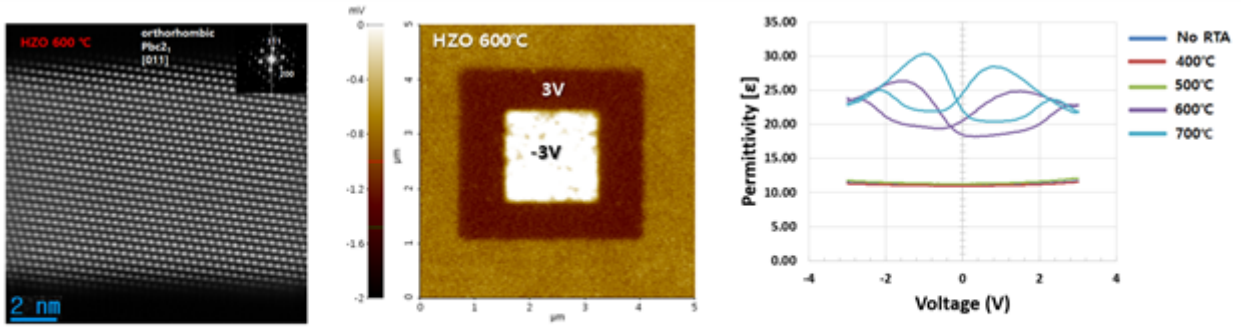


Figure 1. (a) HR-STEM image, (b) EFM image and (c) C-V curve of $Hf_{0.5}Zr_{0.5}O_2$ thin films.

**Keywords:**

$Hf_{0.5}Zr_{0.5}O_2$, Ferroelectricity, HR-STEM, EFM

**Reference:**

[1] Geun Taek Yu et al., New Physics: Sae Mulli, Vol. 71, No. 11, November 2021, pp. 890~900
[2] This research was supported by Basic Science Research Program through the National Research Foundation of Korea (NRF) funded by the Ministry of Education （NRF-2022R1F1A1063776）

1033

# Van der Waals heterostructures of nanopatterned 2D materials for novel device geometries

Michael Schlegel[1,2], Jonas Haas[1,2], Kevin Strobel[1,2], Teresa Tang[2], Prof. Dr. Jannik C. Meyer[1,2]
[1]Institute for Applied Physics at University of Tübingen, Tübingen, Germany, [2]Natural and Medical Sciences Institute at the University of Tübingen, Reutlingen, Germany

Poster Group 2

## Background

As Moore's Law starts to stagnate and the continuous pursuit of smaller and faster devices persists, there is a growing need for new approaches to further push the boundaries of nanofabrication. The modification and stacking of two-dimensional (2D) materials has significant importance in this context [1]. High precision structuring tools, such as a focused electron beam, can be employed to mill a wide range of structures into 2D materials [2], e.g., to modify their electronic properties. For example, creating a band gap in graphene [3] enables its use as a semiconductor in a variety of applications. By using customized sheets of 2D materials as building blocks, it should then become possible to produce almost any three-dimensional (3D) structure with properties that have been finely tuned to suit desired requirements [4].

## Methods

2D materials are structured by using scanning transmission electron microscopy (STEM). Clean samples are essential to the quality of the resulting structures. Therefore, to minimize contamination on the sample, a micro-electro-mechanical system (MEMS) chip is used for its ability to provide in situ heating. Investigation of the manufactured structures is done by transmission electron microscopy (TEM).

## Results

Atomically clean graphene samples have been successfully produced using the in situ heating of the MEMS chip. Furthermore, a wide range of structures using different STEM patterning parameters have been investigated. In order to open up a band gap within the graphene, large areas (600x600 nm) with small holes with a diameter of only 2-3 nm and a periodicity of 8 nm have been patterned. According to theoretical calculations, this introduced a band gap of approximately 0.6 eV into the graphene.

## Conclusion

The ability to work with contamination free 2D materials and the consequent high patterning resolution of the structures is very promising. Smaller structures will be in reach soon and thus, the possibility of larger bandgap openings within graphene becomes available. Ultimately, novel van der Waals heterostructures will be created by stacking modified layers of various 2D materials.

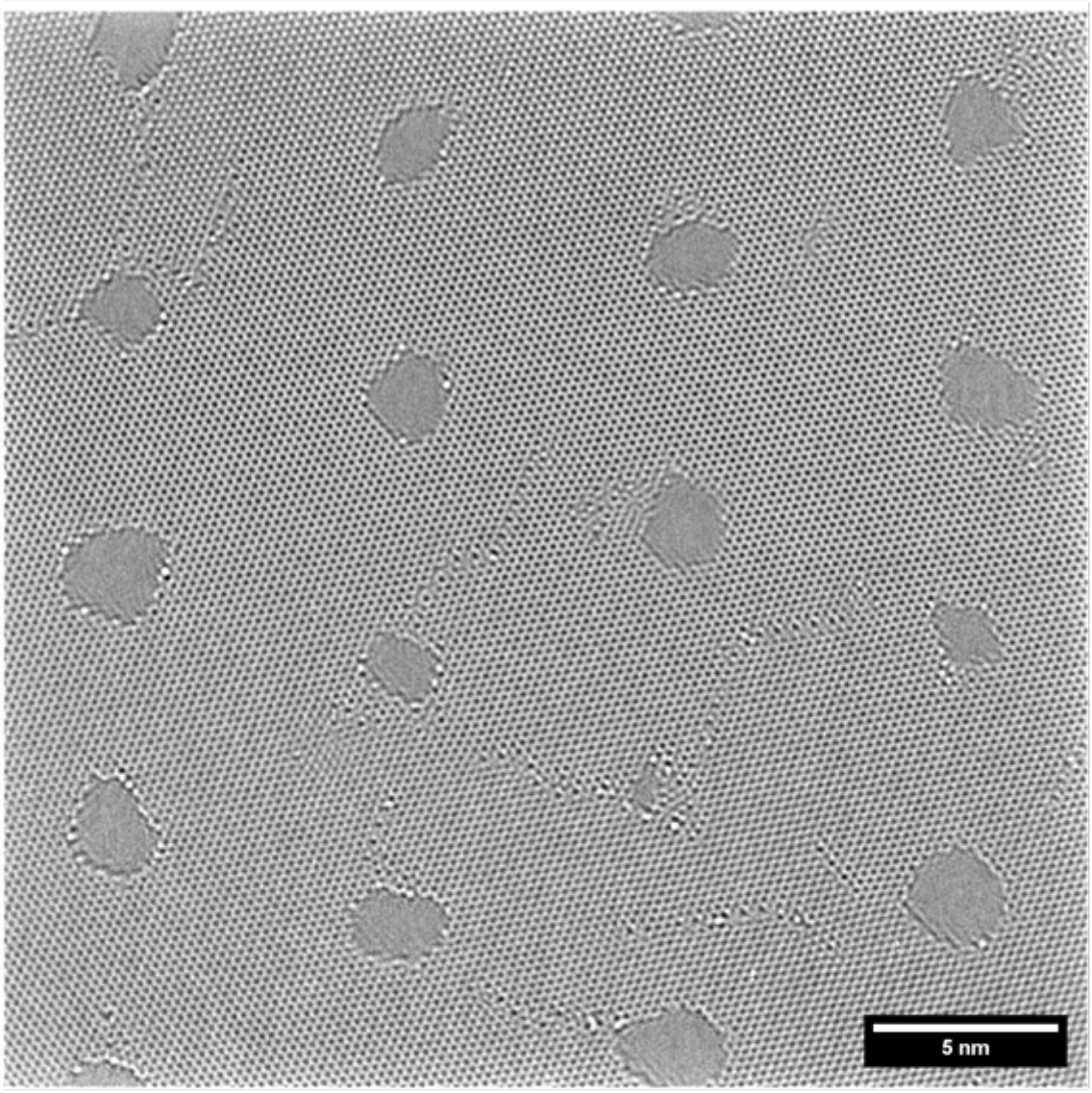


TEM image of atomically clean graphene, structured by STEM. The image is a small cut out from a large structure of over 5600 periodically placed (center to center distance: 8 nm) holes, each about 2-3 nm in diameter.

**Keywords:**

graphene, 2D materials, vdW heterostructures

**Reference:**

[1] M. G. Stanford et al., npj 2D Materials and Applications 2, Art. No: 20 (2018)
[2] M. D. Fischbein and M. Drndic, Appl. Phys. Lett. 93, 113107 (2008)
[3] B. Jessen et al., Nat. Nanotech. 14, 340 (2019)
[4] J. Haas et al., ACS Nano 16, 1836 (2022)
[5] We acknowledge funding by the German Research Foundation (DFG) under project ME3133/6-1.

1055

# Structural characterization of partially relaxed hybrid radial (Pb,Sn)Te/WZ-GaAs nanowires as candidates for topological insulator nano-devices

Dr Maciej Wójcik[1], M.sc Sania Dad[1], M.sc Wiktoria Zajkowska-Pietrzak[1], M.sc Piotr Dziawa[1], Prof. Slawomir Kret[1], Prof. Wojciech Pacuski[2], Prof. Janusz Sadowski[3]
[1]Institute of Physics, Polish Academy of Sciences, Warsaw, Poland, [2]Faculty of Physics, University of Warsaw, Warsaw, Poland, [3]Ensemble3 Centre of Excellence, Warsaw, Poland

Poster Group 2

Background incl. aims
Topological crystalline insulators (TCIs) belong to extensively investigated research area of topological quantum matter. The interest in TCIs stems from the presence of topologically protected Dirac states on high symmetry surfaces of TCI crystals. (Pb,Sn)Te solid solution is one representative of TCIs, with topological phase occurring above some critical Sn content. Since topologically protected states in TCIs are surface properties we have studied this material in quasi one dimensional nanowire (NW) geometry providing high surface-to-volume ratio. To further enhance the surface-related properties we have chosen to investigate core-shell NW heterostructures with wurtzite (WZ) GaAs cores and (Pb,Sn)Te shells instead of uniform NWs.
Methods
Core-shell NW heterostructures have been grown by molecular beam epitaxy using two distinct MBE systems dedicated to III-V, and IV-VI semiconductors. The interface structure of WZ-GaAs/(Pb,Sn)Te NWs is investigated using wide range of characterization techniques, such as high resolution transmission electron microscopy (HR-TEM), scanning transmission electron microscopy (STEM), geometric phase analysis (GPA) and energy dispersive x-ray spectroscopy (EDX).
Results
Misfit dislocations are observed as a direct result of the lattice mismatch between the core and the shell materials. Measured distances of moiré fringes match calculated spacings of misfit dislocations observed to be higher than the calculated values, suggesting the presence of a residual strain within the structures.
Conclusion
We have shown that (Pb,Sn)Te can be successfully grown as continuous full or half-shells on the sidewalls of GaAs NWs. This provides opportunity for investigation of topological surfaces of TCIs in the tubular geometry.
Acknowledgements: Funding from National Science Centre Poland, projects No: 2019/35/B/ST3/03381, 2019/35/B/ST5/03434 and 2017/27/B/ST3/02470

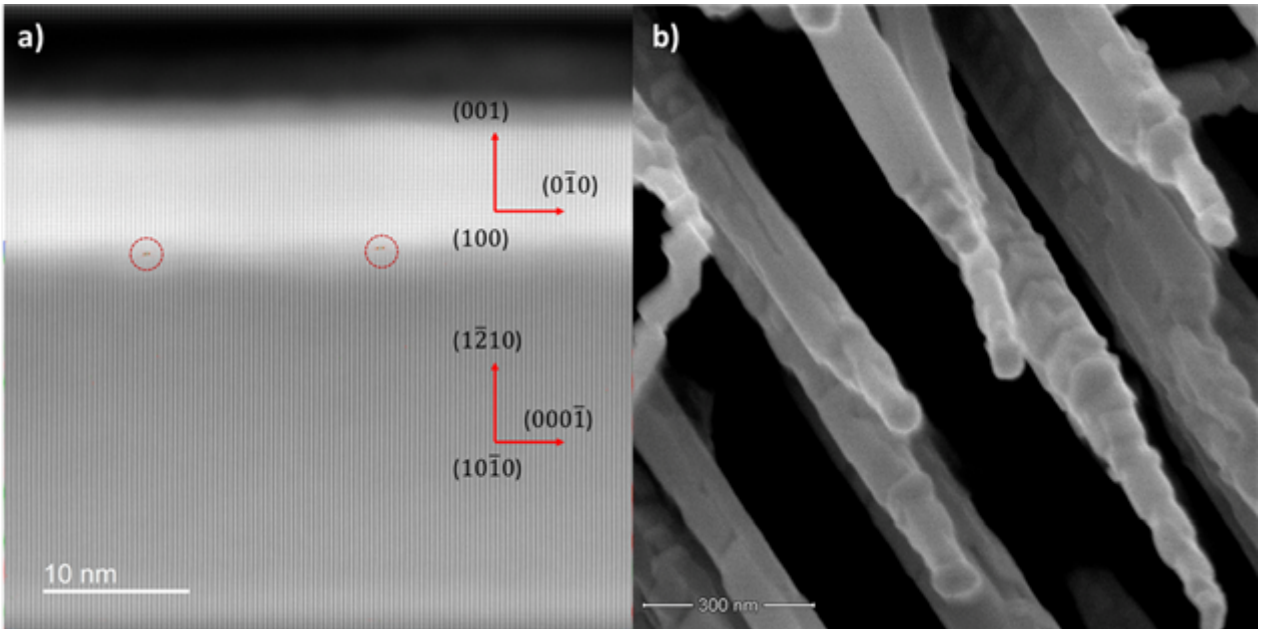


**Keywords:**

TEM, Nanowires, Topological Materials

**Reference:**

[1] Dad, S., Dziawa, P., Zajkowska-Pietrzak, W. et al., Sci Rep 14, 589 (2024)
[2] P. Dziawa, et al., Cryst. Growth Des. 10, 109 (2010)
[3] J. Sadowski, et al., Nanoscale, 10, 20772, (2018)

1096

# Nanowire field emitters fabricated using focused electron, gallium and helium ion beam methods

Ewelina Gacka[1], Krzysztof Kwoka[1], Tomasz Piasecki[1], Gregor Hlawacek[2], Bartosz Pruchnik[1], Ivo W. Rangelow[3], Andrzej Sierakowski[4], Paweł Janus[4], René Hübner[2], Teodor Gotszalk[1]
[1]Department of Nanometrology, Wrocław University of Science and Technology, 50-372, Wrocław, Poland, [2]Institute of Ion Beam Physics and Materials Research, Helmholtz-Zentrum Dresden-Rossendorf, 01328, Dresden, Germany, [3]Technische Universität Ilmenau, 98693, Ilmenau, Germany, [4]The Łukasiewicz Research Network - Institute of Microelectronics and Photonics, , Poland

Poster Group 2

Background incl. aims

Devices whose operation is based on the field emission phenomenon are widely used and continuously developed. Among the numerous categories, vacuum microelectronics stands out. In previous decades, the fabrication of field emitters based on the Spindt method was developed[1]. This is a multi-step method based on etching and deposition of selective areas on a volumetric substrate. The extremely attractive topic of integrating field emitters with microelectromechanical systems (MEMS), acting as nano- and picometrology sensors, has now emerged[2]. However, the fabrication of multicomponent micro- and nanodevices in a single process line is a challenge. Therefore, combining different manufacturing technologies should be considered. A method that enables the creation of planar and three-dimensional nanodevices is a combination of focused-electron-beam-induced deposition (FEBID) and focused-ion-beam-induced deposition (FIBID)[3]. This is a one-step, so-called direct-writing method. The material of the deposited nanodevice is defined by the precursor used. Its shape is determined by the scanning motion of a focused beam with nanometre and sub-nanometre cross sections. The equipment that enables the fabrication of ultra-sharp field emitter tips is the scanning electron microscope (SEM) with a focused gallium ion beam (Ga-FIB) and the helium ion microscope (HIM). A commonly used material is tungsten[4] due to its good thermal and electrical conductivity, low work function and the ability to sustain high current densities. However, platinum is also of interest due to its high chemical inertness[5]. In this work, nanowire platinum and tungsten field emitters fabricated by the FEBID and FIBID (Ga and H) process will be shown for the first time. The field emitters will be integrated into microcantilevers manufactured by photolithography, acting as nanosensors of their deflection. The field emission phenomenon will be studied and the operation of the nanosensors will be evaluated.

Methods

A Helios Nanolab 600i SEM with FIB equipped with MeCpPtMe3 precursor and a Zeiss Orion Nanofab HIM containing W(CO)6 precursor were used for microcantilever modification and deposition of nanowire field emitters. During the FEBID and FIBID process, precursor molecules are injected into the vacuum chamber of the microscope. The primary focused electron/ion beam induces secondary electrons from the sample surface, which have the required energy to decompose the precursor molecules. Hence, in the vicinity of the scan area the material grows, leading to the fabrication of the field emitter nanowire. In order to prepare the microcantilever for field emitter deposition and eliminate the risk of short-circuiting the electrodes due to the existence of the halo effect, the microstructures were modified by milling with a focused gallium/neon beam. Leakage currents between the electrodes were measured before depositing the field emitters on them. The field emission phenomenon was characterised in the vacuum chamber of the microscope, using a self-designed electronic setup, a source measurement unit Keithley 2614 and software written in the LabVIEW environment. Analysis of the nanowire material composition was conducted with an energy-dispersive X-ray detector attached to a transmission electron microscope.

Results

Calibration of the growth of platinum and tungsten nanowires was performed using SEM-FIB and HIM, respectively, for specific values of beam current, accelerating voltage, dwell time, beam spacing, and precursor pressure. Field emission enhancement factor calculations were made to optimise the emitter shape. Microcantilever modifications were performed using a focused gallium and neon ion beam (Figure 1a). Spatial holes were milled between adjacent electrode paths dedicated to the integration of field emitters on the microcantilever. The aim was to separate them permanently, minimising the risk of short-circuiting due to the halo effect associated with the FEBID and FIBID process. Leakage currents between adjacent electrode paths were measured in the range of +/-100 V. Measurement values oscillated in the pA regime. Planar nanowires, as field emitters, were then deposited with a distance of about 100 nm between them (Figure 1b,c). In situ field emission measurements were conducted for the fabricated structures. Field emission from 50 V was recorded for the platinum field emitters with a distance of 150 nm between the electrodes. For tungsten field emitters and a cathode-to-anode distance of 120 nm, the threshold voltage of field emission was equal to 70 V. The stability of the emitter operation over time was verified, together with an analysis of the emitter material composition before and after operation.

Conclusion

This work presents a fabrication technology for nanowire field emitters by the FEBID and FIBID process, using two different precursors - MeCpPtMe3 and W(CO)6. The technique of integrating FEBID/FIBID nanodevices with microcantilevers produced in photolithography steps was developed. The characterisation of the field emission phenomenon was undertaken as a basis for investigating the usability of a microcantilever deflection sensor.

Acknowledgements

Financial support has been received from the National Science Centre, Poland PRELUDIUM-21 grant [“Nanometrology of field emission phenomena from electron beam deposited nanowires operating as nano- and picodeflection sensors – FEmet”, no. 2022/45/N/ST7/03049], a short term scientific mission funded by the COST Action [no. CA19140, http://www.fit4nano.eu/] and the National Science Centre, Poland OPUS grant [“Nanometrology of Nottingham cooling effect using operational microelectromechanical systems”, no. 2020/37/B/ST7/03792]. Furthermore, the use of the HZDR Ion Beam Center TEM facilities is acknowledged.

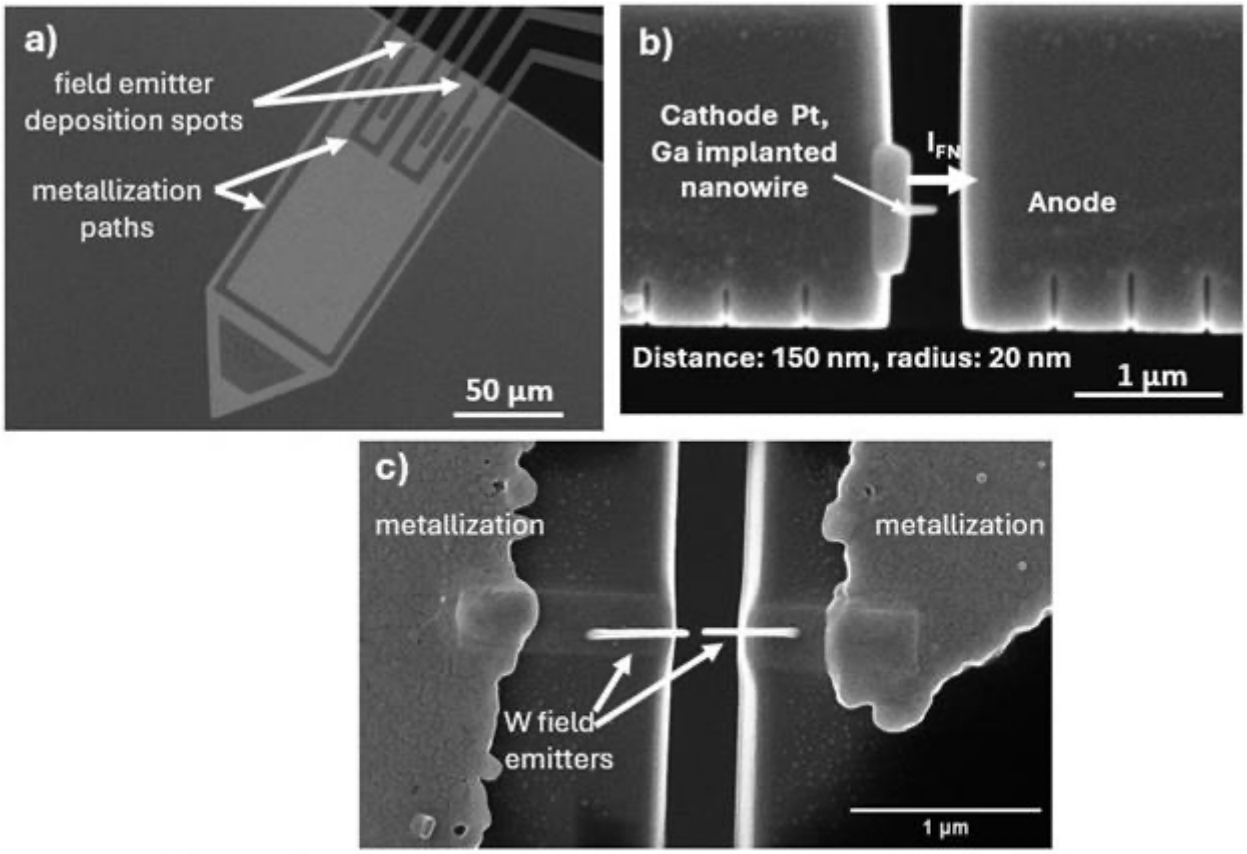


Figure 1: (a) Cantilever as a platform for depositing field emitters; (b) platinum nanowire field emitters deposited by scanning electron microscope; (c) tungsten nanowire field emitters deposited by helium ion microscope.

**Keywords:**

Field emitters, SEM, HIM, MEMS

**Reference:**

[1] C. A. Spindt et al., https://doi.org/10.1109/16.88525.
[2] I. W. Rangelow et al., https://doi.org/10.1116/1.4992073.
[3] I. Utke et al., https://doi.org/10.1116/1.2955728.
[4] A. V. Crewe et al., https://doi.org/10.1063/1.1683910.
[5] T. Piasecki et al., https://doi.org/10.1088/1361-6528/ad13c0

1121

# Investigation of composition and origin of the intermediate layers at the Ga2O3/AlN and Ga2O3/Al2O3 interfaces

Dr. Marco Schowalter[1], S. Raghuvansy[1], Dr. A. Karg[1], Dr. P. Vogt[1,2], Dr. D. Schlom[3], Dr. D. Jena[3], Dr M. Eickhoff[1,2], Dr. A. Rosenauer[1,2]
[1]Institut für Festkörperphysik, Universität Bremen, Bremen, Germany, [2]MAPEX center for material science and processes, Universität Bremen, Bremen, Germany, [3]Department of Material Science and Engineering, Cornell University, Ithaca, USA

Poster Group 2

Background incl. aims
Intermediate layers have been observed at the interfaces between $Ga_2O_3$ and $Al_2O_3$ [1] as well as $Ga_2O_3$ and AlN [2]. These layers exhibit the crystal structure of the substrate but with altered composition. For the first heterostructures, stabilization of the intermediated layer due to strain was proposed under the assumption of pure α-$Ga_2O_3$. Recently, it was shown that the composition is about 25% Ga [3] only. To better understand their physical origin, the composition of samples grown under different conditions were investigated using TEM and complemented by DFT computations.

Methods
For composition determination different methods were employed: energy dispersive x-ray spectroscopy (EDX) evaluated using ThermoFisher's Velox software, composition determination from quantitative HAADF-STEM [4] and strain state analysis from measurement of atomic distances [5]. Measurements were carried out in a probe-corrected ThermoFisher Spectra 300 and an imaging-corrected FEI Titan 80-300 on specimens prepared using a FEI Nova 200 FIB by the lift-out technique. DFT studies were performed using VASP [6]. Specimens were grown by molecular beam epitaxy (MBE), MOCATAXY [2] and suboxide MBE [2].

Results
Fig. 1 a) and b) show a HRSTEM image and a Ga concentration profile measured on a $Ga_2O_3/Al_2O_3$ interface formed by MBE in conditions, where actually no growth can be observed. The afore mentioned α-$(AlGa)_2O_3$ intermediate layer with a Ga concentration of about 25% can be seen as the layer with higher intensity. The composition of this sample formed at 300 °C for 3 minutes was rather similar to samples obtained at 700 °C for 180 minutes and at 700 °C for 3 minutes. This result shows that the composition significantly differs from the one (100% Ga) proposed in Schewski et al. [1]. To elucidate whether the layer stabilizes due to strain for the low concentration, DFT computations were carried out. For that, strained and unstrained α- and β-$Ga_2O_3$ unit cells were generated and Al atoms according to different concentrations were substituted. All possible atomic configurations in 1x1x1 cells were considered. Their mean values and respective standard deviations are displayed in Fig. 2 a) as function of Ga concentration. In general, the strained β-phase has significantly higher energy compared to all other cases due to the very large strain. In the limits (100% Ga and 0% Ga) unstrained β-$Ga_2O_3$ and α-$Al_2O_3$ are found to be energetically lowest as expected. This means that critical concentrations exist at which the energies of the 3 cases cross: Strained α-$(AlGa)_2O_3$ was found lower in energy up to Ga concentrations of 33% compared to β-$(AlGa)_2O_3$. β-$(AlGa)_2O_3$ becomes lower in energy than unstrained α-$(AlGa)_2O_3$ above about 62 % Ga. This shows that the occurrence of the layer can be explained just by its low concentration. In order to elucidate its origin further, $Al_2O_3$ surface slabs were generated in which two Al atoms were substituted by Ga atoms, respectively. Fig. 2 b) shows the energy difference between a cell, in which both Ga atoms were in the 2 topmost layers compared to cells where one Ga atom is in the topmost layer and the second atom is placed deeper in the slab as a function of distance of the second atom to the top atom. Two

cells could be identified for which the second atom being deeper in the crystal was energetically lower than both atoms close to the surface. These special positions were found within the topmost 3 atomic double layers and thus, it could be possible that Ga atoms chemisorbing can diffuse into the topmost 3 double layers of the substrate resulting in an effective concentration of 33% Ga. Fig. 1 c) and d) show HRSTEM images of MOCATAXY (with In as catalyst) and suboxide MBE grown $Ga_2O_3$/AlN samples. A bright layer with wurtzite type crystal structure can be observed similar to the $Ga_2O_3$/$Al_2O_3$ interfaces. In e) respective relative lattice distance profiles are shown for both samples. Simulated lattice distances as a function of Ga concentration are depicted in f). For the suboxide MBE the comparison results in a nearly pure GaN composition of the layer, whereas for the MOCATAXY sample the measured lattice distance is larger than all simulated ones indicating that In atoms have been incorporated into the layer. Note, that we neglected O incorporation in these considerations. Further studies in this direction are under way.

Conclusion

Our measurements and computations for the $Ga_2O_3$/$Al_2O_3$ interface show that the intermediate layer's composition is significantly smaller than assumed in previous publications and its occurrence can be explained by the low Ga concentration. For the $Ga_2O_3$/AlN interface a nearly pure GaN layer was found, possibly containing In in the case of In-mediated MOCATAXY.

Keywords

Composition determination, DFT, $Ga_2O_3$

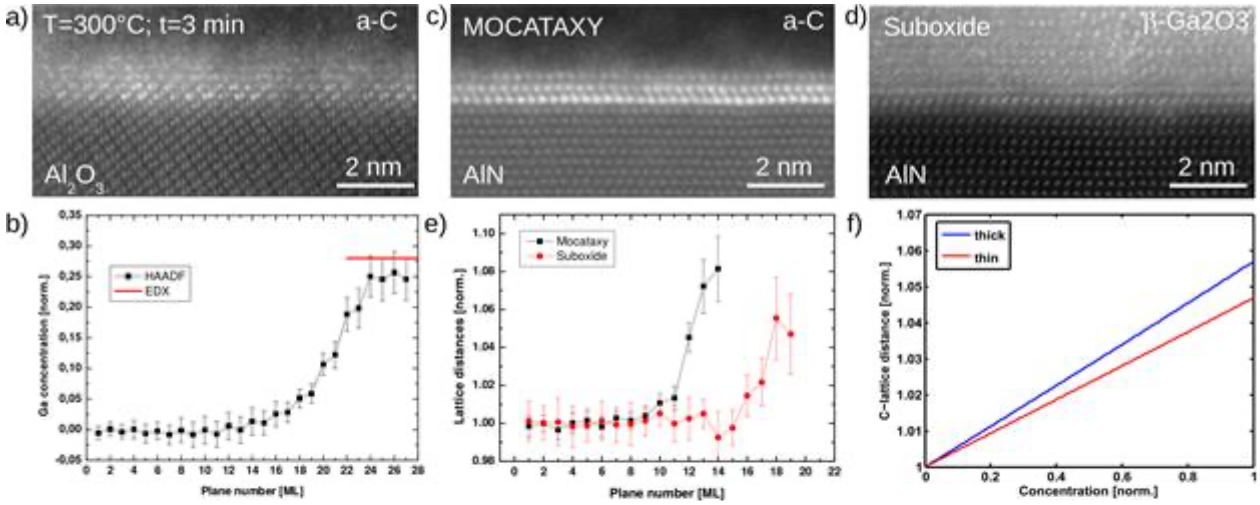


**Fig. 1:** a) HRSTEM image of the $Ga_2O_3/Al_2O_3$ interface. b) Ga concentration measured from HAADF and EDX showing a composition of about 25% and 28%, respectively. The composition is comparable with other samples grown at higher temperatures and for longer growth times. c) and d) HRSTEM images of the $Ga_2O_3$/AlN interface for a MOCATAXY- (In as surfactant) and suboxide grown sample. In both samples the crystal lattice of the substrate is preserved at the interface but a higher contrast indicates a finite Ga concentration e) Measured normalized c-lattice distances for the MOCATAXY and the suboxide sample. f) Computed c-lattice distance as function of Ga concentration. By comparison a nearly pure GaN composition can be determined for the suboxide sample. For the MOCATAXY sample the measured lattice distance is larger than the maximum theoretical one indicating an incorporation of In.

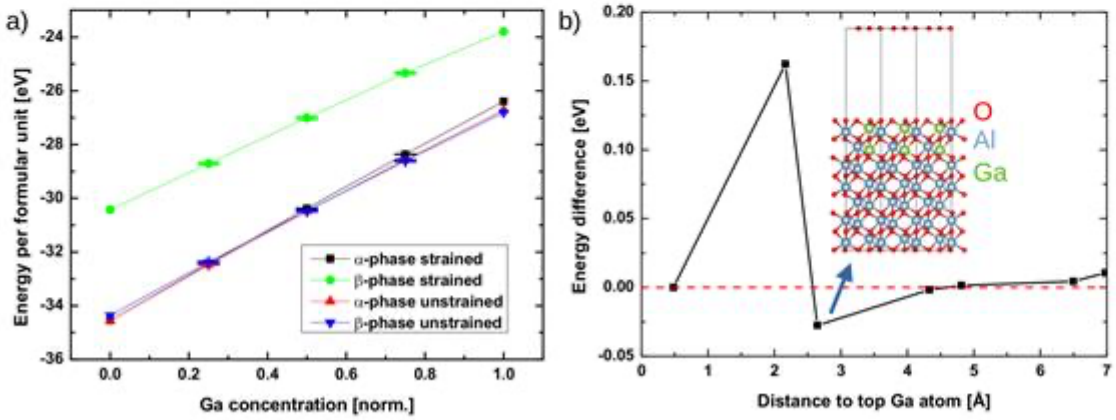


**Fig. 2:** a) Energy per formular unit of unstrained α- and β-phase cells as well as respective cells strained biaxial to the $Al_2O_3$ substrate. For the strained cells lattice plane distances in growth direction were relaxed using DFT. Errorbars indicate standard deviations over all possible atom configurations in the 1x1x1 cells. b) Energy difference of $Al_2O_3$ surface slabs with different substitutions of 2 Al atoms by Ga as a function of distance of the second Ga atom to the top Ga atom. The energy difference is computed w.r.t. the reference structure, which has 2 Ga atoms in the two top metal layers. For the shown series the position of the top atom is kept fixed and the second atom is placed deeper in the slab. Two cells are found to exhibit lower energy as the reference cell.

**Keywords:**

Composition determination, DFT, $Ga_2O_3$

**Reference:**

[1] R. Schewski et al.: Appl. Phys. Exp. 8, 011101 (2015).
[2] S. Raghuvansy et al.: Appl. Phys. Lett. Mater. 11, 111113 (2023).
[3] A. Karg et al.: Cryst. Growth Des. 23, 4435 (2023).
[4] A. Rosenauer et al.: Ultramicroscopy 111, 1316 (2011).
[5] A. Rosenauer et al.: Optik 102, 63 (1996).
[6] G. Kresse and J. Hafner: Phys. Rev. B 47, 558 (1993).

1159

# Real-Time Studies of Resistive Switching Mechanisms

Dr. Janghyun Jo[1], Xue Bai[1], Stephan Aussen[2], Sebastian Walford[3], Susanne Hoffmann-Eifert[2], Martin Salinga[3], Rafal E. Dunin-Borkowski[1]
[1]Ernst Ruska-Centre for Microscopy and Spectroscopy with Electrons, Forschungszentrum Jülich, Jülich, Germany, [2]Peter Grünberg Institut (PGI-7), Forschungszentrum Jülich, Jülich, Germany, [3]Institute of Materials Physics, University of Münster, Münster, Germany

Poster Group 2

Background incl. aims
Demands for increased information density in nanoscale devices used for applications in artificial intelligence and the internet of things (IoT) are resulting in the need for improved data storage and processing technologies. As current memory technologies are approaching their fundamental limits, so the development of architectures for novel memory devices, such as in-memory computing and neuro-inspired computing devices, is becoming more important. Memristive or resistive random-access memor (ReRAM) devices promise to provide non-volatile, fast, low-power and cost-effective technologies, and are leading candidates to replace flash memory in a broad range of applications, including high-density memory, low-power IoT devices, neuromorphic computing, sensors and security applications [1-5]. Phase change memory (PCM) devices based on chalcogenides and valence change memory (VCM) devices based on oxides are promising candidate materials for non-volatile ReRAM devices because they offer possibilities to encode information reversibly and rapidly.
The switching mechanisms of such devices are typically based on local changes in resistivity between a high resistance state (HRS) and a low resistance state (LRS). Local high spatial resolution imaging and spectroscopy, in combination with real-time electrical measurements, are required to understand fundamental aspects of resistive switching in both PCM and VCM devices, and in turn to achieve improvements in scalability, reliability and speed. Transmission electron microscopy (TEM) is a powerful technique that can be used to provide information about local variations in crystal structure, composition, phase, and electronic structure of materials. Therefore, studies of the details of where, when and how resistive switching processes take place in different material systems using TEM are of great interest to unravel resistive switching mechanisms.

Methods
In order to realize real-time electrical biasing in the TEM, either home-made chips with electrical contacts were fabricated using micro-electromechanical systems (MEMS) technologies, or a Nanofactory probing specimen holder was used to provide a moveable electrical contact to a TEM specimen. Reproducible switching of different materials systems was recorded using different TEM techniques, such as off-axis electron holography, four-dimensional scanning TEM (4D-STEM), energy-dispersive X-ray spectroscopy, and electron energy-loss spectroscopy (EELS). Efficient and reliable methods to extract meaningful features from complex and large datasets were developed using machine learning technologies, for example for differentiating between crystalline and amorphous phases, and between different valence states in oxides.

Results
For PCMs, scanning nanobeam electron diffraction in 4D-STEM was used to study $Ge_2Sb_2Te_5$ (GST) thin films to investigate local variations in their crystalline structure. Data processing methods were developed to differentiate between crystalline and amorphous phases, in order to identify local distributions of crystalline phases in amorphous GST thin films. For VCMs, resistive switching mechanisms in $TiO_2$-based ReRAM devices were investigated in real time using correlative transmission X-ray microscopy in the synchrotron and EELS in the TEM. The formation of conductive

filaments in oxides was confirmed by extracting features from noisy spectra using non-negative matrix factorization.

Conclusions

Advanced TEM techniques combined with real-time electrical biasing and machine learning allow resistive switching mechanisms to be studied in different material systems. Local changes in chemical composition, microstructure and electronic properties in PCM and VCM devices during resistive switching can be investigated successfully. These approaches are expected to lay the foundation for the development of advanced next-generation memory devices.

**Keywords:**

TEM, resistive switching, real-time electrical-biasing

**Reference:**

[1] T. Guo et al., ACS Appl. Mater. Interfaces. 12, 54243 (2020).
[2] M. Lanza et al., Science, 376, 1066 (2022).
[3] D. V Christensen et al., Neuromorphic Comput. Eng. 2, 022501 (2022).
[4] W. Banerjee et al., Small, 18, 1 (2022).
[5] S. Brivio et al., Neuromorphic Comput. Eng. 2, 042001 (2022).

1217

# Multi-scale characterisation of laser-induced defects in the production of heterojunction photovoltaic cells

Dr Anacleto Proietti[1], Dr Luca Buccini[1], Dr Pierfrancesco Atanasio[1], Dr. Giancarlo La Penna[1], Dr. Chiara Mancini[1], Dr. Corrado Di Conzo[1,3], Dr. Francesco Mura[1,2], Dr Marco Galiazzo[4], Dr Nicola Frasson[4], Prof. Daniele Passeri[1,2], Prof. Marco Rossi[1,2]
[1]Department of Basic and Applied Sciences for Engineering, Sapienza University of Rome, Rome, Italy, [2]Research Center for Nanotechnology applied to Engineering of Sapienza University of Rome (CNIS), Rome, Italy, [3]Department of Applied Science and Technology (DISAT), Polytechnic of Turin, Turin, Italy, [4]Applied Materials Italia, , Italy

Poster Group 1

Background incl. aims:
Silicon-based HeteroJuncTion solar cells (HJT or SHJ) are a family of photovoltaic cells based on the heterojunction formed between two materials with different bandgaps. They are hybrid devices combining the technology of classical crystalline silicon-based cells and thin-film cells.
HJT are now a well-established reality as they guarantee high efficiency and mass production [1], however they suffer of slight losses of the cell integrity when they are cut and assembled with a shingled structure. In this study, a mass-produced HJT cell surface was scribed for half of its thickness employing an ns-IR laser. Subsequently, the cell is separated in sub-cells by mechanically cleaving. This process is both stressful for the cell structure due to the high level of thermalization and is also locally removing the passivation layer of the newly cut edges. These mechanisms induce a drop in performance at the edges of the cell, hindering the advantages of shingled technology [2].
In this study, defects induced by the cut were characterized using different multi-scale techniques to identify the technological solution that would allow the cell structure to be protected as much as possible.

Methods:
The sample object of the study is a HJT cell with a bulk structure based on n-type silicon and a multi-layer passivation surface composed of 3 thin layers of intrinsic amorphous silicon doped with hydrogen (15-20 nm), n-doped amorphous silicon doped with hydrogen (15-20 nm) and indium thin oxide (ITO) (70-80 nm) provided by Applied Materials. The cut was performed with an ns-IR laser (Rofin Powerline F50) on an entire wafer (156,75 mm side) on several lines, while a second pristine wafer was used as a comparison.
The techniques used were X-Ray Diffraction (Bruker D8 ADVANCE), Raman and Photo-Luminescence spectroscopy (Renishaw InViaTM), Scanning Electron Microscopy (Zeiss Auriga) equipped with EdX Spectroscope (Bruker Quantax) and with Focused Ion Beam (Physics d'Orsay Cobra) and Atomic Force Microscopy (Oxford Instruments Cypher VRS).

Results:
The analyses, focused on the detection and identification of defects in the pristine and post-cut wafer, were initially concentrated on the physical-chemical characterization of the basic structure. The XRD analyses show that after laser cut, the ITO main peak disappears or consistently decreases its intensity, thus indicating a loss of crystallinity or even a detachment from the surface. Moreover, the silicon beneath ITO layers seems affected by the high energy laser treatment and in particular the strongest peak of Si (400) shows an increase in the strained component. In fact the pristine HJT sample shows, by means of XRD, a double peak of Si (400) with two relative maximum values at 30.3 deg and 30.4 deg (with a Mo tube). The relative amount of strained silicon (i.e. the intensity of the

peak at lower angle and therefore higher interplanar distance) appears increased, such behaviour might indicate an annealing of the sample due to the high energy treatment.
Through Raman and PhotoLuminescence (PL) analyses, it was then possible to assess the presence of crystalline defects within the silicon of both the pristine and post-cut wafers, with a clear splitting of the silicon peak in the case of Raman spectroscopy and a decrease in the Band To Band transition of the silicon in the case of PhotoLuminescence spectroscopy.
The morphology and chemical composition of these defects were then studied using scanning electron microscopy and atomic force microscopy. The surface structure is composed of square-based pyramids necessary to maximize the active surface of the cell. The pristine wafer presents mechanical defects derived from the production phase which cause the removal of the surface layer of ITO and thus an initial random decrease in the cell's performance. Once the laser cut has been performed, however, a complete destruction of the structure can be seen in the proximity of the cut. Moving away from the cut up to about 1 mm, a gradual improvement of the integrity of the structure can be seen until its complete recovery. Afterwards, in addition to the vast damage to the structures around the cut area due to the very high temperatures, the presence of silicon-based particles of various sizes scattered throughout the sample was observed causing a masking effect which decreases the cell’s efficiency. Finally, viscoelastic and EDX maps were made on both the intact and cut zones unveiling that the ITO is not completely ablated; on the contrary, it tends to follow the reorganization of the silicon-based substrate, as also demonstrated through FIB-SEM. The viscoelastic maps revealed that the hardness of the sample strongly depends on the size of the ITO layer and, in the areas away from the cut, there is also a clear directional trend in hardness and thus in ITO thickness. This variation in thickness, although not critical, causes a heterogeneity that makes it easier to ablate the ITO in areas close to the cut.

Conclusion:
A complete characterization and identification of defects within HJT cells (both pristine and post-cut) was conducted. Several defectivities, of structural, mechanical and thermal nature were identified and characterized. The defects on the pristine wafer show that there is still room to optimize the synthesis of these materials in order to improve their final performances. Finally, through the study of the cut-induced defects, it was possible to demonstrate the causes of the decrease in the performances of this type of cell after the cutting and shingling process, something which has been already widely reported in literature.

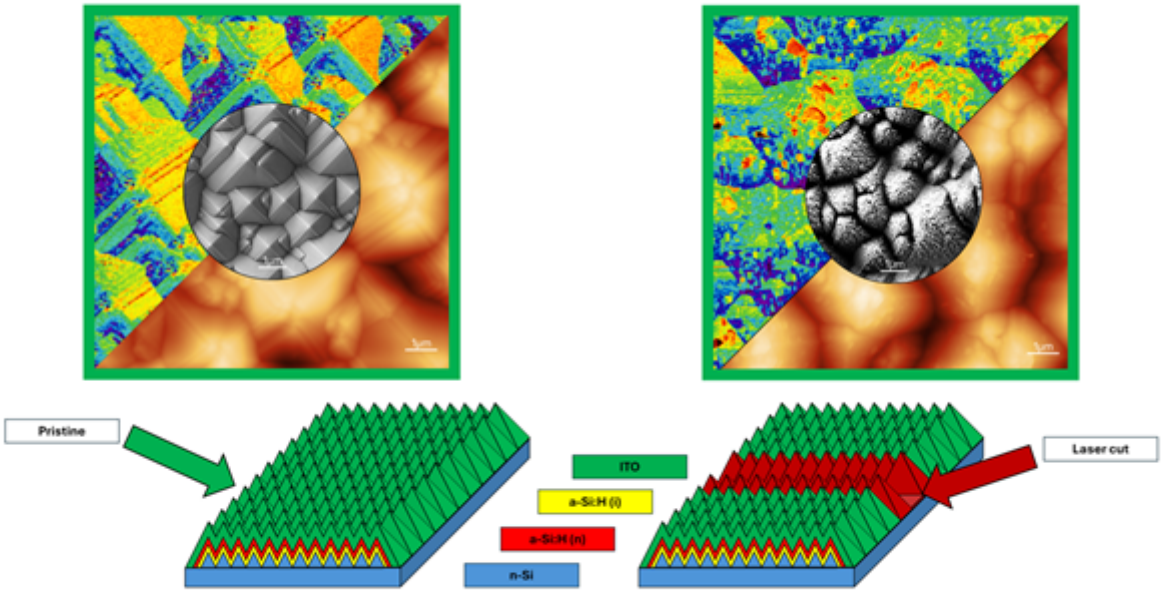


**Keywords:**

Photovoltaic, Multiscale Characterisation, Defect Analysis

**Reference:**

[1] X. Ru, & al., “Silicon heterojunction solar cells achieving 26.6% efficiency on commercial-size p-type silicon wafer”, Joule, Vol. 8 (4), pp. 1092-1104 (2024).
[2] F. Dhainaut, & al., “Edge passivation of shingled poly-Si/SiOx passivated contacts solar cells”, EPJ Photovoltaics, Vol. 14 (22), (2023).

1251

# Phase Transformation of GeO2 Glass to Nanocrystals via High-Temperature Annealing

Dr JIJUN ZHANG[1], Wenshan Chen[2], Thilo Remmele[1], Dr. Hans Tornatzky[2], Dr. Oliver Bierwagen[2], Dr. Dan Zhou[1], Dr. Martin Albrecht[1]
[1]Leibniz - Institut für Kristallzüch, Max-Born-Straße 2, 12489 Berlin, Germany, [2]Paul-Drude-Institut für Festkörperelektronik, Leibniz-Institut im Forschungsverbund Berlin e.V., Hausvogteiplatz 5-7, 10117, Berlin, Germany

Poster Group 1

## Background

Germanium dioxide (GeO2) is an advanced semiconductor material characterized by an ultrawide band gap ranging from approximately 4.6 to 6.2 eV [1], depending on its concrete crystal phase and doping level. This wide gap renders GeO2 well-suited for high-power and high-frequency electronic devices. Establishing precise correlations between thermal processes, structure evolutions, and electrical properties is essential for understanding fundamental mechanisms and achieving high-performance semiconductor materials.
This study utilizes SEM, XRD, and TEM to investigate the phase transformations of GeO2 from amorphous to crystalline phases triggered by a controlled annealing process.

## Methods

An approximately 1 µm thick amorphous GeO2 layer was deposited on c-plane sapphire (Al2O3 {0001}) wafers at 300 °C by plasma-assisted molecular beam epitaxy (PAMBE). These layers were subsequently subjected to annealing in an oxygen environment at temperatures of 1000°C, 1100°C, and 1200°C for a duration of six hours. The resulting samples were directly analyzed by SEM and XRD. And the cross-section samples were prepared by FIB for TEM investigations.

## Results

The figure depicts bright field TEM images, high-resolution TEM images, and corresponding fast Fourier transition (FFT) patterns of $GeO_2$ layers subjected to thermal treatment at temperatures of 1000°C, 1100°C, and 1200°C, respectively. After annealing at 1000°C for 6 hours (figures a-c), mainly circular, with occasional hexagonal crystalline grains of quartz phase GeO2 (α-GeO2) emerged in the amorphous matrix, typically between 10-20 nm in size. With further heating to 1100°C, these nanograins, as seen in figures d-f, evolved within the amorphous matrix to larger crystals between 10 and 60 nm. Further annealing under 1200°C (figures g-i) completely transformed the amorphous phase into crystalline. Meanwhile, a phase transition from the hexagonal quartz to the tetragonal rutile was observed. This transition coincides with non-homogeneous grain growth in GeO2, i.e. one grain grew to over 20 times the mean grain size depicted in figures (g, h). Such grain growth highlights the dynamic nature of the phase transformation process within the GeO2 layers when subjected to elevated temperatures. Further results, such as the XRD patterns and ESD analysis, will be presented on-site.

## Conclusion

This comprehensive investigation provides insights into the structural evolution and phase transformations of $GeO_2$ under varying thermal conditions. It offers valuable information for further understanding of the properties and behaviors in different temperature regimes.

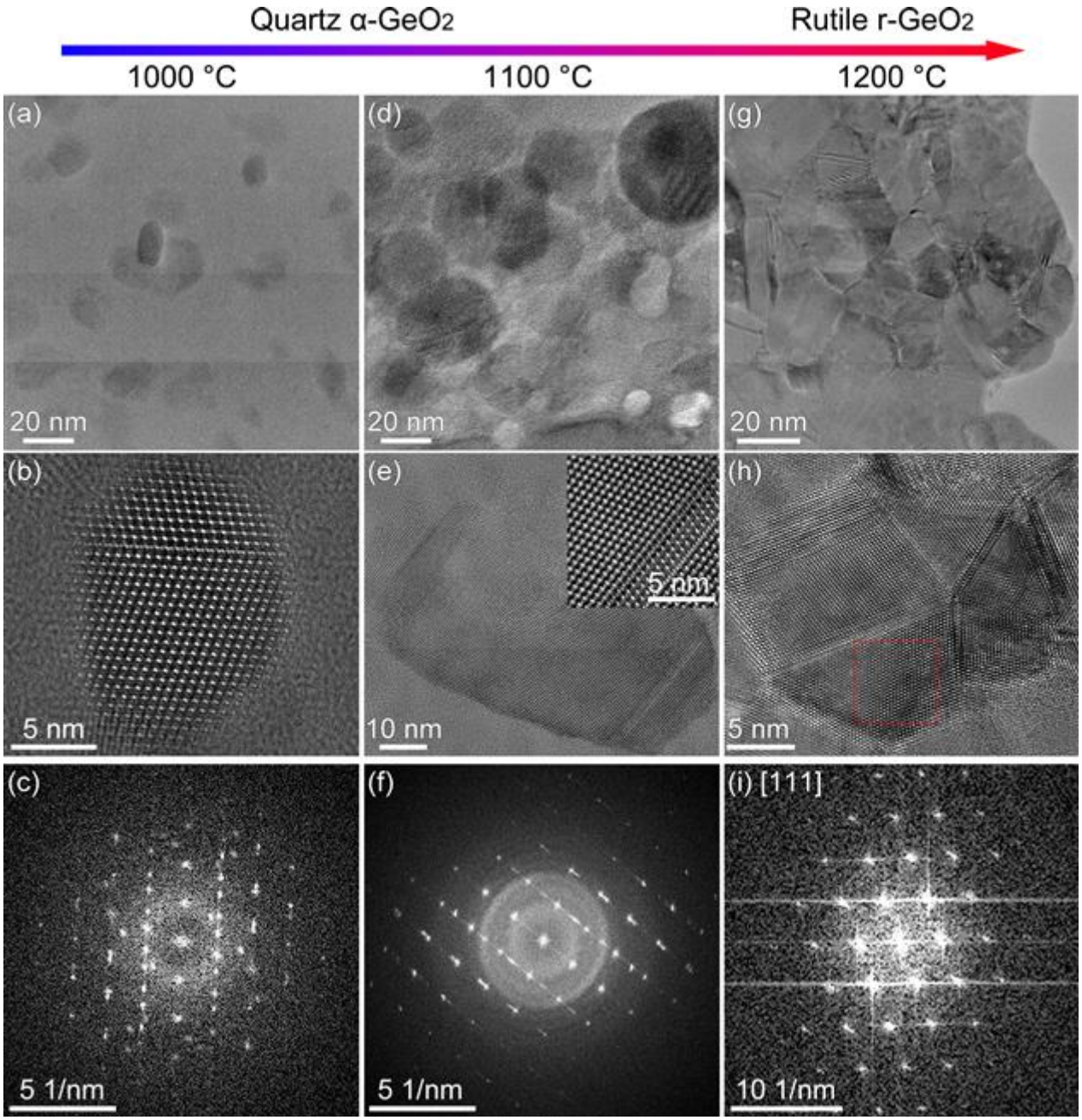


**Keywords:**

GeO2, phase transformation, grain growth

**Reference:**

[1] Nam K, Oh J H, Bae J S, et al. Effects of heat treatment on the microstructure and optical properties of sputtered GeO2 thin films. Advanced Engineering Materials, 2023, 25(17): 2300456

1331

# Screening of surface Fermi level pinning governs contrast of modulation-doped n-type GaN by electron holography

Dr. Keyan Ji[1], Dr. Michael Schnedler[1], Dr. Qianqian Lan[1], Dr. Philipp Ebert[1], Prof. Dr. Rafal E. Dunin-Borkowski[1]
[1]Ernst Ruska-Centre for Microscopy and Spectroscopy with Electrons (ER-C-1), Forschungszentrum Jülich GmbH, Jülich, Germany

Poster Group 1

Background incl. aims
Quantifying electrostatic potentials in semiconductors at high spatial resolution is essential for understanding and optimizing the performance of semiconductor devices. Various electron beam-based microscopy techniques are employed to achieve this goal. Among these techniques, electron holography in a transmission electron microscope (TEM) has proven particularly effective for demonstrating the interface potential in p-n junctions and heterostructures. This technique provides highest energy precision at nm scale resolution, while minimizing electron beam induced damage to the sample. However, previous studies have revealed intriguing results. In particularly, the electron optical phase contrast observed across p-n junctions is always smaller than anticipated, whereas the phase contrast across a n-n+ doping step is larger than expected. This work aims to elucidate the physical origin of the phase contrast measured by electron holography of doping structures, seeking to reconcile these discrepancies and enhance our understanding of the underlying mechanisms.

Methods
We use an n-n+ doping step in GaN with Si concentrations of $8\times10^{17}$ and $3.5\times10^{18}$ $cm^{-3}$ as our As model system. lamellas were prepared using focused ion beam (FIB) milling. The FIB-prepared lamellas are investigated by off-axis electron holography in a TEM (FEI Titan G2 60–300 HOLO, FEI instrument) operated at 300 kV. The lamella is kept at edge-on orientation and tilted away from the [10-10] zone axis to suppress the dynamical diffraction.

Results
An example of a phase map derived from a hologram acquired across GaN doping step is displayed in Fig. 1a. The investigated lamella exhibits a crystalline thickness of 257 ± 6 nm and a damaged layer on the surface due to FIB processing. [1] The corresponding phase change profile is plotted in Fig. 1b, showing that the difference in the phase contrast across the doping step is 0.40 ± 0.02 rad. Lamellas with crystalline thicknesses ranging from 188 to 380 nm were measured, indicating an almost thickness-independent phase contrast across the doping junction. For quantitative interpretation of the measured phase change profiles, self-consistent electrostatic potential calculations are carried out, taking the presence of a surface Fermi-level pinning of the TEM lamellas into consideration. By fitting experimental data with self-consistent electrostatic potential calculations, we revealed a surface Fermi-level pinning of 0.7 eV above the valence band in III-nitride lamella. From the calculation, we find the predominant contribution to the phase contrast is shown to arise from the doping-dependent screening length of the FIB-induced surface Fermi-level pinning occurring in the defect-rich crystalline inner shell (below the outer amorphous shell). This near surface depletion region remains unchanged for lamellas with different thicknesses, resulting in an almost constant electron optical phase contrast vs. thickness. The contribution of the built-in potential is almost negligible since its value is too small for modulation doping and only relevant for large built-in potentials at e.g. p-n junctions. Thus, the weak built-in potential of GaN doping steps adds only a small thickness dependence to the phase contrast. [2]

Conclusion

The electron optical phase contrast probed by electron holography at n-n+ GaN doping steps is found to exhibit a giant enhancement, in sharp contrast to the always smaller than expected phase contrast reported for p-n junctions. We unravel the physical origin of the giant enhancement by combining off-axis electron holography data with self-consistent electrostatic potential calculations. The predominant contribution to the phase contrast is shown to arise from the doping dependent screening length of the surface Fermi-level pinning, induced by FIB-implanted carbon point defects below the outer amorphous shell. The contribution of the built-in potential is negligible for modulation doping and only relevant for large built-in potentials at e.g. p-n junctions. This work provides a quantitative approach to so-called dead layers at TEM lamellas.

Graphic

Fig. 1. (a) Phase map across an n-n+ GaN doping step. The n-GaN layer exhibits a darker contrast. (b) Phase change profile extracted from the phase map averaged over a width of 500 nm. The n-n+ interface is positioned at 0 nm. The phase contrast across the doping step Δφ junction is 0.4 rad.

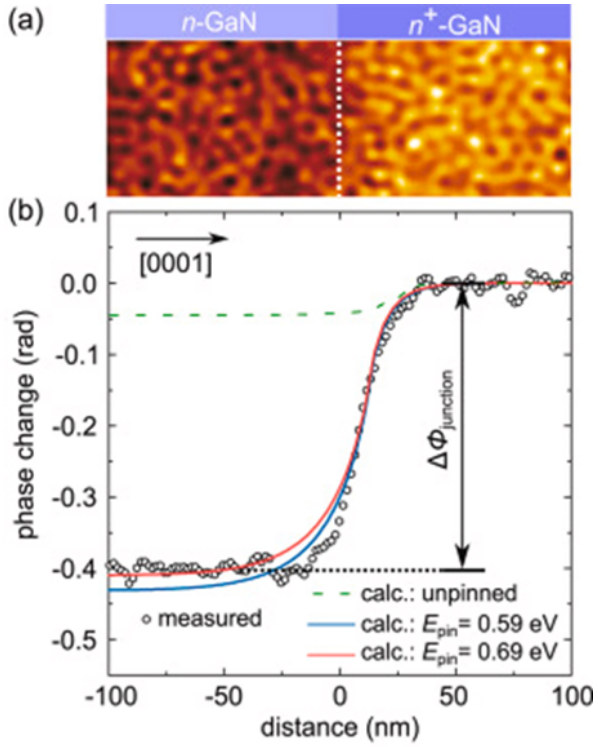


**Keywords:**

GaN, electron holography, surface pinning

**Reference:**

[1] K. Ji, M. Schnedler, Q. Lan, F. Zheng, Y. Wang, Y. Lu, H. Eisele, J.-F. Carlin, R. Butté, N. Grandjean, R.E. Dunin-Borkowski, Ph. Ebert. Appl. Phys. Express, 17 (2024), 016505.
[2] K. Ji, M. Schnedler, Q. Lan, J.-F. Carlin, R. Butté, N. Grandjean, R.E. Dunin-Borkowski, Ph. Ebert, Ultramicroscopy, 264, (2024) 114006.
[2] K. Ji, M. Schnedler, Q. Lan, J.-F. Carlin, R. Butté, N. Grandjean, R.E. Dunin-Borkowski, Ph. Ebert, Ultramicroscopy, 264, (2024) 114006.